

THE UNIVERSITY OF CALGARY

Evaluation of Mm-based NiMH Alloys for Batteries

by

Dusan Milicevic

A THESIS SUBMITTED TO THE FACULTY OF GRADUATE STUDIES
IN PARTIAL FULFILMENT OF THE REQUIREMENTS FOR THE
DEGREE OF MASTER OF SCIENCE

DEPARTMENT OF MECHANICAL ENGINEERING

CALGARY, ALBERTA

MAY, 1998

©Dusan Milicevic 1998



National Library
of Canada

Acquisitions and
Bibliographic Services

395 Wellington Street
Ottawa ON K1A 0N4
Canada

Bibliothèque nationale
du Canada

Acquisitions et
services bibliographiques

395, rue Wellington
Ottawa ON K1A 0N4
Canada

Your file Votre référence

Our file Notre référence

The author has granted a non-exclusive licence allowing the National Library of Canada to reproduce, loan, distribute or sell copies of this thesis in microform, paper or electronic formats.

The author retains ownership of the copyright in this thesis. Neither the thesis nor substantial extracts from it may be printed or otherwise reproduced without the author's permission.

L'auteur a accordé une licence non exclusive permettant à la Bibliothèque nationale du Canada de reproduire, prêter, distribuer ou vendre des copies de cette thèse sous la forme de microfiche/film, de reproduction sur papier ou sur format électronique.

L'auteur conserve la propriété du droit d'auteur qui protège cette thèse. Ni la thèse ni des extraits substantiels de celle-ci ne doivent être imprimés ou autrement reproduits sans son autorisation.

0-612-35022-3

ABSTRACT

This work analyzed the influence of stoichiometry, method of production and heat treatment on nickel metal hydride alloys. The arc melting process is described in details for $Mm_x(Ni-Co-Al)_5$, $x = 0.88-1.09$; $Mm(Ni-Co-Al)_x$ $x = 4.76-5.376$; $Mm_x(Ni-Co-Mn-Al)_5$ $x = 0.92-1.065$ and $Mm(Ni-Co-Mn-Al)_x$ $x = 4.77-5.42$. The induction melting process is described for two stoichiometric alloys, $Mm(Ni-Co-Al)_5$ and $Mm(Ni-Co-Mn-Al)_5$. Melting points were determined by DTA. Heat treatment was conducted in vacuum furnaces at 800°C and 1000 °C. P-C-T curves were measured for two commercial and two stoichiometric in house made alloys at 30°C and 40°C using Sievert's apparatus built in Westaim Co. These alloys were also measured electrochemically at room temperature using a standard Hg/HgO electrode. EDS was used for chemical analysis of matrix and grain boundaries of NiMH alloys. A new understanding of the influence of stoichiometry on crystal structure of NiMH alloys and crystal structure on discharge capacity and rate of discharge capability was achieved. Four new alloys compositions were produced and tested. One of them has a discharge capacity above 300 mAh/g and excellent rate capability. Some of them are not at all sensitive to high current discharge rate.

ACKNOWLEDGMENT

The author would like to express deep respect to his supervisor, Dr. William J. D. Shaw, for his guidance, moral and material support throughout the period of this work. I was never alone in difficulties.

The author would like to thank to The Department of Mechanical Engineering, The University of Calgary for financial help during the study.

Special thanks go out to Dr. John C. Currie and Dr. Bob Weir, Westaim Co. for their help and support and to all other Westaim personnel for their assistance.

DEDICATION

This work is dedicated to my daughters Natasa and Sladjana, my wife Simsa and my parents Jelenka and Simo Milicevic.

TABLE OF CONTENTS

APPROVAL.....	ii
ABSTRACT.....	iii
ACKNOWLEDGEMENT.....	iv
DEDICATION.....	v
TABLE OF CONTENTS.....	vi
LIST OF TABLES.....	xii
LIST OF FIGURES.....	xiii
NOMENCLATURE.....	xxi
ABBREVIATIONS.....	xxii
CHAPTER 1 INTRODUCTION.....	1
1.1 General Background.....	1
1.2 Purpose and Objectives.....	2
CHAPTER 2 HYDROGEN COMPOUNDS, HYDRIDES, LaNi ₅ and Mm-based NiMH ALLOYS.....	4
2.1 Hydrogen compounds, Hydrides.....	4
2.2 Properties of Hydrides.....	4
2.3 Characteristics of Metal Hydrogen System.....	5
2.4 Hysteresis Effect.....	7
2.5 Effect of Impurities.....	9
2.6 Characteristics of LaNi ₅ Alloy.....	9
2.6.1 Methods of Preparation of LaNi ₅	10
2.7 Crystal structure of LaNi ₅	12

2.8 Hydrogen Absorption and Desorption in LaNi_5	14
2.9 Characteristics of LaNi_5 -Hydride.....	16
2.10 The Influence of Partial Substitution in LaNi_5 on the Hydride Properties.....	17
2.11 LaNi_5 Electrode.....	20
2.12 Improvement in Cyclic Life of LaNi_5 Type Alloys.....	22
2.13 Mischmetal-based Nickel Metal Hydride Alloys.....	23
2.14 Sievert's Apparatus	25
2.15 Electrochemical Pressure Concentration Isotherms.....	26
2.16 Methods for Determination of Chemical Composition.....	29
2.17 Production of Mm-based NiMH alloys.....	30
2.18 Heat Treatment of Mm-based NiMH Alloys.....	34
2.19 Crystal Structure of Mm-based NiMH Alloy.....	35
2.20 Microstructure of Mm-based NiMH alloys.....	36
2.21 Mm-based NiMH Electrode.....	39
2.22 Discharge Capacity.....	40
2.23 Cyclic Life of Mm-based NiMH Electrode.....	41
2.24 The Rate Capability of Mm-based NiMH Alloy.....	47
2.25 Influence of Stoichiometry on Electrode Characteristics.....	48
CHAPTER 3 MATERIALS.....	53
3.1 Introduction.....	53
3.2 Materials Used in Melting Processes.....	53
3.3 Alloys Used In Production of Negative Electrodes.....	53

3.4 Materials Used in Sievert's Apparatus.....	55
3.5 Materials Used in Electrochemical Measurement.....	56
CHAPTER 4 EQUIPMENT AND EXPERIMENTAL METHODS	57
4.1 Introduction.....	57
4.2 Arc Melting Unit.....	57
4.2.1 Arc Melting Process.....	58
4.3 Induction Melting Furnace.....	59
4.3.1 Induction Melting Process.....	60
4.4 Measurement of Pressure Concentration Temperature (P-C-T) Curve	60
4.4.1 Sievert's Apparatus.....	60
4.4.2 Method of Measuring Gas Pressure Concentration Temperature Curve.....	62
4.4.3. Electrochemical Measurement of P-C-T Curve.....	65
4.4.3.1 Open Cell.....	65
4.4.3.2 Electrochemical Method of Measurement.....	65
4.5 Chemical Analysis of NiMH Alloys By Means of Inductively Coupled Plasma Optical Emission Spectrometry (ICP)	67
4.5.1 ICP Spectrometer.....	67
4.5.2 Method of Analysis by ICP.....	69
4.6 EDS Analysis and Metallography of NiMH Alloys.....	70
4.6.1 Description of Scanning Electron Microscope.....	70
4.6.1.1 Sample Preparation.....	70
4.6.2 A Determination of Chemical Composition of NiMH Alloys by EDS.....	71
4.7 XRD Analysis of NiMH Alloys.....	72

4.7.1 Diffractometer.....	72
7.7.2 Method of X-Ray Analysis of NiMH Alloys.....	73
4.8 Electrochemical Measurement.....	74
4.8.1 Equipment for Electrochemical Measurement.....	74
4.8.1.1 Negative Electrode.....	74
4.8.1.2 Positive Electrode.....	75
4.8.1.3 Open Cell.....	75
4.8.1.4 Battery Cycler.....	77
4.8.2 Method of Charging and Discharging of NiMH Battery.....	77
4.9 Differential Thermal Analysis of NiMH alloys.....	78
4.9.1 Differential Thermal Analyzer.....	78
4.9.2 Method of DTA Analysis of NiMH Alloys.....	78
CHAPTER 5 EXPERIMENTAL RESULTS.....	80
5.1 Introduction.....	81
5.2 Chemical Composition.....	81
5.2.1 Results of ICP Analysis.....	81
5.2.2 Results of EDS Analysis.....	81
5.3 Pressure Concentration Temperature Curves (P-C-T).....	82
5.3.1 Gas P-C-T Curves.....	82
5.3.2 Electrochemical Pressure Concentration Temperature Curves.....	87
5.4 XRD Results.....	90
5.5 Results of Electrochemical Discharge Capacity and Discharge Rate of NiMH Alloys	94

5.6 The Relationship Between Discharge Capacity and Cell Volume	104
5.7 Metallography of NiMH Alloys.....	108
5.8 Results of DTA Analysis.....	121
CHAPTER 6 GENERAL DISCUSSION AND ANALYSIS.....	123
6.1 Introduction.....	123
6.2 Chemical Composition.....	123
6.3 Pressure Concentration Temperature Curves (P-C-T).....	125
6.4 XRD Results.....	125
6.4.1 XRD Results of NiMH Alloys Without Manganese.....	125
6.4.2 XRD Results of NiMH Alloys With Manganese.....	135
6.5 Discharge Capacity and Rate capability Results.....	144
6.5.1 NiMH Alloys Without Manganese.....	144
6.5.2 NiMH Alloys With Manganese.....	150
6.6 Metallography Results.....	156
6.7 DTA Results.....	158
CHAPTER 7 CONCLUSIONS.....	159
CHAPTER 8 RECOMMENDATIONS FOR FUTURE WORK.....	162
REFERENCES.....	164
APPENDICES.....	173
Appendix 1 Chemical composition of $Mm_{0.99}Ni_{3.45}Co_{0.85}Mn_{0.41}Al_{0.31}IMW$ determined by ICP.....	174
Appendix 2 EDS analysis of matrix, rare earth rich phase, nickel alumina rich phase and oxides of NiMH alloys	175

Appendix 3 Discharge capacity, rate capability and stability of NiMH

alloys	177
--------------	-----

LIST OF TABLES

Table 2.1. Alloy processing condition for $\text{MmNi}_{3.55}\text{Co}_{0.75}\text{Mn}_{0.4}\text{Al}_{0.3}$ alloys	34
Table 2.2 X-Ray diffraction parameters of various Mm-based NiMH alloys.....	37
Table 3.1 Chemical composition of commercial and in Westaim produced alloys determined by ICP.....	54
Table 5.1 XRD results of NiMH alloy.....	91
Table 5.2 Comparison of cell parameters of alloys and hydrides.....	94
Table 6.1 Summary of influence of stoichiometry on cell volume of electrochemical characteristics of NiMH alloys without manganese	150
Table 6.2 The influence of stoichiometry on crystal cell and electrochemical characteristics of NiMH alloys with manganese.....	156

LIST OF FIGURES

Figure 2.1 Schematic phase diagram of metal hydrogen system, comprising the pressure-concentration temperature curves at various temperatures.....	6
Figure 2.2 Atomic arrangement in the RNi_5 ($R = Ni, Co$) structure ($CaCu_5$ structure) ...	12
Figure 2.3 Lattice constants as a function of composition of $LaNi_x$ annealed at 1200 °C and quenched	14
Figure 2.4 a and b. a) Absorption-desorption isotherms of $LaNi_5$ b) Desorption isotherms of $LaNi_5$ at different temperatures	15
Figure 2.5 Structure of the $LaNi_5$ intermetallic compound and two different sites occupied by deuterium	17
Figure 2.6 The capacity of $LaNi_5$ electrodes as function of the number of cycles, using a discharge current of 1.25 C and an additional discharge current 0.1 C (***).....	21
Figure 2.7 Influence of Mn, Al and Co substitution for $MmNi_5$ alloy system	24
Figure 2.8 A schematic diagram of the apparatus for determining pressure-composition isotherm	25
Figure 2.9 Comparison of pressure concentration isotherms by gas pressure and electrochemical methods for $LaNi_5$ anode	28
Figure 2.10 Influence of casting condition on pressure composition isotherms at 20, 40 and 60 °C including a) melt spinning b) arc melting c) arc melting and heat treatment at 1000 °C	31
Figure 2.11 SEM images of a) $LaNi_5$ showing evidence of second phase and b) as cast $MmNi_{3.55}Co_{0.75}Mn_{0.4}Al_{0.3}$ showing distribution of second phase in AB_5 matrix	38

Figure 2.12 Discharge capacity at 93 mA/g vs. cycle number for various mischmetal-based alloys.....	41
Figure 2.13 Influence of casting condition on capacity decay curves at 20 °C for $\text{MmNi}_{3.5}\text{Co}_{0.7}\text{Al}_{0.8}$ alloy prepared by induction melting	42
Figure 2.14 Discharge capacity vs. cycle curves for alloy electrodes at 20 °C (charge 186 mA/g, 2h, discharge; 93 mA/g to - 0.6V/Hg-HgO)	43
Figure 2.15 The influence of heat treatment temperatures of $\text{MmNi}_{3.5}\text{Co}_{0.7}\text{Al}_{0.8}$ alloy on capacity decay curves at 20 °C (charge 186 mA/g for 2 h, discharge 93 mA/g to - 0.6 V (Hg-HgO)	44
Figure 2.16 Effect of stoichiometric deviation on capacity decay curves at 20 °C for $\text{Mm}_x\text{Ni}_{3.5}\text{Co}_{0.8}\text{Mn}_{0.4}\text{Al}_{0.3}$: charge 186 mA/g for 2 h; discharge 93 mA/g to -0.6 V vs. Hg/HgO	46
Figure 2.17 Effect of heat treatment on capacity decay curves at 20 °C for $\text{Mm}_{0.95}\text{Ni}_{3.5}\text{Co}_{0.8}\text{Mn}_{0.4}\text{Al}_{0.3}$: charge 186 mA/g for 2 h, discharge 93 mA/g to -0.6 V vs. Hg/HgO electrode	46
Figure 2.18. Current dependence of discharge capacity at 20°C	47
Figure 2.19 Pressure concentration isotherms of $\text{Mm}(\text{Ni}_{0.64}\text{Co}_{0.2}\text{Al}_{0.04}\text{Mn}_{0.12})_{4.17}$	48
Figure 2.20 Hydrogen storage capacity of $\text{Mm}(\text{Ni}_{0.64}\text{Co}_{0.2}\text{Al}_{0.04}\text{Mn}_{0.12})_{4.17}$	49
Figure 2.21 Influence of method of preparation of $\text{Mm}(\text{Ni}_{0.64}\text{Co}_{0.2}\text{Al}_{0.04}\text{Mn}_{0.12})_{4.17}$ alloys on pressure concentration isotherm	50
Figure 2.22 a) Discharge capacity vs. cycle number and b) discharge efficiency as a function of the discharge current density for $\text{Mm}(\text{Ni}_{3.6}\text{Mn}_{0.4}\text{Al}_{0.3}\text{Co}_{0.7})_x$ alloys	51

Figure 2.23 Plots of hydrogen pressure against unit cell volume for MmB_x type alloy...	52
Figure 4.1 Sievert's apparatus.....	61
Figure 4.2 H-glass cell with standard Hg/HgO electrode.....	66
Figure 4.3 Open cell.....	76
Figure 5.1 P-C-T curves at 30 °C for IBA # 5. The upper curve is absorption and down curve is desorption.....	83
Figure 5.2 P-C-T curves for IBA #5 at 40 °C. The upper curve is absorption and the lower curve is desorption.	84
Figure 5.3 Pressure concentration temperature curves for $Mm_{0.99}Ni_{3.48}Co_{0.7}Al_{0.81}IMW$ at 30 °C. The upper curve is absorption and the lower curve is desorption.....	85
Figure 5.4 P-C-T curves at 30°C for IBA # 6. The upper curve is absorption and the lower curve is desorption.....	86
Figure 5.5 P-C-T curve for IBA # 6 at 40 °C. The upper curve is absorption and the lower curve is desorption.....	88
Figure 5.6 Pressure concentration temperature curve for $Mm_{0.99}Ni_{3.45}Co_{0.85}Mn_{0.41}Al_{0.31}IMW$ at 30 °C. The uppers curve is absorption and the lower curve is desorption.	89
Figure 5.7 Electrochemical pressure concentration temperature curves for IBA # 6 (1); $Mm_{0.99}Ni_{3.45}Co_{0.85}Mn_{0.41}Al_{0.31}IMW$ (2); IBA # 5 (3) and $Mm_{0.99}Ni_{3.48}Co_{0.7}Al_{0.81}IMW$ (4) obtained at room temperature using reference Hg/HgO electrode.....	90
Figure 5.8 Discharge capacity of NiMH alloys without Mn. Charge current was 184 mA/g for 2 h, discharge current were 92, 184, 248 mA/g to 0.6 V against $Ni(OH)_2$	97

Figure 5.9 Rate capability of NiMH alloys without Mn. Charge current was 184 mA/g for 2 h, discharge current were 92, 184, 248 mA/g to 0.6 V against Ni(OH) ₂	98
Figure 5.10 Discharge capacity for NiMH alloys with Mn. Charge current was 184 mA/g for 2 h discharge current were 92, 184, 248 mA/g to 0.6 V against Ni(OH) ₂	99
Figure 5.11 Rate capability of NiMH alloys with Mn. Charge current was 184 mA/g for 2 h, discharge current were 92, 184, 248 mA/g to 0.6 V against Ni(OH) ₂	101
Figure 5.12 Discharge capacity of commercial, arc melted and induction melted NiMH alloys. Charge current was 184 mA/g for 2 h, discharge current were 92, 184, 248 mA/g to 0.6 V against Ni(OH) ₂	102
Figure 5.13 Rate capabilities of arc melted, induction melted and commercial NiMH alloys. Charge current was 184 mA/g for 2 h, discharge current were 92, 184, 248 mA/g to 0.6 V against Ni(OH) ₂	103
Figure 5.14 Relationship between cell volume and discharge capacity mAh/g for NiMH ACW alloys.....	105
Figure 5.15 Relationship between discharge capacity mAh/g and cell volume of NiMH alloys heat treated at 800 °C.....	106
Figure 5.16 Linear relationship between cell volume and discharge capacity of NiMH alloys heat treated at 1000 °C.....	107
Figure 5.17 SEM Backscattered Electron Image (BSE) on Mm _{0.99} Ni _{3.5} Co _{0.7} Al _{0.81} ACW. Magnification 10 KV x 2000.....	109
Figure 5.18 SEM Backscattered Electron Image (BSE) on Mm _{0.99} Ni _{3.5} Co _{0.7} Al _{0.81} heat treated at 800 °C. Magnification 10 KV x 2000.....	110

Figure 5.19 SEM Backscattered Electron Image (BSE) of $\text{Mm}_{0.99}\text{Ni}_{3.5}\text{Co}_{0.7}\text{Al}_{0.81}$ heat treated at 1000 °C. Magnification 10 KV x 1000.....	110
Figure 5.20 SEM Backscattered Electron Image (BSE) on $\text{MmNi}_{3.54}\text{Co}_{0.82}\text{Mn}_{0.34}\text{Al}_{0.3}$ ACW Magnification 10 KV x 850.....	112
Figure 5.21 SEM Backscattered Electron Image (BSE) on $\text{MmNi}_{3.54}\text{Co}_{0.82}\text{Mn}_{0.34}\text{Al}_{0.3}$ heat-treated at 800 °C. Magnification 10 KV x 900.....	113
Figure 5.22 SEM Backscattered Electron Image (BSE) on $\text{MmNi}_{3.54}\text{Co}_{0.82}\text{Mn}_{0.34}\text{Al}_{0.3}$ heat-treated at 1000 °C. Magnification 10 KV x 900.....	113
Figure 5.23 SEM Backscattered Electron Image (BSE) of $\text{Mm}_{0.99}\text{Ni}_{3.48}\text{Co}_{0.7}\text{Al}_{0.81}\text{IMW}$. Magnification 10 KV x 500.....	117
Figure 5.24 SEM Backscattered Electron Image (BSE) of $\text{Mm}_{0.99}\text{Ni}_{3.48}\text{Co}_{0.7}\text{Al}_{0.81}\text{IMW}$ heat-treated at 800°C. Magnification 10 KV x 500.....	117
Figure 5.25 SEM Backscattered Electron Image (BSE) of $\text{Mm}_{0.99}\text{Ni}_{3.48}\text{Co}_{0.7}\text{Al}_{0.81}\text{IMW}$ heat-treated at 1000 °C. Magnification 10 KV x 3700.....	118
Figure 5.26 SEM Backscattered Electron Image (BSE) of $\text{MmNi}_{3.54}\text{Co}_{0.82}\text{Mn}_{0.34}\text{Al}_{0.3}\text{IMW}$. Magnification 10 KV x 500.....	118
Figure 5.27 SEM Backscattered Electron Image (BSE) of $\text{MmNi}_{3.54}\text{Co}_{0.82}\text{Mn}_{0.34}\text{Al}_{0.3}\text{IMW}$ heat-treated at 800 °C. Magnification 10 KV x 500.....	119
Figure 5.28 SEM Backscattered Electron Image (BSE) of $\text{MmNi}_{3.54}\text{Co}_{0.82}\text{Mn}_{0.34}\text{Al}_{0.3}\text{IMW}$ heat-treated at 1000 °C. Magnification 10 KV x 500.....	119
Figure 5.29 SEM Backscattered Electron Image (BSE) of IBA # 5.....	120

Figure 5.30 SEM Backscattered Electron Image (BSE) of IBA # 6.....	120
Figure 6.1 Influence of number of A-side atoms of NiMH alloys ACW (series 1) heat treated at 800 °C (series 2) and 1000 °C (series 3) without manganese on cell volume.....	126
Figure 6.2 Influence of A-side atoms on a -axis of $A_{0.88}B_5$, AB_5 and $A_{1.09}B_5$ -type NiMH alloys ACW (1) heat-treated at 800°C (2) and 1000 °C (3).....	128
Figure 6.3 Figure 6.2 Influence of A-side atoms on c -axis of $A_{0.88}B_5$, AB_5 and $A_{1.09}B_5$ -type NiMH alloys without manganese ACW (1), heat-treated at 800 °C (2) and 1000 °C.....	129
Figure 6.4 Influence of number of B-side atoms on cell volume of AB_x ($x= 4.76-5.376$) NiMH alloys without manganese, ACW (1), heat-treated at 800°C (2) and 1000 °C ...	131
Figure 6.5 Influence of number of B-side atoms on a -axis of AB_x ($x= 4.76-5.376$) NiMH alloys without manganese. ACW (1) heat-treated at 800°C (2) and 1000 °C.....	133
Figure 6.6 Influence of number of B-side atoms on c -axis of AB_x ($x= 4.76-5.376$) NiMH alloys without manganese. ACW (1) heat-treated at 800°C (2) and 1000 °C.....	134
Figure 6.7 Influence of number of A-side atoms on cell volume of A_xB_5 ($x = 0.92-1.065$) NiMH alloys with manganese ACW (1) heat-treated at 800°C (2) and 1000 °C.....	136
Figure 6.8 Influence of number of A-side atoms on a -axis of A_xB_5 ($x = 0.92-1.065$) NiMH alloys with manganese ACW (1) heat-treated at 800°C (2) and 1000 °C.....	137

Figure 6.9 Influence of number of A-side atoms on c-axis of A_xB_y ($x = 0.92-1.065$, $y = 5$) NiMH alloys with manganese ACW (1) heat-treated at 800°C (2) and 1000 °C.....	139
6.10 Influence of number of B-side atoms on cell volume of AB_x ($x = 4.77-5.42$) NiMH alloys with manganese. ACW (1) heat-treated at 800°C (2) and 1000 °C.....	140
Figure 6.11 Influence of number of B-side atoms on a-axis of AB_x ($x = 4.77-5.42$) NiMH alloys with manganese. ACW (1) heat-treated at 800°C (2) and 1000 °C.....	142
Figure 6.12 Influence of number of B-side atoms on a-axis of AB_x ($x = 4.77-5.42$) NiMH alloys with manganese. ACW (1) heat-treated at 800°C (2) and 1000 °C.....	143
Figure 6.13 Influence of heat treatment on discharge capacity of NiMH alloys. Series 1- ACW Series 2- heat-treated at 800°C, Series 3- heat-treated at 1000°C.....	145
Figure 6.14 Influence of number of A-side atoms on discharge capacity and rate capability of A_xB_5 ($x = 0.88-1.09$) NiMH alloys ACW and heat-treated at 800°C and 1000 °C without manganese.....	147
Figure 6.15 Influence of number of B-side atoms on discharge capacity and rate capability of AB_x ($x = 4.82-5.376$) NiMH alloys ACW and heat-treated at 800°C and 1000 °C without manganese.....	149
Figure 6.16. Influence of stoichiometry, method of production and heat treatment on discharge capacity of NiMH alloys with manganese. Series 1- ACW. Series 2-heat treated at 800°C, Series 3-heat treated at 1000°C.....	151

Figure 6.17 Influence of number of A-side atoms on discharge capacity and rate capability of A_xB_5 ($x = 0.92-1.065$) NiMH alloys ACW and heat-treated at 800°C and 1000 °C with manganese.....153

Figure 6.18 Influence of number of B-side atoms on discharge capacity and rate capability of AB_x ($x = 4.77-5.42$) NiMH alloys ACW and heat-treated at 800°C and 1000 °C with manganese.....154

NOMENCLATURE

$a(\text{H}_2\text{O})$	activity of water
$a(\text{H}_2)$	activity of hydrogen
E	electrode potential
E°	standard potential at 25 °C
E_{eq}	equilibrium potential
$E_{\text{eq}}(\text{H})$	equilibrium hydrogen potential
$E^\circ(\text{H})$	standard electrode potential of a $\text{H}_2\text{O}/\text{H}$ couple
$E^\circ(\text{HgO}/\text{Hg})$	standard electrode potential of a HgO/Hg couple
ΔG	free energy change
ΔH	enthalpy change
$p\text{H}_2$	hydrogen plateau pressure
$p_{\text{eq.}}$	equilibrium pressure
T	absolute temperature

ABBREVIATIONS

Ag	chemical abbreviation for silver
ACW	as cast in Westaim
AMW	arc melted in Westaim
α , β , α/β	phases
Al	chemical abbreviation for aluminum
atm.	abbreviation for atmosphere
B	chemical abbreviation for boron
BSE	Backscattered Electron Image
°C	degree Celsius
Ca	chemical abbreviation for calcium
Ce	chemical abbreviation for cerium
Co	chemical abbreviation for cobalt
Cu	chemical abbreviation for copper
dis. cap.	discharge capacity mAh/g
EPMA	electron probe microanalysis
Fe	chemical abbreviation for iron
H ₂	chemical abbreviation for hydrogen gas
Hf	chemical abbreviation for hafnium
Hg	chemical abbreviation for mercury
HgO	chemical abbreviation for mercury oxide
HPGA	high pressure atomization process
IMCs	intermetallic compounds

IMW	induction melted in Westaim
ICP	inductively coupled plasma emission spectroscopy
K	chemical abbreviation for potassium
La	chemical abbreviation for lanthanum
Li	chemical abbreviation for lithium
Mm	mischmetal
Mn	chemical abbreviation for manganese
MPa	megapascal
Mg	chemical abbreviation for magnesium
Ni	chemical abbreviation for nickel
NiMH	nickel metal hydride
Nd	chemical abbreviation for neodymium
O	chemical abbreviation for oxygen
Pd	chemical abbreviation for palladium
P-C-T	pressure concentration temperature
PTFE	polytetrafluoroethylene
PVA	polyvinyl alcohol
Pr	chemical abbreviation for praseodymium
RE	rare earth
SEM	Scanning Electron Microscopy
TEM	Transmission Electron Microscope

Tc	critical temperature
WDS	Wavelength Disperse Spectroscopy
ZAF	fluorescence correction

CHAPTER 1

INTRODUCTION

1.1 General Background

Rechargeable batteries utilizing a metal hydride anode and a NiOOH cathode are called nickel metal hydride batteries and are used in cellular phones, notebook computers, shavers, communication equipment, camcorders and another portable electronic devices. This type of battery is also candidate for development of electric vehicles. The market demand for NiMH battery is growing and could reach 3.5×10^9 cells in year 2005.

Nickel metal hydride alloys (NiMH) are multicomponent alloys, which may consist of nickel, cobalt, alumina, manganese, lanthanum, cerium, praseodymium, neodymium etc. NiMH alloys are intermetallic compounds (IMCs) which have stoichiometry A_aB_b and crystal structure that are different from either of parent elements. Based on stoichiometry there are certain classes of IMCs, in particular AB, AB_2 , A_2B and AB_5 . IMCs can react reversibly with hydrogen (H_2) to form hydride type $A_aB_bH_x$. The emphasis of this work is an investigation of AB_5 alloys and hydrides.

$LaNi_5$ alloy was studied for many years. In contact with hydrogen, $LaNi_5$ reacts rapidly [1] and absorbs and desorbs six hydrogen atoms at the ambient temperature and at pressures less than 0.25 MPa. $LaNi_5$ exhibits low hysteresis at room temperatures. It crystallizes in a hexagonal crystal structure. During hydrogen absorption and desorption the cell volume enlarges or decreases more than 23 %. $LaNi_5$ is not good a battery material because it has a good initial capacity but poor durability in KOH.

An advantage of AB_5 compounds is the ability for partial substitution of A and B-side elements with a variety of elements that may alter the characteristics of the alloys [1-5].

AB_5 compounds for electrode application should have plateau pressure below atmospheric and could be accomplished by partial substitution of nickel atoms with elements such as Al, Mn and Co.

Pure La is expensive. Mischmetal is a lower cost unrefined rare earth mixture and can replace La. The composition of mischmetal (Mm) depends on the mineral and ore body from which it is produced but usually consists of La, Ce, Pr and Nd. Partial replacement of La with Mm gives $MmNi_5$ alloy which exhibits a high plateau pressure at room temperature and hysteresis. Partial replacement of Co, Mn, Al into the Ni-side of $MmNi_5$ alloys lowers the plateau pressures and reduces hysteresis. For example $MmNi_{3.5}Co_{0.7}Al_{0.8}$ and $MmNi_{3.5}Co_{0.8}Mn_{0.4}Al_{0.3}$ compounds have a low plateau pressure, high discharge capacity and good durability or cyclic life in battery applications. In comparison with $LaNi_5$ Mm-based alloys have lower initial discharge capacity but much better cyclic life.

1.1 Purpose and Objectives

The purpose of this investigation was to study the influence of stoichiometry, methods of production and heat treatment on crystal structure and electrochemical characteristics of Mm-based NiMH alloys with and without manganese.

The objective was to evaluate and develop Mm-base NiMH alloys for use in new battery development. The work was concentrated on evaluation of two commercial available

alloys and developing nonstoichiometric and stoichiometric in house made alloys based upon current literature information as well as preliminary results obtained from this project. The in house made alloys were evaluated in comparison with two chosen commercial alloys. As a part of objective new unknown chemical composition of NiMH alloys has been developed and evaluated having high discharge capacity and excellent rate capability.

CHAPTER 2

HYDROGEN COMPOUNDS, HYDRIDES, LaNi_5 and Mm-based NiMH ALLOYS

2.1 Hydrogen Compounds, Hydrides

Hydrogen reacts with many elements to form hydrides. If hydrogen reacts with a pure element the product of reaction is a binary hydride. All hydrides can be divided in four classes: (1) gaseous or volatile hydrides, (2) polymeric hydrides, (3) salt-like hydrides, and (4) metallic hydrides. There are also the ternary compounds of hydrogen. The ternary compounds of hydrogen are called alloy hydrides.

Researchers [1-5] have been interested in the reaction of hydrogen with intermetallic compounds of transition elements. Some properties of these metallic hydrides are important for the description of the formation of ternary hydrogen compounds. All transition elements can be expected to form metallic hydrides. Some of them [2] have not been observed because they would be stable at only extremely high pressures.

The main difference between all metallic true ternary hydrides and binary ones is that ternaries are metastable as a rule.

2.2 Properties of Hydrides

A basic property of hydrides is the storage of hydrogen to a density, which often exceeds the density of liquid. The reversibility of reaction is a very useful property because this characteristic is used in rechargeable batteries. Large numbers of alloys, elements and

compounds reacts with hydrogen in a reversible manner. The absorption (formation of hydride) and desorption (formation of hydrogen and an alloy) take place at the same pressure and temperature. Some alloys in contact with hydrogen exhibits hysteresis. Intermetallic compounds that react reversibly at room temperature and atmospheric pressure are promising materials for hydrogen storage and battery applications. Other properties in addition to reversibility of reaction and storage capacity are the rate of absorption (kinetics of reaction) and desorption, constancy of equilibrium pressure during the reaction at constant temperature and sensitivity of reaction products to impurities.

2.3 Characteristics of Metal Hydrogen System

The absorption and desorption of hydrogen by metals is most conveniently represented [2,3] by a pressure composition temperature (P-C-T) curve. A schematic diagram of such a curve is given in Figure 2.1.

A small amount of hydrogen dissolves in a metallic host according to reaction:



where M is nickel metal hydride alloy, y is number of hydrogen atoms and x is number of hydrogen atoms in a hydride.

The absorbed hydrogen atoms occupy interstitial site [3] in the metallic lattice and their concentration depends strongly on hydrogen pressure. The next steps involves absorption of hydrogen atoms after the solid solution is saturated:



The transition to MH_x is the absorption process, the reverse reaction is the desorption process.

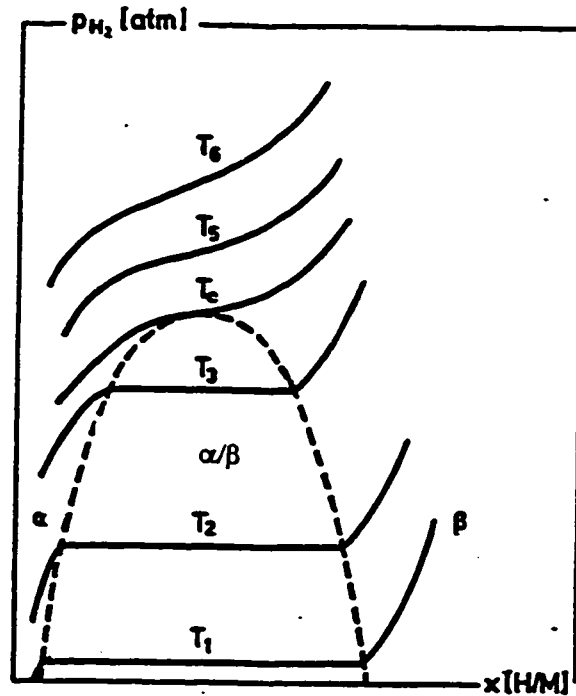


Figure 2.1 Schematic phase diagram of metal hydrogen system, comprising the pressure-concentration temperature curves at various temperatures [2,3]

Since the reaction is exothermic the heat of reaction must be supplied during desorption by external heating. At low hydrogen concentration there is strong dependence of hydrogen pressure. The region on Figure 2.1 the so called α phase is a metal phase unable to dissolve a large amount of hydrogen. The next is α/β region where the saturated solid solution in α phase is in equilibrium with the hydrogen deficient β phase.

Ideally during α/β transition the equilibrium pressure remains constant according to [3,4] Gibbs' rule $F=C-P+2$. Two components C (H_2 and metal) and three phases P (two solids and one gaseous) are present and the number of degrees of freedom is one. At a given temperature, the pressure is constant. This pressure is called the plateau pressure. Further absorption process is accompanied by an increase of equilibrium pressure. The concentration region determined by the horizontal parts of isotherms can be regarded as the miscibility gap between two well-defined phases [1,3]. It originates from the fact that partial heat of solution of hydrogen, starting from a hydrogen free compound becomes more exothermic so that it is more favorable for hydrogen atoms to be concentrated locally rather than being distributed evenly throughout the metal [1,3]. At higher temperatures the influence of entropy counteracts this tendency to form two separate phases so the miscibility gap may disappear. This point is critical temperature T_c .

2.4 Hysteresis Effect

Absorption or desorption of hydrogen is accompanied by a large volume change [1-5] in all hydride systems. This leads to elastic strains in the system when the material has high yield strength or when elasto-plastic strains have occurred in material that has low yield strength. Therefore during the hydrogen absorption the β phase grows under compressive stresses, alternately during desorption the α phase grows under tensile stresses. The process [6] of hydrogen absorption and desorption is not strictly reversible and this results in hysteresis. In most hydrogen systems, the origin of hysteresis is due to elastic or

elastoplastic accommodation of the volume changes that occur during hydride formation and decomposition.

Three type of hysteresis [6] can be identified in a metal hydrogen system: pressure hysteresis, solvus hysteresis and thermal hysteresis. At a fixed temperature, the equilibrium hydride formation pressure is always greater than the equilibrium hydride decomposition pressure. This is referred to as the pressure hysteresis. At a fixed temperature, solvus hysteresis is the phenomenon where the thermal solid solubility of hydrogen in the metal is higher during hydride formation than during hydride decomposition. In thermal hysteresis, at a fixed hydrogen concentration, the hydride formation temperature during cooling down of metal containing hydrogen is lower than the hydride decomposition temperature when heating the metal.

Hysteresis could be attributed to the metastable nature of the α and β phases which leads to oversaturation of the α phase on absorption and undersaturation of the β phase on desorption.

Hysteresis may be related to the defects in the lattice and some authors [1,2,5] propose that desorption pressure should be the actual pressure for nonstoichiometric hydrides because the removal of hydrogen from stoichiometric hydrides creates hydrogen vacancies in the nonstoichiometric hydride.

Hysteresis loss of energy could be related [6] to the energy required for dislocation production in the matrix during hydride formation and decomposition. Hysteresis loss could be related thermodynamically to dislocation formation in the metal matrix during hydride formation.

2.5 Effect of Impurities

The effects of non-transition metals impurities on the stability and hydrogen absorption characteristics are highly relevant. The contamination [7] by oxygen, nitrogen and other non-transition metal impurities present a great problem. For instance, the effect of oxygen on LaNi_5 would be the precipitation of La_2O_3 and an equivalent amount of Ni metal. Since neither of these two phases contributes to the absorption isotherm, this would result in decrease of absorption capacity.

If nickel is retained in the lattice [8] by quenching the alloy from high temperatures, the effect of oxygen leads to changing the absorption isotherms from that of LaNi_5 to that of $\text{LaNi}_{5.4}$.

2.6 Characteristics of LaNi_5 Alloy

LaNi_5 reacts rapidly with hydrogen at room temperature and equilibrium pressure about 0.2 MPa. It can store 6 hydrogen atoms per mole LaNi_5 . Partial replacement of Ni atoms by Co decreases the storage capacity and the cell volume change. The cell volume change decreases from about 23 % to about 15 %. Partial replacement of Ni atoms by Al and Mn [1,2,5,8] lowers the plateau pressure. After a couple cycles of hydrogenation, LaNi_5 , becomes a very fine powder. In contact with KOH LaNi_5 has an initial discharge capacity about 370 mAh/g but very poor durability.

2.6.1 Methods of Preparation of LaNi₅

LaNi₅ can be prepared by arc melting under argon along with a water-cooled copper base plate, induction melting and high-pressure gas atomization [1-4,9].

In order to prepare the alloy pellets in the arc unit, the metal mixture in a correct weight ratio, has to be introduced in the arc furnace, outgased for many minutes [1,2,4] and purged with argon. The argon gas is necessary to produce the arc. The metal mixture is melted in an arc between a movable, water-cooled tungsten rod and the sample on a water-cooled copper plate. To obtain better homogeneity, the sample has to be turned over a couple times and remelted. After melting, the sample has to be annealed [1, 5]. Samples have to be placed in Al₂O₃ crucibles, which are then sealed into small-evacuated silica tubes [5]. After a heat treatment lasting 3-7 days at 950 °C the silica tube has to be quenched in water [5]. An annealing temperature $t > 1100$ °C in argon has been reported [1]. Homogeneous alloys up to 20 g can be prepared this way.

For the preparation of larger quantities an induction unit must be used. The nickel is put in a fireclay crucible positioned in a radio frequency coil. The lanthanum is kept in a special holder above the crucible to avoid loss by evaporation. The furnace must be evacuated and Ni outgased during the heating period. When nickel melts, argon is introduced into the furnace at a pressure of 0.025 kPa and small pieces of lanthanum are rapidly dropped into the melt. The melt is poured out into a graphite crucible or water-cooled copper plate in order to induce rapid cooling. In this way a sample over 3 kg. can be prepared.

Al_2O_3 crucible does not react with the melt as long as the temperature of the melt is kept within 100-200 ° C of the alloy melting point [7].

A high-pressure gas atomization process (HPGA) can be used in production of LaNi_5 alloy [9]. The discrete jet/confined feed atomization nozzle directs cold (20 °C to -40 °C) argon gas traveling at speeds of about mach three to disintegrate a stream of molten alloy into fine spherical droplets. A key advantage for HPGA is better homogeneity because of a rapidly solidified microstructure. LaNi_5 alloys used for reversible hydrogen storage have very specific compositional requirements since the hydrogen is stored in the interstitial sites in the hexagonal compound. Variation in the size of the interstitial sites due to compositional variation leads to local variation in hydrogen storage capacity and transport that can result in reduced overall material performance. Even though the LaNi_5 has an invariant melting point, an unusual variation in the high -temperature solid solubility appears to be responsible for the common observation that ingot casting produces a microstructure with segregation across primary LaNi_5 dendrites even in a stoichiometric high purity alloy. This inhomogeneity leads to inconsistent hydrogen absorption properties and limits the performance of devices produced from these materials. In fact, a common practice is to anneal cast ingots of the alloy for periods of about one month to homogenize the typical cast microstructure. This method (HPGA) provides an alloy with a very high degree of homogeneity.

Chemical composition of LaNi_5 can vary because of evaporation of La. The microprobe analysis was reported [10] as $\text{LaNi}_{5\pm 0.02}$. In contact with oxygen, La forms La_2O_3 or $\text{La}(\text{OH})_3$. With each cycle of hydrogenation the segregation (diffusion of La to the surface) continues and the fresh nickel precipitates out [11].

LaNi₅ has a congruent melting point at 1350 °C [1,12] with a relatively large homogeneity region. On the Ni-rich side the sample with a composition outside of the homogeneity region has a fine nickel precipitate on the grain boundary as well as inside the grains. The nickel deficient sample, after quenching has a microstructure with small amounts of Ni-deficient phase on the grain boundaries.

2.7 Crystal structure of LaNi₅

The RCo₅ and RNi₅ (R = La, Ce, Pr, Nd) compounds crystallize in the hexagonal CaCu₅ type of structure [1,5]. Figure 2.2 shows the atomic arrangement, consisting of an alternate stacking along the c-axis of two different layers.

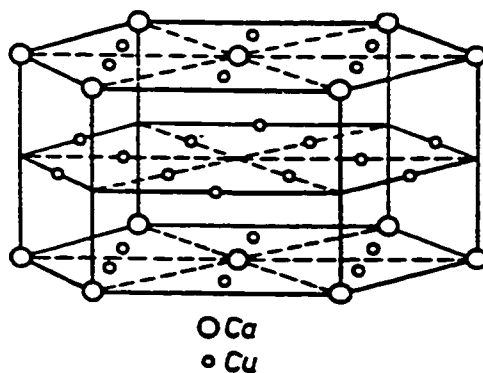


Figure 2.2 Atomic arrangement in the RNi₅ (R = Ni, Co) structure (CaCu₅ structure) [5].

The layer at $z = 0$ is closed packed and contains one La atom and two Ni atoms per unit cell. The layer at $z = \frac{1}{2}$ is close-packed with a quarter of the atoms missing, leaving three Ni atoms per unit cell. It is stacked relative to the layer at $z = 0$ in such a way that the

vacancies are centered on the nearest neighbor La-La connecting lines. Thus the La atoms are surrounded by six Ni atoms in each of the layers at $z = 0$ and $z = \pm \frac{1}{2}$, giving a total coordination number for La by Ni of 18.

The crystal structure is described in space group $P6/mmm$ with the atomic positions: La on 1a viz. (0,0,0) Ni^I on 2c, viz. (1/3, 1/3, 0), (2/3, 1/3, 0), and Ni^{II} on 3g viz. (1/2, 0, 1/2), (0, 1/2, 1/2), (1/2, 1/2, 1/2).

The formation of the hexagonal AB_5 type of structure is in accordance with the Dwight's rule that the hexagonal form is only stable if the radius ratio of the elements $r_a / r_b > 1.3$. Compounds with smaller atomic ratio than 1.3 crystallize in UNi_5 type of structure. It was shown that the limit 1.3 is not critical in the sense that cubic structures are not stable at larger values. There are compounds with radius ratios up to 1.42, which has the cubic UNi_5 structure.

The variation of cell parameters with change of number of nickel atoms in $LaNi_5$ is depicted in Figure 2.3. The deviation towards nickel deficient side causes decrease of c -axis and increase of a -axis. The deviation towards nickel sufficient side causes increases of c -axis and decreases of a -axis.

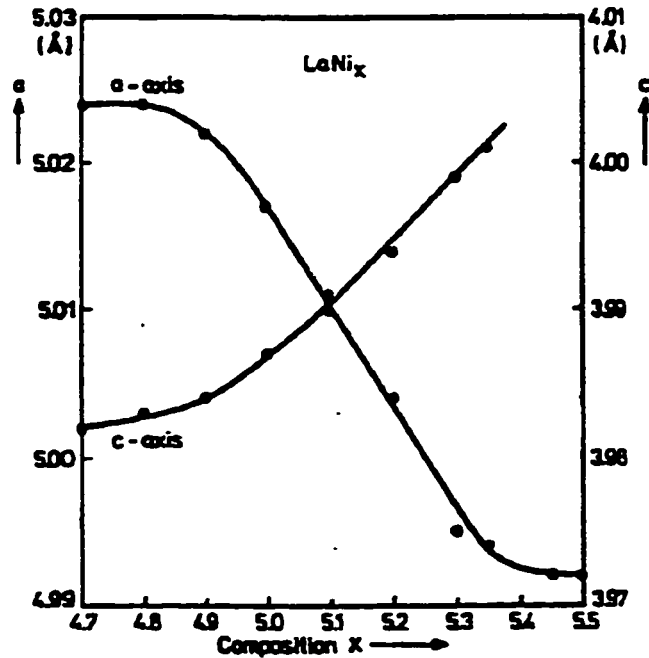
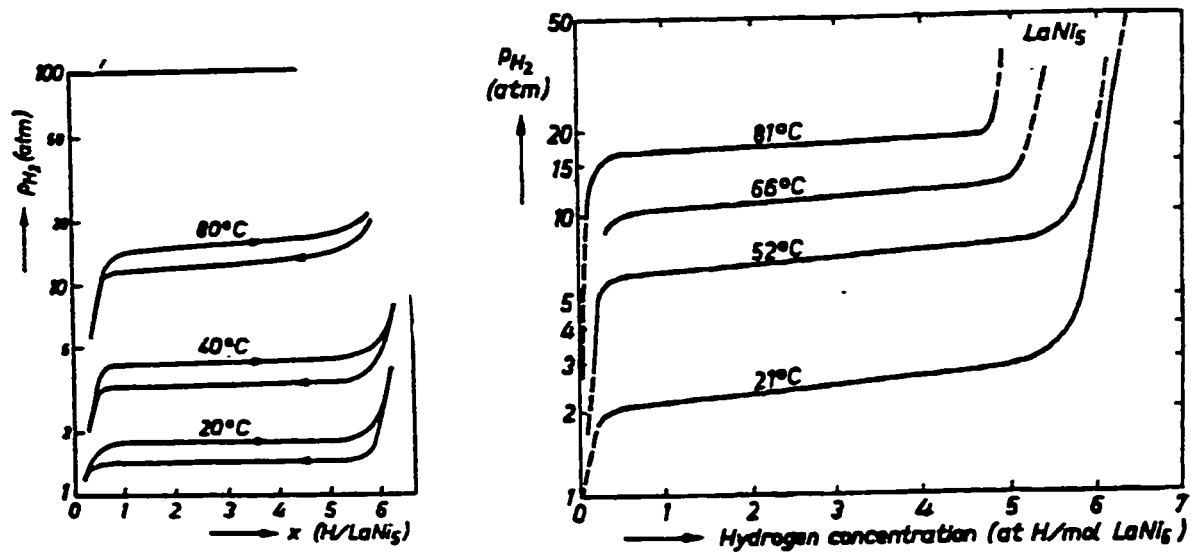


Figure 2.3 Lattice constants as a function of composition of LaNi_x annealed at 1200 °C and quenched [1,12].

2.8 Hydrogen Absorption and Desorption in LaNi_5

Absorption and desorption isotherms (P-C-T) for LaNi_5 at 20 °C, 40 °C and 80 °C and desorption isotherms at 21 °C, 52 °C, 66 °C and 81 °C are depicted in Figure 2.4. There is no difference in desorption pressure at 80 °C for LaNi_5 . The only differences are due to inhomogeneity.

Samples with a high degree of homogeneity [1] show an almost horizontal part in the P-C-T curve. A "sloping" plateau indicates samples having more inhomogeneity [14].



a) b)
Figure 2.4 a and b. a) Absorption-desorption isotherms of LaNi₅ [1] b) Desorption isotherms of LaNi₅ at different temperatures [14]

The change in number of nickel atoms causes the change of lattice constants. For LaNi_x the cell volume as well as the stability of the hydride decreases from 86.96 Å³ for $x = 4.9$ in to 86.41 Å³ for $x = 5.4$ [1,12]. The equilibrium pressure increases and absorption capacity decreases from LaNi_{4.9} (3 atm) to LaNi_{5.4} (9 atm). The variation in cell volume can be explained by a random substitution of a pair of nickel atoms for some of the lanthanum [1,12,13].

2.9 Characteristics of LaNi₅-Hydride

Numerous studies have been conducted to gain an understanding of factors that influence the hydride behavior of various intermetallic compounds in terms of their stability, stoichiometry and the preferred interstitial sites for occupation by hydrogen atoms [1-5,10,12-15]. One of the factors, which have an influence on hydride behavior, is critical lattice parameter i.e. minimum cell size [16, 17]. For each type of structure, there must be a critical hole size for hydrogen occupation. In stable hydrides, occupation sites by hydrogen is possible only for interstices that can accommodate a sphere of radius $r > 0.4\text{\AA}$. The distance between two H-H atoms appears to be never less than 2.1 \AA . The repulsive interaction near-neighbor hydrogen atoms is widely accepted and can help explain why hydrogen atoms do not fill all seemingly available interstices.

This was the basis for a so-called geometric model. This model explained why hydrogen atoms occupy only 6 position in alloy cell, but did not explain or rationalize stability of hydrides.

The generally accepted model for the location [18] of hydrogen atoms in the LaNi₅H_x has the hydrogen atoms occupying two different sites: an octahedral site (Figure 2.5) D(1) composed of two La, two Ni(1) and two Ni(2) atoms, and a tetrahedral site D(2) composed of two La and two Ni(2) atoms. The LaNi₅ stores three hydrogen atoms at D(1) sites and three hydrogen atoms at D (2) sites, causing lattice expansion of the **a**-axis ($\Delta a / a$) by about 6% and of the **c**-axis $\Delta c / c$ by about 6 % i.e. change of the cell volume (V) by 24,3 % .The estimated volume of hydrogen in LaNi₅H_x is 2.4 \AA^3 or 1.44 cc/mole [18].

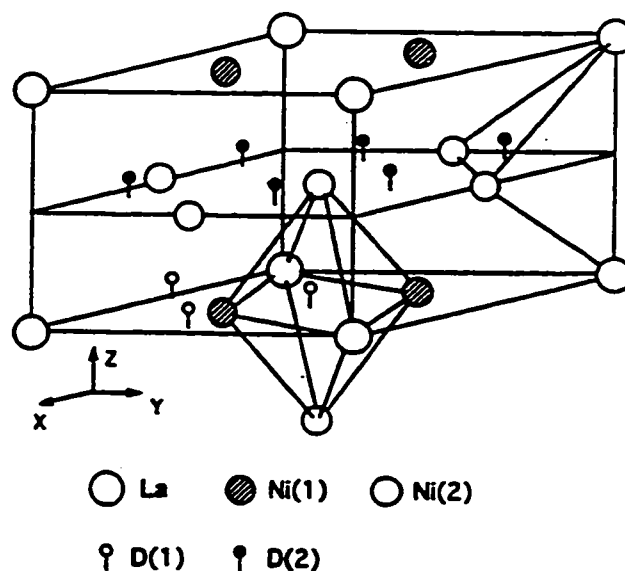


Figure 2.5 Structure of the LaNi_5 intermetallic compound and two different sites occupied by deuterium [18].

2.10 The Influence of Partial Substitution in LaNi_5 on the Hydrating Properties

LaNi_5 is an isostructural binary compound [19]. Isostructural pseudobinary compounds can be obtained by replacing some of either the lanthanum atoms or the nickel atoms by a third metal.

Replacing nickel atoms by cobalt in LaNi_5 has a large effect on the stability of the hydrides. System $\text{LaCo}_{5x}\text{Ni}_{5-5x}$ ($x = 0$ to 1) exhibits two plateau pressures. The first hydrides of all compounds except $x = 0$ have a limiting concentration of about 3.5 hydrogen atoms per mole of the compound [1, 13]. XRD analysis showed that increase in

x value leads to a marked increase of a-axis, whereas the c-axis shows only a relatively small variation [13].

Replacing nickel atoms by other transition metals also has a large influence on the stability of hydrides. The pressure concentration isotherms for system LaNi_4M ($\text{M} = \text{Pd}, \text{Ag}, \text{Cu}, \text{Co}, \text{Fe}, \text{Cr}$) shows that the lowest hydride stability occurs when $\text{M} = \text{Pd}$. Replacement of nickel atoms with other elements tends to increase stability. The compound LaNi_4Cr forms the most stable hydrides. The replacement of Ni atoms by Mn causes a strong increase in stability of hydride; 10% of Mn is sufficient to reduce plateau pressure to below one atm. The intermetallic compound LaNi_4Cu forms a hydride with a constant plateau pressure at room temperature and relatively large sorption capacity ($\text{LaNi}_4\text{CuH}_{5.6}$).

Replacing La atoms by a third element also has a large influence on the stability of hydrides. Replacement of 20 % of La atoms in LaNi_5 by Nd, Gd, Y, and Er causes a big decrease in the stability of the hydride [1].

The stability of hydrides decreases if the La atoms are replaced by Zr or Th atoms [1,19]. Whilst the $\text{La}_{1-x}\text{R}_x\text{Ni}_5$ solid solution exists over the whole range of concentrations, this is not always the case in LaNi_{5-x} series [19]. The limit of substitution varies according to the substitution element x (Si) = 0.6; x (Fe) = 1.2; x (Al) = 1.3; x (Mn) = 2.2 and x (Cu) = x (Co) = x (Pt) = 5. This limit depends strongly on the atomic size, electronic properties of elements, and also on the annealing treatment.

The dimensions of unit cells changes by substitution. The volume varies linearly with the number of substitution x : it decreases in $\text{La}_{1-x}\text{R}_x\text{Ni}_5$ and it increases in $\text{LaNi}_{5-x}\text{M}_x$. The distribution of the substitution atoms has been studied by neutron powder diffraction

analysis in some $\text{LaNi}_{5-x}\text{M}_x$ [17,19,20] compounds and by Mossbauer spectroscopy in the case of iron substitution for Ni [21]. The partial substitution of Ni has been found to occur in a disordered fashion but mainly in the $z = 1/2$ plane which is a less dense atomic plane: in $\text{LaNi}_{5-x}\text{Al}_x$ ($x < 1$) and $\text{LaNi}_{4.5}\text{Si}_{0.5}$ Aluminum and silicon atoms occupy only the 3g position, whereas some cobalt [13], manganese [17,19,20] and iron [21] atoms occupy also the 2c position of the basal plane in LaNi_4Co , $\text{LaNi}_{5-x}\text{Mn}_x$ ($x < 2$) and LaNi_4Fe respectively. An exception is for copper atoms in LaNi_4Cu , which are found [19] in both atomic planes with a slight preference for 2c sites.

As a general rule, the partial substitution in LaNi_5 results in a smaller hydrogen content of related hydrides. Among the $\text{LaNi}_{5-x}\text{M}_x\text{H}_y$ series, the absorption and desorption capacity is strongly affected by the type and rate of substitution.

When aluminum is substituted for nickel, absorption capacity decreases from 6.2 hydrogen atoms per mole in $\text{LaNi}_{4.9}\text{Al}_{0.1}$ to 4.8 hydrogen atoms per mole in LaNi_4Al [10,17,19,20]. Whereas in the manganese substituted series absorption capacity is nearly equal to six hydrogen atoms per mole over the whole range of substitution ($0 < x < 2$). LaNi_4Al compound has a smaller capacity because aluminum atoms occupy $z = 1/2$ plane and 4h and 120 sites are very close to metallic atoms in $z = 1/2$ plane and that two sites are no longer able to contain hydrogen atoms when aluminum atoms occupy this plane.

The replacement of lanthanum, in the LaNi_5 alloy by cerium, praseodymium, neodymium and samarium increases the equilibrium pressure. Samarium and cerium have a significant influence on the equilibrium pressure of hydrogen. Cerium produces a significant hysteresis effect in $\text{La}_{1-x}\text{Ce}_x\text{Ni}_5$ system [22]. Partial replacement of lanthanum

in LaNi_5 generally leads to an increase of the equilibrium plateau pressure. In contrast, partial replacement of nickel leads to the lowering of equilibrium pressure. Manganese and aluminum substituted compounds form very stable hydrides: at 40 °C $p_e \approx 5 \times 10^{-3}$ atm. for $\text{LaNi}_4\text{MnH}_6$ and $p_e \approx 1.6 \times 10^{-2}$ atm for $\text{LaNi}_4\text{AlH}_{4.8}$ compared with 3.7 atm. for $\text{LaNi}_5\text{H}_{6.4}$. Exceptions occur with platinum and palladium substitution for which an increase in p_e is found.

At any given temperature, the equilibrium pressure of hydrides decrease exponentially when the unit cell volume of intermetallic increases. This allows the prediction of required plateau pressure for the corresponding cell volume and the rate of substitution according to a substitution family. This correlation is equivalent to the one, which shows that ΔG increase linearly with cell volume. This rule is valid for most pseudobinary AB_5 compounds, but deviation from the general rule has been observed for platinum, cooper, and iron and silicon substitution.

2.11 LaNi_5 Electrode

A galvanic cell is a device [3,4,23-25] that converts chemical energy directly into electrical energy. Such a cell consists of two electrodes, spatially separated from each other but in contact via an electrolyte. Whereas one of the electrodes is oxidized, releasing electrons (the negative electrode) the other one is preferentially reduced accepting electrons (positive electrode). When the electrons flow through an external load from the negative electrode to the positive electrode the cell is discharged and the

electrical energy is induced. A cell is rechargeable if the cell reaction can be made to proceed in the opposite direction by imposing an external potential difference.

During charge/discharge cycles in KOH the capacity of LaNi_5 electrodes declined drastically. Storage capacity of a LaNi_5 electrode as a function of the number of charge/discharge cycles as depicted in Figure 2.6.

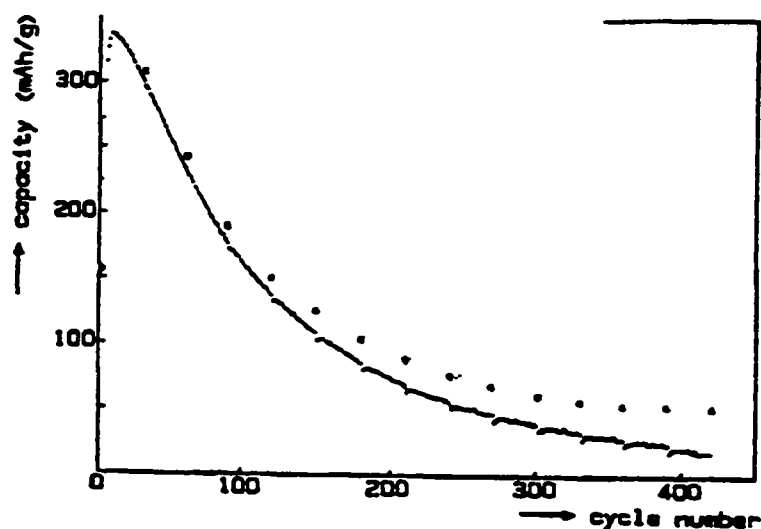


Figure 2.6 The capacity of LaNi_5 electrodes as function of the number of cycles, using a discharge current of 1.25 C and an additional discharge current 0.1 C (***) [3,4,26]

After cycling, tested electrodes showed additional X-Ray diffraction peaks due to La(OH)_3 [3,4] and metallic nickel. A rapid increase in BET (Brunauer-Emmet-Teller method of measuring specific surface area) surface was [26] due to the formation of La(OH)_3 . From the thermodynamic aspect, the oxidation of lanthanum in KOH solution

is unavoidable. The free energy change of LaNi_5 oxidation, $\Delta G = -472 \text{ kJ/mole}$ is almost two times the enthalpy change of LaNi_5 formation, $\Delta H = -273 \text{ kJ/mole}$, giving the alloy a strong driving force for segregation in the aqueous solution. The surface layer, [3,4,27] composed of lanthanum oxides and metallic nickel, would give the alloy a kinetic barrier for further oxidation of lanthanum. However, LaNi_5 is brittle. The large lattice expansion during cycling [1-5,26] causes cracking of the alloy, damaging the protective layer and forming continuously fresh surfaces. During 1000 cycles of gas absorption and desorption, LaNi_5 powder starting in the range of $100 \mu\text{m}$ was pulverized to fine powder of $2.6 \mu\text{m}$ in diameter [11]. It was proposed [27] that there was direct oxidation of LaNi_5 to $\text{La}(\text{OH})_3$ and $\text{Ni}(\text{OH})_2$ during cycling followed by the reaction of the $\text{Ni}(\text{OH})_2$ with underlying LaNi_5 . The decay rate decreased with increase of the initial oxygen content although the capacity greatly decreased. When only 40 percent of the alloy oxidized, the discharge capacity became zero because the remaining alloy would be completely isolated from the current collector. The decay rate of the electrode increased with increasing contact time with KOH solution. The decrease in KOH concentration from 6M to 0.6 M leads to a drastic decrease in the discharge capacity because of the increase in electrolyte resistance.

2.12 Improvement in Cyclic Life of LaNi_5 Type Alloys

Reduction of the lattice expansion during hydriding leads to a more stable hydride electrode [3-5,8,18]. Partial substitution of cobalt for nickel results in a considerable

reduction of cell expansion during hydrogen absorption. The stability of the electrodes which was expressed by the capacity ratio of the initial cycle to the 400th cycle, becomes higher with increasing cobalt content from $x = 0$ to $x = 3.3$ i.e. with decreasing volume cell expansion from 24.3% for LaNi_5 to 15.1 % for $\text{LaNi}_{2.5}\text{Co}_{2.5}$. The volume expansion ratio decreased especially in the c-axis direction. The lattice expansion along the c-axis is expected to have more influence on cracking because the alloys have a layered structure with ABAB stacking sequences. The same anisotropic effect of lattice expansion has silicon substituted for nickel. In addition to volume expansion during hydrogen formation, the decrepitation rate decreased with decreasing Vickers hardness in the order of $M = \text{Mn} > \text{Ni} > \text{Cu} > \text{Cr} > \text{Al} > \text{Co}$ for $\text{LaNi}_{5-x}\text{M}_x$, thus increasing the cyclic life of alloys [18,28,29]. The addition of cobalt was useful to improve the mechanical properties i.e. to give the alloy more ductility. The LaNi_4Al alloy has very low plateau pressure and long cyclic life. The substitution of manganese provided the alloy with a higher hardness and shorter cyclic life. The replacement of La by Zr was effective for improving the cyclic life because Zr prevents decrepitation.

2.13 Mischmetal-based Nickel Metal Hydride Alloys

Replacement of La atoms by mischmetal in LaNi_5 leads to MmNi_5 alloy [8,30-33]. It is less expensive because of the lower price of mischmetal as compared to lanthanum. Mischmetal is a mixture of rare earth. Mm consists of La, Ce, Pr, Nd, Sm and other rare earth depending on the ore. Chemical composition can vary. For example, mischmetal could have La 28 %, Ce 40 %, Pr 14 %, Nd 4 %, other rare earth 7 %, Fe 5 % and Al, Ca,

Mg 2% [31] or La 28%, Ce 40 %, Pr 4 %, Nd 14 %, other rare earth 7 %, Fe 5%, Al, Mg, Ca 2 % [32] or La 30%, Ce 52%, Pr 5%, Nd 13 % [33] by weight percentage. Different chemical composition affects some characteristics of the alloys such as plateau pressure, sensitivity to oxidation and crystal structure. That is why alloys with the same nominal composition sometimes have different characteristics. MmNi_5 has a high plateau pressure [8]. Pressure concentration isotherms for MmNi_5 and compounds with manganese, aluminum and cobalt partially substituted for nickel, are depicted in Figure 2.7.

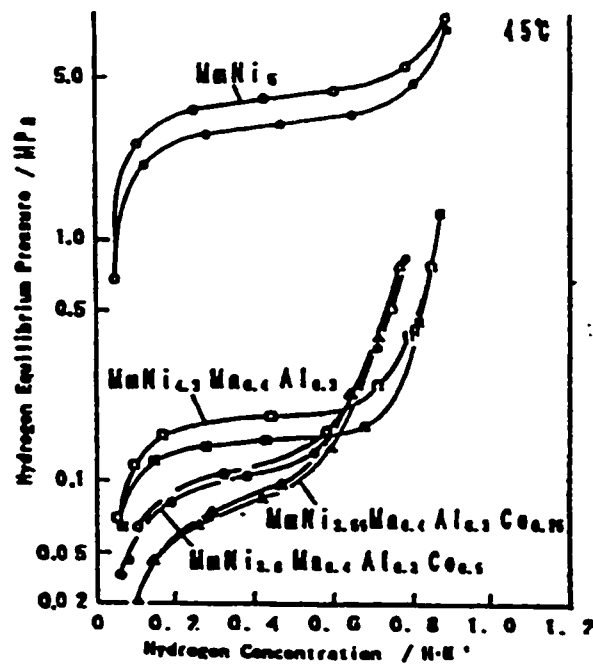


Figure 2.7 Influence of Mn, Al and Co substitution for MmNi_5 alloy system [30]

2.14 Sievert's Apparatus

A schematic diagram of apparatus for determining pressure composition isotherms is given in Figure 2.8.

The apparatus consists of 10-ml stainless steel reactor, a pressure gauge, a pressure transducer, a gas meter and a water bath or an electric furnace. An alloy sample (5-10 g) was placed in the reactor and activated. The reactor was connected to a high-pressure manifold, also made from stainless steel, with connections to a pressure gauge, a vacuum pump and a high-pressure hydrogen gas cylinder [31-36].

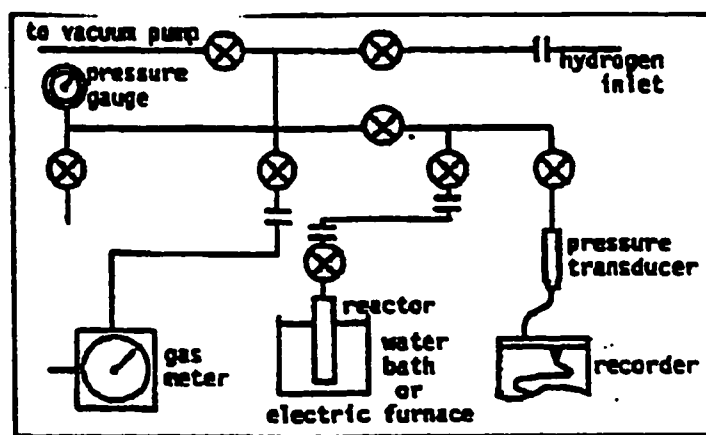


Figure 2.8 A schematic diagram of the apparatus for determining pressure-composition isotherm [34].

Activation of an alloy consisted of heating a sample in a vacuum (10^{-2} Torr) to 80-200 °C, cooling the sample to 5 °C or room temperature, introducing hydrogen to a pressure of 8-30-60 atm [31,32,34] and waiting until the reaction occurs, reducing pressure below 1 atm. and repeating all the cycles two to three times.

Pressure -composition isotherms were measured as follows. Prior to measurements the sample was fully saturated with hydrogen at 60 atm. [21,32,34,35]. Desorption isotherms were obtained by withdrawing hydrogen from the system in small amounts and measuring the equilibrium pressure after the system had been left for a period of about 30 min. This step was repeated successively until equilibrium pressure was less than 1 atm; the sample was heated to 200 °C and any further hydrogen evolved was measured. The number of hydrogen atoms per mole was determined using the ideal gas law and a value of 140 for the average atomic weight of the mischmetal.

2.15 Electrochemical Pressure Concentration Isotherms

In an equilibrium state, the potential of the anode corresponds to a pressure of hydrogen gas on the surface, which is equilibrated with atomic hydrogen in the hydride ($H_2 \leftrightarrow 2H$) according to Nernst equation:

$$E(H) - E(Hg/HgO) = [E(H)^\circ - E(HgO/Hg)^\circ] + RT \ln / 2F \ln [a(H_2O) / a(H_2)] = [E(H)^\circ - E(HgO/Hg)^\circ] + RT / 2F \ln [a(H_2O) / \gamma(H_2) p H_2] \quad (3)$$

where $[E(H)^\circ - E(HgO/Hg)^\circ]$ is the standard potential of the electrode, $a(H_2O)$ is the activity of water, $p(H_2)$ is the hydrogen partial pressure, γ is fugacity coefficient, R is gas constant and F is Faraday's constant.

The reaction with respect to Hg/HgO reference electrode is:



Hydrogen pressure calculated from the equilibrium potential using data in a concentrated KOH solution [38] is in good agreement [37] with the equilibrium pressure obtained by Sieverts' method. It is possible [37] to obtain electrochemical pressure concentration isotherms by converting the equilibrium potential to hydrogen pressure at each temperature according to equation 3. Comparison of pressure concentration isotherms by gas pressure isotherms and electrochemical methods for $LaNi_5$ anode are depicted in Figure 2.9

Equilibrium potential or discharge potential vs. capacity can be obtained by fully charging the anode and then repeating the following two processes; discharge of a small amount of capacity at 10 to 20 mA and then rest at open circuit until the potential becomes almost constant. The cut off voltage is -0.5 to -0.7 V vs. Hg/HgO reference electrode [28,38]. A potential change of approximately 30 mV corresponds to a pressure change by one order of magnitude. Since the measured potentials have an error of 1-2 mV, the calculated pressure values are accurate to within 10 %.

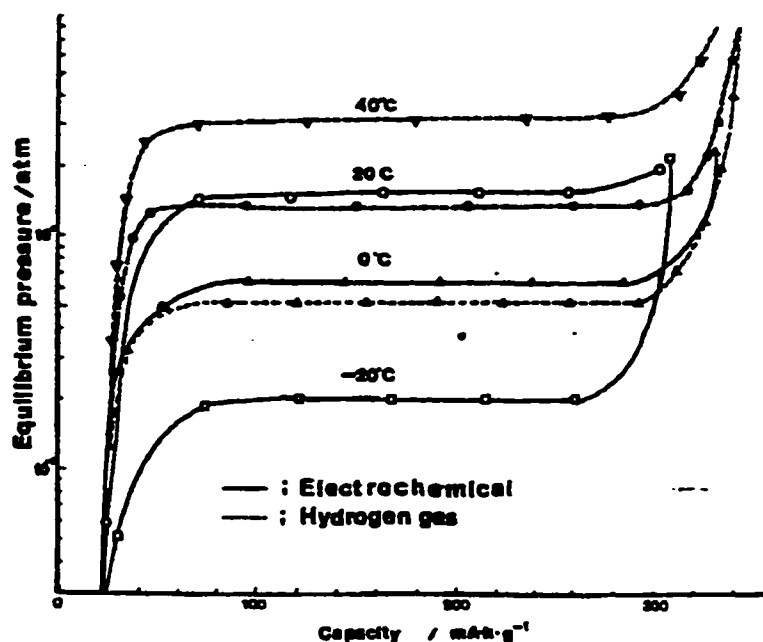


Figure 2.9 Comparison of pressure concentration isotherms by gas pressure and electrochemical methods for LaNi₅ anode [28].

The pressure calculated from the electrochemical data agreed with the equilibrium pressure obtained by the gas method although the former method provided values a little higher than the latter. The electrochemical method is very useful for examining the charging and discharging levels of hydrogen in an anode although the calculated pressure pertains to a quasi-equilibrium state.

Equation 3 can be written in simplified form [18,39]:

$$E_{\text{eq}}(\text{H}) \text{ vs. } E_{\text{eq}}(\text{Hg/HgO}) = -0.9324 - 0.0291 \log p\text{H}_2 \quad (5)$$

This method is useful to obtain pressure concentration isotherms over a wide pressure range from 10^{-2} to 10^{-8} atm. with small amount of sample (several milligrams).

2.16 Methods for Determination of Chemical Composition

The chemical composition of Mm-based nickel metal hydride alloys were determined using an electron probe microanalysis (EPMA) with X-Ray emission detection which is specific for the chemical elements considered (La, Nd, Ni, Co, Si)[40,41] and inductively coupled plasma emission spectroscopy ICP [42-44]. More accurate results of element distribution were obtained when the electron beam was fixed on a small spot. The resolution of EPMA is determined by the penetration depth of the electron beam and is of the order of 0.5 μm at the acceleration voltage used (15kV) [40]. Chemical composition of nonstoichiometric and stoichiometric alloys was examined by EPMA [33,45,46,47,48,49] with atomic number correction, absorption correction and fluorescence correction (ZAF).

The comparison between ICP and EPMA results for $\text{MmNi}_{3.5}\text{Co}_{0.7}\text{Al}_{0.8}$ and $\text{MmNi}_{3.5}\text{Co}_{0.8}\text{Mn}_{0.4}\text{Al}_{0.3}$ alloys indicated that EPMA results have higher nickel content than ICP analysis because the analytical depth in EPMA was only several micrometers on the surface confirming that the nickel was enriched on the surface region. The enrichment is due to surface oxidation [50].

Chemical analysis of grains and grain boundaries showed that in Mm-deficient alloys, Ni precipitated on grain boundaries as well as Al in Ni_3Al formation. Deviation to the Mm-rich side causes precipitation of Mm on grain boundaries [42,47-49]. In the manganese containing alloys manganese precipitates on the grain boundaries with deviation to both Mm-deficient and Mm-rich composition. The precipitated manganese diffuses to the bulk after heat treatment at 1100 $^{\circ}\text{C}$. The larger ions [49] or atoms tend to precipitate

preferentially at grain boundaries in the order: manganese (1.5 Å) > aluminum (1.43 Å) > nickel (1.25 Å), for Mm-deficient side and also in order: lanthanum (1.88 Å) > cerium (1.83 Å), neodymium (1.82 Å) for Mm-rich side. Since the deviation to the Mm-deficient side severely damages the endurance of the alloys, it was suggested [44, 49] it would be better to add the Mm in a little excess for mass production.

2.17 Production of Mm-based NiMH alloys

Mm-based NiMH alloys can be produced by arc melting, induction melting, melt spinning, gas atomizing, by a reduction diffusion method and by mechanical alloying. Arc melting and induction melting processes were described in 2.6.1 and are the same as for LaNi_5 . It was found that cell cycle life of $\text{MmNi}_{3.5}\text{Co}_{0.7}\text{Al}_{0.8}$ alloy was sensitive to the cooling rate of the melt and heat treatment temperature [18,41,42,43,48,49]. An arc unit was used when a small amount of alloy was required. Large quantities of $\text{MmNi}_{3.5}\text{Co}_{0.7}\text{Al}_{0.8}$ alloy were prepared by induction melting furnace. The cast ingot showed microstructure consisting of an equiaxial structure sandwiched between outer layers of the columnar structure. The columnar structure showed a longer cyclic life than the equiaxial structure because of smaller grain size. The crystal growth was perpendicular to c-axis. The columnar structure exhibits less lattice strain and less pulverization. The columnar grain growth caused the high resistance to pulverization [43]. A Mm consisting of 30 wt. % La, 52 wt. % Ce, 5 wt. % Pr and 13 wt. % Nd (purity 99.5 % Santoku Metal Industry Co. Ltd) was used [48, 49].

Heat treatment at 1000 °C causes a decrease in cyclic life. This is ascribed to grain growth from 10 μm to 50μm and precipitation of excess elements at the grain boundaries.

Since the cracking occurs first on the grain boundaries and then across the grains, it is believed that the protective surface layer formed on the smaller grains would remain more effective after decrepitation [18,48,49].

Pressure concentration isotherms for $\text{MmNi}_{3.5}\text{Co}_{0.7}\text{Al}_{0.8}$ alloy for different type of casting conditions are depicted in Figure 2.10.

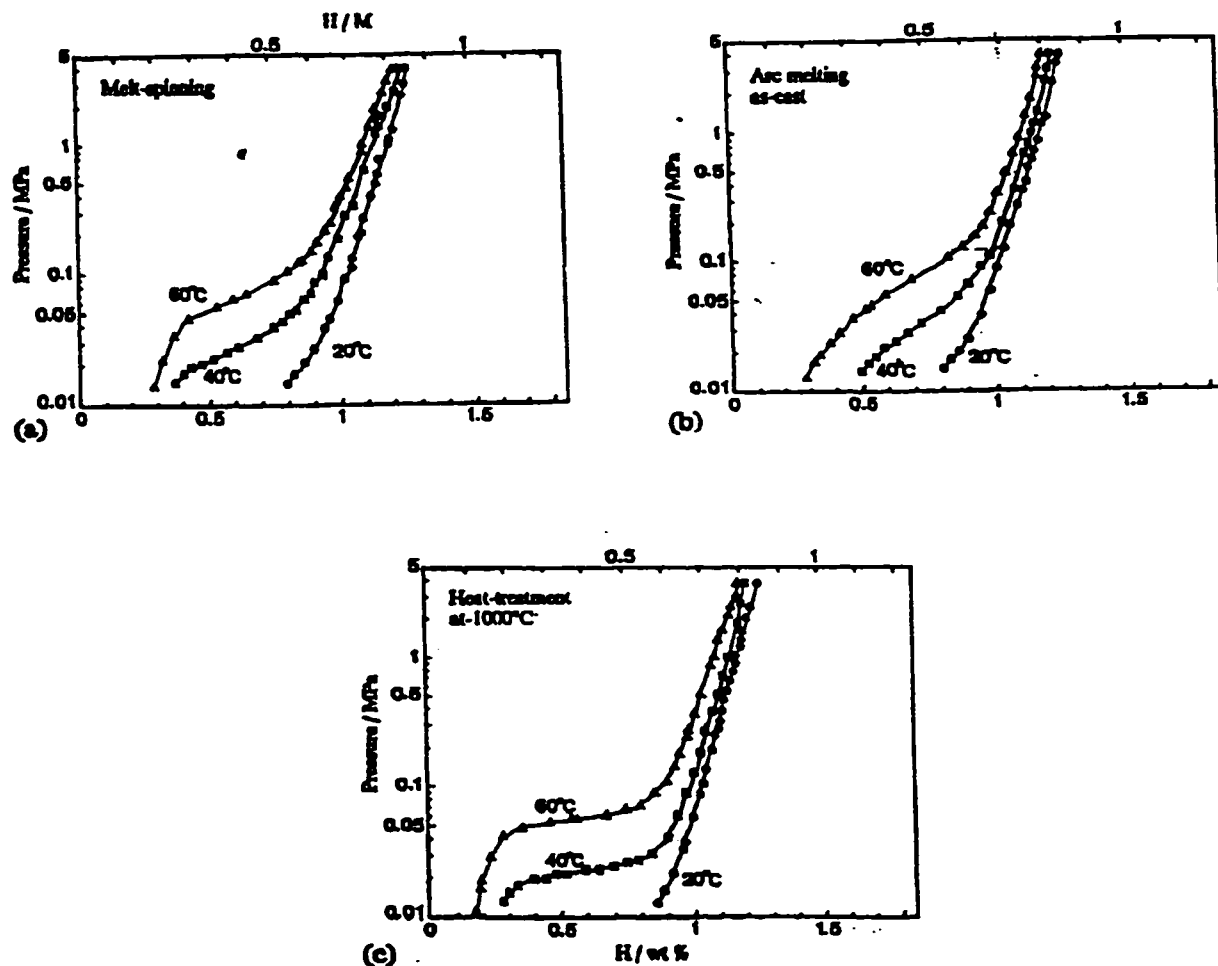


Figure 2.10 Influence of casting condition on pressure composition isotherms at 20, 40 and 60 °C including a) melt spinning b) arc melting c) arc melting and heat treatment at 1000 °C [49].

Melt spinning with a solidification rate of 10^5 °K/s resulted in a flake like alloy with much clearer columnar structure and much smaller grain size (2-3 µm). This material showed a longer cyclic life, lower decrepitation rate and flatter plateau pressure. Heat treatment at low temperature (400 °C) of $\text{LaNi}_4\text{Co}_{0.6}\text{Al}_{0.4}$ alloy improved cycle life by removing lattice defects such as dislocations. The decrease in lattice defects might improve the ductility of the alloy, depressing the pulverization ratio and also disintegration of the alloy [51].

A gas atomizing method produces small spherical powders (30-40 µm) with small grain size (10 µm). This leads to several improvements such as fewer electrode activation cycles, higher rate capability and longer cycle life after suitable heat treatment. The improvements are attributed to a more homogeneous composition without segregation and to smaller grain size [9,18,43].

The partial replacement of Al by Mn [43,48,49] such as in $\text{MmNi}_{3.5}\text{Co}_{0.8}\text{Mn}_{0.4}\text{Al}_{0.3}$ significantly changes the metallurgical macrostructure. Mn could reside on both Ni sites (2c and 3g) in LaNi_5 , without reducing the storage capacity. The non-selective substitution of Mn for Ni caused the isotropic lattice expansion in both a-axis and c-axis during hydride formation.

An ingot obtained by induction melting and rapid solidification process (10^2 ° K/s) had an equiaxial structure composed of fine particles (diameter 20 - 30 µm) suggesting that Mn affects nucleation. The cast ingot showed more lattice strain [43] with more sloping plateau pressure and broader XRD peaks than had the $\text{MmNi}_{3.5}\text{Co}_{0.7}\text{Al}_{0.8}$ alloy. The

formation of fine crystal grains with more lattice strains would accelerate the pulverization of the alloy.

Heat treatment at 1000 °C of $\text{MmNi}_{3.5}\text{Co}_{0.8}\text{Mn}_{0.4}\text{Al}_{0.3}$ improved the cyclic life and self-discharge of electrode [43].

The reduction-diffusion process [52] is another method to produce fine powder with average diameter around 20-50 μm . Alloys exhibited low lattice strain because the alloy is prepared by heating the mixture of mischmetal oxide, the reductant (Ca) and metal powder such as Ni, Co, Mn, Al at 900 - 1000 °C. Alloys prepared by induction or arc melting had very similar characteristics to alloys prepared by the reduction-diffusion process. Alloys without manganese show lower characteristics because of the nature of this process [18,49,52].

Mechanical alloying is a suitable method for alloy preparation in the laboratory. Mechanical alloying [53] is a high-energy ball-milling process that repeatedly cold welds and fractures powder particles. The microstructure that forms [53] during mechanical alloying consists of layers of the starting material; the thickness of the material decreases with increase in mechanical alloying time leading to true alloy formation down to atomic level. Phases formed are usually metastable in respect to structure and morphology. Amorphous alloys (nano-crystallinity) are easily obtained by controlling the alloying time. Alloying has to be carried out in a protective helium atmosphere, using ultra pure elements. This method is suitable for lab scale production. Alloys prepared in the way described above have similar characteristics to alloys prepared by arc melting. The alloy

prepared by mechanical alloying achieved maximum electrochemical capacity without prior activation [53].

2.18 Heat Treatment of Mm-based NiMH Alloys

Heat treatment of Mm-based NiMH alloys depends on the method of preparation and chemical composition. Alloys containing Mn should be annealed. The heat treatment of $\text{MmNi}_{3.5}\text{Co}_{0.8}\text{Mn}_{0.4}\text{Al}_{0.3}$ was conducted in vacuum (10^{-4} Torr) at 800 - 1000 °C for 5 hours [46]. The annealing time of 3 days at 900 °C was reported [54,55] for $\text{MmNi}_{3.55}\text{Co}_{0.75}\text{Mn}_{0.4}\text{Al}_{0.3}$ after arc melting.

The influence of the method of heat treatment of $\text{MmNi}_{3.55}\text{Co}_{0.75}\text{Mn}_{0.4}\text{Al}_{0.3}$ on hardness and absorption capacity is depicted in Table 2.1. MH-01 to 04 are designations for $\text{MmNi}_{3.55}\text{Co}_{0.75}\text{Mn}_{0.4}\text{Al}_{0.3}$ and method of heat treatment.

Table 2.1. Alloy processing condition for $\text{MmNi}_{3.55}\text{Co}_{0.75}\text{Mn}_{0.4}\text{Al}_{0.3}$ alloys [42].

Specimens	Metallurgical Treatment	Hardness (Knoop)	pH_2 (atm.)
MH-01	Normal cooled, as cast	640	0.93
MH-02	Fast quenched, as cast	620	0.93
MH-03	Annealed MH-01 at 950C for 6 h.	570	0.88
MH-04	Annealed MH-02 at 950C for 6 h.	540	0.85

Fast quenched and annealed alloy gives the best performance i.e. the lowest hardness and plateau pressure.

The alloy $\text{MmNi}_{4.0}\text{Mn}_{0.2}\text{Al}_{0.2}\text{Co}_{0.6}$ was annealed at 1150 °C for 6 hours [56].

In order to examine the influence of the oxide mixture (RuO_2 , Cr_2O_3) on the characteristics of NiMH alloys, the $\text{MmNi}_{3.6}\text{Mn}_{0.4}\text{Al}_{0.3}\text{Co}_{0.7}$ alloy was prepared by arc melting then adding oxide mixture and annealing at 1100 °C for 2 hours [57]. Generally annealed samples show flat and wide plateau regions. Although $\text{La}_{0.99}\text{Ni}_{4.74}\text{Mn}_{0.27}$ annealed for 36-84 hours at 900 °C was reported to be satisfactorily homogeneous [58]. $\text{LaNi}_{4.8}\text{Mn}_{0.2}$ and $\text{LaNi}_{4.55}\text{Al}_{0.45}$ annealed for 8 hours at 1000 and 1050 °C still had precipitation of Mn-rich and Al-rich phases, respectively. The NiMH alloy of nominal composition $\text{Mm}_{0.96}\text{Ti}_{0.05}\text{Ni}_{3.85}\text{Co}_{0.45}\text{Mn}_{0.35}\text{Al}_{0.35}$ (Mm = 43,3 wt. % La, 3.5 wt. % Ce, 13,3 wt. % Pr and 38.9 wt. % Nd) was prepared by induction melting and rapid cooling and annealed at 900 °C for 10 hours in vacuum [59].

2.19 Crystal Structure of Mm-based NiMH Alloy

NiMH alloys AB_5 type are mostly single-phase having CaCu_5 hexagonal crystal structure, space group P6 / mmm. The lattice parameters are depicted in Table 2.2.

The alloys with the same nominal chemical compositions have different lattice parameters [50,57,60] for $\text{MmNi}_{3.5}\text{Co}_{0.7}\text{Al}_{0.8}$. The alloys with the same nominal compositions have the same lattice parameters for $\text{MmNi}_{3.5}\text{Co}_{0.8}\text{Mn}_{0.4}\text{Al}_{0.3}$ after heat

treatment [46,50]. $\text{MmNi}_{3.55}\text{Co}_{0.75}\text{Mn}_{0.4}\text{Al}_{0.3}$ exhibits the biggest cell volume 88.255 \AA^3 and volume change 11.12-16.3 %. The **a**-axis increases by 4.91 % and **c**-axis increases by 1.89 % [54]. The **a**-axis and **c**-axis for $\text{MmNi}_{3.5}\text{Co}_{0.8}\text{Mn}_{0.4}\text{Al}_{0.3}$ and $\text{Mm}_{1.1}\text{Ni}_{3.5}\text{Co}_{0.8}\text{Mn}_{0.4}\text{Al}_{0.3}$ alloys increase after heat treatment and decrease for the $\text{Mm}_{0.95}\text{Ni}_{3.5}\text{Co}_{0.8}\text{Mn}_{0.4}\text{Al}_{0.3}$ alloy (Table 2.2). Mm-deficient alloy has the biggest cell volume in comparison with stoichiometric and Mm-rich alloy [46]. All results were obtained using X-Ray diffraction analysis (Cu $K\alpha$ radiation).

The cell volume of hydrides was determined after full saturation of hydride phase under 10 atm. and introducing CO in the reactor. The temperature of the reactor was 78 °K. After that the reactor was slowly warmed to 298 °K and the sample removed. This procedure kept the hydrogen in hydride form because the surface of alloy was poisoned [54].

2.20 Microstructure of Mm-based NiMH alloys

The microstructure examination was usually conducted by scanning electron microscopy (SEM) using a backscattered electron image [49]. Stoichiometric $\text{MmNi}_{3.5}\text{Co}_{0.7}\text{Al}_{0.8}$, $\text{MmNi}_{3.5}\text{Co}_{0.8}\text{Mn}_{0.4}\text{Al}_{0.3}$ and $\text{MmNi}_{3.55}\text{Co}_{0.75}\text{Mn}_{0.4}\text{Al}_{0.3}$ alloys have to be single-phase alloys. Deviation to Mm-rich side causes precipitation of rare earth on grain boundaries such as MmNi, which is less resistant to oxidation. Deviation to Mm-deficient side causes precipitation of aluminum and nickel at the grain boundaries in the Ni_3Al form. The microstructure of $\text{MmNi}_{3.55}\text{Co}_{0.75}\text{Mn}_{0.4}\text{Al}_{0.3}$ alloy is depicted in Figure 2.11.

Table 2.2 X-Ray diffraction parameters of various Mm-based NiMH alloys

Lattice parameters		a (Å)	c (Å)	V (Å ³)
MmNi _{3.5} Co _{0.7} Al _{0.8} [57]		4.9979	4.066	87.9
MmNi _{3.5} Co _{0.7} Al _{0.8} [60]		4.9734	4.066	87.097
MmNi _{3.3} Co _{0.7} Al _{0.8} [60]		4.9734	4.070	87.183
Mm _{0.95} Ni _{3.5} Co _{0.8} Mn _{0.4} Al _{0.3} [46] as cast		4.9881	4.098	88.127
	1000° C	4.9856 [46]	4.074	87.698
MmNi _{3.5} Co _{0.8} Mn _{0.4} Al _{0.3} [46] as cast		4.9776	4.0612	87.140
	1000° C	4.9839 [46]	4.0633	87.507
Mm _{1.1} Ni _{3.5} Co _{0.8} Mn _{0.4} Al _{0.3} [46] as cast		4.9788	4.0564	87.081
	1000° C	4.9923 [46]	4.0632	87.675
MmNi _{3.5} Co _{0.7} Al _{0.8} [50]		4.969	4.070	87.02
MmNi _{3.5} Co _{0.8} Mn _{0.4} Al _{0.3} [50]		4.984	4.063	87.41
MmNi _{3.55} Co _{0.75} Mn _{0.4} Al _{0.3}				
normal cooled as cast		5.015 [42]	4.052	88.255
MmNi _{3.55} Co _{0.75} Mn _{0.4} Al _{0.3}				
commercial Mm [55]		4.9623	4.054	86.27
MmNi _{3.55} Co _{0.75} Mn _{0.4} Al _{0.3} H _{3.34} [55]		5.209	4.1309	97.07
MmNi _{3.55} Co _{0.75} Mn _{0.4} Al _{0.3}	synthetic Mm [54]			87.39
MmNi _{3.55} Co _{0.75} Mn _{0.4} Al _{0.3} H _{4.3}	synthetic Mm [54]			101.65
MmNi _{3.55} Co _{0.75} Mn _{0.4} Al _{0.3}	commercial Mm [54]			86.27
MmNi _{3.55} Co _{0.75} Mn _{0.4} Al _{0.3} H _{3.6}	commercial Mm [54]			97.07

The expectation at LaNi_5 is a single-phase material but practice indicated that impurities exist in two phases can be seen in Figure 2.11. The SEM reveals some porosity and a second phase that appears to be sandwiched between as cast grains of $\text{MmNi}_{3.55}\text{Co}_{0.75}\text{Mn}_{0.4}\text{Al}_{0.3}$. Using a Transmission Electron Microscope (TEM) and bright field image of the second phase, it was found that the second phase was enriched in rare earth and Co compared to the matrix.



Figure 2.11 SEM images of a) LaNi_5 showing evidence of second phase and b) as cast $\text{MmNi}_{3.55}\text{Co}_{0.75}\text{Mn}_{0.4}\text{Al}_{0.3}$ showing distribution of second phase in AB_5 matrix [42].

Combining the EDS results with the measured d spacing, it was found that second phase is a laves (AB_2) type phase. $LaNi_2$ is a cubic structure $a = 7.387 \text{ \AA}$ while the second phase observed, exhibited a tetragonal symmetry. Probably the multicomponent composition resulted in a complex crystal structure. There was evidence that the second phase was twinned. Fine scale twinning and the resulting high density of stacking faults was commonly observed in the laves phase microstructure [42]. The microstructure of $AB_{5.5}$ consists of AB_5 alloy surrounded with a highly electrocatalytic phase. The purpose of double phase alloys is to improve the electrocatalytic activity of NiMH alloys. This second phase should be composed of the appropriate combination of transition elements for which according to the Brewer Engel theory, a synergistic effect was reported. Synergistic effects might be expected when transition metals having vacant d-orbital are alloyed with elements having internally paired d-orbitals [61-63]. As the result of the interaction of both metals an optimum electron configuration for hydrogen reaction would occur. It was argued that binary compounds such as $MoCo_3$, $MoNi_3$ and WNi_3 are the most promising alloys [61,62,63]. After galvanic codeposition of a small amount of Mo and Co onto various substrates, it was found that the overpotential for the hydrogen evolution reaction was dramatically reduced over the entire current density range and was even lower than those found at Pt electrodes.

2.21 Mm-based NiMH Electrode

There are two methods of preparation : cold pressing and hot pressing. Mm-based NiMH alloy might be prepared using a mixture of 100 mesh NiMH alloy, Teflon and carbon

black in the weight ratio of 17 % Teflon 33 % carbon black and 50 % of alloy. The total weight of AB₅ alloy is typically 0.075 g [54]. The mixture was cold pressed onto a nickel mesh screen, attached to a nickel wire electrical connection. The electrode was placed in 6M KOH and open to the atmosphere. The electrode surface area is 2 cm² [53,54]. Alternatively a mixture of polyvinyl alcohol and the alloy can be used and pasted on a nickel mesh and then dried in vacuum. Specifically, the alloy particles (100 mg) were mixed with 2 wt. % polyvinyl alcohol (PPA) as a binder and loaded in a porous nickel substrate (1 x 2.5 cm). After drying at 120 °C in vacuum for 1 hour the alloy-loaded substrate was covered with a porous nickel sheet and then pressed at 1200 kg/cm² [45]. This is the cold method. The hot method consists of hot pressing a mixture of powder and binder. Specifically, the electrode was prepared using a mixture of 10 wt. % FEP (Dakai, tetrafluorethylene-hexafluoropropylene copolymer) cold pressed to a pellet (13 mm in diameter) which is sandwiched between nickel mesh and then hot pressed at 300 °C under 400 kg/cm² [28].

2.22 Discharge Capacity

The discharge capacity of MmNi_{3.5}Co_{0.7}Al_{0.8} alloy has been reported as 199 mAh/g [60]) or 220 mAh/g [57] or 250 mAh/g [18,33,48,49].

The discharge capacity of MmNi_{3.5}Co_{0.8}Mn_{0.4}Al_{0.3} has been reported as 270 mAh/g [41] or 280 mAh/g [18,33,49]

The discharge capacity of MmNi_{3.55}Co_{0.75}Mn_{0.4}Al_{0.3} is 283 mAh/g for synthetic mischmetal with 26 % La, 52 % Ce, 16 % Nd, 6% Pr (in atom percentage) and 231

mAh/g for natural mischmetal with 18-28 % La, 50-55 % Ce, 12-18 % Nd, 6 % Pr and 2 % others (in atom percentage) [54,55,65] or 211 mAh/g [60]. The discharge capacity depends on chemical composition, methods of casting and heat treatment.

2.23 Cyclic Life of Mm-based NiMH Electrode

The discharge capacity vs. cycle curves of various Mm based NiMH electrodes are depicted in Figure 2.12 [33].

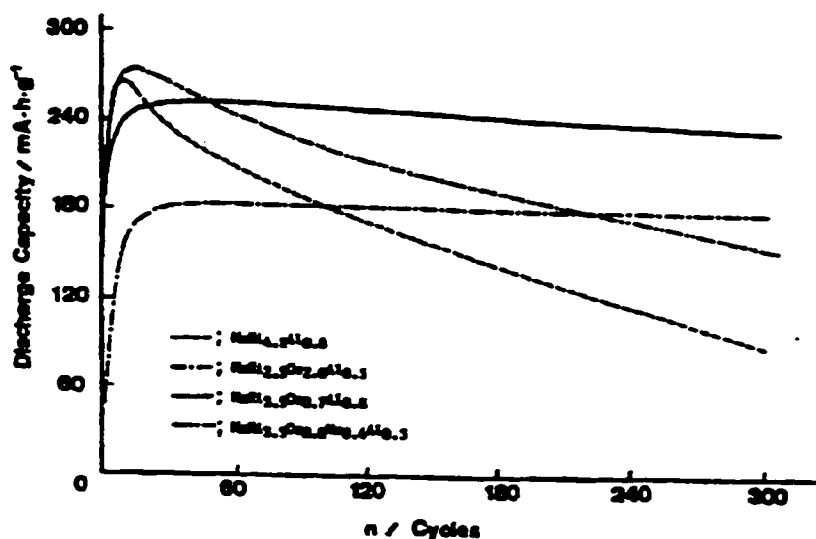


Figure 2.12 Discharge capacity at 93 mA/g vs. cycle number for various mischmetal - based alloys[33]

The maximum capacity (260 mAh/g) of the $\text{MmNi}_{4.2}\text{Al}_{0.8}$ electrode decreases more than 60 % after 300 cycles [18,33,48,49]. A small replacement of a nickel by cobalt significantly improved cyclic lifetime. The alloy $\text{MmNi}_{3.5}\text{Co}_{0.7}\text{Al}_{0.8}$ exhibits very long

cyclic lifetime (capacity decay after 300 cycles is 7 % of 250 mAh/g). A further increase of cobalt content causes a decrease in capacity and an increase in the activation cycles. No capacity decay was observed after 300 cycles for $\text{MmNi}_{2.5}\text{Co}_{2.0}\text{Al}_{0.5}$ (maximum capacity 185 mAh/g).

Replacement of nickel by manganese is useful for lowering the equilibrium pressure. The alloy $\text{MmNi}_{3.5}\text{Co}_{0.8}\text{Mn}_{0.4}\text{Al}_{0.3}$ shows a higher capacity than $\text{MmNi}_{3.5}\text{Co}_{0.7}\text{Al}_{0.8}$ but the cyclic lifetime is not long, about 40 % of the maximum capacity being lost after 300 cycles.

The influence of method of production on cyclic life of $\text{MmNi}_{3.5}\text{Co}_{0.7}\text{Al}_{0.8}$ is depicted in Figure 2.13. The alloys with very small grain size have longer lifetimes.

A fast cooling rate for $\text{LaNi}_{4.5}\text{Si}_{0.5}$ decreases the cycle life. Slow cooling or annealing increased the cyclic stability [66].

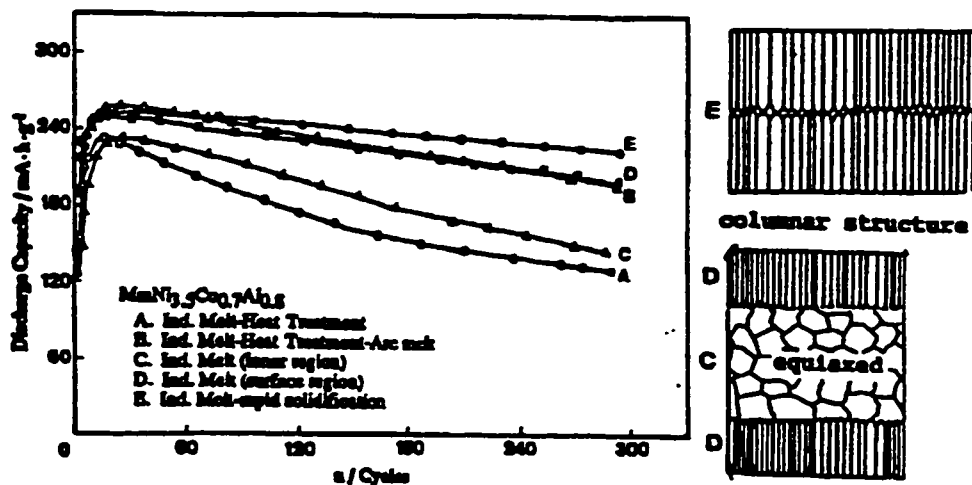


Figure 2.13 Influence of casting condition on capacity decay curves at 20 °C for $\text{MmNi}_{3.5}\text{Co}_{0.7}\text{Al}_{0.8}$ alloy prepared by induction melting [33,41,48,49].

The influence of stoichiometry and nickel content on discharge capacity of $\text{MmNi}_{3.5}\text{Co}_{0.7}\text{Al}_{0.8}$ alloy vs. cycle curves is depicted in Figure 2.14 [41]. The deviation towards Mm-rich or Mm-deficient side means lower discharge capacity and cycle life. The increase in nickel content decreases the cycle life.

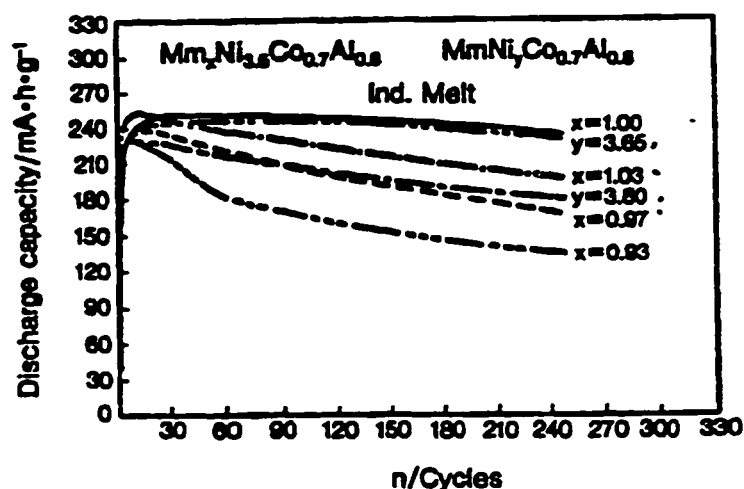


Figure 2.14 Discharge capacity vs. cycle curves for alloy electrodes at 20 °C (charge 186 mA/g, 2h, discharge; 93 mA/g to - 0.6V/Hg-HgO) [42].

The influence of heat treatment of $\text{MmNi}_{3.5}\text{Co}_{0.7}\text{Al}_{0.8}$ alloy on capacity decay is depicted in Figure 2.15. The best cycle lives are obtained with non-heat treated alloy. Annealing at 800-1000 °C causes increase in grain size and decrease in corrosion resistance of the alloy [49].

The capacity decay of $\text{MmNi}_{3.5}\text{Co}_{0.7}\text{Al}_{0.8}$ alloy is less than 10 % after 2000 cycles in a prismatic cell because of very little decomposition of alloy to $\text{Mm}(\text{OH})_3$ and metallic nickel [49].

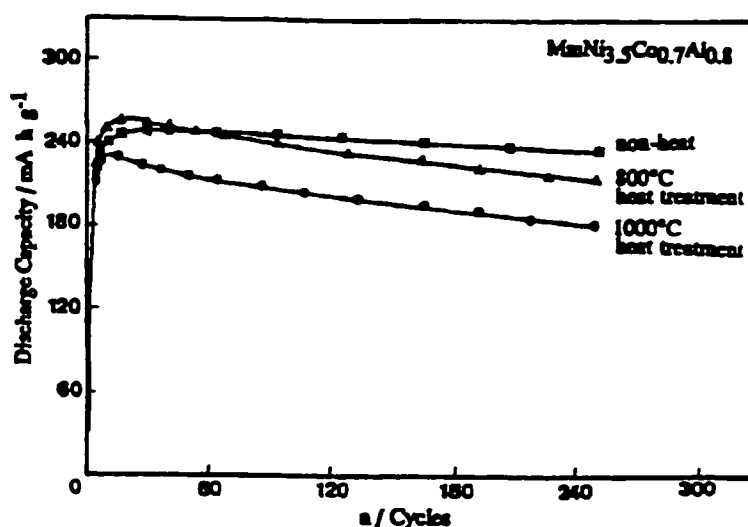


Figure 2.15 The influence of heat treatment temperatures of $\text{MmNi}_{3.5}\text{Co}_{0.7}\text{Al}_{0.8}$ alloy on capacity decay curves at 20 °C (charge 186 mA/g for 2 h, discharge 93 mA/g to - 0.6 V (Hg-HgO) [49].

We have discussed the influence of the casting condition of $\text{MmNi}_{3.5}\text{Co}_{0.8}\text{Mn}_{0.4}\text{Al}_{0.3}$ on microstructure with the statement that high cooling rate has positive effects on cycle life. The deviation to Mm-rich side of $\text{Mm}_x\text{Ni}_{3.5}\text{Co}_{0.8}\text{Mn}_{0.4}\text{Al}_{0.3}$ ($x > 1$) had a small effect on the cycling life, because heavier elements such as rare earth precipitate at the grain

boundaries. Lanthanum is highly concentrated at the grain boundaries. The heat treatment from 800 - 1000 °C causes further concentration of rare earth elements on the grain boundaries. Manganese [46] precipitates together with rare earth elements at the grain boundaries and the precipitated manganese diffuses into the bulk material when heat-treated at 800 °C [47].

In contrast , a severe decrease in cyclic life was observed for the Mm-deficient alloy ($x < 1$), as is shown in Figure 2.16. The lighter elements such as nickel, cobalt, aluminum and manganese precipitate at the grain boundaries. In particular elements such as manganese and aluminum are highly concentrated. The heat treatment at 1000 °C significantly improved the cyclic life of the Mm-deficient alloy. The influence of heat treatment on capacity decay curves for $\text{Mm}_{0.95}\text{Ni}_{3.5}\text{Co}_{0.8}\text{Mn}_{0.4}\text{Al}_{0.3}$ is depicted in Figure 2.17. The effect of the heat treatment could be ascribed to an alloying of the precipitated elements, thus improving the resistance of aluminum, manganese and cobalt in KOH solution [47]. It was found that the $\text{MmNi}_{5-x}(\text{MnAl})_x$ alloy shows continuous dissolution of Mn during cycling. About 25 wt. % of the total Mn in $\text{MmNi}_{4.2}\text{Mn}_{0.6}\text{Al}_{0.2}$ was lost from the alloy and precipitated on the alloy surface as oxides. With increasing the Co content the dissolving rate of manganese is greatly decreased to 14.3 wt % for $\text{MmNi}_{3.6}\text{Co}_{0.6}\text{Mn}_{0.6}\text{Al}_{0.2}$ and $\text{MmNi}_{3.0}\text{Co}_{1.2}\text{Mn}_{0.6}\text{Al}_{0.2}$ although about 3-4 wt % of the total Co was found to precipitate on the surface oxide layer [18].

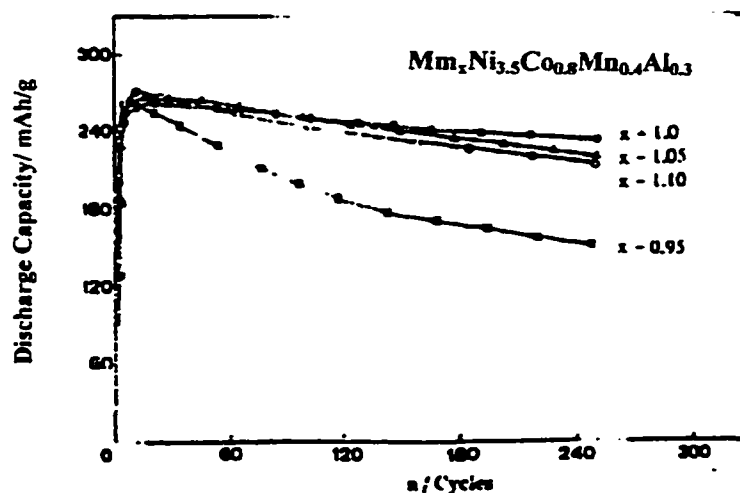


Figure 2.16 Effect of stoichiometric deviation on capacity decay curves at 20 °C for $Mm_xNi_{3.5}Co_{0.8}Mn_{0.4}Al_{0.3}$: charge 186 mA/g for 2 h; discharge 93 mA/g to -0.6 V vs. Hg/HgO [46]

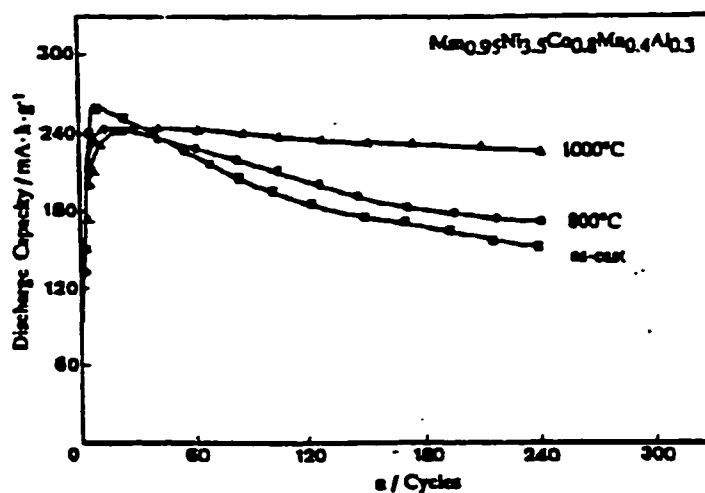


Figure 2.17 Effect of heat treatment on capacity decay curves at 20 °C for $Mm_{0.95}Ni_{3.5}Co_{0.8}Mn_{0.4}Al_{0.3}$: charge 186 mA/g for 2 h, discharge 93 mA/g to -0.6 V vs. Hg/HgO electrode [46].

The composition of mischmetal has an influence on discharge capacity of $\text{MmNi}_{3.55}\text{Co}_{0.75}\text{Mn}_{0.4}\text{Al}_{0.3}$ [55].

The rate of loss of electrochemical capacity per charge discharge cycle is significantly decreased due to presence of Ce. Cerium can form a protective oxide film thereby enhancing corrosion resistance and electrode lifetime. Two of the major components of mischmetal, Pr and Nd also form four valent oxides. Thus the use of mischmetal in the formulation of battery electrodes, chosen because of cost consideration, is also desirable in terms of electrode stability and lifetime [54,55].

2.24 The Rate Capability of Mm-based NiMH Alloy

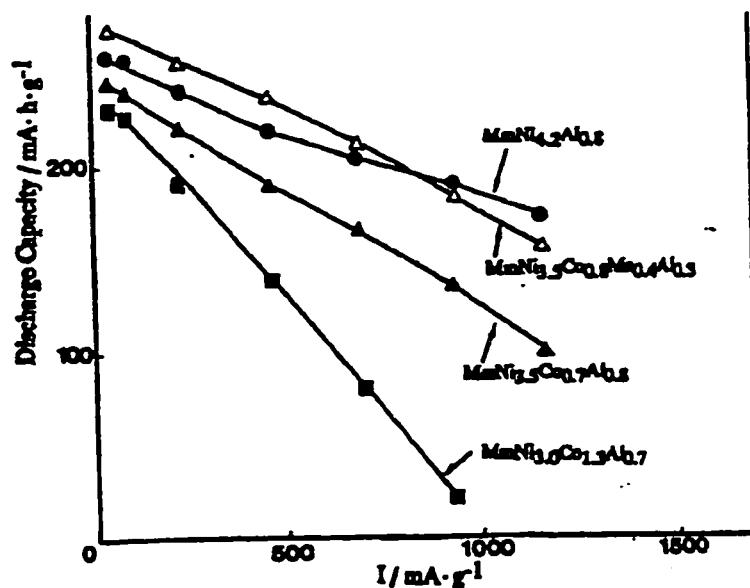


Figure 2.18. Current dependence of discharge capacity at 20°C [48,49].

$\text{MmNi}_{3.5}\text{Co}_{0.8}\text{Mn}_{0.4}\text{Al}_{0.3}$ has higher capacity, better rate capability and shorter cycle life than the $\text{MmNi}_{3.5}\text{Co}_{0.7}\text{Al}_{0.8}$ alloy. Some alloys [53] even at the 3C rate of charge, have about 90 % of maximum capacity without significant loss in the potential of electrode. The current dependence of discharge capacity at 20 °C for various Mm-based NiMH alloys is depicted in Figure 2.18. The rate capability depends on Co content. The increase in Co content causes the decrease of discharge capacity and rate capability. The alloy $\text{MmNi}_{3.0}\text{Co}_{1.3}\text{Al}_{0.7}$ has the lowest discharge capacity and rate capability.

2.25 Influence of Stoichiometry on Electrode Characteristics

The influence of stoichiometric ratio on equilibrium pressure of $\text{Mm}(\text{Ni-Co-Mn-Al})_x$ $5.4 > x > 4.17$ system is depicted in Figure 2.19. The lowest plateau pressure and the highest absorption capacity occurs for the alloy $\text{Mm}(\text{Ni}_{0.64}\text{Co}_{0.2}\text{Al}_{0.04}\text{Mn}_{0.12})_{4.17}$ [67].

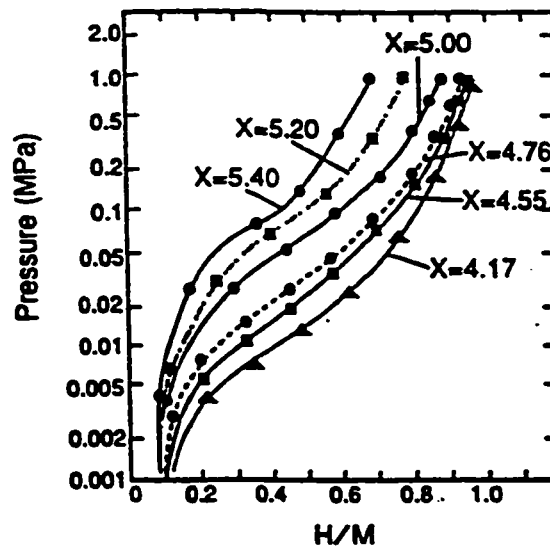


Figure 2.19 Pressure concentration isotherms of $\text{Mm}(\text{Ni}_{0.64}\text{Co}_{0.2}\text{Al}_{0.04}\text{Mn}_{0.12})_{4.17}$ [67].

The relationship between the value x and the discharge capacity per weight measured at 5 atmospheres with a discharge current of 50 mAh/g is shown in Figure 2.20. A discharge capacity of 330 mAh/g was obtained when x was 4.55 or 4.76, which is approximately 10 % higher than the capacity when x was 5.00. A heat treatment and method of production have positive influence on electrode characteristics. Heat treatment up to 1000 °C causes a more uniform distribution of each element in the CaCu_5 structure. The discharge capacities of alloys annealed at 800 °C and 1000 °C were higher than that of the non-annealed one.

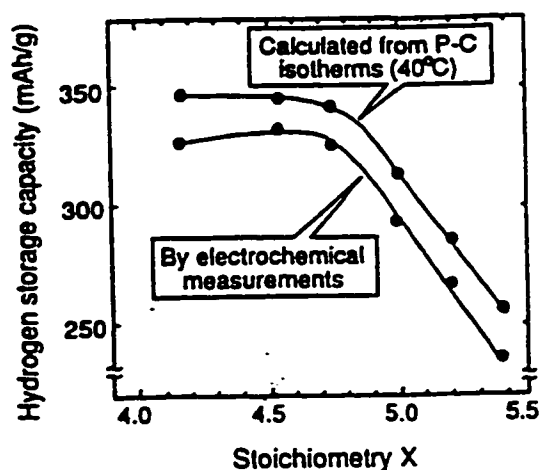


Figure 2.20 Hydrogen storage capacity of $\text{Mm}(\text{Ni}_{0.64}\text{Co}_{0.2}\text{Al}_{0.04}\text{Mn}_{0.12})_{4.17}$ [68].

The influence of method of production on pressure concentration isotherms is depicted in Figure 2.21. The pressure concentration isotherms for induction melted and as cast alloy show no plateau region while the rapid quenched and annealed alloy shows a clear plateau region between 0.2 and 0.6 H/M indicating that rapid quenching and /or

annealing process homogenized the microstructure. The rapid quenched and annealed alloy has capacity of 295 mAh/g after 3000 cycles and retention ratio of 92 % in a sealed battery test.

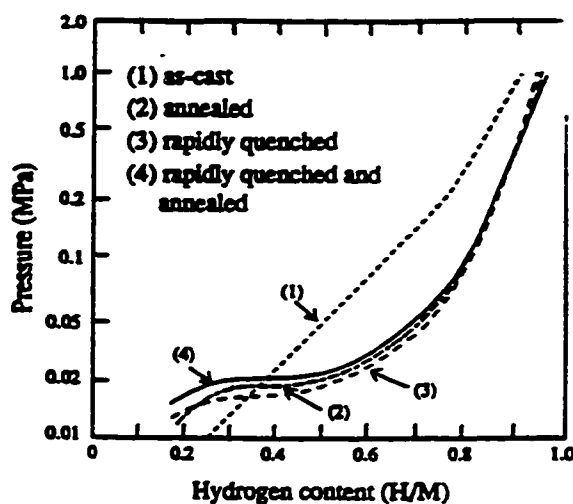


Figure 2.21 Influence of method of preparation of $\text{Mm}(\text{Ni}_{0.64}\text{Co}_{0.2}\text{Al}_{0.04}\text{Mn}_{0.12})_{4.17}$ alloys on pressure concentration isotherm [68].

The chemical composition on the surface of the electrode plays a major role in electrochemical reactions. Surface layer must be enriched with Ni and Co, which provides high reactivity of the electrode in alkaline solutions. The surface layer is a passive film layer that protects the bulk alloy in the alkaline solution [68]. Alloy $\text{MmNi}_{3.2}\text{Co}_{1.0}\text{Al}_{0.2}\text{Mn}_{0.6}$ has more Co than alloys discussed in 2.23 and is good example of stable alloy in KOH.

The discharge capacity vs. cycle number and discharge efficiency for alloy systems $\text{Mm}(\text{Ni}_{3.6}\text{Mn}_{0.4}\text{Al}_{0.3}\text{Co}_{0.7})_x$ is depicted in Figure 2.22 [44].

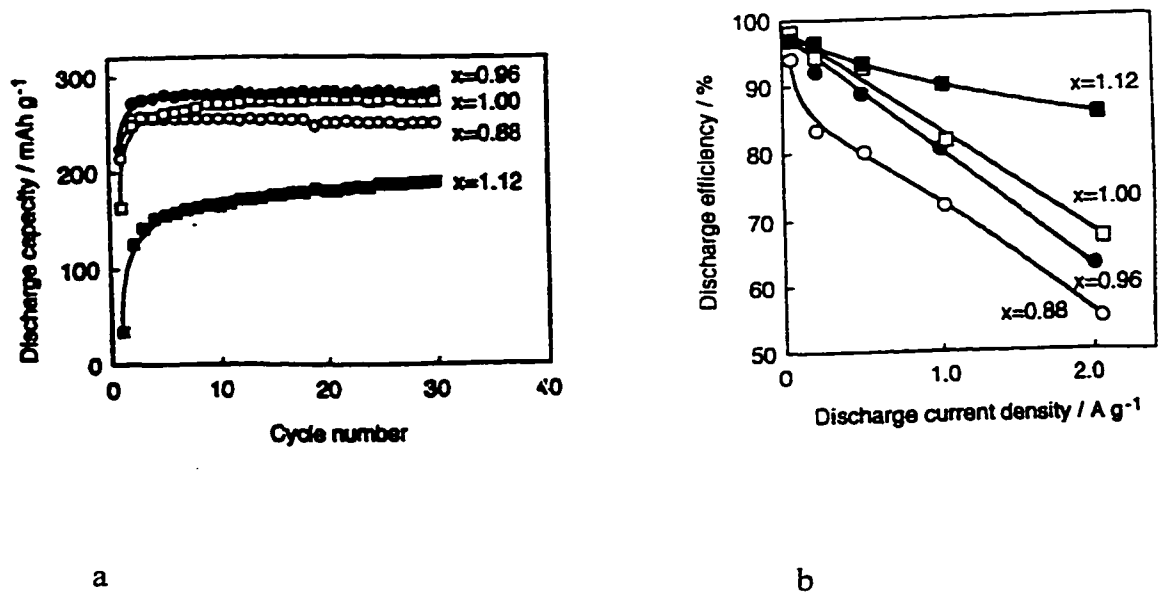


Figure 2.22 a) Discharge capacity vs. cycle number and b) discharge efficiency as a function of the discharge current density for $\text{Mm}(\text{Ni}_{3.6}\text{Mn}_{0.4}\text{Al}_{0.3}\text{Co}_{0.7})_x$ alloys [44].

Discharge capacity for $\text{Mm}(\text{Ni}_{3.6}\text{Mn}_{0.4}\text{Al}_{0.3}\text{Co}_{0.7})_x$ alloys for $x = 0.88, 0.96, 1, 1.12$ obeys the same rule. The highest discharge capacity is for an alloy when $x = 0.96$ but exhibits a low discharge efficiency. When the discharge rate was low, the discharge efficiencies were almost the same, irrespective of alloy composition. In contrast they increased with increasing x value when the discharge rate becomes high. The charge efficiency is about 85.5 % for nonstoichiometric $x = 1.12$ alloy and 66.8 % for the stoichiometric alloys Figure 2.22 [44].

As the stoichiometric ratio x becomes smaller, the unit cell volume increases. The relationship between hydrogen equilibrium pressure and unit cell volume is depicted in Figure 2.23. The lowest hydrogen pressure and the biggest cell volume has nonstoichiometric alloy MmB_x , $x = 4.17$ [36].

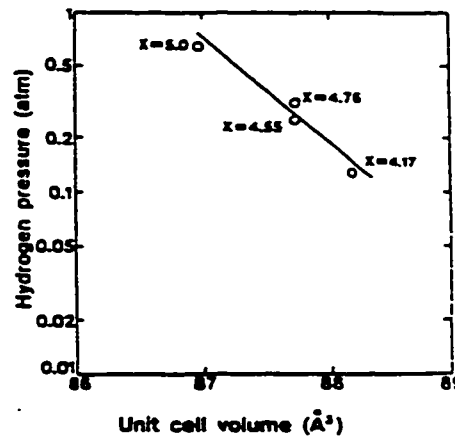


Figure 2.23 Plots of hydrogen pressure against unit cell volume for MmB_x type alloy [36].

It appears that the reason for high capacities in nonstoichiometric alloys comes from the enrichment of content A (rare earth element) above its content in the stoichiometric composition AB_5 that inherently forms stable hydride with content B (sum of Ni and Ni-substituted elements). This probably stabilizes the hydrogen atom in the alloy and increases hydrogen absorption volume [36].

CHAPTER 3

MATERIALS

3.1 Introduction

The materials used in all experiments are described in this chapter. The pure elements, gases, solution and alloys were used in the experiments. The data about purity, producer or true chemical compositions are described.

3.2 Materials Used in Melting Processes

The pure elements and gasses were used in arc and induction melting processes. The elements La 99.42 %, Ce 99%, Nd 99.9 % were produced by Zibo, Shandog, China; Pr 99.9% was produced by Advanced Material Resource, Mn 99.9% and Al 99.9 % were produced by Johnson Mathey Electronics, Ni and Co produced by Specialty Metals Sherritt Gordon Limited. Ultrapure argon 99.9999 % was used in arc melting unit and commercial 99.99% quality was used in the induction-melting unit.

3.3 Alloys Used In Production of Negative Electrodes

Alloys used in production of negative electrodes are mischmetal based nickel metal hydride alloys having two compositions: mischmetal based nickel metal hydride alloys with and without manganese. Chemical composition is presented in Table 3.1.

Table 3.1 Chemical composition of commercial and Westaim produced alloys determined by ICP

Nr	wt %	La	Ce	Pr	Nd	Ni	Co	Mn	Al	SUM
1.	IBA #5	7.94	17.6	1.84	5.75	51.3	10.2		5.31	99.94
2.	IBA #6	16.3	11.1	1.14	3.73	49.9	10.6	5.08	1.87	101.59
3.	Mm _{0.9} Ni _{3.5} Co _{0.7} Al _{0.8} (nom.comp.)	9.58	16.62	1.58	4.15	52.1	10.46		5.47	99.96
4.	Mm _{0.88} Ni _{3.43} Co _{0.71} Al _{0.76} (analysis)	9.7	16.4	1.65	4.35	52	10.9		5.65	100.63
5.	MmNi _{3.5} Co _{0.7} Al _{0.8} (nom. comp)	10.28	17.83	1.71	4.46	50.31	10.1		5.28	99.97
6.	Mm _{0.99} Ni _{3.5} Co _{0.7} Al _{0.81} (analysis)	10.4	17.4	1.66	4.6	50.6	10.1		5.4	100.16
7.	Mm _{1.02} Ni _{3.5} Co _{0.7} Al _{0.8} (nom. comp.)	10.42	18.05	1.73	4.51	49.97	10.03		5.25	99.96
8.	Mm _{0.99} Ni _{3.47} Co _{0.73} Al _{0.81} (analysis)	10.3	17.6	1.7	4.63	49.8	10.6		5.37	100
9.	Mm _{1.025} Ni _{3.5} Co _{0.7} Al _{0.8} (nom.comp.)	10.45	18.12	1.74	4.53	49.88	10.02		5.24	99.98
10.	MmNi _{3.48} Co _{0.71} Al _{0.81} (analysis)	10.6	17.8	1.75	4.72	50	10.3		5.4	100.57
11.	Mm _{1.1} Ni _{3.5} Co _{0.7} Al _{0.8} (nom. comp.)	10.94	18.96	1.82	4.74	48.64	9.76		5.1	99.96
12.	Mm _{1.09} Ni _{3.45} Co _{0.72} Al _{0.85} (analysis)	10.9	18.6	1.92	4.92	48.2	10.2		5.45	100.19
13.	MmNi _{3.33} Co _{0.66} Al _{0.76} (nom. comp.)	10.62	18.41	1.77	4.6	49.46	9.93		5.2	99.99
14.	Mm _{0.92} Ni _{3.33} Co _{0.69} Al _{0.8} (analysis)	10.4	0.4	0.38	22.4	49.7	10.4		5.5	99.18
15.	MmNi _{3.78} Co _{0.756} Al _{0.864} (nom.comp.)	9.77	16.94	1.62	4.23	51.62	10.36		5.42	99.96
16.	Mm _{0.99} Ni _{3.78} Co _{0.756} Al _{0.84} (analysis)	9.85	16.4	1.67	4.64	51.9	10.4		5.5	100.35
17.	MmNi _{3.5} Co _{0.8} Mn _{0.4} Al _{0.3} (nom. comp.)	17.22	9.94	1.65	4.3	48.6	11.15	5.2	1.91	99.97
18.	MmNi _{3.54} Co _{0.82} Mn _{0.34} Al _{0.3} (analysis)	17.3	11.2	1.08	3.7	49.7	11.6	4.51	1.92	101.01
19.	Mm _{0.9} Ni _{3.5} Co _{0.8} Mn _{0.4} Al _{0.3} (nom.comp.)	16.03	9.25	1.54	4	50.27	11.54	5.37	1.97	99.97
20.	Mm _{0.92} Ni _{3.48} Co _{0.83} Mn _{0.29} Al _{0.31} (analysis)	16.4	9.43	1.16	4.21	51.7	12.4	4	2.1	101.4

21. Mm _{1.1} Ni _{3.5} Co _{0.8} Mn _{0.4} Al _{0.3} (nom.comp.)	18.34	10.58	1.76	4.58	47.04	10.8	5.03	1.85	99.98
22. Mm _{1.065} Ni _{3.51} Co _{0.83} Mn _{0.37} Al _{0.3} (analysis)	18.4	10.4	1.16	4.68	47.7	11.3	4.7	1.98	100.32
23. MmNi _{3.33} Co _{0.76} Mn _{0.38} Al _{0.28} (nom.comp.)	17.79	10.26	1.74	4.45	47.8	10.97	5.11	1.88	100.0
24. Mm _{0.98} Ni _{3.33} Co _{0.79} Mn _{0.35} Al _{0.3} (analysis)	17.7	9.95	1.1	4.59	47.4	11.3	4.7	1.97	98.71
25. Mm _{0.99} Ni _{3.48} Co _{0.7} Al _{0.81} IMW	10.5	17.4	1.14	4.74	49.6	10.1		5.32	99.94
26. Mm _{0.99} Ni _{3.45} Co _{0.85} Mn _{0.4} Al _{0.3} IMW	17.3	11.0	1	3.7	48.5	12	5.36	2.0	100.8

Two commercial alloys are stoichiometric alloys denoted as IBA # 5 and IBA #6. Each alloy is labeled with “nom.comp.” or with “analysis”. The label “nom.comp.” means nominal composition, which was, expected for a certain type of alloy and is based on calculation of chemical composition. The label “analysis” means the chemical composition of an alloy determined by ICP. Each alloy has its own chemical formula, which was obtained from weight percentage of elements determined by ICP. The SUM gives an indication on precision of the ICP measurements.

3.4 Materials Used in Sievert's Apparatus

Nickel metal hydride alloys with chemical compositions presented in Table 1 (alloys number 1, 2, 25 and 26) and ultrapure hydrogen 99.9999 % were used in pressure concentration temperature measurement. The cooling and heating media was Dow Therm oil produced by Dow Chemical. All alloys were used for negative electrodes.

3.5 Materials Used in Electrochemical Measurement

Potassium hydroxide KOH with minimum assay of 85% produced by BDH Inc. Toronto was used to make the 30-wt % KOH in distilled water as the electrolyte. Nickel hydroxide purity more than 99 %, lot 50037, with Ni + Co content of 62.12 % produced by Westaim, Fort Saskatchewan, Alberta, Canada, was employed as the positive electrode. Cobalt-oxide powder was added to the nickel hydroxide electrodes to improve utilization of nickel hydroxide. A Teflon slurry was used as a binder for positive electrodes. Distilled water and very fine Teflon powder was used to make a slurry. The mixture of nickel hydroxide, cobalt oxide, aqueous solution of 1- % carboxymethyl cellulose, sodium chloride salt viscosity 3000-6000 centipoises were used for the positive electrodes. The slurry was pasted on nickel foam (produced by Eltech International Corporation) with an average weight of 490.4 g/m^2 to produce a positive electrode. A mixture of nickel metal hydride alloys, Teflon in powder and super black carbon was pasted on nickel Eltech foam, and employed as a negative electrode. Polyamide non-woven cloth was used as a separator between positive and negative electrodes.

CHAPTER 4

EQUIPMENT AND EXPERIMENTAL METHODS

4.1 Introduction

This chapter describes equipment and methods for production of nickel metal hydride alloys as well as the equipment and methods for evaluation of those alloys. The arc melting unit, induction melting unit, Sievert's apparatus, inductively coupled plasma optical emission spectrometer, scanning electron microscope, x-ray diffractometer, differential thermal analyzer and electrochemical battery tester are described in detail.

The methods of production of nickel metal alloys, chemical analysis using ICP, EDS and WDS, gas and electrochemical absorption desorption characteristics of nickel metal hydride alloys, metallography, methods of determination of melting points and methods of determination of electrochemical characteristics of nickel metal hydride alloys, are described in detail.

4.2 Arc Melting Unit

The arc-melting unit consists of a water-cooled copper crucible, arc stringer, melting chamber and rough vacuum pump. The air was evacuated through an outlet port in the chamber. Argon was introduced into the chamber through the same port. Rubber sealing was placed between the chamber and a water-cooled plate to protect the molten metal from oxidation. One relief valve was placed on the wall of the chamber to keep the argon

pressure in the chamber at approximately 2 Pa. The temperature of the cooling water was kept at 5°C and the pressure of the water was about 3 kPa to maintain high flow rate. The producer of the arc unit is Material Research Furnaces Inc. The melting was conducted using a tungsten electrode mounted on an arc water-cooled stringer. The stringer was moveable.

4.2.1 Arc Melting Process

The pure alloys were cut and weighed using a balance with an accuracy of ± 0.01 g. The weight was checked two times for each of the elements and total weights were checked against calculated weights. The elements Ni, Co and Al were ultrasonically cleaned using an ultrasonic cleaner with methanol. Although the rare earth elements were stored in a glove box under argon the surface still was oxidized. Each portion of rare earth elements was mechanically cleaned with a file to remove the oxide. All elements were placed in a copper crucible. The Ni was placed on the top of the Mn. Using this placement sequence the retention of Mn during the melting is higher than if Mn were placed on the top. The melting chamber was evacuated four times to 28 mm Hg and purged with argon. The argon pressure was set slightly above atmospheric pressure prior to starting the melting process. The whole process was monitored through a window on the chamber. The melting process began when the arc formed between the copper crucible and tungsten electrode. The arc was moved close to the elements, melting Ni, Co and Mn first and then other elements. The melting process took two minutes. The stringer was moved around the melt to provide homogeneity. After melting the alloys took 30–40 s to cool down to

about 500°C. The alloys were cooled down to room temperature over the next 10 minutes. The current was 270 A. After the first melting, the cool buttons were weighed and placed in the melting chamber again. The whole procedure was repeated. Each alloy was melted two times for two minutes. Each alloy was weighed before and after melting. After melting the samples twice they were then crushed mechanically using a porcelain mortar and pestle and sieved in three sizes. Powders with a diameter of 53-75 μm were employed in the electrochemical measurements. Powder with a diameter greater than 75 μm were used for metallography and XRD analysis. Powders with a diameter less than 63 μm were used in Sievert's apparatus to determine P-C-T curves.

4.3 Induction Melting Furnace

The induction-melting unit consists of a chamber with induction coils, an Al_2O_3 crucible, a water-cooled copper plate and vacuum pump. Air was evacuated and argon was introduced into the melting chamber under pressure slightly greater than atmospheric. The chamber was purged with argon four times before the melting started. Temperature was measured by a type-K thermocouple inserted in a protective Al_2O_3 shield. The radio frequency coils around the crucible were isolated with high temperature insulation cloth. A special alloy holder was placed above the crucible. The alloy holder was movable. The position of the alloy holder had to be adjusted over the crucible providing that all amounts of alloys were transferred from the holder to the crucible. The rough vacuum pump was employed to achieve 10^{-2} Torr. The diffusion pump was not activated.

4.3.1 Induction Melting Process

The same process was used for weighing the alloys for the induction melting process as for the arc melting process. First the crucible and thermocouple were weighed. The weight of crucible, thermocouple and all amounts of Ni, Co and Al were weighed two times before melting. The amount of rare earth elements and manganese were weighed before they were placed in alloy holder. The rare elements were rid of oxides by mechanical cleaning. Based on the total weight of crucible and thermocouple before melting and total weight of the crucible, thermocouple and melted alloy after melting, the estimation of weight loss of the alloy was obtained. The chamber was purged with argon four times before melting. The temperature was raised by increasing the power in the radio frequency coils from 0 to 13.5 kW over one hour. As a result the temperature increased from room temperature to 1480 °C. When the temperature achieved 1480 °C the power was decreased to about 40 % of maximum power and the rare earth elements with or without manganese were poured into the crucible. The crucibles were discharged after two minutes onto a water-cooled copper plate. This technique produced two one-kilogram samples.

4.4 Measurement of Pressure Concentration Temperature (P-C-T) Curve

4.4.1 Sievert's Apparatus

Sievert's apparatus is depicted in Figure 4.1 and was used for measurement of P-C-T curves.

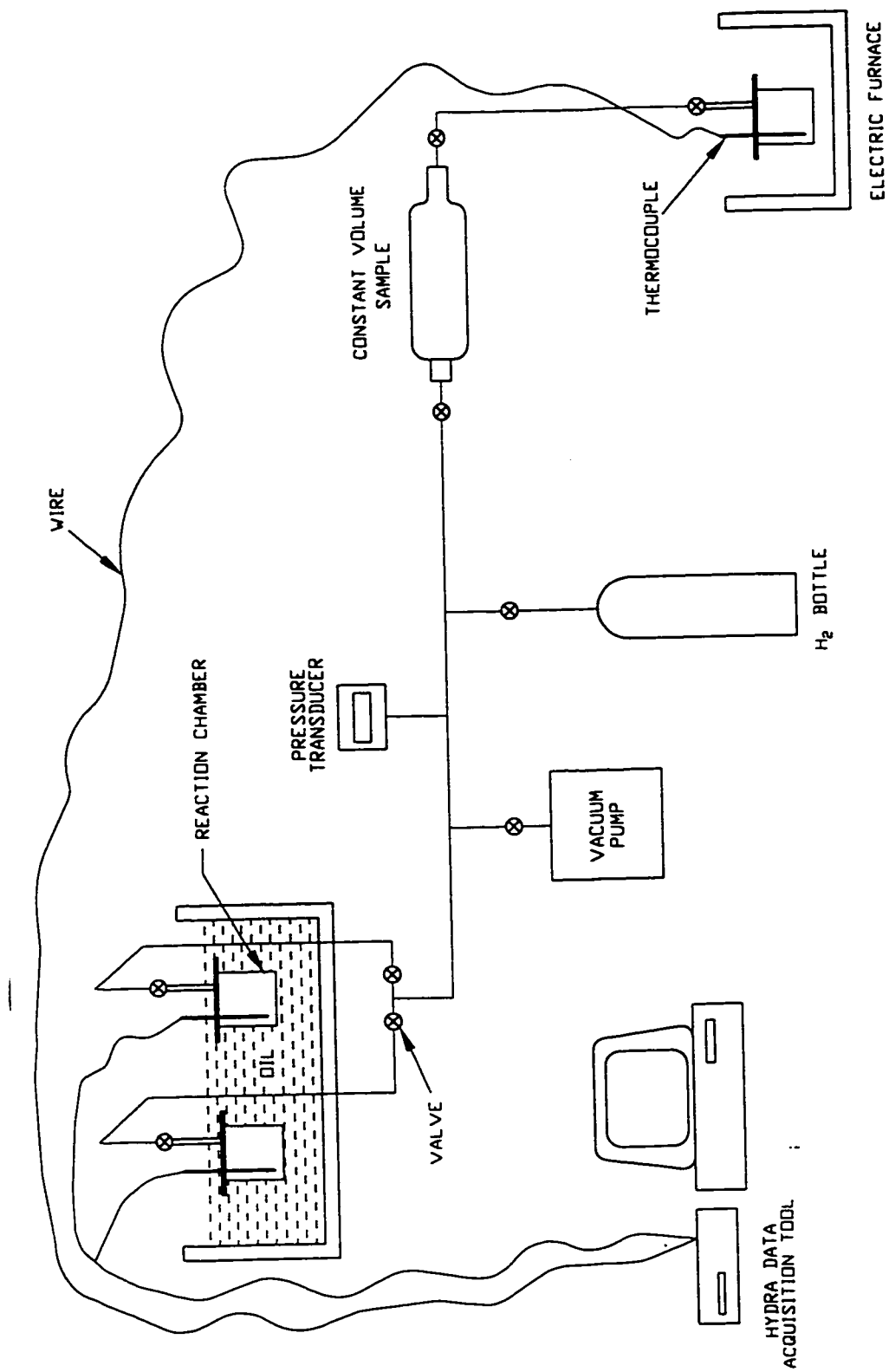


Figure 4.1 Sievert's apparatus

It was built of a vacuum pump, reaction chambers with inserted thermocouples, oil bath, electric furnace, manifold, pressure transducer Sensotec model AG-300, with a pressure range from 0-200 psia and an accuracy 0.035 % of full scale, Hydra data acquisition tool 2620-A for temperature readings and computer storage of data. A part of the manifold was a constant volume sample (75ml) and LB-150 gas purifier. The vacuum pump was an Edwards's model EXT70 turbomolecular pump. Ultrapure hydrogen was stored in a hydrogen bottle. The reaction chambers, pumps, hydrogen inlet and constant volume samples were separated from each other by ball/plug Swagelok valves.

The volume of the reaction chamber was 23 ml. The total volume of Sievert's apparatus was 0.11 l. The manifold, reaction chamber and valves were made from stainless steel. The lead of reaction chamber was attached with eight screws to the lower part of the chamber. A copper gasket sealed the chamber from the air.

4.4.2 Method of Measuring Gas Pressure Concentration Temperature Curve

A procedure for the determination of the gas pressure concentration temperature (P-C-T) curve had two steps: activation of the alloys, and the absorption and desorption of hydrogen.

The activation step was performed as follows. The alloys were placed in the reaction chamber of Sievert's apparatus. The amount of alloy varied between 4 and 5 g. The alloys were powders with a diameter less than 55 μm . The chamber was closed with screws, tightened and placed in an electric furnace. Using a Swagelok connection, the chamber was connected to the Sievert's apparatus and evacuated. A leak test was

performed after evacuation of air. The chamber was heated to 180 °C and evacuated simultaneously. When the temperature reached 180 °C, the valve between the vacuum pump and the chamber was closed and the valve between the hydrogen cylinder and the reaction chamber was opened. The hydrogen pressure in the reaction chamber was held at 12.4 MPa for about 5 minutes. During this period a slow reaction (absorption) of hydrogen with the NiMH alloy occurred. The pressure of hydrogen dropped down between 0.34 to 0.68 MPa. The chamber was then evacuated to 10^{-2} Torr. The evacuation took up to two hours. During evacuation, 1-2 °C variation of temperature in the chamber was observed. During absorption the temperature increased approximately 1-2°C. The process was repeated twice. During repeating the process, an increase of temperature variation and rate of absorption was observed. A fully activated alloy reacted thoroughly in five minutes (alloy with Mn) or within one hour (alloy without Mn) with temperature variations up to ± 10 °C occurring over one or two minutes.

The hydrogen absorption desorption step-followed activation. After activation the chamber was transferred from the electric furnace to an oil bath, connected with the Sievert's apparatus and evacuated. During transfer the chamber valve was closed protecting the alloys from air. When the pressure in the manifold dropped to at least 10^{-2} Torr, the chamber valve was opened and the chamber evacuated to 10^{-2} Torr or better. The temperatures of the alloys were set at 30 and 50 °C respectively. One sample was used for measurement at both temperatures.

Hydrogen was introduced in the constant volume sample and manifold with a pressure of 13.08 MPa when the vacuum in the chamber was at least 10^{-2} Torr. At that time the chamber valve was closed. When the chamber valve was opened the pressure in the

system increased to 10.67 MPa. The reaction occurred immediately for NiMH alloys with Mn and gradually for NiMH alloys without Mn. The temperature changed about 8-10 °C i.e. it increased because of absorption. When the pressure in the chamber equilibrated (becomes constant for at least 15 minutes) the desorption process could then start. The chamber valve was closed and hydrogen was evacuated from the manifold and constant volume sample. When the pressure reached less than 10^{-2} Torr, the pump valve was closed, the chamber valve was opened and the pressure throughout the system was noted. The system was not in equilibrium anymore. The hydride started to release hydrogen and increased the pressure in the system. Simultaneously, the temperature of the alloy was noted using the Hydra acquisition system, which recorded both the temperature and pressure. When the pressure increased to the (20 –60 minutes) equilibrium pressure the chamber valve was again closed and the manifold with the constant volume sample was evacuated. The procedure was repeated until the main portion of hydrogen was desorbed. Knowing the total volume of Sievert's, and the volume of manifold with a constant volume sample and the pressure, it was possible to calculate the number of desorbed hydrogen atoms. The total amount of absorbed hydrogen atoms was calculated from the differences between introduced and equilibrated hydrogen pressures.

If the hydrogen was introduced in small portions in the reaction chamber, the pressure dropped because of absorption. The difference between the introduced and equilibrium pressure was the basis for the calculation of hydrogen atoms. The total number of absorbed hydrogen atoms is the sum of each step.

4.4.3. Electrochemical Measurement of P-C-T Curve

4.4.3.1 Open Cell

The equipment for electrochemical measurement consists of an Arbin Battery Tester, H-glass cell, positive and negative electrodes and an electrolyte. The electrodes were prepared the same way as for the electrochemical measurement of discharge capacity (see section 4.8). The negative electrode was placed between two PVC holders in one compartment of the H-glass cell and the positive electrode in another. The standard Hg/HgO electrode together with H-glass cell is depicted in Figure 4.2.

4.4.3.2 Electrochemical Method of Measurement

The battery tester had four-probe connectors for a battery. The green and black connectors had to be connected to the negative NiMH electrode and white and red connectors to the positive nickel hydroxide electrode in the open cell. In the case of using a standard Hg/HgO electrode the white connector was connected to the platinum wire in the bottom of the standard glass bottle and red connector was connected to the positive electrode. Green and black connectors were connected to the negative NiMH electrode. The charging current and charging time was 186 mA/g and 2 hours respectively. The discharge current was – 93 mA/g until the potential dropped to 0.6 V against the Hg/HgO electrode. When the discharge voltage became constant a pulse discharge was applied. This involves a fully charged electrode that is discharged with a current of –93 mA/g for

900 seconds then held at open circuit for 1800 seconds and discharged again at a current of a -93 mA/g.

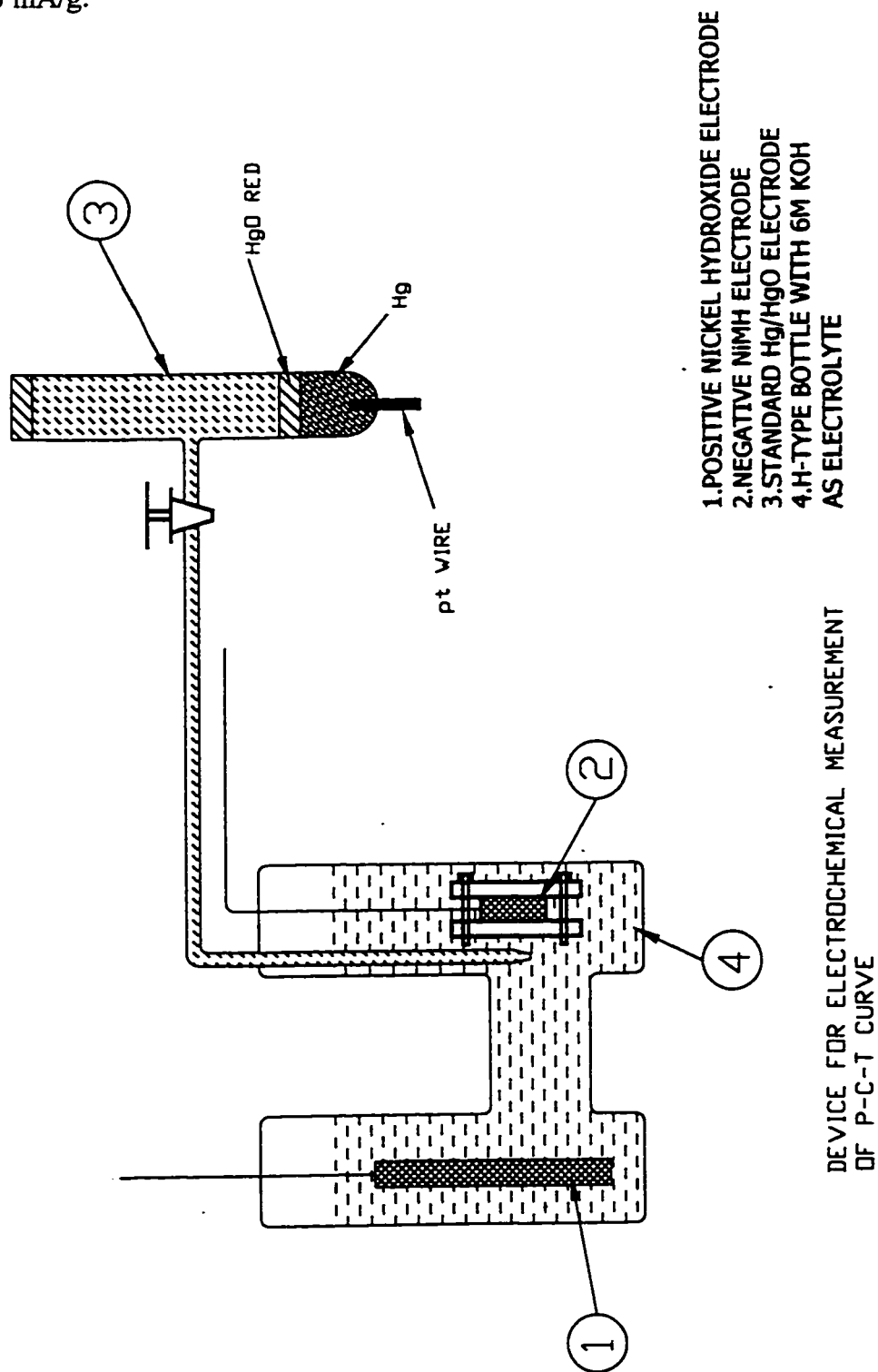


Figure 4.2 H-glass cell with standard Hg/HgO electrode

The pulse discharge was repeated until the negative electrode was fully discharged. The rest voltage was based upon calculation of equilibrium pressure (Nernst equation). The rest voltage is the voltage, which the electrode achieved during the rest period.

4.5 Chemical Analysis of NiMH Alloys By Means of Inductively Coupled Plasma Optical Emission Spectrometry (ICP)

4.5.1 ICP Spectrometer

Chemical analyses of NiMH alloys were performed using a Perkin Elmer Plasma 2000 Emission Spectrometer. The spectrometer consisted of a sample introduction system, plasma radio frequency source, plasma torch and one or double one-meter monochromators. The standard Plasma 2000 is equipped with one 3600 lines/mm and one 1800/ mm grating. Monochromator selection can be automatically controlled by a microcomputer depending on the wave length range required or can be selected by the operator. Each element wavelength is rapidly and accurately located by scanning the gratings at the normal value steps of 0.001 nm. A minimum of 10 steps is normally taken across an analyte peak at half height. The monochromator is thermostated at 32°C. A six-position filter wheel controlled by a microcomputer was used for effective reduction of stray light and second order radiation. The overall analytical speed is up to 40 elements per minute over 600-nm wavelength and at a precision of 3 % or better.

The Myers-Tracy signal reduced the short-term noise and signal fluctuation. It corrects for real time fluctuation in plasma background that may diminish the correlation between the analyte and reference signals at low concentration.

Each monochromator incorporates a two-channel filter photometer with each channel having 1 nm bandpass. One channel monitors the scandium 424.683 nm line and the other monitors argon lines between 419 and 420 nm. The light passing to the filter photometer is the same light that passes through the optical system for the analyte measurement. The three signals, argon, scandium and analyte are measured simultaneously. For each analyte intensity measurement, the appropriate scaled signal from the background channel (argon) of the photometer is subtracted from the analyte and reference (scandium) intensities. The ratio of background-subtracted analyte signal and the background-subtracted reference signal produces the final compensated intensity value.

The argon gas that forms the plasma is directed through the load coil by means of a quartz torch. There are three gas flows through the torch. One is plasma gas flow, second is auxiliary gas flow and third is sample gas flow. The standard torch injector is made from alumina, which can be used, with corrosive samples. A cross-flow nebulizer with injection tips molded on Rayton, a corrosion resistant material, is provided. A nebulizer is employed to convert the solution to an aerosol suitable for transportation into the plasma. A cross flow nebulizer consists of two capillaries held perpendicular and close together. A crystal-controlled, solid state, bipolar exciter, operating at 27.12 MHz, provides approximately 90 Watts of power at 50 ohms. A grounded grid triode amplifies this signal to a power level of 1800 Watts.

The plasma 2000 was a sophisticated computer program designed to automate atomic emission analysis by controlling the operation of the hardware and coordinating this operation with automatic calculation and storage results. The software is controlled from the main menu.

The plasma PE 2000 spectrometer uses an IBM PS/2 Model 70 computer. The UNIX-based operation system allows true multi-tasking.

4.5.2 Method of Analysis by ICP

The samples were dissolved by using 25 ml of deionized water, after which 110 ml 1 % nitric acid was added, heated until the samples were totally dissolved and cooled to 20 °C. The above mixture was diluted 1:100 with 2 % HNO₃.

The concentrations of elements were determined using blank, low and high standards. Blank standard solution didn't have any element that is present in NiMH alloys. The low standard solution corresponded to low limit of concentration of elements presented in NiMH alloys. High standard corresponded to an upper limit of elements presented in NiMH alloys.

First the blank samples were analyzed. After that low standard concentrations were analyzed three times. The concentration of elements were averaged and compared with the known concentration of the low standards. The same procedures were used for the high concentration standard. The concentrations of unknown alloys were determined using solutions of NiMH alloys prepared as described above. The sample was analyzed

three times and results were averaged. If the total concentration of all the elements were less than 99 % or greater than 101 % the analysis were redone.

4.6 EDS Analysis and Metallography of NiMH Alloys

4.6.1 Description of Scanning Electron Microscope

EDS analysis and metallography were performed on a JSM-6300F electron microscope. The microscope consists of an electron optical column, a control and displays, a power supply and pump box. The control and optical system consists of two control panels, keyboard, power supply control panel and photographic recording system. Some of the performance resolution are:

- Secondary electron image resolution (at 30 kV) at 8 mm working distance, 1.5 nm
- Backscattered electron image resolution (at 30 kV) at 8 mm working distance, 3.0 nm.

It uses a cold-cathode field emission. Acceleration voltage is 0.5 to 30 kV.

4.6.1.1 Sample Preparation

Powders were mounted in a cold mount compound (three parts of epoxy resin and one part of hardener) and polished to a final polishing stage using 320-600 grit SiC for planar grinding stage, 6-1 μm diamond for sample integrity and Mastermet 0.05 μm for the final polishing stage. The molds were 25 mm in diameter.

All samples were carbon coated in an Edwards coating system E306A.

4.6.2 A Determination of Chemical Composition of NiMH Alloys by EDS

The main problem of EDS (Electron Disperse Spectroscopy) of NiMH is overlapping of Pr-spectra with other rare earth elements. One way to determine the chemical composition of NiMH alloys is to establish good standard spectra for these types of alloys and run the analysis against the standard. The standard specimen was melted in arc melting unit. A comparison of the total weight of elements before melting and the weight of the alloy button after melting showed that the weight loss during the melting process was negligible. That means that starting chemical composition did not change and the bulk chemical composition of the specimen was known. That fact was confirmed by electron probe microanalysis (EPMA). The analysis was performed at the University of Alberta, Edmonton, Department of Earth and Atmospheric Science on a JOEL JXA-8900R superprobe. The pure metals Ni, Co, Mn, Al and LaPO_4 , CePO_4 , PrPO_4 and NdPO_4 were used for standards. The Wavelength Disperse Spectroscopy (WDS) confirmed the expected bulk chemical composition. The EDS analysis of the standard sample was performed using pure metals Ni, Co, Mn, Al, La, Ce, Pr and Nd for standard. It used 2000 counts per second (CPU), 13 nA probe current, 15 kV acceleration voltage for 200 seconds. The bulk analysis was done by changing position of the sample (half button) every 20 seconds at 90x magnification. The results obtained with EDS analysis were very close to WDS results and the expected chemical composition.

EDS analysis of NiMH alloys were performed on 10 points for each sample for 200 seconds at above-mentioned settings. After each three to five samples, the standard specimen was analyzed to confirm the accuracy and precision.

Images were done using 10 kV acceleration voltage and a backscattered electron image. Five photographs were obtained for each sample using Polaroid Polapan 450 4x5" sheet film. The images were also stored on a microfloppy disc. This was done by IMIX (Integrated Microanalyses for Imaging and X-Ray) software version 9 from Princeton Gamma-Tech, Inc. (PGT). The same software enabled the phase analysis of alloys in order to assess the area fraction of each phase. The phase analysis consists of area fraction and EDS analysis of each fraction. Each phase was analyzed by point analysis using the same settings as for the matrix.

4.7 XRD Analysis of NiMH Alloys

4.7.1 Diffractometer

X-Ray diffraction analysis (XRD) was used to determine the lattice parameters of NiMH alloys. The analyses were performed on Siemens D5000 diffractometer. D5000 is composed of a goniometer, X-ray tube stand, aperture diaphragm holder, sample changer, detector diaphragm holder, detector (scintillation counter), kristaloflex X-Ray generator and computer.

Radiation from the X-ray tube is diffracted from the sample and recorded by the detector. The detector rotates around the sample keeping the diffracted angle two times larger than the angle of primary X-Ray beam. The Bragg-Brentano law is employed for focusing the X-Ray beam. The diffracted radiation has to be focused when it hits the detector. Detector diaphragm, sample and focus are located on a focusing circle and the detector diaphragm and focus is on the measuring circle. An aperture diaphragm is located

between the X-ray tube and the sample. A scattered radiation diaphragm and $K\beta$ filter are located between the detector and the sample. D 5000 has FK 60X-04 air isolated X-Ray tube with a Cu anode.

The scintillation counter enables X-Ray measurement in the wavelength range between 0.05 and 0.27 nm.

D 5000 requires a IBM PS/2 computer that is composed of a 80286 processor having 640 kB RAM, a serial and parallel adapter, a diskette drive a color display and the mouse. The X-ray analysis is governed by DIFFRACT-AT integrated software package developed by Siemens. The software provides measuring routines for analysis, diffraction database, the quantitative routine and the graphic evaluation package.

4.7.2 Method of X-Ray Analysis of NiMH Alloys

Two to three grams of NiMH alloys powder were placed in the sample holder. Each analysis required 15 minutes. The computer calculated the parameter d (interplanar spacing) for each 2θ and diffraction peak. The computer produced the diffraction pattern of unknown alloys. Based on a database from the International Center for Diffraction Data (ICDD) the characteristic lines of known spectra were inserted in the diffraction pattern of unknown spectra. If wavelength of characteristic peaks of a known alloy matched the characteristic peaks of the unknown alloy, the plane indices might be assumed. Based on known lattice parameters from ICDD, the c/a ratios were assumed. Using the assumed c/a ratios and formula:

$$\frac{1}{d^2} = \frac{4}{3} \frac{h^2 + hk + k^2}{a^2} + \frac{l^2}{c^2} \quad (4.1)$$

the lattice parameters a for each peak were calculated. The plane indices (hkl) were also assumed based on a known alloy. A diagram a against $\cos^2\theta / \sin\theta$ was made and a straight line was plotted using least squares method for the best fit. If the line was not a straight, the c/a ratio was assumed incorrectly and the procedure had to be repeated. If the line was straight the c/a ratio was taken as being correct and the lattice parameter c calculated. Knowing the lattice parameters a and c the crystal structure is known.

The systematic error was minimized by calibration procedures of the diffractometer. The calibration implied measuring quartz crystal parameters and comparing the results with published data. The calibration also was done by blank measurements (X-Ray tube to the detector without crystal). The random error was minimized by proper placement of the specimen in the diffractometer. The same procedure was employed to determine the lattice parameters of hydride. The surface of hydride had to be poisoned with CO_2 to keep hydrogen in the hydride.

4.8 Electrochemical Measurement

4.8.1 Equipment for Electrochemical Measurement

4.8.1.1 Negative Electrode

The negative electrode is a NiMH electrode. It consists of a mixture of NiMH alloys in powder form (63-75 μm in diameter), Teflon powder and carbon powder, nickel mesh and nickel wire. All negative electrodes were produced mixing 75 mg of NiMH alloys

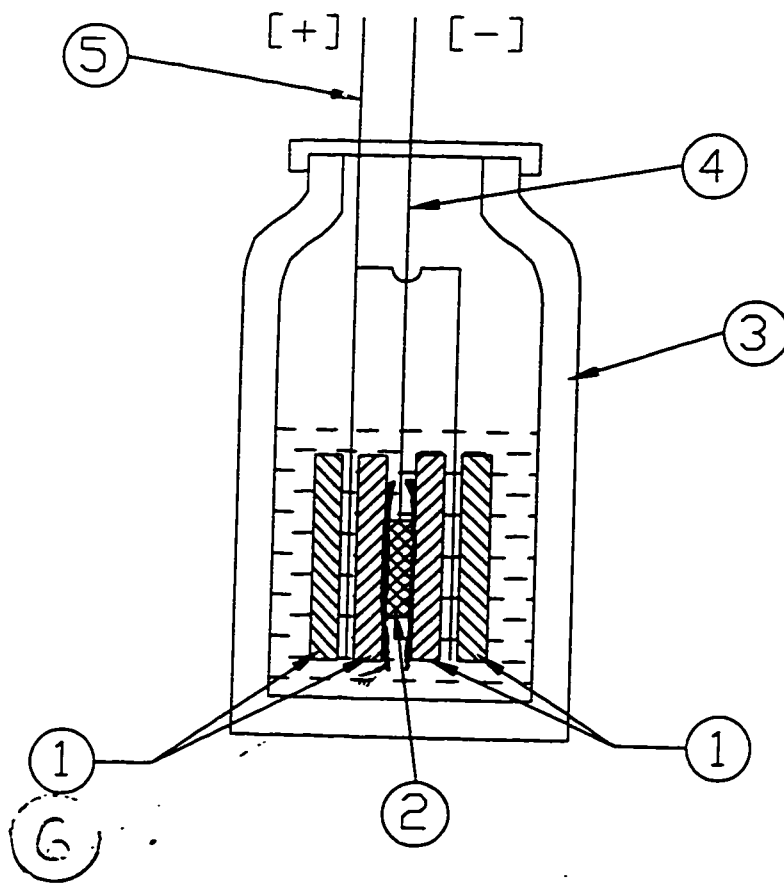
with 25 mg of Teflon powder and 40 mg of carbon powder. Three-digit balance was used. The NiMH alloys were handled in the ambient air atmosphere without special precaution. The alloys were mechanically crushed and thoroughly mixed with Teflon and carbon. The nickel foam 15 x30 mm in size was used as a current collector and mixture holder. The alloys with Teflon and carbon were sandwiched in nickel foam. The cold pressing method was applied to press the mixture into the nickel foam. A 1 ton / cm² press was used. The nickel wire was pressed together with nickel foam containing the NiMH alloys mixture.

4.8.1.2 Positive Electrode

Positive electrodes were produced using 0.6 g nickel hydroxide, 0.36 g cobalt oxide and 1.9 g cellulose slurry as a binder. These mixtures were pasted on 25 x 75 mm nickel foam, dried at 65 °C in an oven and pressed at 0.55 ton /cm² force. After that the electrodes were divided in four parts.

4.8.1.3 Open Cell

The open cell consists of polyvinyl chloride (PVC) container; one negative electrode 15x15 mm sandwiched between two positive electrodes one from each side and separated by pella cloth. The open cell is depicted in Figure 4.3. The capacity of the cell is limited by the capacity of the negative electrode. The electrodes were assembled between two pieces of Teflon and placed in a PVC container containing 100 ml 6M KOH.



- 1. NICKEL HYDROXIDE ELECTRODE
- 2. NiMH NEGATIVE ELECTRODE
- 3. PVC CONTAINER WITH KOH
- 4 NICKEL WIRE
- 5. NICKEL WIRE
- 6. PELON CLOTH

Figure 4.3 Open cell

The electrolyte was prepared with deionized water. The connections to the Arbin Battery System were made with nickel wires. Two wires from the positive electrode were connected to the positive terminal connector (red and white) and one wire from the negative electrode was connected to the negative terminal connector (green and black). The cells were operated open to the air.

4.8.1.4 Battery Cyclers

The charge/discharge processes were controlled by the Arbin Battery Testing System. There were two systems, one with 64 channels and a second with 24 channels. The batteries were tested on both. All major system functions were defined, controlled and monitored through Microsoft Windows NT interface. The data regarding charging current, charging time, discharging current and end voltage were entered into the computer. The software provided information of discharge capacity, discharge current, voltage efficiency and graphs for each channel. All data was saved in files.

4.8.2 Method of Charging and Discharging of NiMH Battery

Negative electrodes were charged with 186 mAh/g for 2 hours and discharged with 93 mAh/g to 0.6 V against nickel hydroxide electrode. The discharge capacity of 250 mAh/g for nickel metal hydride alloys without Mn and 270 mAh/g for NiMH alloys with Mn were reported [18,37,41]. This rate of charging provided that all the NiMH alloys in the

electrodes were fully charged. The amount of alloy in each electrode was calculated based on the weight of electrode before and after cold pressing.

These charge/discharge regimes were applied for 15-20 cycles. When the discharge capacity became constant, the discharge current increased from -93 mA/g to -186 mA/g for 4-8 cycles and then to 240 mA/g for next 4-8 cycles. The exception is alloy $\text{Mm}(\text{Ni-Co-Mn-Al})_{5.42}$ which had about 200 cycles in total. The other alloys had 35- 40 cycles.

4.9 Differential Thermal Analysis of NiMH Alloys

4.9.1 Differential Thermal Analyzer

The analyses were performed on SHIMADZU DTA 50 differential thermal analyzer. It consists of a number of major sections: DTA section with furnace, detector and interface, electrical section with DTA amplifier, A/D converter, CPU memory and panel section with keyboard, display and balance control knob.

4.9.2 Method of DTA Analysis of NiMH Alloys

The temperature of sample (NiMH alloy) and reference material (Al_2O_3) were raised to 1550 °C at the heating rate of 10 °C per minute. The atmosphere was 5 % hydrogen and 95 % argon. Ten milligrams of sample were loosely distributed into alumina cells and covered with platinum lids. Heat energy was consumed during the fusion process of NiMH alloys and the temperature stopped rising. The difference between the temperature of the NiMH alloy at melting point and the reference substance is the DTA signal (peak).

The results were depicted in graphs with voltage-time and temperature-time ordinates. The temperature difference between alumina and NiMH were transformed into the voltage signal (μV).

CHAPTER 5

EXPERIMENTAL RESULTS

5.1 Introduction

Chapter 5 deals with experimental results. The results of the pressure concentration temperature curve for two commercials and two IMW (induction-melted in Westaim) hydrogen storage alloys are described. The curves were obtained using Sievert's apparatus and electrochemical measurements. Chemical composition for 13 alloys produced by AMW (arc melted in Westaim) and determined by ICP are described in this chapter. Chemical compositions for two IMW alloys as determined by ICP are described. Chemical compositions of two commercial alloys determined by ICP are described in comparison with the alloys produced in Westaim. Chemical composition of ACW (as cast Westaim) and heat-treated alloys (48 samples) was obtained by EDS and compared with ICP results and expected results. SEM images for two commercial alloys, two IMW and thirty-nine AMW and heat-treated alloys are described. The images of two commercial alloys and four ACW alloys are presented. The description of all phases in nonstoichiometric and stoichiometric alloys is given. The work was designed to determine the characteristics of $\text{Mm}_{0.88}(\text{Ni-Co-Al})_5$; $\text{Mm}(\text{Ni-Co-Al})_5$; $\text{Mm}_{1.09}(\text{Ni-Co-Al})_5$; $\text{Mm}(\text{Ni-Co-Al})_{4.76}$; $\text{Mm}(\text{Ni-Co-Al})_{5.376}$; $\text{Mm}_{0.92}(\text{Ni-Co-Mn-Al})_5$; $\text{Mm}(\text{Ni-Co-Mn-Al})_5$; $\text{Mm}_{1.065}(\text{Ni-Co-Mn-Al})_5$; $\text{Mm}(\text{Ni-Co-Mn-Al})_5$; $\text{Mm}(\text{Ni-Co-Mn-Al})_{4.77}$ and $\text{Mm}(\text{Ni-Co-Mn-Al})_{5.42}$ alloys. Alloys were produced in an arc furnace and two stoichiometric alloys $\text{Mm}(\text{Ni-Co-Mn-Al})_5$ and $\text{Mm}(\text{Ni-Co-Al})_5$ were produced in an induction-melting unit. XRD analysis was performed on all alloys. Electrochemical measurement results of discharge capacity and discharge rate for all alloys (two

commercial and 13 Westaim produced alloys) are described. The melting points for alloys were obtained by Differential Thermal Analysis .

5.2 Chemical Composition

5.2.1 Results of ICP Analysis

Bulk chemical compositions of all NiMH alloys were determined by the ICP method. The results are presented in Table 3.1. Chemical compositions of two commercial alloys were determined using the same method.

In order to determine the precision and accuracy of the ICP results, a procedure recommended by ASTM E 1277 was followed. The procedure recommended ten measurements of the same sample and recommended slightly different wavelength for La (3988.5 Å). The results for alloy $\text{Mm}_{0.99}\text{Ni}_{3.45}\text{Co}_{0.85}\text{Mn}_{0.41}\text{Al}_{0.31}\text{IMW}$ are presented in Appendix 1. The values for lanthanum (wavelength 3988.5 Å and 3988 Å) are very close to each other. The chemical composition of the same alloy presented in Table 3.1 are very close to the result obtained by averaging ten results for each element.

5.2.2 Results of EDS Analysis

EDS analysis were performed on commercial, arc melted, induction melted and heat treated alloys. EDS analysis of matrix, rare earth rich phase, nickel-cobalt-alumina or nickel –cobalt manganese-alumina rich phase and oxides were conducted. The results are depicted in Appendix 2. The alloys have the same names as in Table 3.1. The names were given based on ICP analysis. The results of EDS analysis are somewhat different than ICP and one can see that the

composition of alloys in Appendix 2 doesn't fit perfectly to the nominal composition name. The names were kept in order to compare EDS and ICP results for the same alloys. The chemical composition of oxide, nickel-cobalt-alumina or nickel-cobalt-manganese-alumina rich phase rare earth rich phases are given for almost all alloys in ACW and heat-treated conditions. The chemical composition of two commercial alloys defined the same way as in the house made alloys, are given as well. Using Table 3.1 and Appendix 2, the nominal composition and determined chemical composition by ICP and EDS can be compared.

5.3 Pressure Concentration Temperature Curves (P-C-T)

5.3.1 Gas P-C-T Curves

Pressure concentration temperature curves were determined for two commercial alloys at two temperatures (30 °C and 40 °C) and two in house made alloys designated as $\text{Mm}_{0.99}\text{Ni}_{3.48}\text{Co}_{0.7}\text{Al}_{0.81}\text{IMW}$ and $\text{Mm}_{0.99}\text{Ni}_{3.45}\text{Co}_{0.85}\text{Mn}_{0.41}\text{Al}_{0.31}\text{IMW}$ at 30 °C. P-C-T curves consists of two parts: absorption and desorption. The P-C-T curves of IBA # 5 are depicted in Figure 5.1 and 5.2. It can be seen from Figure 5.1 that the total number of desorbed hydrogen atoms is 3.2 per mole of alloy below atmospheric pressure. The P-C-T curves for the same alloy at 40 °C is depicted in Figure 5.2. The total number of desorbed hydrogen atoms is 3.51 at 40 °C and 0.87 MPa. The total number of desorbed hydrogen atoms at 40 °C is 3.68 at 0.88 MPa. The equilibrium pressures are lower at 30 °C than at 40 °C. Both curves exhibit hysteresis, which is larger at 40 °C than at 30 °C. The alloy $\text{Mm}_{0.99}\text{Ni}_{3.48}\text{Co}_{0.7}\text{Al}_{0.81}\text{IMW}$ desorbs 4.12 hydrogen

atoms at 30 °C and 0.55 MPa but exhibits significant hysteresis. The pressure temperature curve for $\text{Mm}_{0.99}\text{Ni}_{3.48}\text{Co}_{0.7}\text{Al}_{0.81}\text{IMW}$ at 30 °C is given in Figure 5.3.

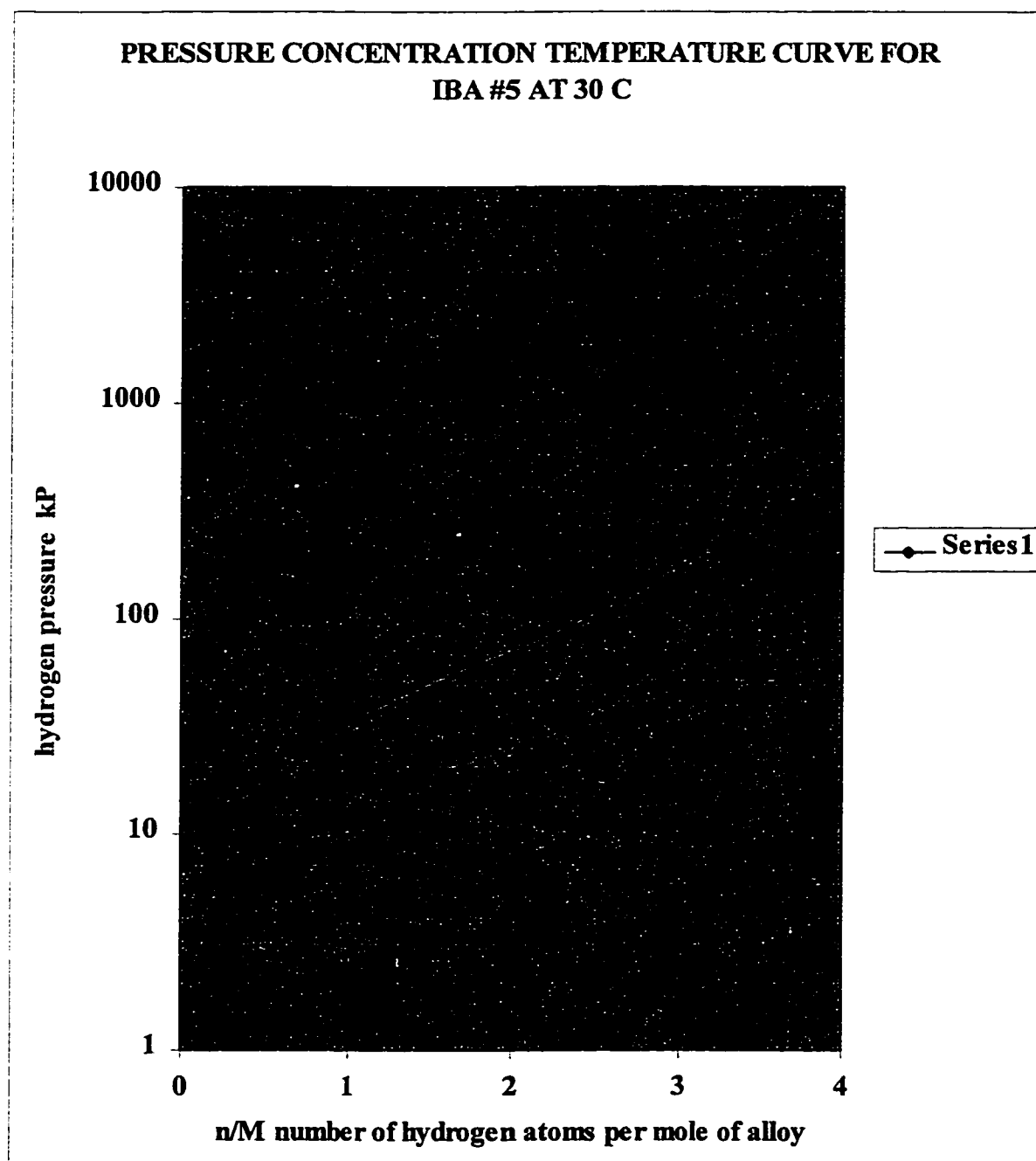


Figure 5.1 P-C-T curves at 30 °C for IBA # 5. The upper curve is absorption and down curve is desorption.

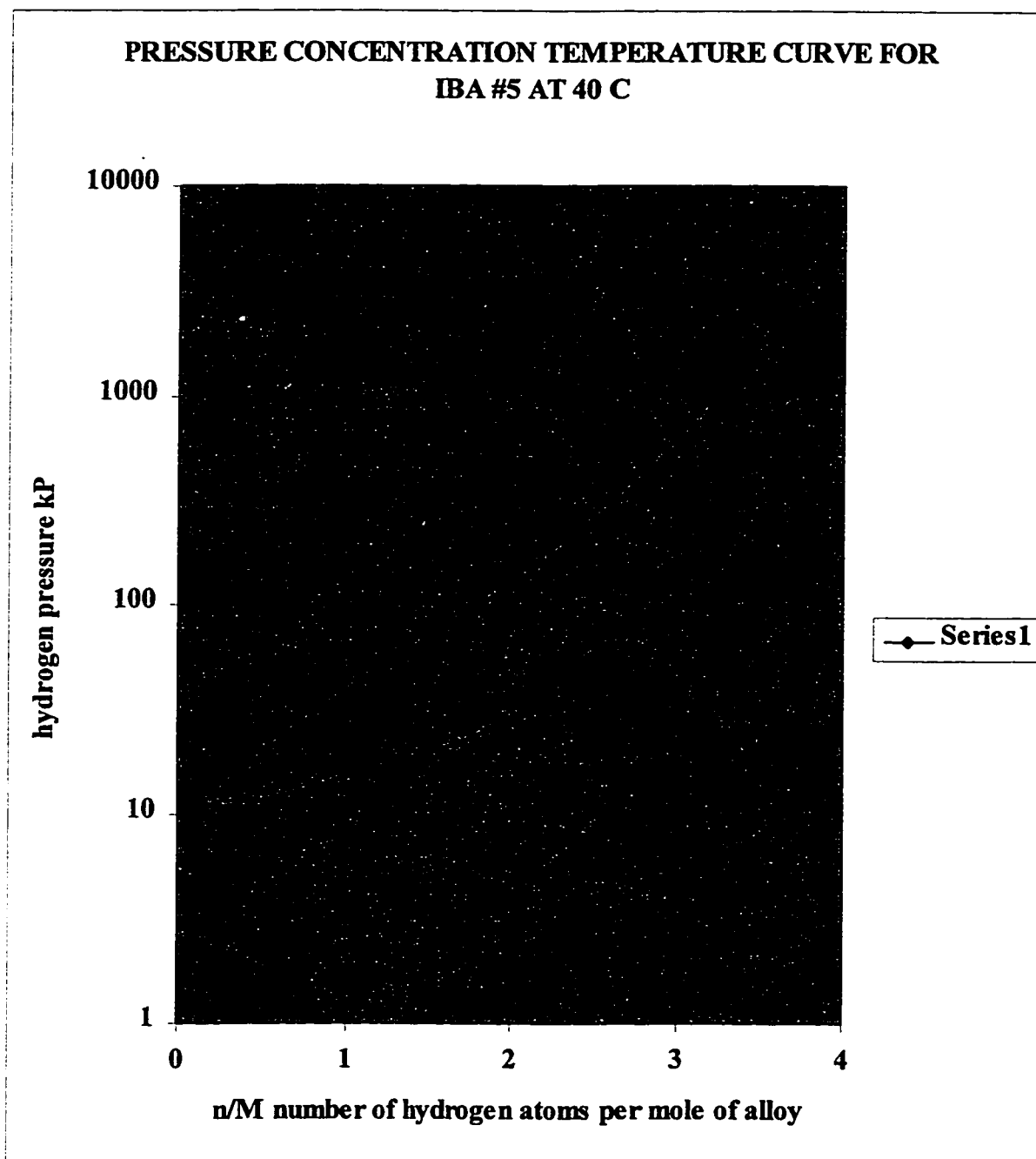


Figure 5.2 P-C-T curves for IBA #5 at 40 °C. The upper curve is absorption and the lower curve is desorption.

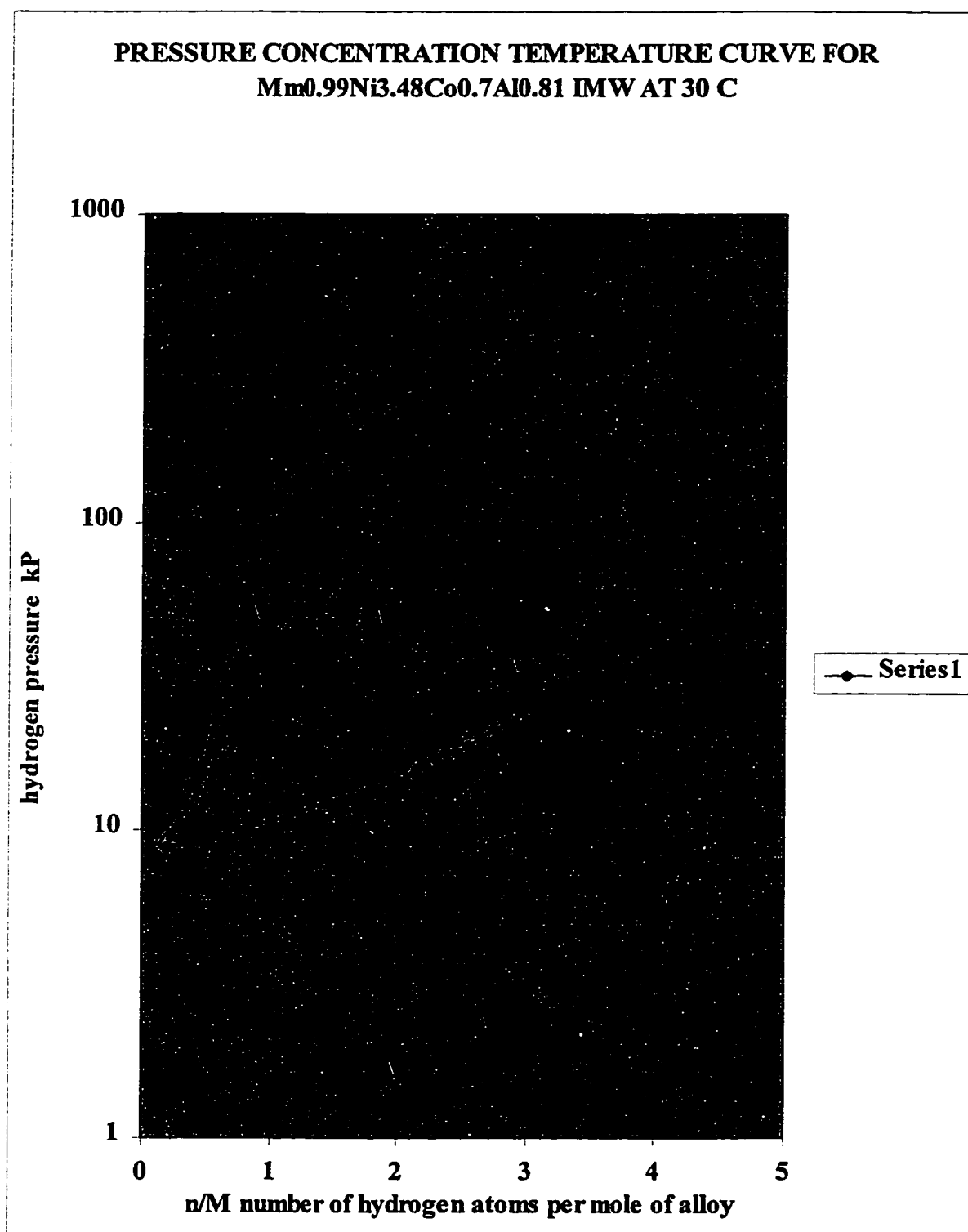


Figure 5.3 Pressure concentration temperature curves for $Mm_{0.99}Ni_{3.48}Co_{0.7}Al_{0.81}$ IMW at 30 °C. The upper curve is absorption and the lower curve is desorption.

The pressure concentration curves for IBA #6 are depicted in Figures 5.4 and 5.5. The pressure concentration temperature curve for $\text{Mm}_{0.99}\text{Ni}_{3.45}\text{Co}_{0.85}\text{Mn}_{0.41}\text{Al}_{0.31}\text{IMW}$ is depicted in Figure 5.6.

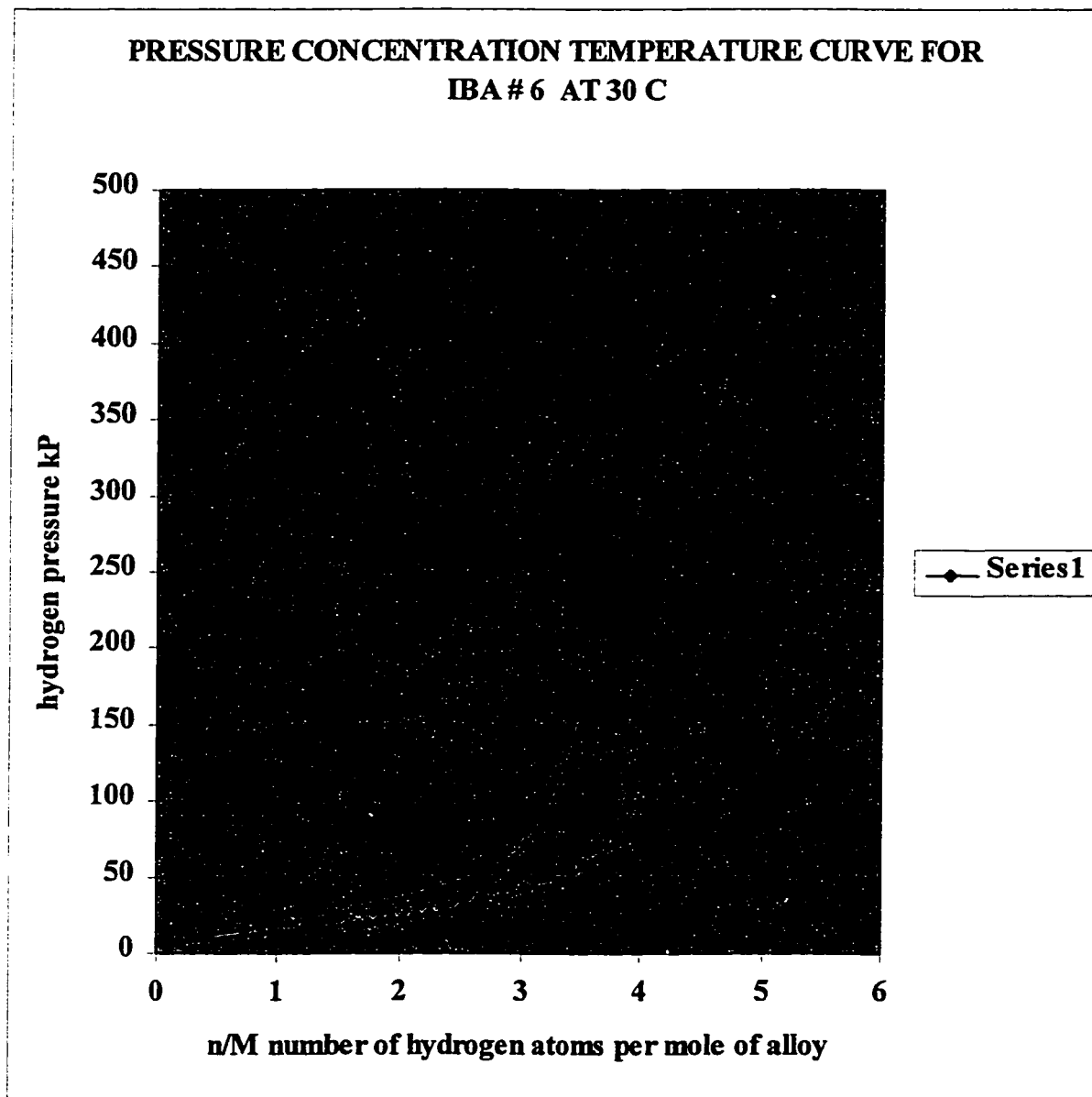


Figure 5.4 P-C-T curves at 30°C for IBA # 6. The upper curve is absorption and the lower curve is desorption.

The total number of hydrogen desorbed atoms for IBA # 6 is 4.93 per mole of alloy at 0.43 MPa. This alloy has a small hysteresis and low equilibrium pressure. The same alloy at 40 °C desorbs 4.78 hydrogen atoms at 0.43 MPa and exhibits much higher hysteresis. The pressure concentration temperature curve is depicted at Figure 5.5.

The total number of desorbed hydrogen atoms in $\text{Mm}_{0.99}\text{Ni}_{3.45}\text{Co}_{0.85}\text{Mn}_{0.41}\text{Al}_{0.31}\text{IMW}$ at 30 °C is 4.83 per mole of alloys at the pressure of 0.32 MPa. The alloy exhibits similar hysteresis as IBA #6 at 30 °C.

5.3.2 Electrochemical Pressure Concentration Temperature Curves

Electrochemical pressure concentration temperature curves obtained at room temperature (20°C) for two commercial alloys and two in house made alloys are depicted in Figure 5.7.

The equilibrium pressure is the same for IBA #6 and $\text{Mm}_{0.99}\text{Ni}_{3.45}\text{Co}_{0.85}\text{Mn}_{0.41}\text{Al}_{0.31}\text{IMW}$ and $\text{Mm}_{0.99}\text{Ni}_{3.48}\text{Co}_{0.7}\text{Al}_{0.81}\text{IMW}$ has lower equilibrium pressure than IBA # 5. The potential of NiMH negative electrodes was determined against reference the Hg/HgO electrode.

The discharge capacity for IBA # 6 is 283.6 mAh/g, for $\text{Mm}_{0.99}\text{Ni}_{3.45}\text{Co}_{0.85}\text{Mn}_{0.41}\text{Al}_{0.31}\text{IMW}$ is 266.33 mAh/g for IBA #5 is 232.78 mAh/g and for $\text{Mm}_{0.99}\text{Ni}_{3.48}\text{Co}_{0.7}\text{Al}_{0.81}\text{IMW}$ is 240.3 mAh/g.

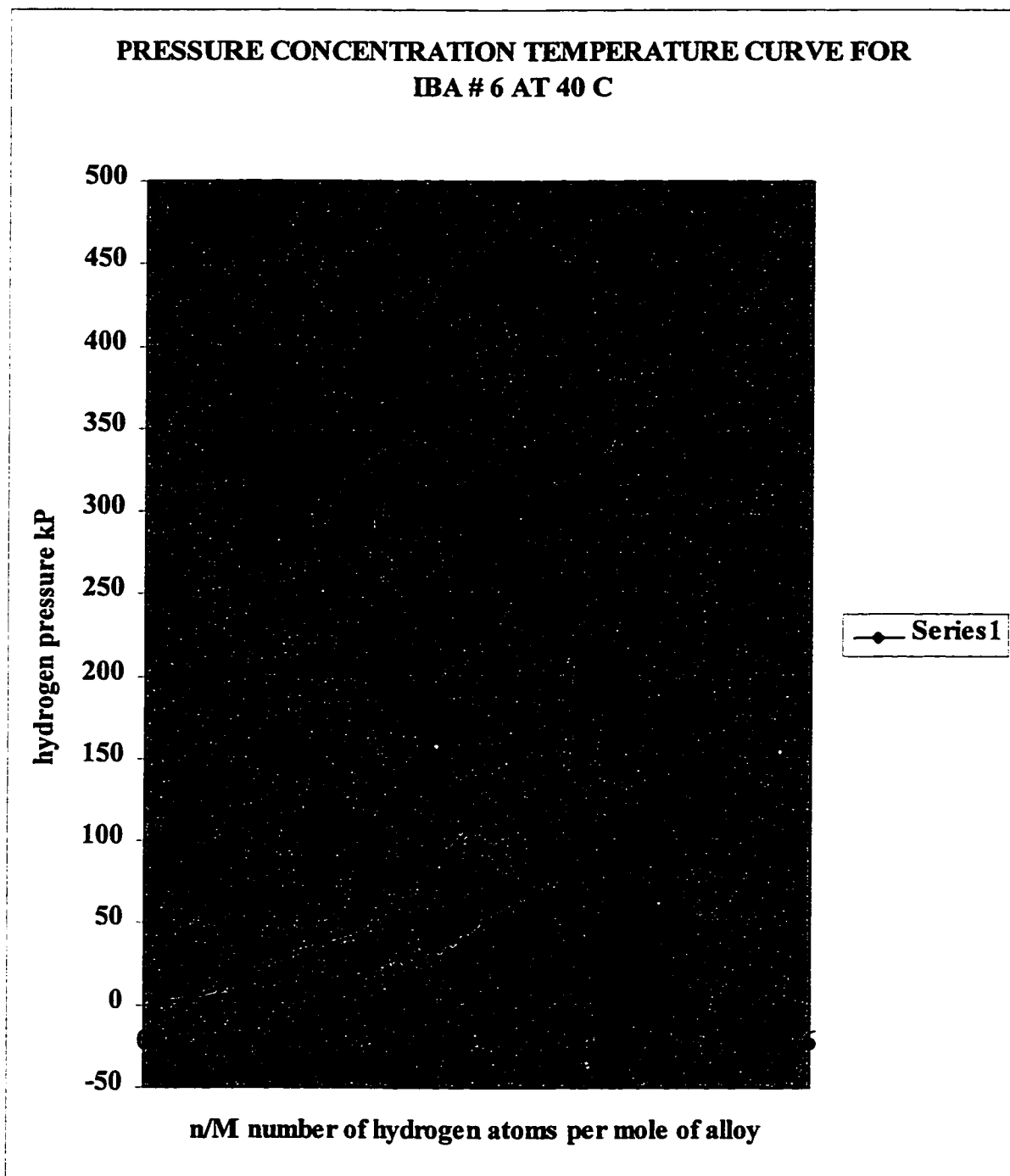


Figure 5.5 P-C-T curve for IBA # 6 at 40 °C. The upper curve is absorption and the lower curve is desorption.

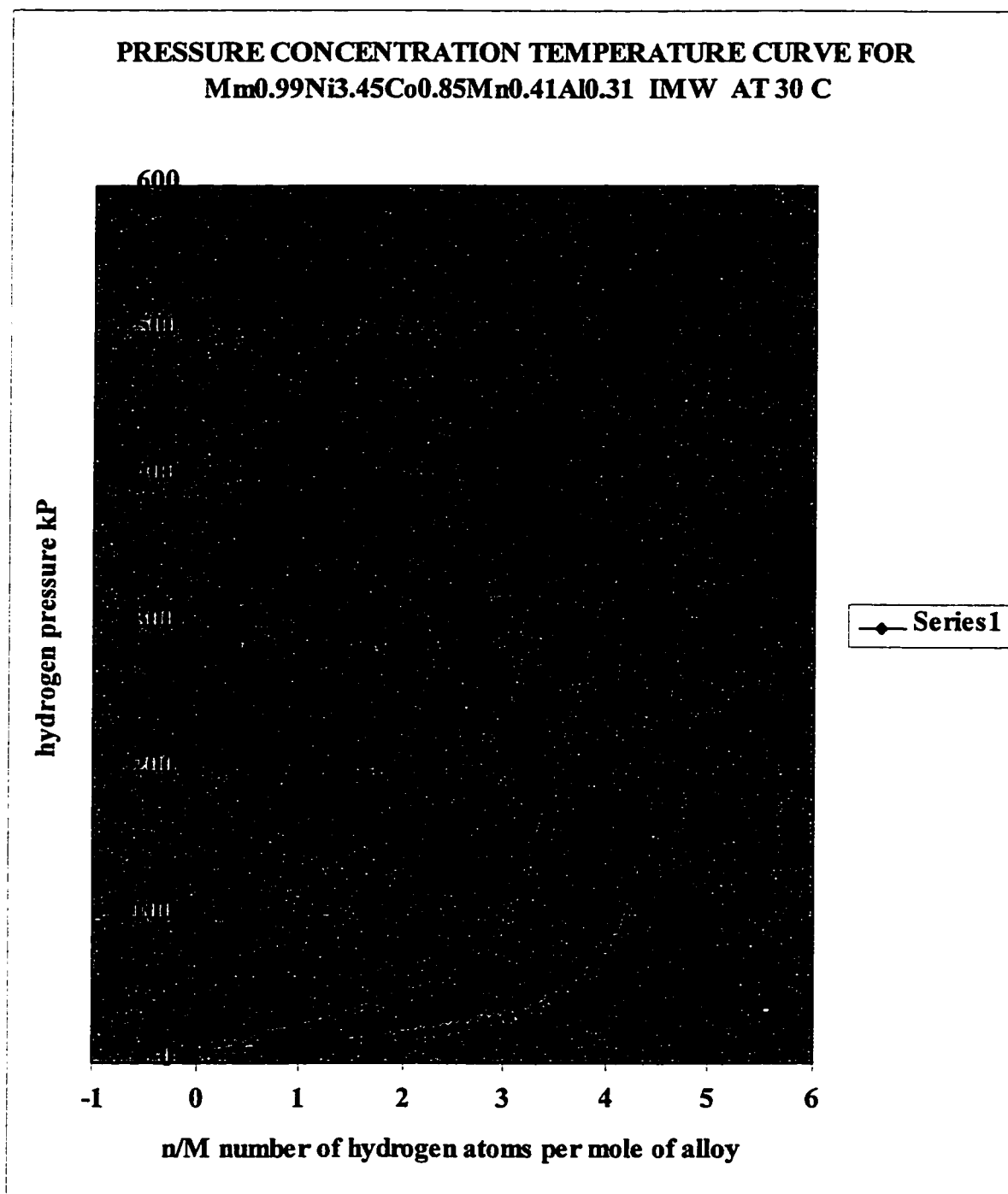


Figure 5.6 Pressure concentration temperature curve for $Mm_{0.99}Ni_{3.45}Co_{0.85}Mn_{0.41}Al_{0.31}IMW$ at 30 °C. The upper curve is absorption and the lower curve is desorption.

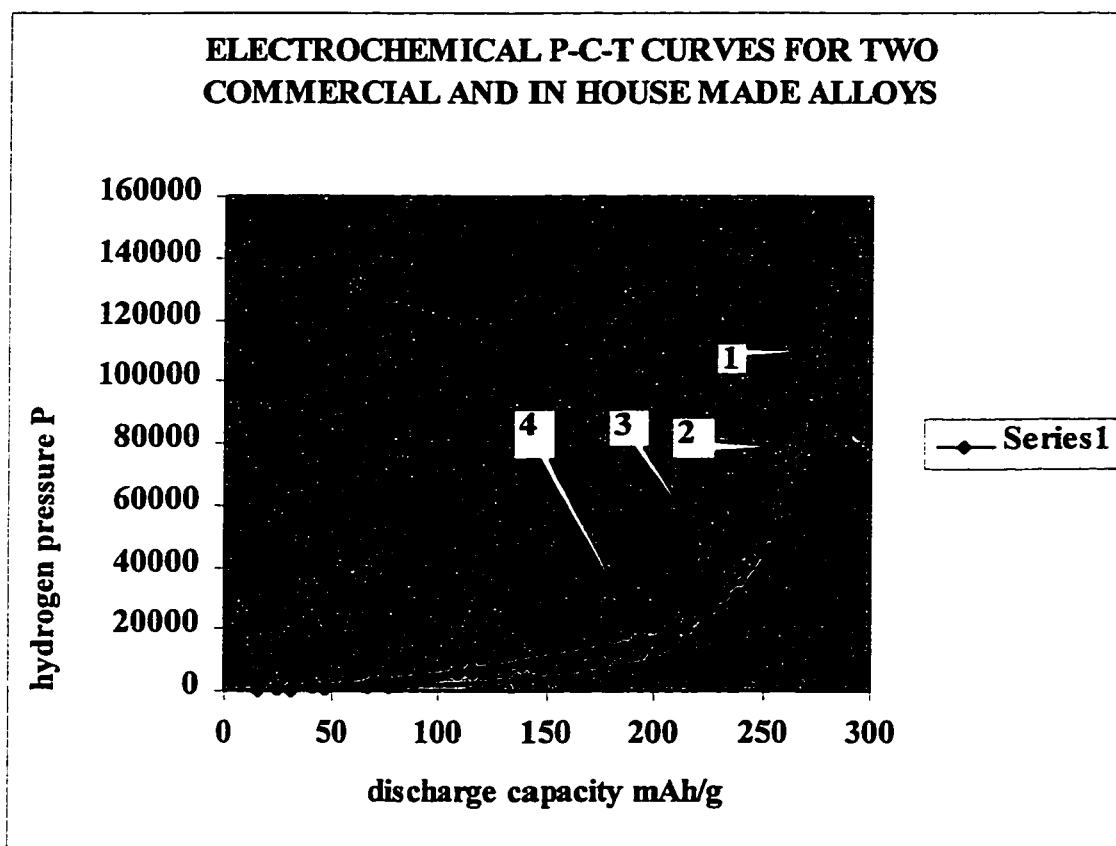


Figure 5.7 Electrochemical pressure concentration temperature curves for IBA # 6 (1); $\text{Mm}_{0.99}\text{Ni}_{3.45}\text{Co}_{0.85}\text{Mn}_{0.41}\text{Al}_{0.31}\text{IMW}$ (2); IBA # 5 (3) and $\text{Mm}_{0.99}\text{Ni}_{3.48}\text{Co}_{0.7}\text{Al}_{0.81}\text{IMW}$ (4) obtained at room temperature using reference Hg/HgO electrode.

5.4 XRD Results

Parameters of crystal cells for NiMH alloys are depicted in Table 5.1. The name of alloys is the same as in Table 3.1. First name is nominal composition of alloys followed by the name based on ICP analysis. The a , c , c/a and V parameters are given with the name of alloys obtained by ICP analysis. Heat-treated alloys keep the same name as the as-cast alloys. Parameters a and c are the cell parameters in Å and V is the volume of crystal cell in Å³. The increase of cell

parameters because of absorption of hydrogen for hydrides of IBA #5, IBA #6, $\text{Mm}_{0.99}\text{Ni}_{3.48}\text{Co}_{0.7}\text{Al}_{0.81}\text{IMW}$ and $\text{Mm}_{0.99}\text{Ni}_{3.45}\text{Co}_{0.85}\text{Mn}_{0.41}\text{Al}_{0.31}\text{IMW}$ alloys are presented in Table 5.2.

Table 5.1 XRD results of NiMH alloy

	a (Å)	c (Å)	c/a	V(Å ³)
1. IBA #5	4.978±0.005	4.072±0.003	0.8180±0.0005	87.384
2. IBA #6	5.010±0.008	4.053±0.008	0.8089±0.0014	88.09
3. $\text{Mm}_{0.9}\text{Ni}_{3.5}\text{Co}_{0.7}\text{Al}_{0.8}$ (nom.comp.)				
4. $\text{Mm}_{0.88}\text{Ni}_{3.43}\text{Co}_{0.71}\text{Al}_{0.76}$ *	4.986±0.010	4.046±0.01	0.811±0.002	87.213
$\text{Mm}_{0.88}\text{Ni}_{3.43}\text{Co}_{0.71}\text{Al}_{0.7}$ **	4.97±0.004	4.056±0.004	0.8160±0.001	86.764
$\text{Mm}_{0.88}\text{Ni}_{3.43}\text{Co}_{0.71}\text{Al}_{0.56}$ ***	4.977±0.006	4.056±0.006	0.8148±0.001	87.008
5. $\text{MmNi}_{3.5}\text{Co}_{0.7}\text{Al}_{0.8}$ (nom. comp)				
6. $\text{Mm}_{0.99}\text{Ni}_{3.5}\text{Co}_{0.7}\text{Al}_{0.8}$ *	4.978±0.03	4.069±0.06	0.8174±0.0005	87.322
$\text{Mm}_{0.99}\text{Ni}_{3.5}\text{Co}_{0.7}\text{Al}_{0.81}$ **	4.98±0.003	4.067±0.003	0.8168±0.0005	87.347
$\text{Mm}_{0.99}\text{Ni}_{3.5}\text{Co}_{0.7}\text{Al}_{0.81}$ ***	4.98±0.003	4.068±0.003	0.8168±0.0005	87.369
7. $\text{Mm}_{1.02}\text{Ni}_{3.5}\text{Co}_{0.7}\text{Al}_{0.8}$ (nom. comp.)				
8. $\text{Mm}_{0.99}\text{Ni}_{3.47}\text{Co}_{0.73}\text{Al}_{0.81}$ *	4.980±0.005	4.073±0.005	0.8178±0.0005	87.478
$\text{Mm}_{0.99}\text{Ni}_{3.47}\text{Co}_{0.73}\text{Al}_{0.81}$ **	4.980±0.004	4.069±0.004	0.8170±0.0007	87.39
$\text{Mm}_{0.99}\text{Ni}_{3.47}\text{Co}_{0.73}\text{Al}_{0.81}$ ***	4.982±0.002	4.068±0.002	0.8167±0.0003	87.43
9. $\text{Mm}_{1.025}\text{Ni}_{3.5}\text{Co}_{0.7}\text{Al}_{0.8}$ (nom.comp.)				
10. $\text{MmNi}_{3.48}\text{Co}_{0.71}\text{Al}_{0.81}$ *	4.991±0.005	4.069±0.005	0.8152±0.0005	87.779
$\text{MmNi}_{3.48}\text{Co}_{0.71}\text{Al}_{0.81}$ **	4.983±0.004	4.070±0.004	0.8167±0.0007	87.517
$\text{MmNi}_{3.48}\text{Co}_{0.71}\text{Al}_{0.81}$ ***	4.984±0.003	4.070±0.003	0.8166±0.0005	87.555
11. $\text{Mm}_{1.1}\text{Ni}_{3.5}\text{Co}_{0.7}\text{Al}_{0.8}$ (nom. comp.)				

12.	Mm _{1.09} Ni _{3.45} Co _{0.72} Al _{0.85} *	4.986±0.004	4.072±0.004	0.8152±0.0007	87.668
	Mm _{1.09} Ni _{3.45} Co _{0.72} Al _{0.85} **	4.984±0.007	4.073±0.007	0.8172±0.0012	87.61
	Mm _{1.09} Ni _{3.45} Co _{0.72} Al _{0.85} *** (nom. comp.)	4.987±0.001	4.077±0.010	0.8175±0.0016	87.811
13.	MmNi _{3.33} Co _{0.66} Al _{0.76} (nom. comp.)				
14.	Mm _{0.92} Ni _{3.33} Co _{0.69} Al _{0.8} *	4.975±0.020	4.026±0.020	0.8093±0.004	86.295
	Mm _{0.92} Ni _{3.33} Co _{0.69} Al _{0.8} **	5.023±0.006	4.056±0.006	0.8075±0.0010	88.518
	Mm _{0.92} Ni _{3.33} Co _{0.69} Al _{0.8} ***	5.025±0.004	4.052±0.004	0.8063±0.0006	88.607
15.	MmNi _{3.78} Co _{0.756} Al _{0.864} (nom.comp.)				
16.	Mm _{0.99} Ni _{3.78} Co _{0.756} Al _{0.84} *	4.973±0.006	4.063±0.006	0.8170±0.0001	87.019
	Mm _{0.99} Ni _{3.78} Co _{0.756} Al _{0.84} **	4.973±0.005	4.062±0.005	0.8167±0.0008	86.997
	Mm _{0.99} Ni _{3.78} Co _{0.756} Al _{0.84} ***	4.975±0.008	4.054±0.008	0.8148±0.0012	86.896
	MmNi _{3.5} Co _{0.8} Mn _{0.4} Al _{0.3} (nom. comp.)				
18.	MmNi _{3.54} Co _{0.82} Mn _{0.34} Al _{0.3} *	5.007±0.007	4.062±0.007	0.8114±0.0015	88.19
	MmNi _{3.54} Co _{0.82} Mn _{0.34} Al _{0.3} **	5.009±0.007	4.065±0.007	0.8115±0.0012	88.326
	MmNi _{3.54} Co _{0.82} Mn _{0.34} Al _{0.3} ***	5.007±0.004	4.052±0.004	0.8093±0.0006	87.974
19.	Mm _{0.9} Ni _{3.5} Co _{0.8} Mn _{0.4} Al _{0.3} (nom.co				
20.	Mm _{0.92} Ni _{3.48} Co _{0.83} Mn _{0.29} Al _{0.31} *	4.968±0.015	4.059±0.015	0.817±0.002	86.758
	Mm _{0.92} Ni _{3.48} Co _{0.83} Mn _{0.29} Al _{0.31} **	4.999±0.0008	4.055±0.0008	0.8119±0.0012	87.582
	Mm _{0.92} Ni _{3.48} Co _{0.83} Mn _{0.29} Al _{0.31} ***	0.004	4.055±0.015	0.8138±0.0006	87.197
21.	Mm _{1.1} Ni _{3.5} Co _{0.8} Mn _{0.4} Al _{0.3} (nom.comp.)				
22.	Mm _{1.065} Ni _{3.51} Co _{0.83} Mn _{0.37} Al _{0.32} *	5.013±0.012	4.051±0.012	0.808±0.002	88.163
	Mm _{1.065} Ni _{3.51} Co _{0.83} Mn _{0.37} Al _{0.32} **	5.025±0.008	4.047±0.008	0.8053±0.0015	88.498
	Mm _{1.065} Ni _{3.51} Co _{0.83} Mn _{0.37} Al _{0.32} ***	5.021±0.006	4.044±0.006	0.8054±0.002	88.292
23.	MmNi _{3.33} Co _{0.76} Mn _{0.38} Al _{0.28} (nom.				
24.	Mm _{0.98} Ni _{3.33} Co _{0.79} Mn _{0.35} Al _{0.3} *	5.007±0.012	4.045±0.012	0.808±0.002	87.82
	Mm _{0.98} Ni _{3.33} Co _{0.79} Mn _{0.35} Al _{0.3} **	5.020±0.004	4.052±0.004	0.8071±0.0006	88.431
	Mm _{0.98} Ni _{3.33} Co _{0.79} Mn _{0.35} Al _{0.3} ***	5.022±0.004	4.048±0.004	0.8062±0.0006	88.414

25.	$\text{mNi}_{13.78}\text{Co}_{0.86}\text{Mn}_{0.43}\text{Al}_{0.32}$ (nom.comp.)				
26.	$\text{Mm}_{0.99}\text{Ni}_{3.79}\text{Co}_{0.9}\text{Mn}_{0.4}\text{Al}_{0.33}^*$	4.993 ± 0.012	4.039 ± 0.012	0.809 ± 0.02	87.16
	$\text{Mm}_{0.99}\text{Ni}_{3.79}\text{Co}_{0.9}\text{Mn}_{0.4}\text{Al}_{0.33}^{**}$	4.999 ± 0.005	4.049 ± 0.005	0.8099 ± 0.008	87.52
	$\text{Mm}_{0.99}\text{Ni}_{3.79}\text{Co}_{0.9}\text{Mn}_{0.4}\text{Al}_{0.33}^{***}$	4.988 ± 0.005	4.062 ± 0.006	0.8144 ± 0.001	87.52
27.	$\text{Mm}_{0.99}\text{Ni}_{3.48}\text{Co}_{0.7}\text{Al}_{0.81}$ IMW*	4.987 ± 0.012	4.07 ± 0.012	0.8161 ± 0.001	8 ¹ 7.657
	$\text{Mm}_{0.99}\text{Ni}_{3.48}\text{Co}_{0.7}\text{Al}_{0.81}$ IMW**	4.985 ± 0.005	4.07 ± 0.005	0.8164 ± 0.008	87.58
	$\text{Mm}_{0.99}\text{Ni}_{3.48}\text{Co}_{0.7}\text{Al}_{0.81}$ IMW***	4.988 ± 0.002	4.069 ± 0.002	0.8158 ± 0.003	87.68
28.	$\text{Mm}_{0.99}\text{Ni}_{3.45}\text{Co}_{0.85}\text{Mn}_{0.41}\text{Al}_{0.31}$ IMW*	5.004 ± 0.004	4.049 ± 0.004	0.8091 ± 0.007	87.8
	$\text{Mm}_{0.99}\text{Ni}_{3.45}\text{Co}_{0.85}\text{Mn}_{0.41}\text{Al}_{0.31}$ IMW**	5.008 ± 0.006	4.059 ± 0.002	0.8104 ± 0.0003	88.15
	$\text{Mm}_{0.99}\text{Ni}_{3.45}\text{Co}_{0.85}\text{Mn}_{0.41}\text{Al}_{0.31}$ IMW***	5.006 ± 0.002	4.058 ± 0.002	0.8106 ± 0.003	88.06
29.	$\text{Mm}_{0.99}\text{Ni}_{3.48}\text{Co}_{0.7}\text{Al}_{0.81}\text{H}_{4.12}$ IMW *	5.264 ± 0.002	4.202 ± 0.002	0.7982 ± 0.0003	100.83
30.	$\text{Mm}_{0.99}\text{Ni}_{3.45}\text{Co}_{0.85}\text{Mn}_{0.41}\text{Al}_{0.31}\text{H}_{4.83}$ IMW *	5.309 ± 0.003	4.205 ± 0.003	0.792 ± 0.005	102.63
31.	IBA #5 $\text{H}_{3.2}$	5.252 ± 0.004	4.194 ± 0.004	0.7986 ± 0.006	100.18
32.	IBA #6 $\text{H}_{4.93}$	5.356 ± 0.004	4.245 ± 0.0004	0.7926 ± 0.0006	105.45

¹ *- ACW

** - heat treated at 800°C

*** - heat treated at 1000°C

Table 5.2 Comparison of cell parameters of alloys and hydrides

	a(Å)	c(Å)	$\Delta a/a$	$\Delta c/c$	$\Delta V/V$
IBA #5	4.978±0.005	4.072±0.003			
IBA #5 hydride	5.252±0.004	4.194±0.004	5.5%	2.96%	14.65%
Mm _{0.99} Ni _{3.48} Co _{0.7} Al _{0.81} IMW	4.987±0.012	4.070±0.012			
Mm _{0.99} Ni _{3.48} Co _{0.7} Al _{0.81} H _{4.12} IMW*	5.264±0.002	4.202±0.002	5.55%	3.24%	15.02%
IBA #6	5.01±0.008	4.053±0.008			
IBA #6 hydride	5.356±0.004	4.245±0.0004	6.9%	4.6%	19.7%
Mm _{0.99} Ni _{3.45} Co _{0.85} Mn _{0.41} Al _{0.31} IMW	5.004±0.004	4.049±0.004			
Mm _{0.99} Ni _{3.45} Co _{0.85} Mn _{0.41} Al _{0.31} H _{4.83} IMW *	5.309±0.003	4.205±0.003	6.09%	3.85%	17.08%

Table 2 represents the cell parameter of two commercial alloys and their hydrides and two IMW alloys and their hydrides. The increase of **a** and **c** parameters and total cell volume because of absorption of hydrogen are presented in percentage.

5.5 Results of Electrochemical Discharge Capacity and Discharge Rate of NiMH Alloys

The discharge capacity of Mm_{0.88}Ni_{3.43}Co_{0.71}Al_{0.76} ACW is about 214 mAh/g after five cycles using 92 mA/g discharge current. The discharge capacity of all alloys in further text is described using this discharge rate. Higher discharge rates are also used in experiments and are described in further text for each particular case. The alloy is sensitive to the higher discharge current. The

heat-treated alloy at 800°C has a discharge capacity about 217 mAh/g after four cycles and is not at all sensitive to the higher discharge current. The heat-treated alloy at 1000°C has the highest discharge capacity (254 mAh/g after 10 cycles) among the three above mentioned alloys and has a moderate sensitivity to the higher discharge current.

$\text{Mm}_{0.99}\text{Ni}_{3.5}\text{Co}_{0.7}\text{Al}_{0.81}$ ACW is a stoichiometric alloy and has a discharge capacity about 224 mAh/g after 11 cycles and moderate sensitivity to the discharge current up to 184 mA/g. The alloy is very sensitive to discharge currents higher than 184 mA/g. Heat treatment at 800 °C increases the discharge capacity up to 240 mAh/g after 21 cycles and decreases the alloy sensitivity to the higher discharge current. Heat treatment at 1000°C decreases the discharge capacity down to 206 mAh/g after 10 cycles and strongly increases the alloy's sensitivity to the higher discharge current.

$\text{Mm}_{0.99}\text{Ni}_{3.47}\text{Co}_{0.73}\text{Al}_{0.81}$ ACW has a discharge capacity about 240 mAh/g after 14 cycles. The alloy is not sensitive to higher discharge current up to 184 mA/g and exhibits moderate sensitivity to higher discharge currents. Heat treatment at 800°C increases the discharge capacity up to 276 mAh/g in 18 cycles and markedly decreases sensitivity of alloy to higher discharge current. Among 21 NiMH alloys without manganese examined in this work, this alloy exhibits the highest performance. Heat treatment at 1000 °C considerably decreases the discharge capacity and rate capability of alloys (Figure 5.9).

$\text{MmNi}_{3.48}\text{Co}_{0.71}\text{Al}_{0.81}$ ACW has a discharge capacity about 240 mAh/g after 15 cycles. The rate capability of this alloy is good. The discharge capacity at a discharge current of 248 mA/g is about 218 mAh/g. Heat treatment at 800°C increases the discharge capacity up to 250 mAh/g and rate capability (Figure 5.9). Heat treatment at 1000 °C decreases the discharge capacity and rate

capability considerably. Among 21 NiMH alloys examined this one exhibits the poorest performance.

$\text{Mm}_{1.09}\text{Ni}_{3.45}\text{Co}_{0.72}\text{Al}_{0.85}$ ACW has a discharge capacity about 236 mAh/g after 5 cycles and good rate capability. Heat treatment at 800°C increases the discharge capacity up to 260 mAh/g in 10 cycles and the rate capability. This alloy has the best rate capability among 21 examined NiMH alloys without manganese. Heat treatment at 1000°C decreases the discharge capacity and rate capability considerably.

So far the A-side of A_xB_5 alloys was varied between $x = 0.88 - 1.09$. The next two alloys are nonstoichiometric AB_x , $x = 4.76 - 5.4$, type. $\text{Mm}_{0.92}\text{Ni}_{3.33}\text{Co}_{0.69}\text{Al}_{0.8}$ ACW has a discharge capacity about 231 mAh/g in 12 cycles. The alloy has a very poor rate capability. This alloy also contains less mischmetal atoms than stoichiometry and the composition of mischmetal is different. The mischmetal is made of La and Nd. Heat treatment at 800 °C slightly improves the characteristic of the alloy. Heat treatment at 1000°C drastically decreases the discharge capacity and rate capability.

$\text{Mm}_{0.99}\text{Ni}_{3.78}\text{Co}_{0.756}\text{Al}_{0.84}$ ACW has a discharge capacity about 230 mAh/g in 17 cycles. The alloy exhibits acceptable rate capability. Heat treatment does not change the characteristics significantly. Heat-treated alloy at 1000°C has the best characteristics for this type of alloy. This alloy has a discharge capacity about 240 mAh/g in 15 cycles. The discharge capacity of the above mentioned alloys are depicted in Figure 5.8. The discharge rate was measured against $\text{Ni}(\text{OH})_2$ standard electrode. Figure 5.8 also depicts rate capabilities of each alloy. The discharge capabilities as a function of discharge current are depicted in Figure 5.9. Numbers 1.0, 1.1 and 1.2 etc. represent alloys as cast, heat-treated at 800°C and 1000 °C, respectively. The influence of heat treatment on rate capabilities is depicted as well.

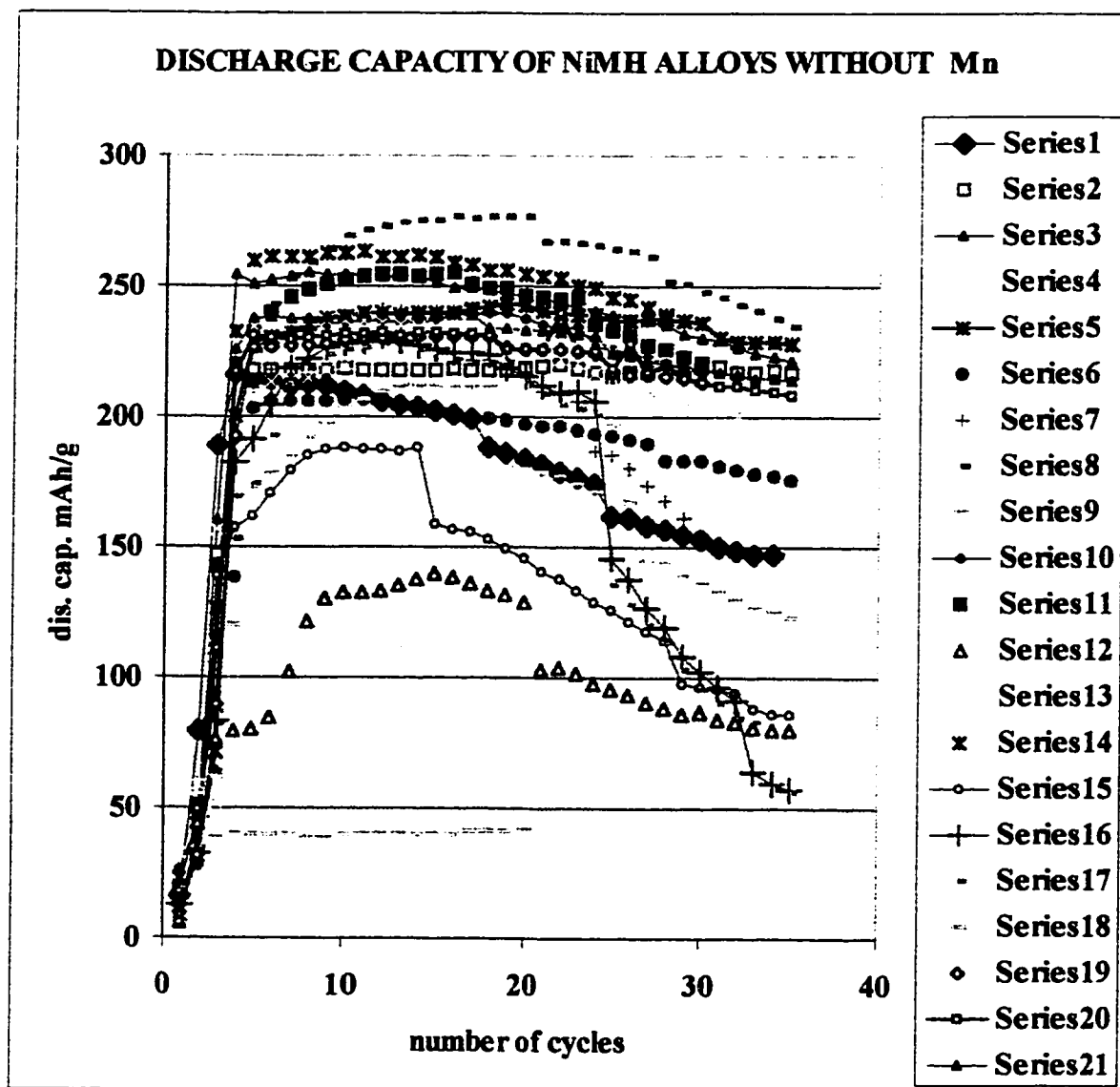


Figure 5.8 Discharge capacity of NiMH alloys without Mn. Charge current was 184 mA/g for 2 h, discharge current were 92, 184, 248 mA/g to 0.6 V against Ni(OH)₂. Series1,2,3 are $Mm_{0.88}Ni_{3.43}Co_{0.71}Al_{0.76}$ ACW, h. t. at 800°C, h.t. at 1000°C respectively; Series 4,5,6 are $Mm_{0.99}Ni_{3.5}Co_{0.7}Al_{0.81}$ ACW, h.t. at 800 °C, h.t. at 1000°C respectively; Series 7,8,9 are $Mm_{0.99}Ni_{3.47}Co_{0.73}Al_{0.81}$ ACW, h.t. at 800 °C, h.t. at 1000°C respectively; Series 10, 11, 12 are $MmNi_{3.48}Co_{0.71}Al_{0.81}$ as cast ACW, h.t. at 800 °C, h.t. at 1000°C respectively; Series 13,14,15 are $Mm_{1.09}Ni_{3.45}Co_{0.72}Al_{0.85}$ ACW, h.t. at 800 °C, h.t. at 1000°C respectively; Series 16, 17, 18 are $Mm_{0.92}Ni_{3.33}Co_{0.69}Al_{0.8}$ ACW, h.t. at 800 °C, h.t. at 1000°C respectively; Series 19,20 ,21 are $Mm_{0.99}Ni_{3.78}Co_{0.756}Al_{0.84}$ ACW, h.t. at 800 °C, h.t. at 1000°C respectively;

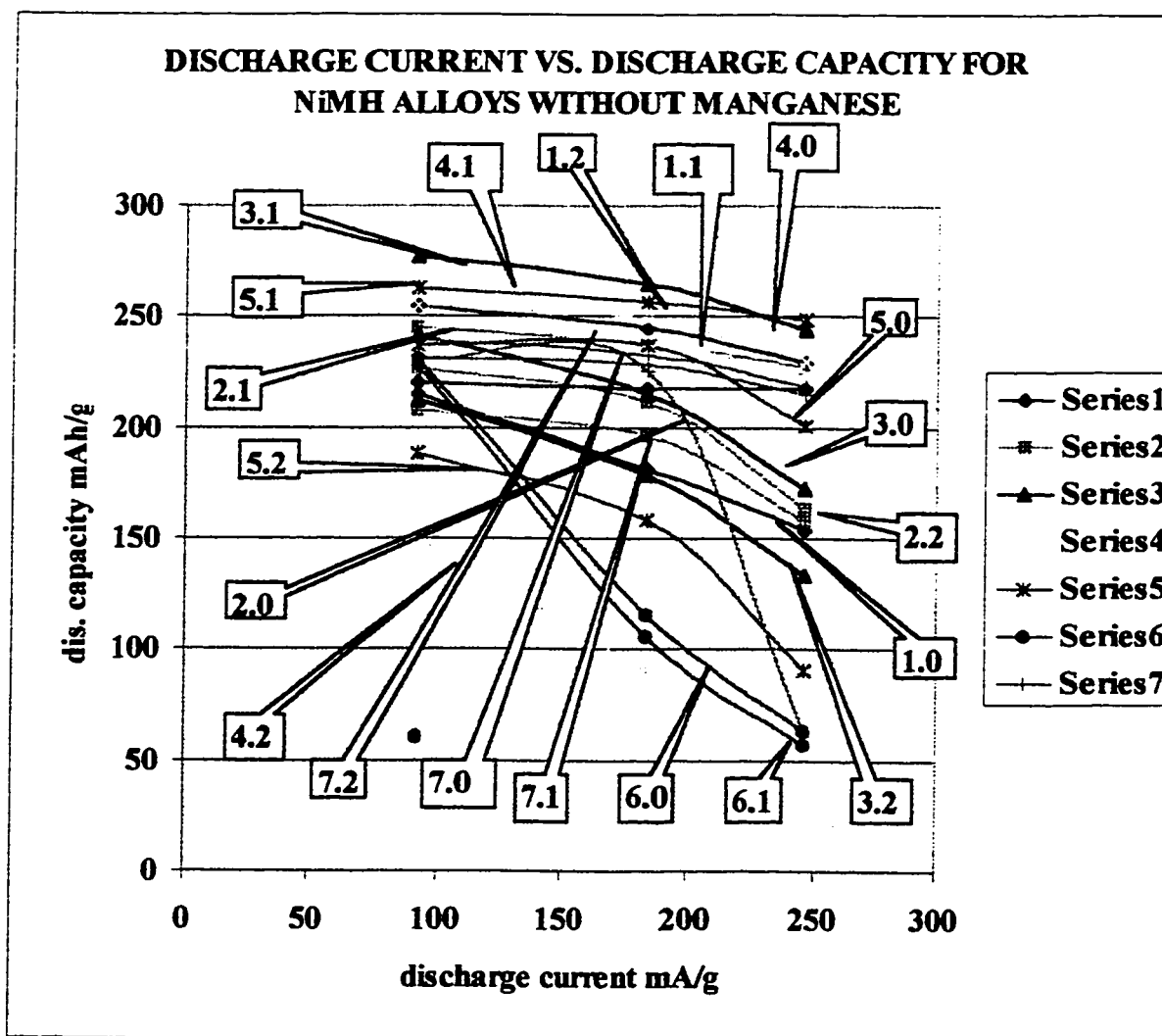


Figure 5.9 Rate capability of NiMH alloys without Mn. Charge current was 184 mA/g for 2 h, discharge current were 92, 184, 248 mA/g to 0.6 V against Ni(OH)₂. 1.0, 1.1, 1.2 are $\text{Mm}_{0.88}\text{Ni}_{3.43}\text{Co}_{0.71}\text{Al}_{0.76}$ ACW, h. t. at 800 °C, h.t. at 1000°C respectively; 2.0, 2.1, 2.2 are $\text{Mm}_{0.99}\text{Ni}_{3.5}\text{Co}_{0.7}\text{Al}_{0.81}$ ACW, h.t. at 800 °C, h.t. at 1000°C respectively; 3.0, 3.1, 3.2 are $\text{Mm}_{0.99}\text{Ni}_{3.47}\text{Co}_{0.73}\text{Al}_{0.81}$ ACW, h.t. at 800 °C, h.t. at 1000°C respectively; 4.0, 4.1, 4.2 are $\text{MmNi}_{3.48}\text{Co}_{0.71}\text{Al}_{0.81}$ ACW, h.t. at 800°C, h.t. at 1000°C respectively; 5.0, 5.1, 5.2 are $\text{Mm}_{1.09}\text{Ni}_{3.45}\text{Co}_{0.72}\text{Al}_{0.85}$ ACW, h.t. at 800°C, h.t. at 1000°C respectively; 6.0, 6.1 are $\text{Mm}_{0.92}\text{Ni}_{3.33}\text{Co}_{0.69}\text{Al}_{0.8}$ ACW, h.t. at 800°C; 7.0, 7.1, 7.2 are $\text{Mm}_{0.99}\text{Ni}_{3.78}\text{Co}_{0.756}\text{Al}_{0.84}$ ACW, h.t. at 800°C, h.t. at 1000°C respectively.

The NiMH with Mn were examined the same way as NiMH alloys without Mn. The discharge capacity was obtained against Ni(OH)₂ reference electrode. The charge and discharge were the same as for above described alloys. The discharge capacity for NiMH alloys with Mn is depicted in Figure 5.10.

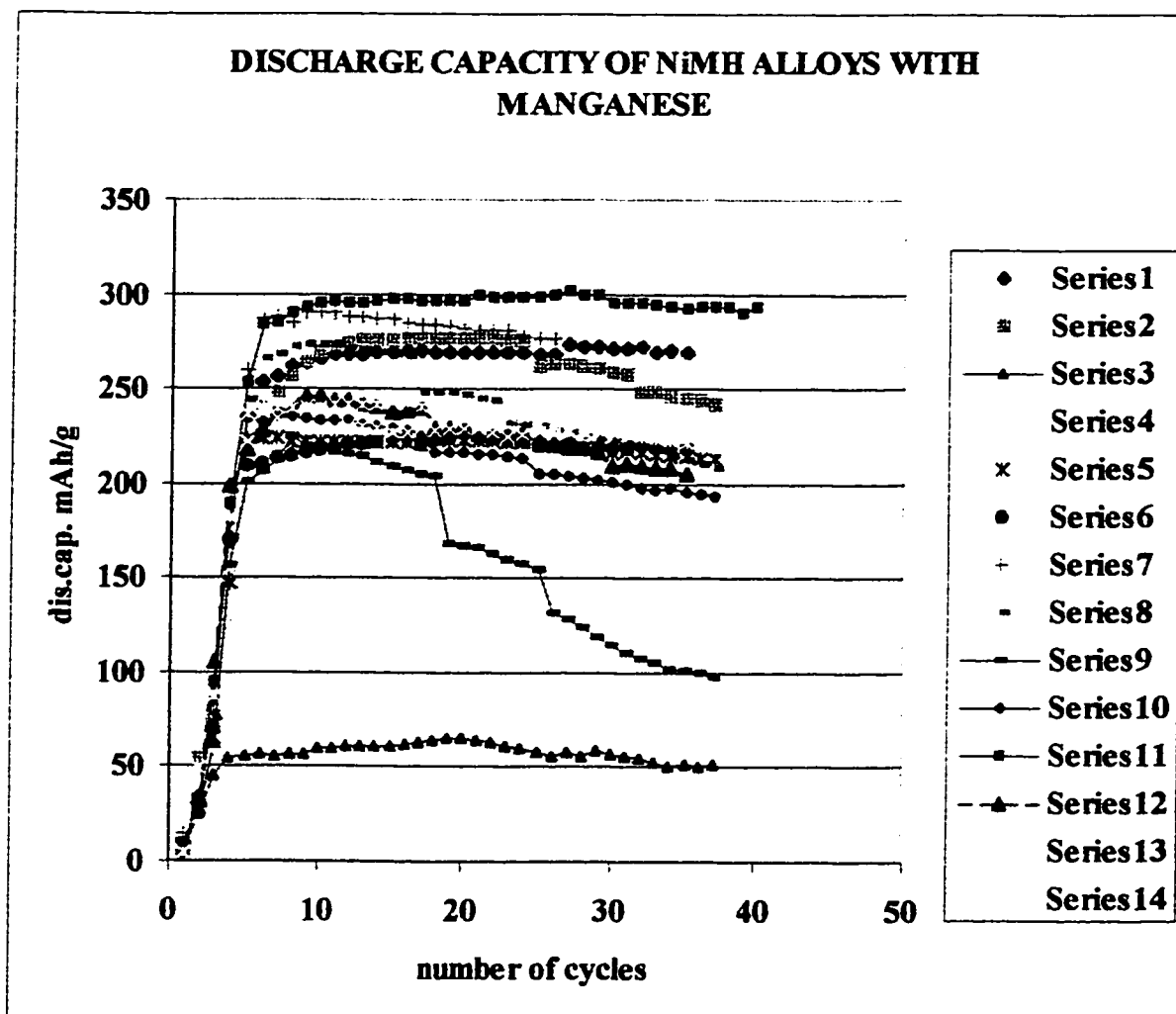


Figure 5.10 Discharge capacity for NiMH alloys with Mn. Charge current was 184 mA/g for 2 h discharge current were 92, 184, 248 mA/g to 0.6 V against Ni(OH)₂. Series 1,2,3 are $\text{MmNi}_{3.54}\text{Co}_{0.82}\text{Mn}_{0.34}\text{Al}_{0.3}$ ACW h.t. at 800°C, h. t. at 1000°C respectively; Series 4, 5, 6 are $\text{Mm}_{0.92}\text{Ni}_{3.48}\text{Co}_{0.83}\text{Mn}_{0.29}\text{Al}_{0.31}$ ACW, h.t. at 800°C, h. t. at 1000°C respectively; Series 7,8,9 are $\text{Mm}_{1.065}\text{Ni}_{3.51}\text{Co}_{0.83}\text{Mn}_{0.37}\text{Al}_{0.32}$ ACW, h.t. at 800°C, h. t. at 1000°C respectively; Series 10,11, 12 are $\text{Mm}_{0.98}\text{Ni}_{3.33}\text{Co}_{0.79}\text{Mn}_{0.35}\text{Al}_{0.3}$ ACW, h.t. at 800°C, h. t. at 1000°C respectively; Series 13, 14 are $\text{Mm}_{0.99}\text{Ni}_{3.79}\text{Co}_{0.9}\text{Mn}_{0.4}\text{Al}_{0.33}$ ACW and h.t. at 800°C, respectively.

$\text{MmNi}_{3.54}\text{Co}_{0.82}\text{Mn}_{0.34}\text{Al}_{0.3}$ ACW has a discharge capacity about 269 mAh/g after 10 cycles. The increase of discharge current (184, 248 mA/g) causes a slight increase of discharge capacity up to 276 mAh/g. Heat treatment at 800°C increases the discharge capacity slightly and decreases

the rate capability of the alloy. Heat treatment at 1000°C decreases the discharge capacity and rate capability drastically.

$\text{Mm}_{0.92}\text{Ni}_{3.48}\text{Co}_{0.83}\text{Mn}_{0.29}\text{Al}_{0.31}$ ACW has a discharge capacity about 225 mAh/g after 5 cycles. The increase of discharge current to 184mA/g and 248 mA/g increases the discharge capacity up to 236 mAh/g. Heat treatment at 800°C does not affect the discharge capacity but decreases the rate capability of the alloy. Heat treatment at 1000°C slightly increases the discharge capacity. The rate capability of this alloy is good.

$\text{Mm}_{1.065}\text{Ni}_{3.51}\text{Co}_{0.83}\text{Mn}_{0.37}\text{Al}_{0.32}$ ACW has a discharge capacity about 287 mAh/g after five cycles. The rate capability of this alloy is very good. Heat treatment at 800°C decreases the discharge capacity and rate capability. Heat treatment at 1000°C further decreases the discharge capacity (223 mAh/g) and rate capability.

$\text{Mm}_{0.98}\text{Ni}_{3.33}\text{Co}_{0.79}\text{Mn}_{0.35}\text{Al}_{0.3}$ ACW has a discharge capacity about 234 mAh/g in 6 cycles. The rate capability of this alloy is poor. Heat treatment at 800°C drastically increases the discharge capacity up to 312 mAh/g and rate capability in 10 cycles. This alloy has the best characteristics among 15 NiMH alloys with Mn. Heat treatment at 1000°C gives slightly better characteristics than ACW alloys.

$\text{Mm}_{0.99}\text{Ni}_{3.79}\text{Co}_{0.9}\text{Mn}_{0.4}\text{Al}_{0.33}$ ACW has a discharge capacity about 231 mAh/g after 8 cycles. The alloy has very good rate capabilities. Heat treatment at 800°C increases the discharge capacity up to 240 mAh/g after 4 cycles and improves the rate capability at the rate up to 184 mA/g of discharge current. Higher discharge current decreases the discharge capacity and the rate capability. Heat treatment at 1000°C gives similar discharge capacity after 100 cycles. The rate capabilities of NiMH alloys with Mn are depicted in Figure 5.11.

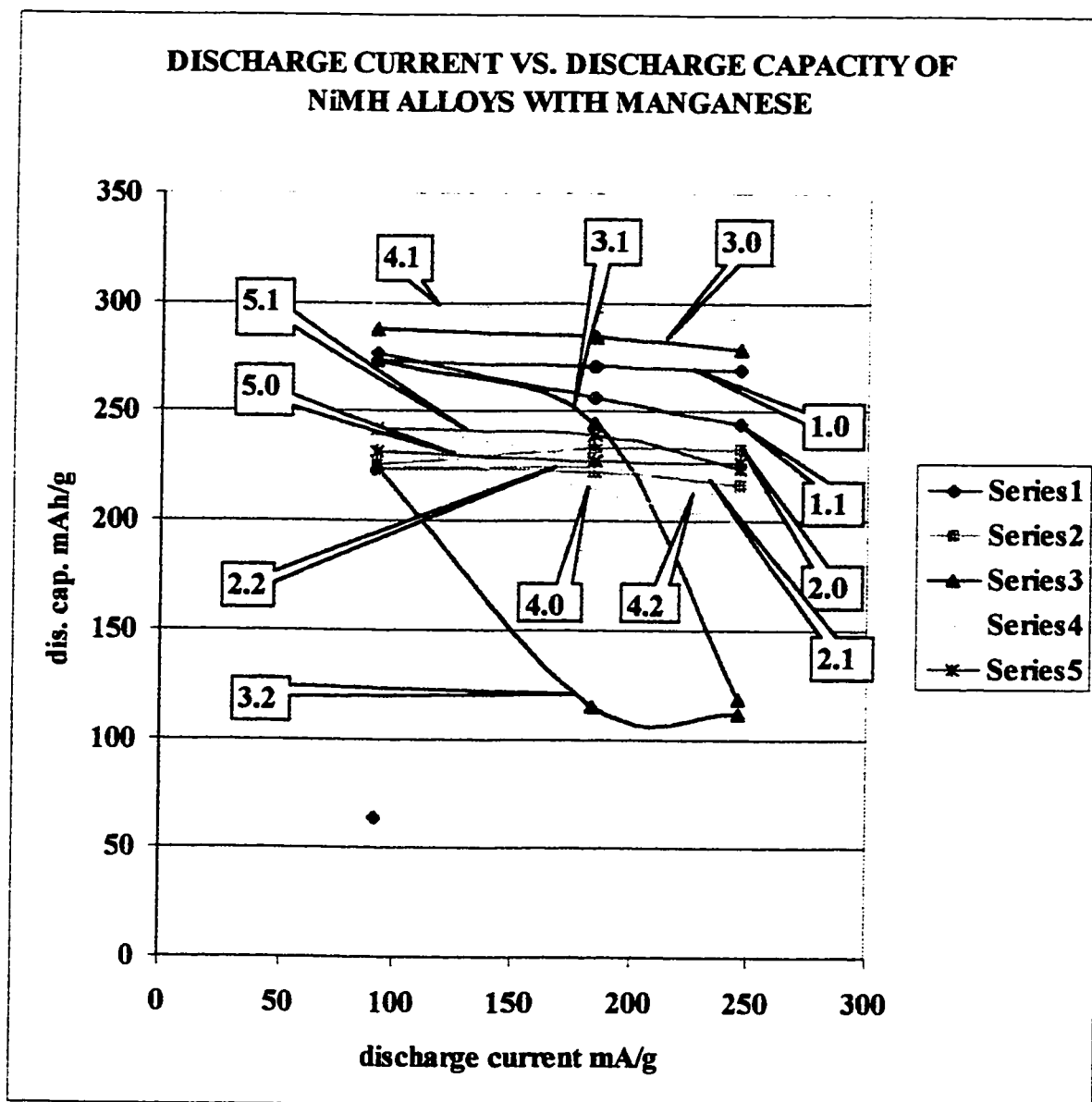


Figure 5.11 Rate capability of NiMH alloys with Mn. Charge current was 184 mA/g for 2 h, discharge current were 92, 184, 248 mA/g to 0.6 V against $\text{Ni}(\text{OH})_2$. In diagram 1.0, 1.1, 1.2 are $\text{MmNi}_{3.54}\text{Co}_{0.82}\text{Mn}_{0.34}\text{Al}_{0.3}$ ACW, h.t. at 800°C, h.t. at 1000°C respectively; 2.0, 2.1, 2.2 are $\text{Mm}_{0.92}\text{Ni}_{3.48}\text{Co}_{0.83}\text{Mn}_{0.29}\text{Al}_{0.31}$ ACW, h.t. at 800°C, h.t. at 1000°C respectively; 3.0, 3.1, 3.2 are $\text{Mm}_{1.065}\text{Ni}_{3.51}\text{Co}_{0.83}\text{Mn}_{0.37}\text{Al}_{0.32}$ ACW, h.t. at 800°C, h.t. at 1000°C respectively; 4.0, 4.1, 4.2 are $\text{Mm}_{0.98}\text{Ni}_{3.33}\text{Co}_{0.79}\text{Mn}_{0.35}\text{Al}_{0.3}$ ACW, h.t. at 800°C, h.t. at 1000°C respectively; 5.0, 5.1 are $\text{Mm}_{0.99}\text{Ni}_{3.79}\text{Co}_{0.9}\text{Mn}_{0.4}\text{Al}_{0.33}$ ACW, h.t. at 800°C, h.t. at 1000°C respectively.

The alloys described above were produced in the arc melting unit. The characteristics of alloys produced in the induction-melting unit are depicted in Figure 5.12 and 5.13. The discharge

capacity of IMW alloys is depicted in Figure 5.12 together with the discharge capacity of two commercial alloys and two stoichiometric AMW alloys.

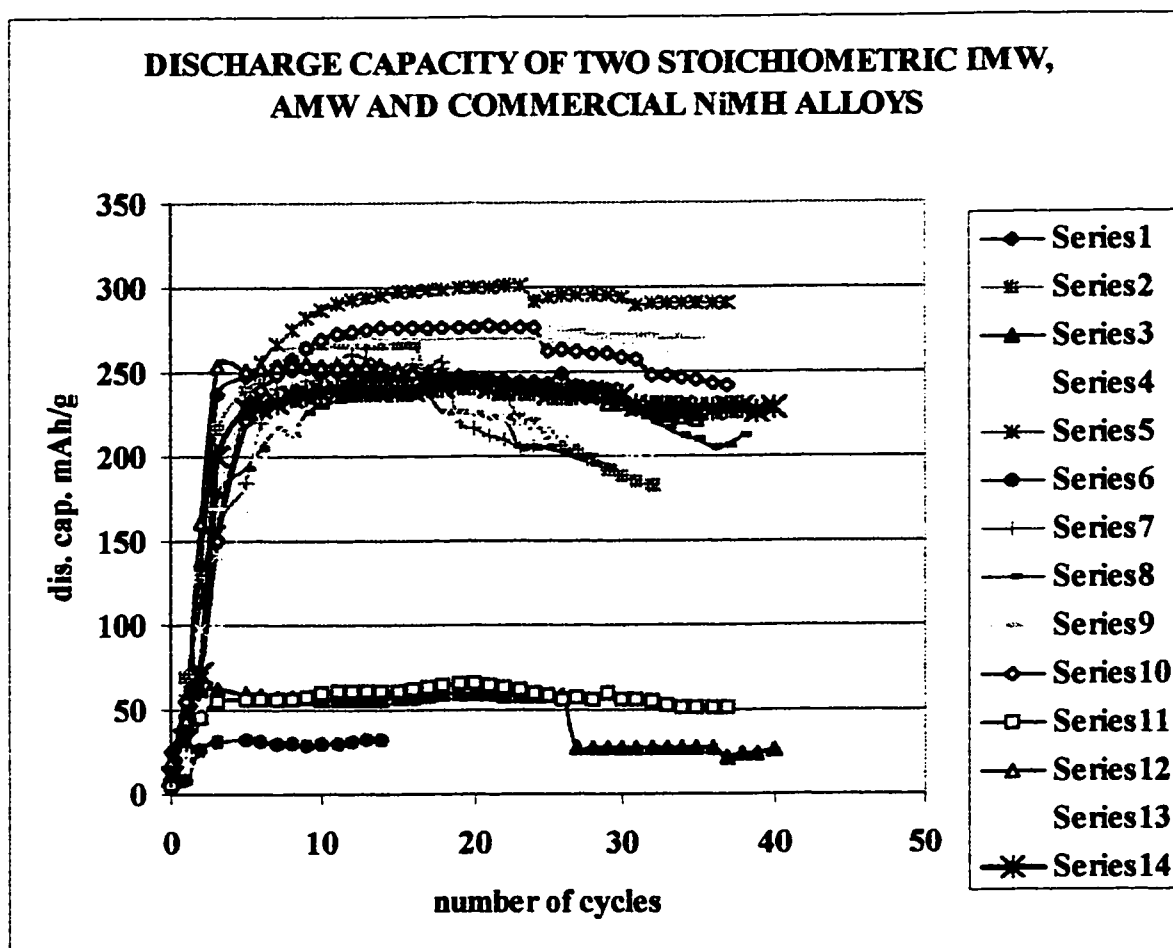


Figure 5.12 Discharge capacity of commercial, arc melted and induction melted NiMH alloys. Charge current was 184 mA/g for 2 h, discharge current were 92, 184, 248 mA/g to 0.6 V against $\text{Ni}(\text{OH})_2$. Series 1, 2, 3 are $\text{Mm}_{0.99}\text{Ni}_{3.48}\text{Co}_{0.7}\text{Al}_{0.81}\text{IMW}$, h.t. at 800°C, h.t. at 1000°C respectively; Series 4,5,6 are $\text{Mm}_{0.99}\text{Ni}_{3.45}\text{Co}_{0.85}\text{Mn}_{0.41}\text{Al}_{0.31}\text{IMW}$, h.t. at 800°C, h.t. at 1000°C respectively; Series 7 is IBA #6; Series 8 is IBA #5; Series 9,10, 11 are $\text{MmNi}_{3.54}\text{Co}_{0.82}\text{Mn}_{0.34}\text{Al}_{0.3}\text{ACW}$, h.t. at 800°C, h.t. at 1000°C respectively; Series 12, 13, 14 are $\text{Mm}_{0.99}\text{Ni}_{3.5}\text{Co}_{0.7}\text{Al}_{0.81}\text{ACW}$, h.t. at 800°C, h.t. at 1000°C respectively;

DISCHARGE CURRENT VS. DISCHARGE CAPACITY OF COMMERCIAL, ARC MELTED AND INDUCTION MELTED NiMH ALLOYS

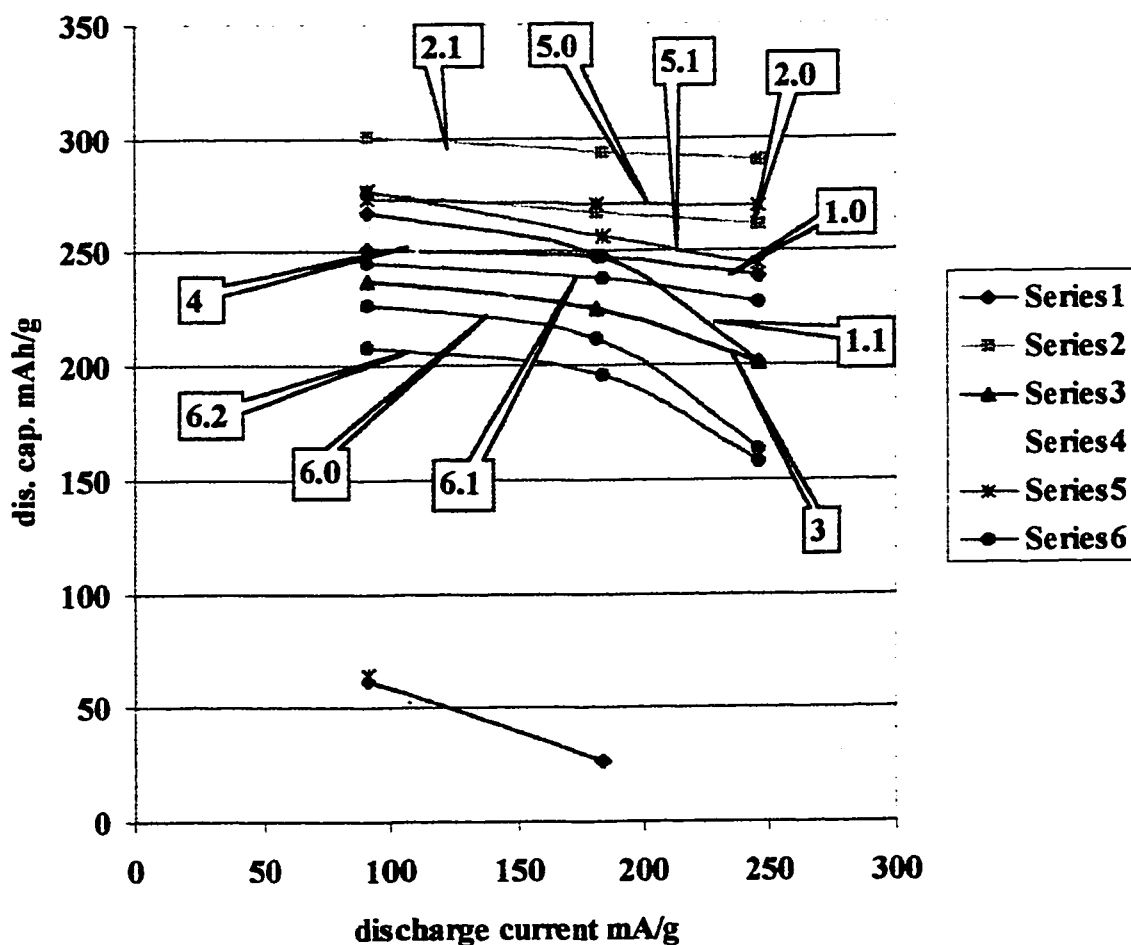


Figure 5.13 Rate capabilities of arc melted, induction melted and commercial NiMH alloys. Charge current was 184 mA/g for 2 h, discharge current were 92, 184, 248 mA/g to 0.6 V against Ni(OH)₂. Series 1.0, 1.1, 1.2 are Mm_{0.99}Ni_{3.48}Co_{0.7}Al_{0.81}IMW, h.t. at 800°C, h.t. at 1000°C respectively; Series 2.0, 2.1 are Mm_{0.99}Ni_{3.45}Co_{0.85}Mn_{0.41}Al_{0.31}IMW and h.t. at 800°C, Series 3 is IBA #5; Series 4 is IBA # 6; Series 5.0 and 5.1 are MmNi_{3.54}Co_{0.82}Mn_{0.34}Al_{0.3} ACW, h.t. at 800 °C, respectively; Series 6.0, 6.1, 6.2 are Mm_{0.99}Ni_{3.5}Co_{0.7}Al_{0.81} ACW, h.t. at 800 °C, h.t. at 1000°C respectively;

$\text{Mm}_{0.99}\text{Ni}_{3.48}\text{Co}_{0.7}\text{Al}_{0.81}\text{IMW}$ has a discharge capacity about 266 mAh/g after 11 cycles. The rate capability up to a discharge current of 184 mA/g is very good. Higher discharge current than 184 mA/g decreases the discharge capacity but not too much. Heat treatment at 800 °C decreases the discharge capacity and rate capability of alloys more seriously. Heat treatment at 1000°C decreases the discharge capacity and rate capability drastically.

$\text{Mm}_{0.99}\text{Ni}_{3.45}\text{Co}_{0.85}\text{Mn}_{0.41}\text{Al}_{0.31}\text{IMW}$ has a discharge capacity about 277 mAh/g after 21 cycles. The rate capability of this alloy is very good. Heat treatment at 800°C increases the discharge capacity to about 300 mAh/g and the alloy exhibits excellent rate capabilities. This alloy is one of the best alloys. Heat treatment at 1000 °C virtually destroys the charge discharge characteristics of this alloy.

IBA # 5 has a discharge capacity about 237 mAh/g after 16 cycles and quite low rate capabilities. IBA #6 has a discharge capacity about 261 mAh/g and very poor rate capabilities. The two arc-melted alloys were described before.

5.6 The Relationship Between Discharge Capacity and Cell Volume

The relationship between cell volume and discharge capacity for ACW and heat-treated alloys at 800 °C and 1000°C are depicted in Figures 5.14, 5.15 and 5.16 respectively. The straight-line trend in this figures was drawn using Microsoft Word trend line tool which uses a least square fit in all figures. The increase of cell volume increases the discharge capacity for ACW and heat treated at 800 °C. The increase of cell volume causes the decrease of discharge capacity for the heat treated alloy at 1000°C.

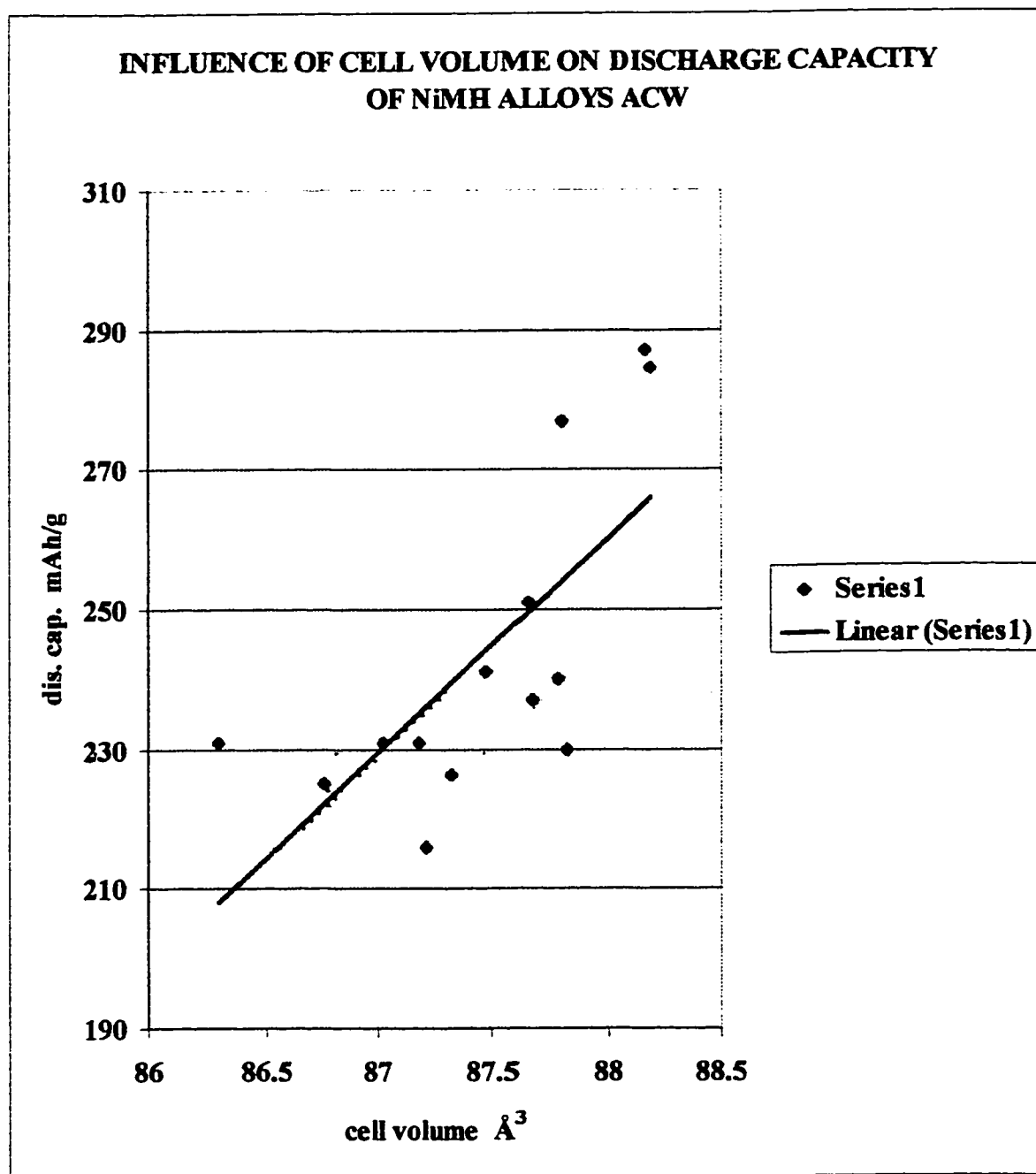


Figure 5.14 Relationship between cell volume and discharge capacity mAh/g for NiMH ACW alloys.

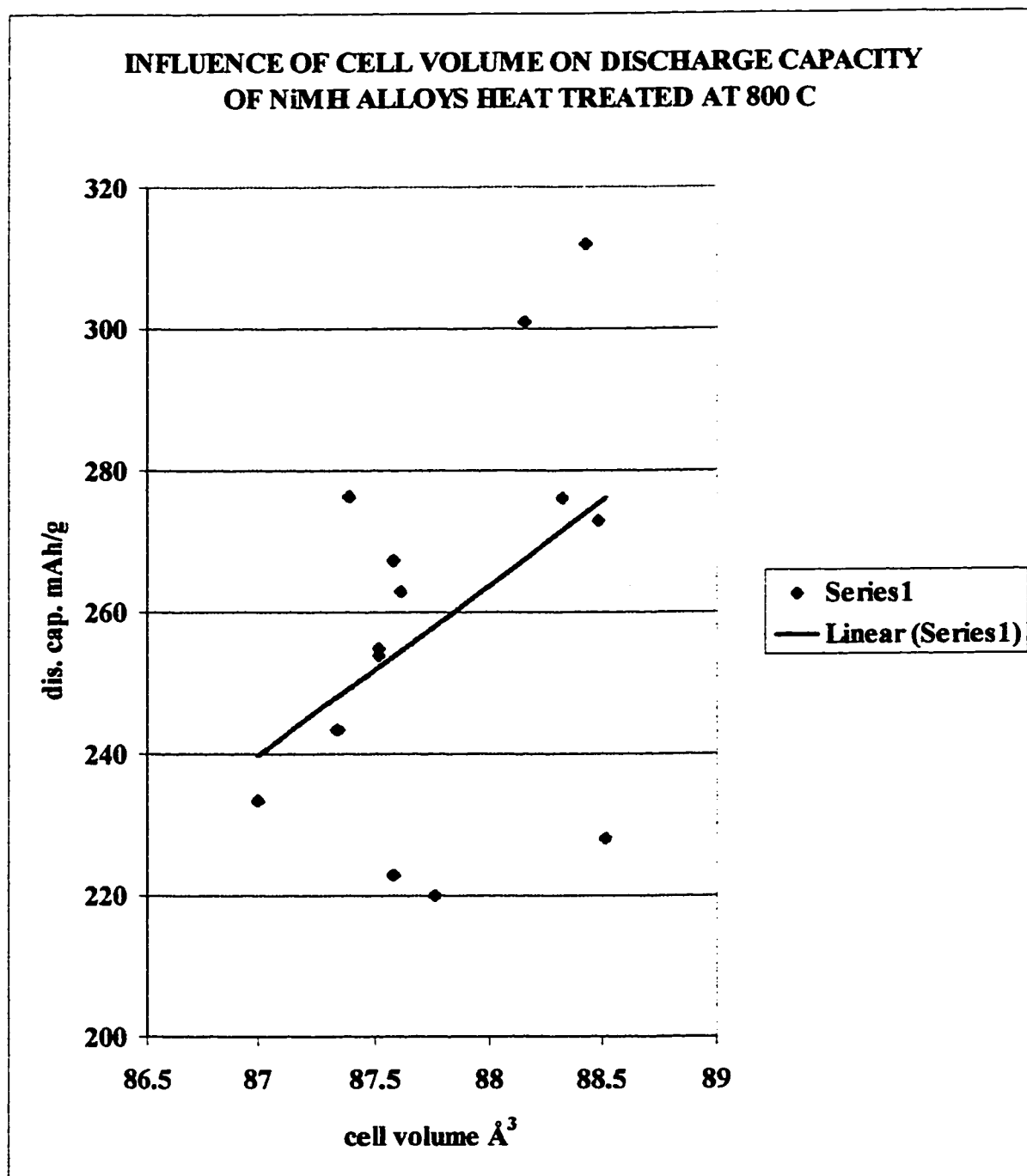


Figure 5.15 Relationship between discharge capacity mAh/g and cell volume of NiMH alloys heat treated at 800 °C.

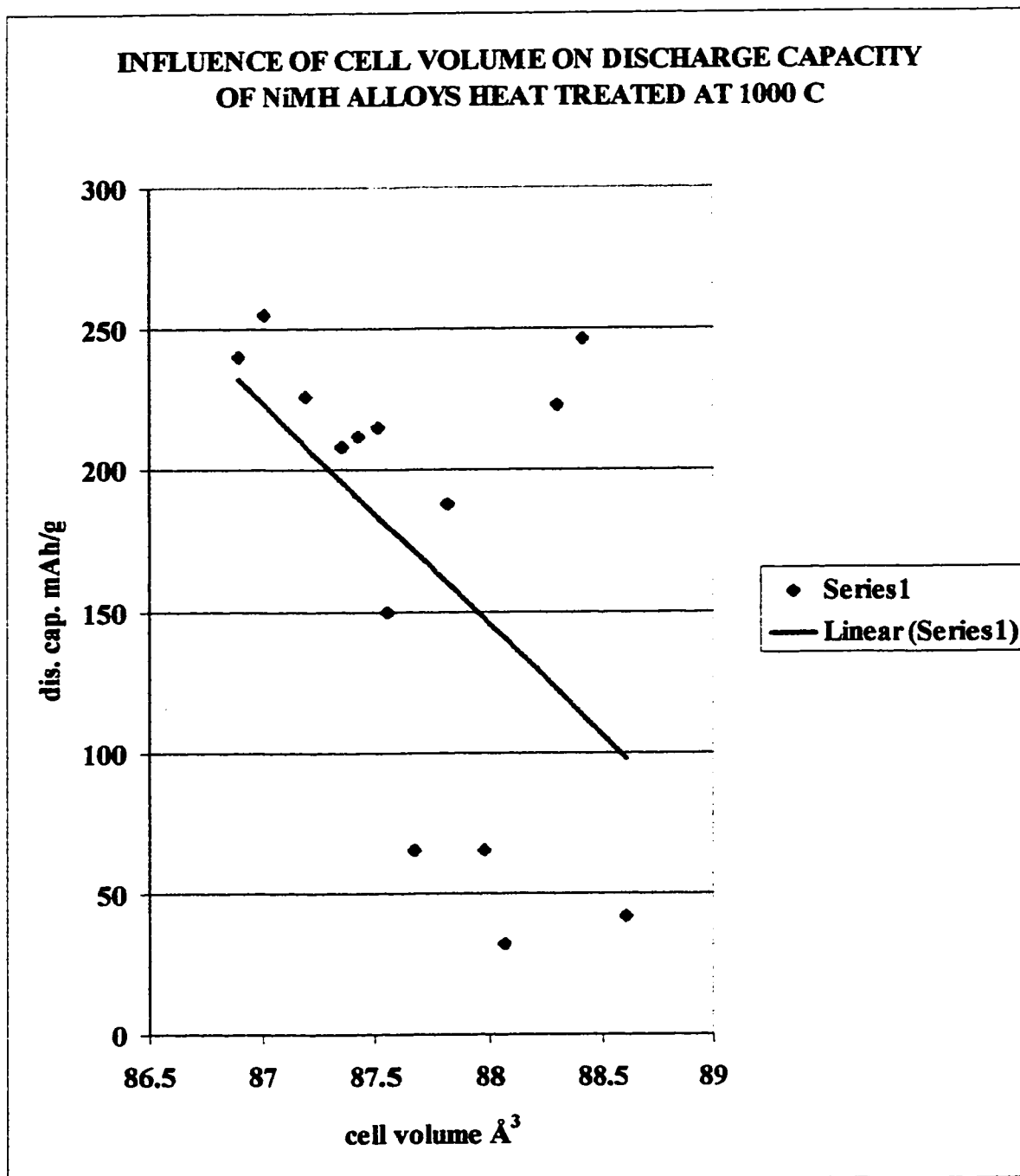


Figure 5.16 Linear relationship between cell volume and discharge capacity of NiMH alloys heat treated at 1000 °C.

5.7 Metallography of NiMH Alloys

$\text{Mm}_{0.88}\text{Ni}_{3.43}\text{Co}_{0.71}\text{Al}_{0.76}$ ACW consists of three phases. Ni-Co-Al phase is located on the grain boundaries and takes up 13.66 % of the surface area of the SEM image. Matrix is basically AB_5 type alloy. There is a very small amount of oxide. The oxides are concentrated on the bottom of the alloy sample (button). The average grain size is estimated to be 40 – 50 μm .

$\text{Mm}_{0.88}\text{Ni}_{3.43}\text{Co}_{0.71}\text{Al}_{0.76}$ heat treated at 800 °C has the same phases as the above described alloy. Ni-Co-Al phase is present as 11.8 % of the surface area of the SEM image.

$\text{Mm}_{0.88}\text{Ni}_{3.43}\text{Co}_{0.71}\text{Al}_{0.76}$ heat-treated at 1000 °C consists of the same phases as above described alloys. Ni-Co-Al phase takes 11.6 % of the surface area of SEM image and the grain size is estimated to 50- 70 μm . The impression is that the Ni-Co-Al phase around the AB_5 grains is partially dissolved in the matrix and two or more matrix grains are now together without the Ni-Co-Al phase between them.

$\text{Mm}_{0.99}\text{Ni}_{3.5}\text{Co}_{0.7}\text{Al}_{0.81}$ ACW (Figure 5.17) consists of three phases. Matrix is NiMH alloy. The oxide (white spots in Figure 5.17) and Ni-Co-Al phases are incorporated in the matrix in less than 1 vol.%. The presence of Ni-Co-Al (dark spots in Figure 5.17) phase corresponds to the name of alloy. Dark lines in Figure 5.17 are cracks. The intention was to produce a stoichiometric alloy without Ni-Co-Al phase. This phase appears when an alloy has a lower amount of mischmetal. The size of Ni-Co-Al phase is 1-3 μm in diameter. The phase is located close to the oxides.

$\text{Mm}_{0.99}\text{Ni}_{3.5}\text{Co}_{0.7}\text{Al}_{0.81}$ heat-treated at 800 °C (Figure 5.18) consists of three phases. Matrix is AB_5 alloy. The grains of Ni-Co-Al (dark spots in Figure 5.18) phase are located closer to each

other and they are bigger in size than in the as cast alloy. The size of Ni-Co-Al phase is about 5 μm in diameter. Third phase is oxide.

$\text{Mm}_{0.99}\text{Ni}_{3.5}\text{Co}_{0.7}\text{Al}_{0.81}$ heat-treated at 1000 °C (Figure 5.19) further increases the size of Ni-Co-Al grains (dark spot in Figure 5.19) and the Ni-Co-Al precipitates are much closer to each other. The phase starts to appear on the grain boundaries.

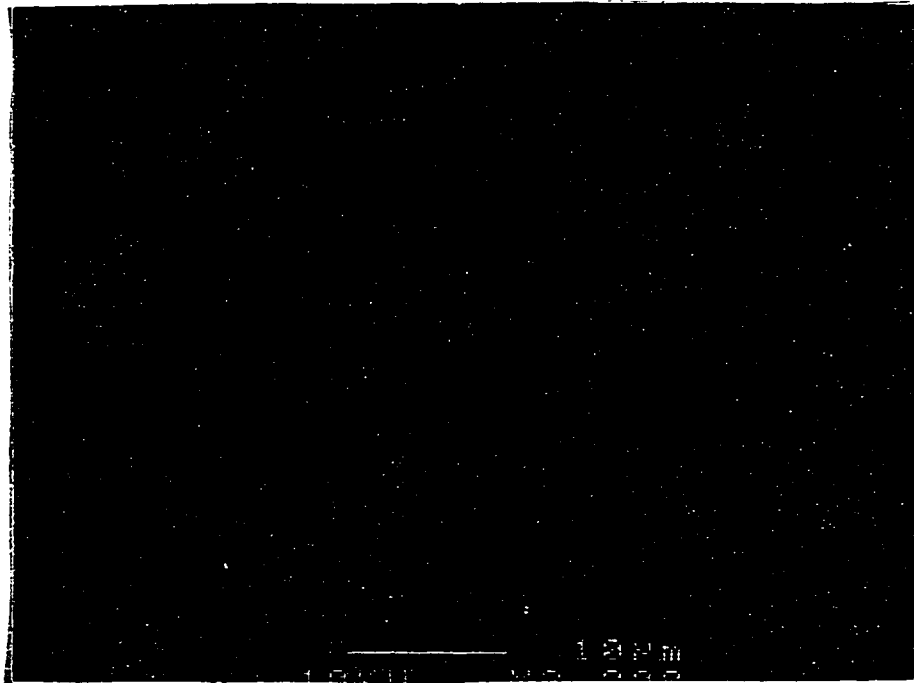


Figure 5.17 SEM Backscattered Electron Image (BSE) on $\text{Mm}_{0.99}\text{Ni}_{3.5}\text{Co}_{0.7}\text{Al}_{0.81}\text{ACW}$. Magnification 10 KV x 2000.

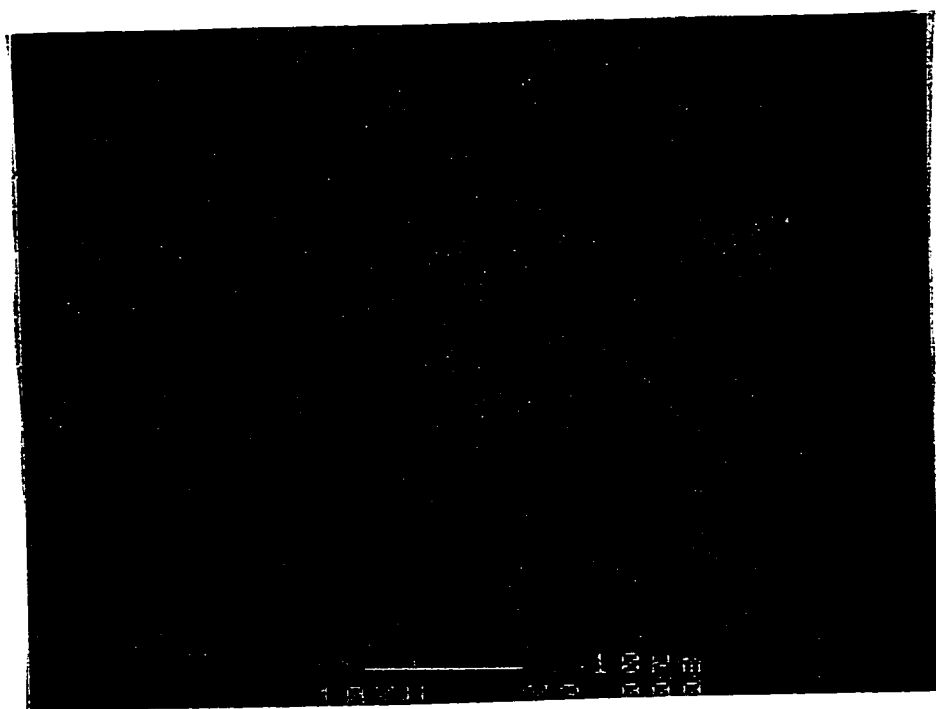


Figure 5.18 SEM Backscattered Electron Image (BSE) on $\text{Mm}_{0.99}\text{Ni}_{3.5}\text{Co}_{0.7}\text{Al}_{0.81}$ heat treated at 800 °C. Magnification 10 KV x 2000

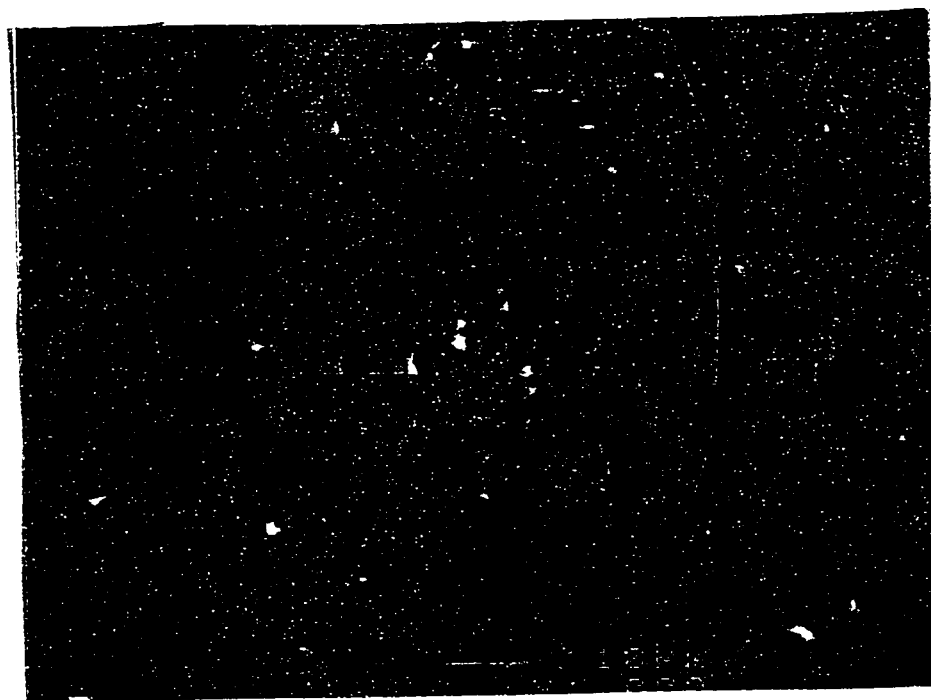


Figure 5.19 SEM Backscattered Electron Image (BSE) of $\text{Mm}_{0.99}\text{Ni}_{3.5}\text{Co}_{0.7}\text{Al}_{0.81}$ heat treated at 1000 °C. Magnification 10 KV x 1000

$\text{Mm}_{0.99}\text{Ni}_{3.47}\text{Co}_{0.73}\text{Al}_{0.81}$ ACW consists of AB_5 matrix, Ni-Co-Al phase and oxides. The alloy has a similar microstructure as $\text{Mm}_{0.99}\text{Ni}_{3.5}\text{Co}_{0.71}\text{Al}_{0.81}$.

$\text{MmNi}_{3.48}\text{Co}_{0.71}\text{Al}_{0.81}$ ACW consists of AB_5 matrix, oxides and a rare earth rich phase. This alloy has about 1 vol. % of rare earth rich phase and much less than 1 vol. % of oxide. The grain size of AB_5 alloy is about 30 μm in diameter. The grain size of rare earth phase is about 5 μm .

$\text{Mm}_{1.09}\text{Ni}_{3.45}\text{Co}_{0.72}\text{Al}_{0.85}$ ACW consists of AB_5 matrix and rare earth rich phases. The inclusions of rare earth are about 10 μm in diameter although they have mostly no regular shape. The rare earth phase takes 18.79 % of the surface area.

$\text{Mm}_{1.09}\text{Ni}_{3.45}\text{Co}_{0.72}\text{Al}_{0.85}$ heat -treated at 800°C has a similar microstructure as the non heat-treated alloy. The inclusions of rare earth are more rounded and slightly bigger.

$\text{Mm}_{1.09}\text{Ni}_{3.45}\text{Co}_{0.72}\text{Al}_{0.85}$ heat -treated at 1000°C has the biggest rare earth inclusions, which are about 15 μm in diameter and takes about 27.4 % of the surface area.

$\text{Mm}_{0.92}\text{Ni}_{3.33}\text{Co}_{0.69}\text{Al}_{0.8}$ ACW consists of AB_5 matrix and very small amount of rare earth rich phase. The rare earth rich phase takes 1.61 % of the surface area. Rare earth inclusions have longitudinal shape and they are distributed randomly.

$\text{Mm}_{0.92}\text{Ni}_{3.33}\text{Co}_{0.69}\text{Al}_{0.8}$ heat -treated at 800°C has a similar microstructure as a cast alloy. The rare earth inclusions are more rounded and take 2.8 % of the surface area. Rare earth inclusions take only 1.2 % of the surface area in the alloy heat-treated at 1000 °C.

$\text{Mm}_{0.99}\text{Ni}_{3.78}\text{Co}_{0.756}\text{Al}_{0.84}$ ACW has AB_5 grains surrounded by Ni-Co-Al phase at the grain boundaries. The AB_5 grains are about 50 μm in diameter. Ni-Co-Al phase takes 6.8 % of the surface area. The alloy has much less than 1 vol. % of oxide.

$\text{Mm}_{0.99}\text{Ni}_{3.78}\text{Co}_{0.756}\text{Al}_{0.84}$ heat-treated at 800 °C has variation in grain size from 50 μm to 80 μm in diameter. The Ni-Co-Al phase takes about 5.5 % of the surface area.

$\text{MmNi}_{3.54}\text{Co}_{0.82}\text{Mn}_{0.34}\text{Al}_{0.3}$ ACW consists of AB_5 matrix, oxide and Ni-Co-Al phase surrounded with oxide. Very bright spots in Figure 5.20 are oxides, bright spots are rare earth rich phase and gray is AB_5 matrix. Rare earth phase takes 12.6 % of the surface area.

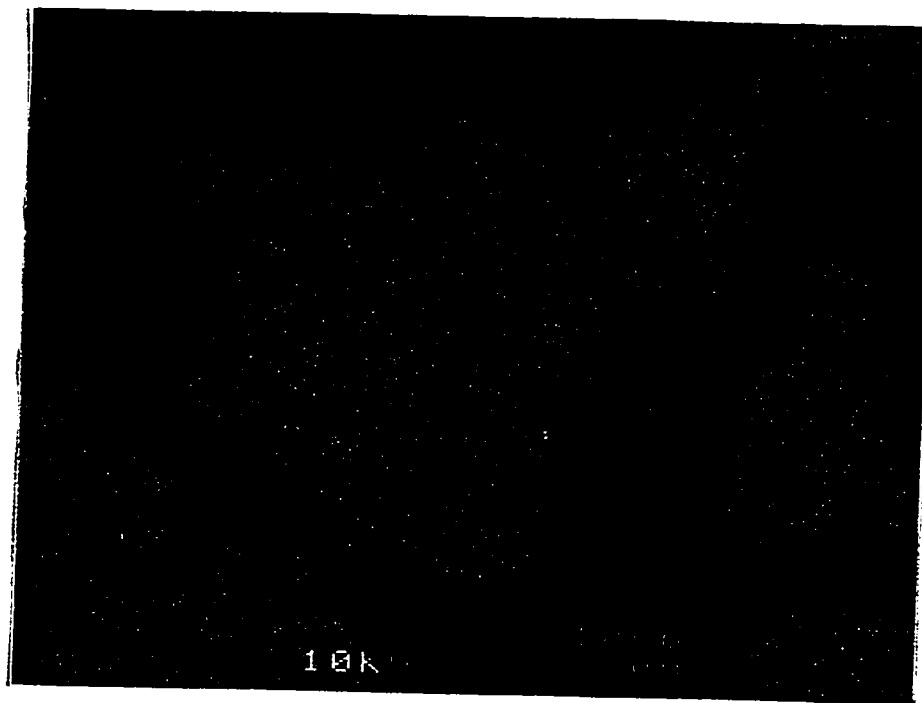


Figure 5.20 SEM Backscattered Electron Image (BSE) on $\text{MmNi}_{3.54}\text{Co}_{0.82}\text{Mn}_{0.34}\text{Al}_{0.3}$ ACW Magnification 10 KV x850.

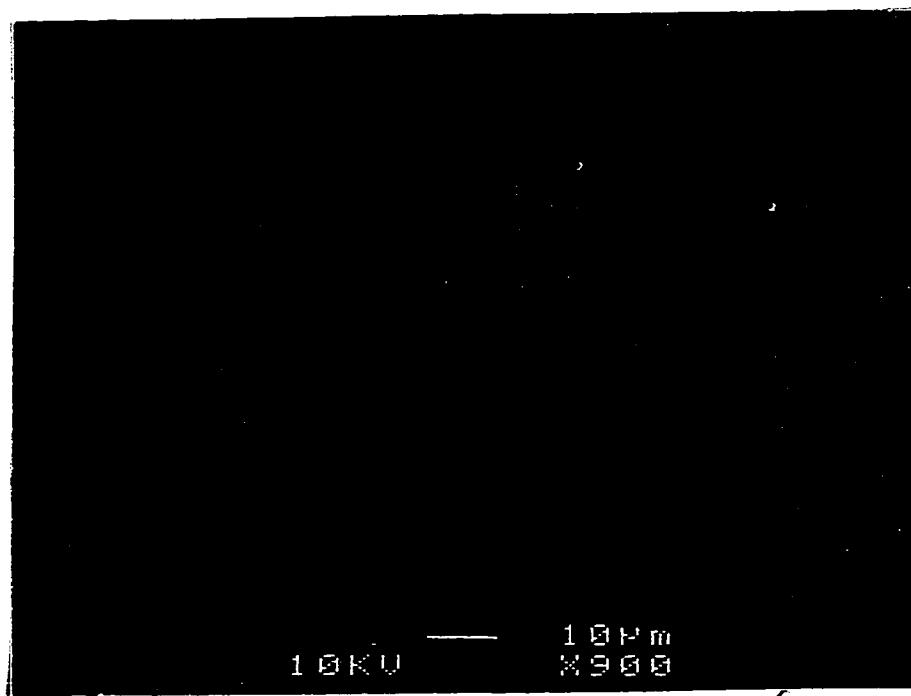


Figure 5.21 SEM Backscattered Electron Image (BSE) on $\text{MmNi}_{3.54}\text{Co}_{0.82}\text{Mn}_{0.34}\text{Al}_{0.3}$ heat-treated at 800 °C. Magnification 10 KV x 900.

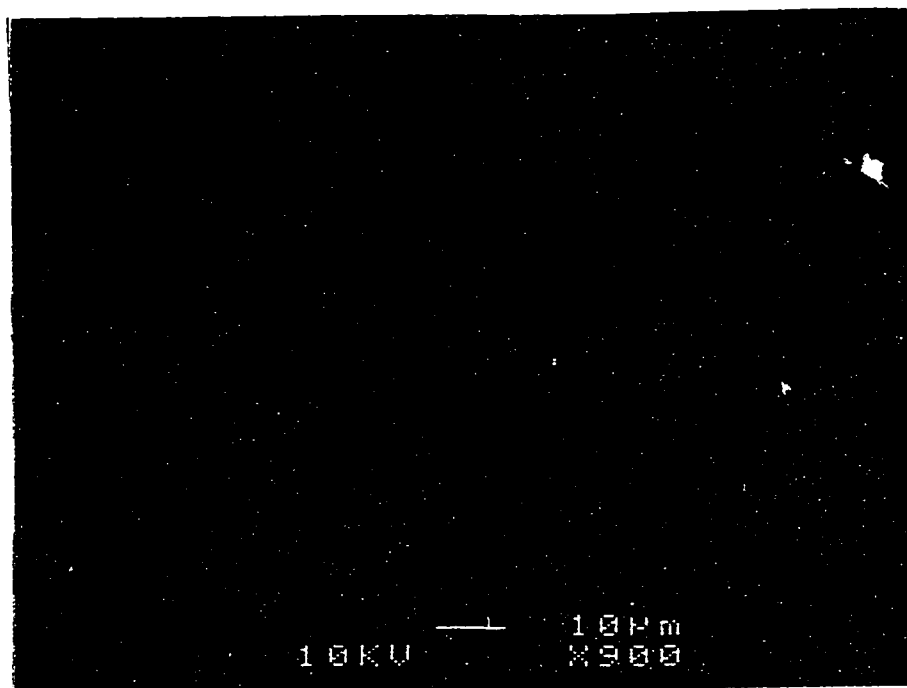


Figure 5.22 SEM Backscattered Electron Image (BSE) on $\text{MmNi}_{3.54}\text{Co}_{0.82}\text{Mn}_{0.34}\text{Al}_{0.3}$ heat-treated at 1000 °C. Magnification 10 KV x 900.

$\text{MmNi}_{3.54}\text{Co}_{0.82}\text{Mn}_{0.34}\text{Al}_{0.3}$ heat-treated at 800 °C (Figure 5.21) consists of the same phases as the as cast alloy. Bright spots in Figure 5.21 are rare earth rich phase. The impression is that this alloy contains less rare earth than the as cast alloy. The size of rare earth inclusions is about 1-3 μm .

$\text{MmNi}_{3.54}\text{Co}_{0.82}\text{Mn}_{0.34}\text{Al}_{0.3}$ heat-treated at 1000 °C (Figure 5.22) has about 0.24 % of the surface area of oxides (very bright spots in Figure 5.22) and 0.04 % of the surface area of rare earth rich phase (bright spots in Figure 5.22). Dark spots in the same Figure are surface contamination.

$\text{Mm}_{0.92}\text{Ni}_{3.48}\text{Co}_{0.83}\text{Mn}_{0.29}\text{Al}_{0.31}$ ACW consists of AB_5 matrix, Ni-Co-Mn-Al phase randomly distributed through matrix and oxides surrounded with Ni-Co-Mn-Al phases. Ni-Co-Mn-Al phase coexists alone and with oxide. It takes about 3.89 % of the surface area. The diameter of oxides is about 10 μm .

$\text{Mm}_{0.92}\text{Ni}_{3.48}\text{Co}_{0.83}\text{Mn}_{0.29}\text{Al}_{0.31}$ heat-treated at 800 °C consists of the same phase as the ACW alloys. The impression is that the Ni-Co-Mn-Al phase starts to dissolve in the matrix. $\text{Mm}_{0.92}\text{Ni}_{3.48}\text{Co}_{0.83}\text{Mn}_{0.29}\text{Al}_{0.31}$ heat-treated at 1000 °C has less Ni-Co-Mn-Al phase than ACW alloys. This phase occupies 2.77 % of the surface area.

$\text{Mm}_{1.065}\text{Ni}_{3.51}\text{Co}_{0.83}\text{Mn}_{0.37}\text{Al}_{0.32}$ ACW consists of rare earth rich phase distributed in parallel 10- μm thick layers and AB_5 matrix. The distance between two neighbour's layers is about 50- 70 μm . AB_5 matrix is positioned between two rare earth layers containing rare earth inclusions spherically shaped and randomly distributed. These spherically shaped inclusions are about 8-10 μm in diameter. Rare earth phase occupies 37.8 % of the surface area.

$\text{Mm}_{1.065}\text{Ni}_{3.51}\text{Co}_{0.83}\text{Mn}_{0.37}\text{Al}_{0.32}$ heat-treated at 800 °C has the same features and phases as the as cast alloy. The impression is that the spherical rare earth rich phase has disappeared but not thoroughly. Rare earth rich phase occupies 24.8 % of the surface area.

$\text{Mm}_{1.065}\text{Ni}_{3.51}\text{Co}_{0.83}\text{Mn}_{0.37}\text{Al}_{0.32}$ heat-treated at 1000 °C has the same layers but more irregularly distributed through matrix. Rare earth rich phase occupies 37 % of the surface area.

$\text{Mm}_{0.98}\text{Ni}_{3.33}\text{Co}_{0.79}\text{Mn}_{0.35}\text{Al}_{0.3}$ as cast consists of rare earth rich phase longitudinally distributed, AB_5 matrix and oxides. Rare earth rich phase occupies 10.52 % of the surface area.

$\text{Mm}_{0.98}\text{Ni}_{3.33}\text{Co}_{0.79}\text{Mn}_{0.35}\text{Al}_{0.3}$ heat-treated at 800 °C consists of the same phases as the ACW alloy. Ni-Co-Mn-Al phase is formed accompanied with oxide in a very small amount. Rare earth rich phase occupies 12.03 % of the surface area.

$\text{Mm}_{0.98}\text{Ni}_{3.33}\text{Co}_{0.79}\text{Mn}_{0.35}\text{Al}_{0.3}$ heat-treated at 1000 °C consists of AB_5 matrix, rare earth rich phase and oxide accompanied with Ni-Co-Mn-Al phase. Rare earth rich phase occupies 10.08 % of the surface area. Oxide and Ni-Co-Mn-Al are presented in much less than one percentage.

$\text{Mm}_{0.99}\text{Ni}_{3.79}\text{Co}_{0.9}\text{Mn}_{0.4}\text{Al}_{0.33}$ as cast consists of AB_5 matrix, Ni-Co-Mn rich phase on grain boundaries and oxides. Ni-Co-Mn rich phase occupies 13.73 % of the surface area.

$\text{Mm}_{0.99}\text{Ni}_{3.79}\text{Co}_{0.9}\text{Mn}_{0.4}\text{Al}_{0.33}$ heat-treated at 800 °C has better defined grain boundaries than the as cast alloy. Ni-Co-Mn rich phase occupies 10.62 % of the surface area.

$\text{Mm}_{0.99}\text{Ni}_{3.79}\text{Co}_{0.9}\text{Mn}_{0.4}\text{Al}_{0.33}$ heat-treated at 1000 °C consists of Ni-Co-Mn-Al phase on the grain boundaries, AB_5 matrix and oxides. Ni-Co-Mn-Al phase becomes dissolved in matrix and the

visibility of grain boundaries is just partial. Most of the image is AB₅ matrix and very small amount of oxides. Ni-Co-Mn-Al phase occupies 5.19 % of the surface area.

Mm_{0.99}Ni_{3.48}Co_{0.7}Al_{0.81}IMW (Figure 5.23) consists of AB₅ matrix, rare earth rich phase (bright spots) and oxide (very bright spots). This alloy has a very small amount of oxide. Rare earth rich phase occupies 1.36 % of the surface area. This alloy is very close to being a single-phase alloy.

Mm_{0.99}Ni_{3.48}Co_{0.7}Al_{0.81}IMW heat -treated at 800°C (Figure 5.24) has the same phases as the as cast alloy. Rare earth rich phase occupies 1.33 % of the surface area. White spots in Figure 5.24 are rare earth rich phase.

Mm_{0.99}Ni_{3.48}Co_{0.7}Al_{0.81}IMW heat -treated at 1000°C (Figure 5.25) has the same phases as the as cast and heat -treated alloy at 800°C.

MmNi_{3.54}Co_{0.82}Mn_{0.34}Al_{0.3}IMW, consists of AB₅ matrix and rare earth rich phase. Rare earth rich phase occupies 0.14 % of the surface area (white spots). The alloy has a very low amount of oxide. The alloy is very close to be single- phase alloy. The BSE is depicted in Figure 5.26. Heat treatment at 800°C didn't change the microstructure of alloy. It appears that rare earth phase (white spots) is a very small amount and starts to dissolve in the matrix. The BSE is depicted in Figure 5.27.

Heat treatment at 1000 °C makes the appearance of rare earth phase (white spots) less visible. The BSE is depicted in Figure 5.28.

BSE of the commercial alloys are depicted in Figures 5.29 and 5.30. Both alloys have AB₅ matrix and rare earth rich phases (white spots).

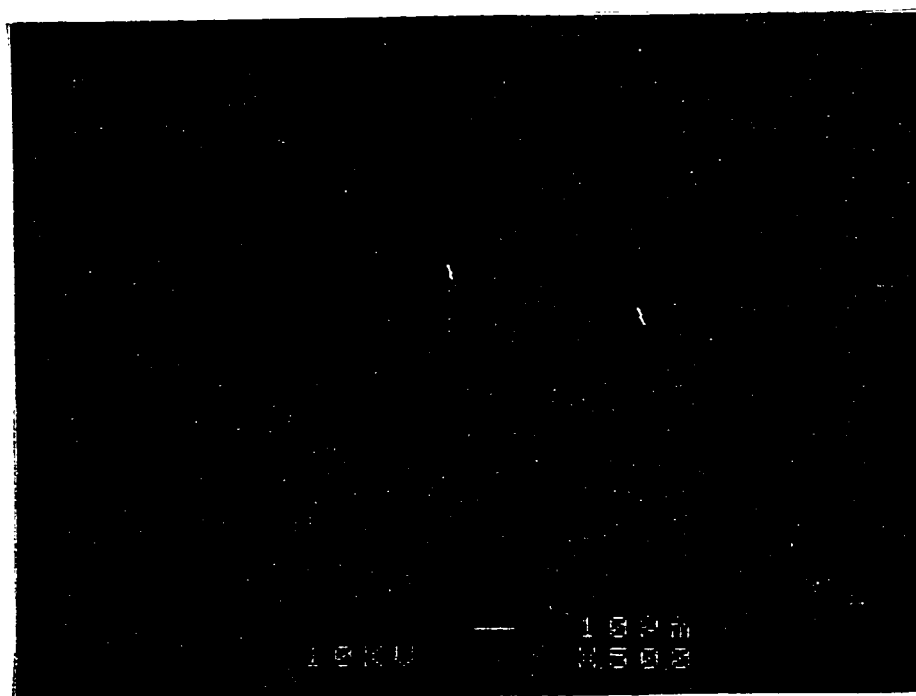


Figure 5.23 SEM Backscattered Electron Image (BSE) of $\text{Mm}_{0.99}\text{Ni}_{3.48}\text{Co}_{0.7}\text{Al}_{0.81}\text{IMW}$. Magnification 10 KV x 500.

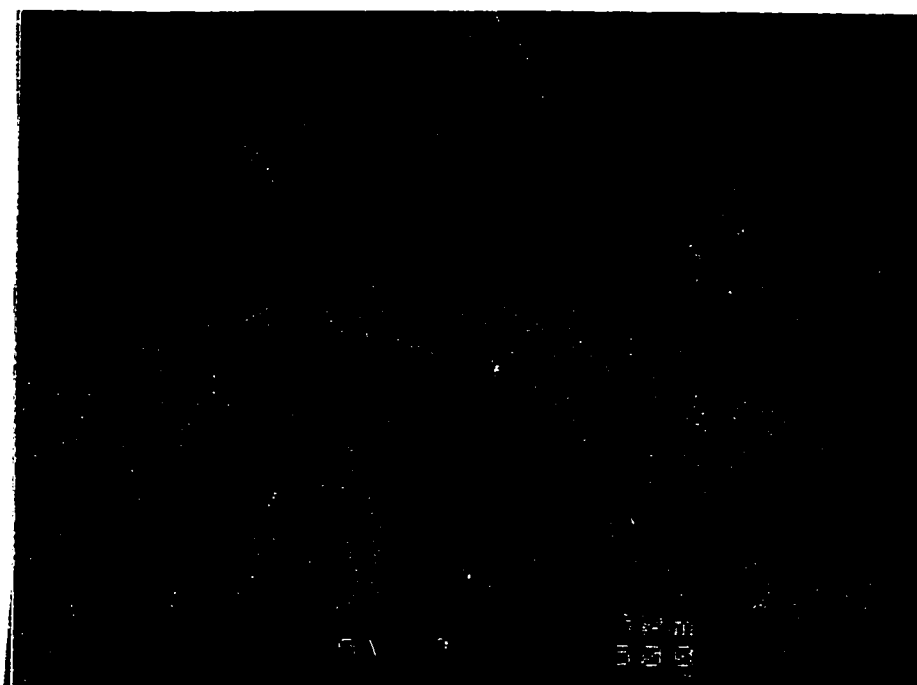


Figure 5.24 SEM Backscattered Electron Image (BSE) of $\text{Mm}_{0.99}\text{Ni}_{3.48}\text{Co}_{0.7}\text{Al}_{0.81}\text{IMW}$ heat-treated at 800°C. Magnification 10 KV x 500.

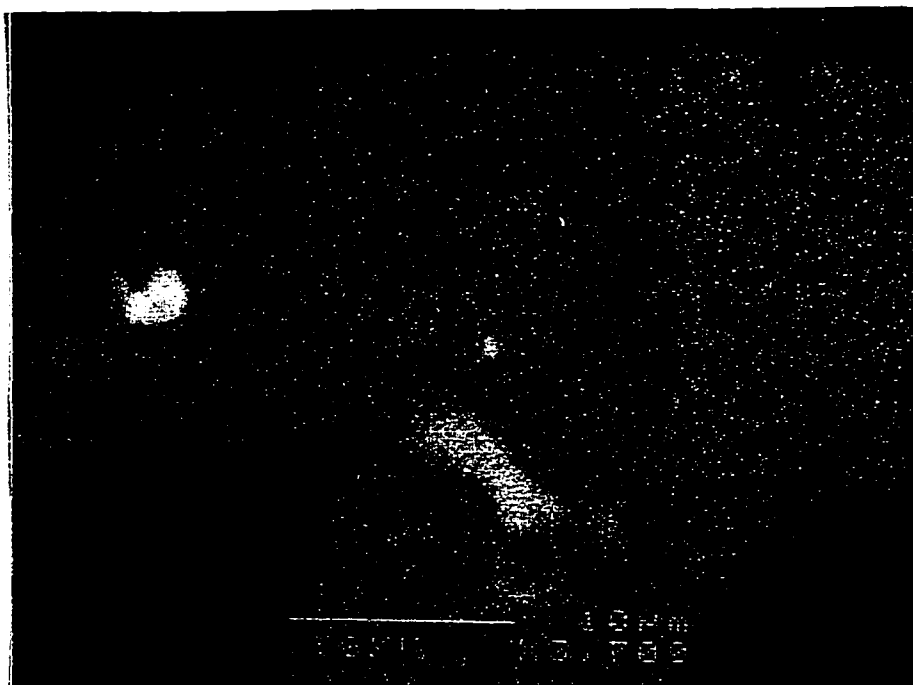


Figure 5.25 SEM Backscattered Electron Image (BSE) of $\text{Mm}_{0.99}\text{Ni}_{3.48}\text{Co}_{0.7}\text{Al}_{0.81}\text{IMW}$ heat-treated at 1000 °C. Magnification 10 KV x 3700.

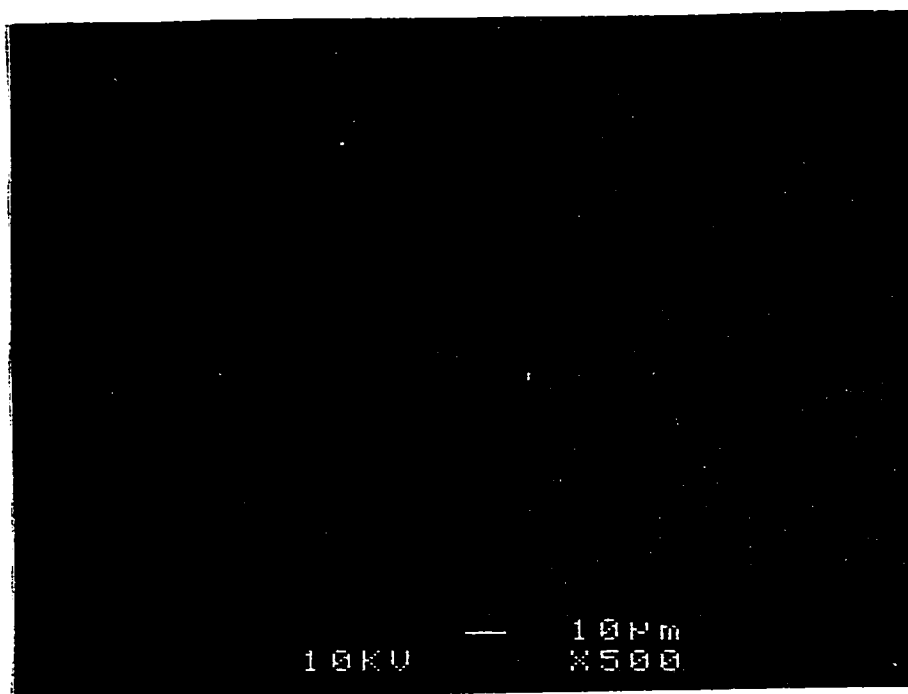


Figure 5.26 SEM Backscattered Electron Image (BSE) of $\text{MmNi}_{3.54}\text{Co}_{0.82}\text{Mn}_{0.34}\text{Al}_{0.3}\text{IMW}$. Magnification 10 KV x 500.

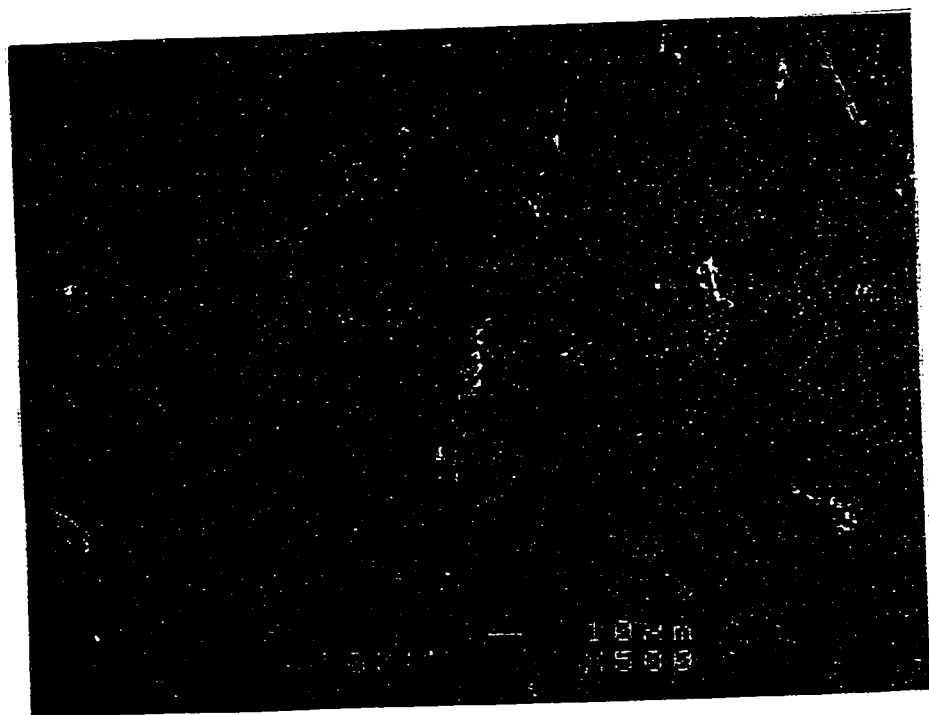


Figure 5.27 SEM Backscattered Electron Image (BSE) of $\text{MmNi}_{3.54}\text{Co}_{0.82}\text{Mn}_{0.34}\text{Al}_{0.3}\text{IMW}$ heat-treated at 800 °C. Magnification 10 KV x 500

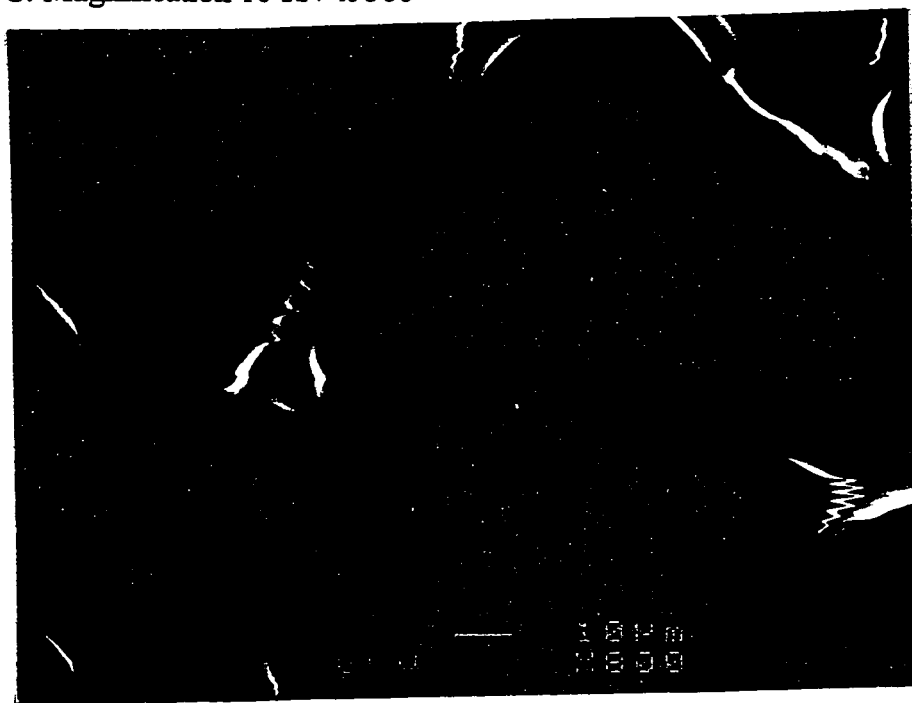


Figure 5.28 SEM Backscattered Electron Image (BSE) of $\text{MmNi}_{3.54}\text{Co}_{0.82}\text{Mn}_{0.34}\text{Al}_{0.3}\text{IMW}$ heat-treated at 1000 °C. Magnification 10 KV x 500



Figure 5.29 SEM Backscattered Electron Image (BSE) of IBA # 5



Figure 5.30 SEM Backscattered Electron Image (BSE) of IBA # 6

5.8 Results of DTA Analysis

$\text{Mm}_{0.88}\text{Ni}_{3.43}\text{Co}_{0.71}\text{Al}_{0.76}$ displays a regularly shaped single endothermic peak at 1467.85 °C.

$\text{Mm}_{0.99}\text{Ni}_{3.47}\text{Co}_{0.73}\text{Al}_{0.81}$ displays a regularly shaped single endothermic peak at 1468.67 °C.

$\text{Mm}_{1.09}\text{Ni}_{3.45}\text{Co}_{0.72}\text{Al}_{0.85}$ displays a regularly shaped single endothermic peak at 1466.88 °C on the heating side and endothermic peak at 1445.06 °C on the cooling side. There are two smaller peaks at about 1200 °C, which could indicate the presence of two or more phases.

$\text{Mm}_{0.92}\text{Ni}_{3.33}\text{Co}_{0.69}\text{Al}_{0.8}$ shows an endothermic peak at 1463.47 °C at the heating side and an endothermic peak at 1436.18 °C at the cooling side.

$\text{Mm}_{0.99}\text{Ni}_{3.78}\text{Co}_{0.756}\text{Al}_{0.84}$ shows an endothermic peak at 1464.93 °C on the heating side and an endothermic peak at 1448.75 °C on the cooling side. The second run shows an endothermic peak at 1464.60 °C. The difference between two measurement is 0.33 °C.

$\text{MmNi}_{3.54}\text{Co}_{0.82}\text{Mn}_{0.34}\text{Al}_{0.3}$ shows an endothermic peak at 1455.06 °C.

$\text{Mm}_{0.92}\text{Ni}_{3.48}\text{Co}_{0.83}\text{Mn}_{0.29}\text{Al}_{0.31}$ shows an endothermic peak at 1456.21 °C.

$\text{Mm}_{1.065}\text{Ni}_{3.51}\text{Co}_{0.83}\text{Mn}_{0.37}\text{Al}_{0.32}$ shows two endothermic peaks at 1435.19 °C and 1454.72°C on the heating side and three peaks at similar temperature at the cooling side. The presence of two or three phase is clearly indicated.

$\text{Mm}_{0.98}\text{Ni}_{3.33}\text{Co}_{0.79}\text{Mn}_{0.35}\text{Al}_{0.3}$ shows one endothermic peak at 1453.57 °C on the heating side of diagram and two or three small peaks at about 1200 °C on the cooling side.

$\text{Mm}_{0.99}\text{Ni}_{3.79}\text{Co}_{0.9}\text{Mn}_{0.4}\text{Al}_{0.33}$ has two endothermic peaks at 1438.54 °C and 1456.62 °C on heating side and two or three endothermic peaks at 1205.62 °C on the cooling side.

$\text{Mm}_{0.99}\text{Ni}_{3.48}\text{Co}_{0.7}\text{Al}_{0.81}\text{IMW}$ shows one endothermic peak at 1472.68 °C on the heating side and four endothermic peaks at 1453.56 °C, 1422.69°C, 1400.43 °C and 1393.28 °C. Examination of a second sample shows an endothermic peak at 1469.29 °C on the heating side and five peaks on the cooling side at 1448.79 °C, 1445.45 °C, 1438.31 °C, 1426.06 °C and 1414.52 °C.

$\text{MmNi}_{3.54}\text{Co}_{0.82}\text{Mn}_{0.34}\text{Al}_{0.3}\text{IMW}$ shows one endothermic peak at 1445.87 °C on heating side and three endothermic peaks at about 1232 °C.

CHAPTER 6

GENERAL DISCUSSION AND ANALYSIS

6.1 Introduction

This chapter deals with a discussion and analysis of overall results presented in chapter 5. An attempt was made to explain relationships between the chemical composition of NiMH alloys, crystal structure, discharge capacity, rate capability, gas absorption capacity, microstructure, methods of processing and heat treatment. The analyses were made on NiMH alloys produced in arc and induction furnaces non heat-treated without manganese and heat-treated at 800 °C and 1000 °C. The same procedure was used to analyze NiMH alloys with manganese. A comparison between commercial and in house made alloys is also discussed.

6.2 Chemical Composition

Chemical composition of NiMH alloys determined by ICP is very close to the expected chemical composition of most of the analyzed NiMH alloys. The difference between expected and measured chemical composition is due to the method of processing. The arc melting process exhibits more oxides in the microstructure because of higher melting temperature and easier access of oxygen (air) to the molten metal due to design of the arc furnace. The results indicate less mischmetal present in the alloy and the formation of Ni-Co-Al or Ni-Co- Mn- Al phase in stoichiometric alloys located in regions very close to the oxides. The loss by evaporation of rare earth elements is also possible. The final composition usually has 0.01 % less mischmetal (Appendix 2) than is expected and

because of that a small increase of cobalt or aluminum and a decrease of nickel takes place. Manganese easily evaporates during the melting process and makes low melting point alloys with nickel, cobalt and alumina. Alloys produced by arc melting have lower manganese content because of evaporation. The difference between expected and achieved manganese content is about 25 to 5 % of the starting amount. The starting amount of manganese before melting was always a stoichiometric one. The excess amount of manganese was not added in any case. Chemical composition of induction melted alloy is very close to the expected value (Table 3.1) because the processing temperature is 300- 400 °C lower than in arc melting unit. The manganese was also added at the end of the process. Lower temperature and shorter time in the melt bath caused no manganese and mischmetal loss in the $Mm_{0.99}Ni_{3.45}Co_{0.85}Mn_{0.41}Al_{0.31}IMW$ alloy. The difference between expected and achieved chemical composition for $Mm_{0.99}Ni_{3.48}Co_{0.7}Al_{0.81}IMW$ alloy is due to nickel content. The alloy has 0.8 wt. % lower nickel content according to Table 3.1. EDS analysis of NiMH alloys provides information about chemical composition of matrix and other phases present in the alloys. The comparison between ICP results (Table 3.1) and EDS results (Appendix 2) does not lead to a firm conclusion about accuracy and precision of both methods. ICP results are closer to expected results and to expected microstructure. EDS results of chemical composition of Ni-Co-Al or Ni-Co-Mn-Al phase present in some alloys or oxides depends on the size of phases or oxides. The results are not highly accurate if the phases present are about 1 μm in diameter. For example, Ni-Co-Al phase in Appendix 2 for alloy $Mm_{0.99}Ni_{3.5}Co_{0.7}Al_{0.81}$ contains 3.37 wt. % of cerium and 2.14 wt. % lanthanum. The content of rare earth elements in this phase should be about zero.

6.3 Pressure Concentration Temperature Curves (P-C-T)

The P-C-T curves of IBA # 5 and $\text{Mm}_{0.99}\text{Ni}_{3.48}\text{Co}_{0.7}\text{Al}_{0.81}\text{IMW}$ depicted in Figures 5.1, 5.2, 5.3 exhibit pressure hysteresis. The comparison of P-C-T curves of IBA #5 at 30 °C and $\text{Mm}_{0.99}\text{Ni}_{3.48}\text{Co}_{0.7}\text{Al}_{0.81}\text{IMW}$ at 30 °C shows that $\text{Mm}_{0.99}\text{Ni}_{3.48}\text{Co}_{0.7}\text{Al}_{0.81}\text{IMW}$ has higher hysteresis than IBA # 5. The comparison of P-C-T curves of IBA # 6 at 30 °C and $\text{Mm}_{0.99}\text{Ni}_{3.45}\text{Co}_{0.85}\text{Mn}_{0.41}\text{Al}_{0.31}\text{IMW}$ alloy at 30 °C shows the same behavior. $\text{Mm}_{0.99}\text{Ni}_{3.45}\text{Co}_{0.85}\text{Mn}_{0.41}\text{Al}_{0.31}\text{IMW}$ alloy has higher hysteresis than IBA #6. $\text{Mm}_{0.99}\text{Ni}_{3.48}\text{Co}_{0.7}\text{Al}_{0.81}\text{IMW}$ alloy has a bigger cell volume, cell distortion, more lanthanum and less nickel than IBA#5. $\text{Mm}_{0.99}\text{Ni}_{3.45}\text{Co}_{0.85}\text{Mn}_{0.41}\text{Al}_{0.31}\text{IMW}$ alloy has smaller cell volume, cell distortion, more lanthanum and less nickel and cobalt than IBA # 6. The alloys with smaller amounts of nickel and more lanthanum exhibit higher hysteresis. The comparison of gas pressure concentration temperature curves and electrochemical pressure concentration temperature shows that equilibrium pressure obtained by gas method is a little higher (6-10 %) than the equilibrium pressure obtained by the electrochemical method. Similar results were reported previously [28].

6.4 XRD Results

6.4.1 XRD Results of NiMH Alloys Without Manganese

The influence of number of A-side atoms (stoichiometry), methods of production and heat treatment on cell volume of NiMH alloys without manganese is presented in Figure 6.1.

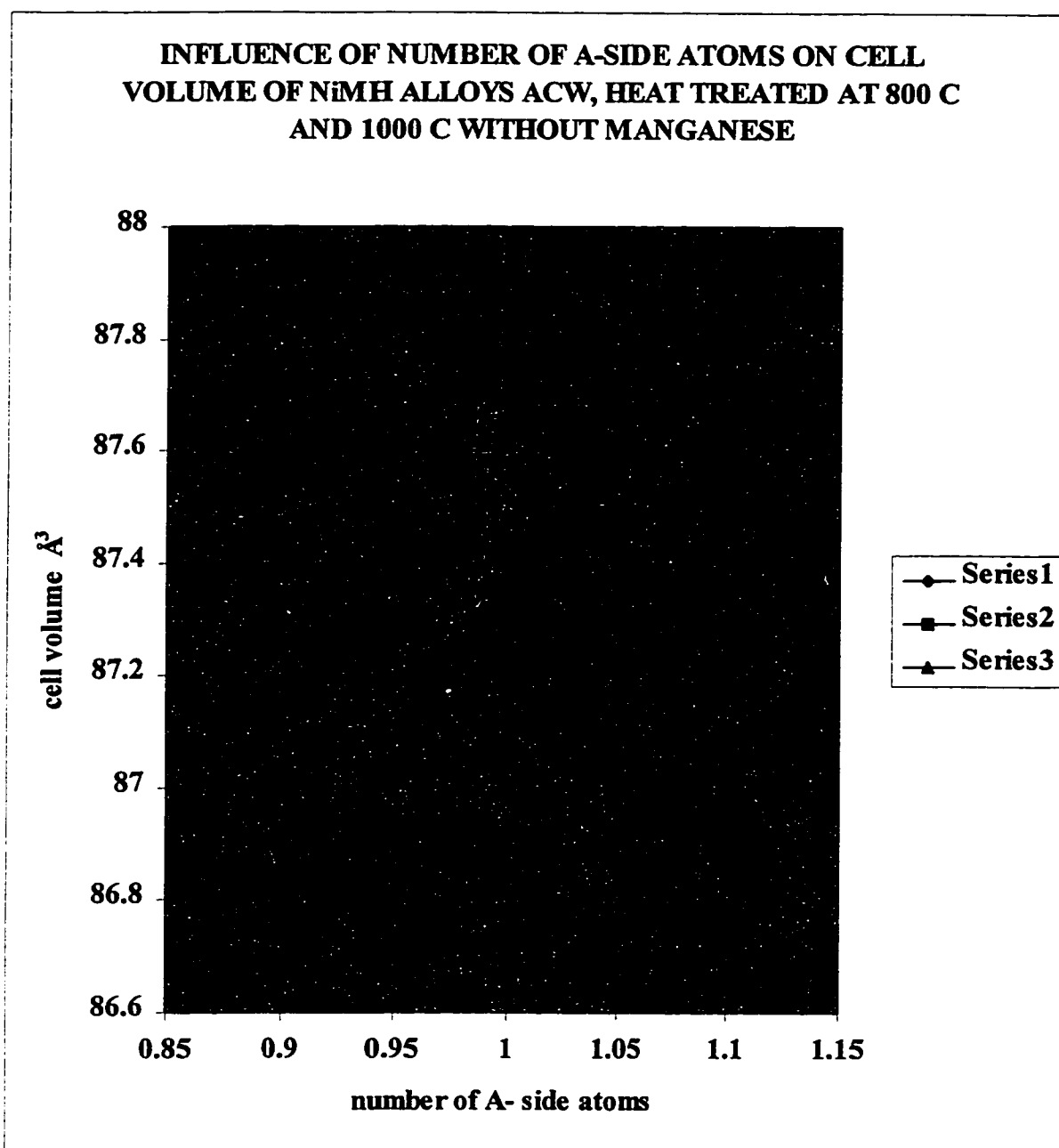


Figure 6.1 Influence of number of A-side atoms of NiMH alloys ACW (series 1) heat treated at 800 °C (series 2) and 1000 °C (series 3) without manganese on cell volume. Points from left to right are $\text{Mm}_{0.88}\text{Ni}_{3.43}\text{Co}_{0.71}\text{Al}_{0.76}$, $\text{Mm}_{0.99}\text{Ni}_{3.5}\text{Co}_{0.7}\text{Al}_{0.81}$, $\text{Mm}_{0.99}\text{Ni}_{3.47}\text{Co}_{0.73}\text{Al}_{0.8}$, $\text{MmNi}_{3.48}\text{Co}_{0.71}\text{Al}_{0.81}$, $\text{Mm}_{0.99}\text{Ni}_{3.48}\text{Co}_{0.7}\text{Al}_{0.81}\text{IMW}$, $\text{Mm}_{1.09}\text{Ni}_{3.45}\text{Co}_{0.72}\text{Al}_{0.85}$

The increase of number of A-side atoms from 0.88 to 1.09 causes the increase of cell volume in all ranges for ACW NiMH alloys. ACW alloys having chemical composition

close to stoichiometric composition exhibit big variations of cell volume. The biggest cell volume among stoichiometric alloys is $Mm_{0.99}Ni_{3.48}Co_{0.7}Al_{0.81}$ IMW without heat treatment. Stoichiometric ACW alloy has smaller cell volume than IMW alloy although the cooling rate is higher. This is because of a small difference in chemical composition between the two alloys. Cell volumes of AB_5 -stoichiometric ACW alloy is bigger than the cell volume of the same alloy heat-treated at 800 °C and smaller than the cell volume of the same alloys heat treated at 1000 °C. The ACW AB_5 alloys have the biggest **a**-axis range among the three types of alloys. Those alloys have such **a**-axis range because the A-side atoms are outside of equilibrium position and the distortion of cell volume is the highest (Table 5.1). The values of **c**-axis of AB_5 -stoichiometric alloys are not affected strongly with number of A-side atoms. ACW, heat-treated and IMW alloys have a very similar value of **c**-axis. That means that cell volumes of AB_5 -stoichiometric NiMH alloys without manganese is a function of number of A-side atoms and **a**-axis. **c**-axis is nearly a constant.

Heat treatment of AB_5 -stoichiometric alloys at 800 °C (Figure 6.1) causes decrease of cell volume range because of cell relaxation. The A-side atoms are in equilibrium position and cell distortion is less than the ACW AB_5 stoichiometric alloys (Table 5.1).

a-axis is smaller than the ACW AB_5 -stoichiometric alloys and **c**-axis does not change very much. The influence of number of A-side atoms on **a**-axis and **c**-axis in NiMH alloys without manganese is presented in Figures 6.2 and 6.3. The NiMH alloys are $A_{0.88}B_5$, AB_5 and $A_{1.09}B_5$. Heat treatment of AB_5 -stoichiometric alloys at 1000 °C (Figure 6.1) causes increase of cell volume of NiMH alloys without manganese due to an increase of the **a**-axis. The amount of mischmetal atoms is slightly higher in the matrix of

NiMH alloys heat-treated at 1000 °C than at 800 °C (Appendix 2, alloy number 14). A-side atoms diffuse easier in the matrix at 1000 °C than at 800 °C.

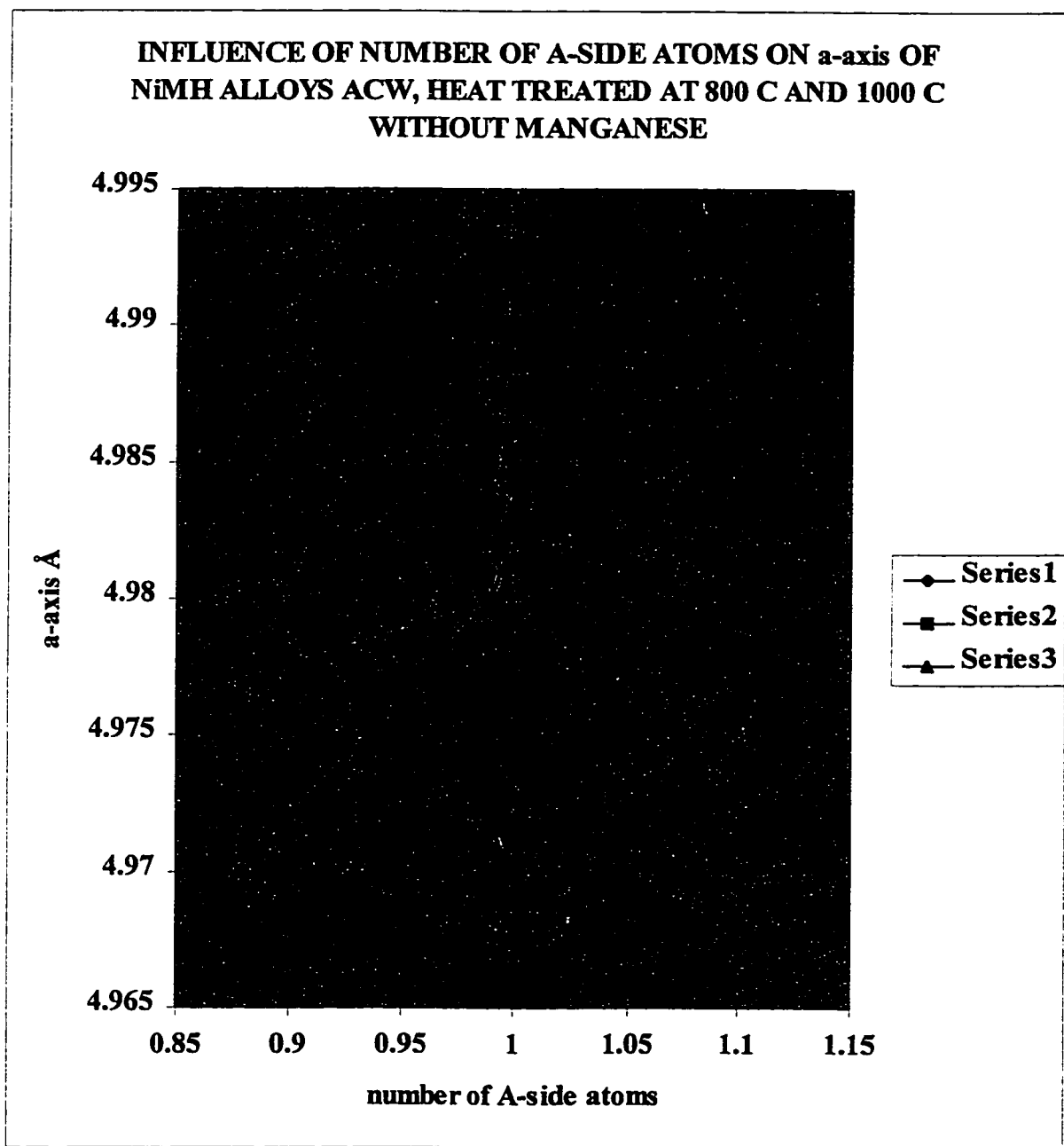


Figure 6.2 Influence of A-side atoms on a-axis of $A_{0.88}B_5$, AB_5 and $A_{1.09}B_5$ -type NiMH alloys ACW (1), heat-treated at 800°C (2) and 1000 °C (3). $Mm_{0.88}Ni_{3.43}Co_{0.71}Al_{0.76}$, $Mm_{0.99}Ni_{3.5}Co_{0.7}Al_{0.81}$, $Mm_{0.99}Ni_{3.47}Co_{0.73}Al_{0.8}$, $MmNi_{3.48}Co_{0.71}Al_{0.81}$, $Mm_{0.99}Ni_{3.48}Co_{0.7}Al_{0.81}$ IMW, $Mm_{1.09}Ni_{3.45}Co_{0.72}Al_{0.85}$

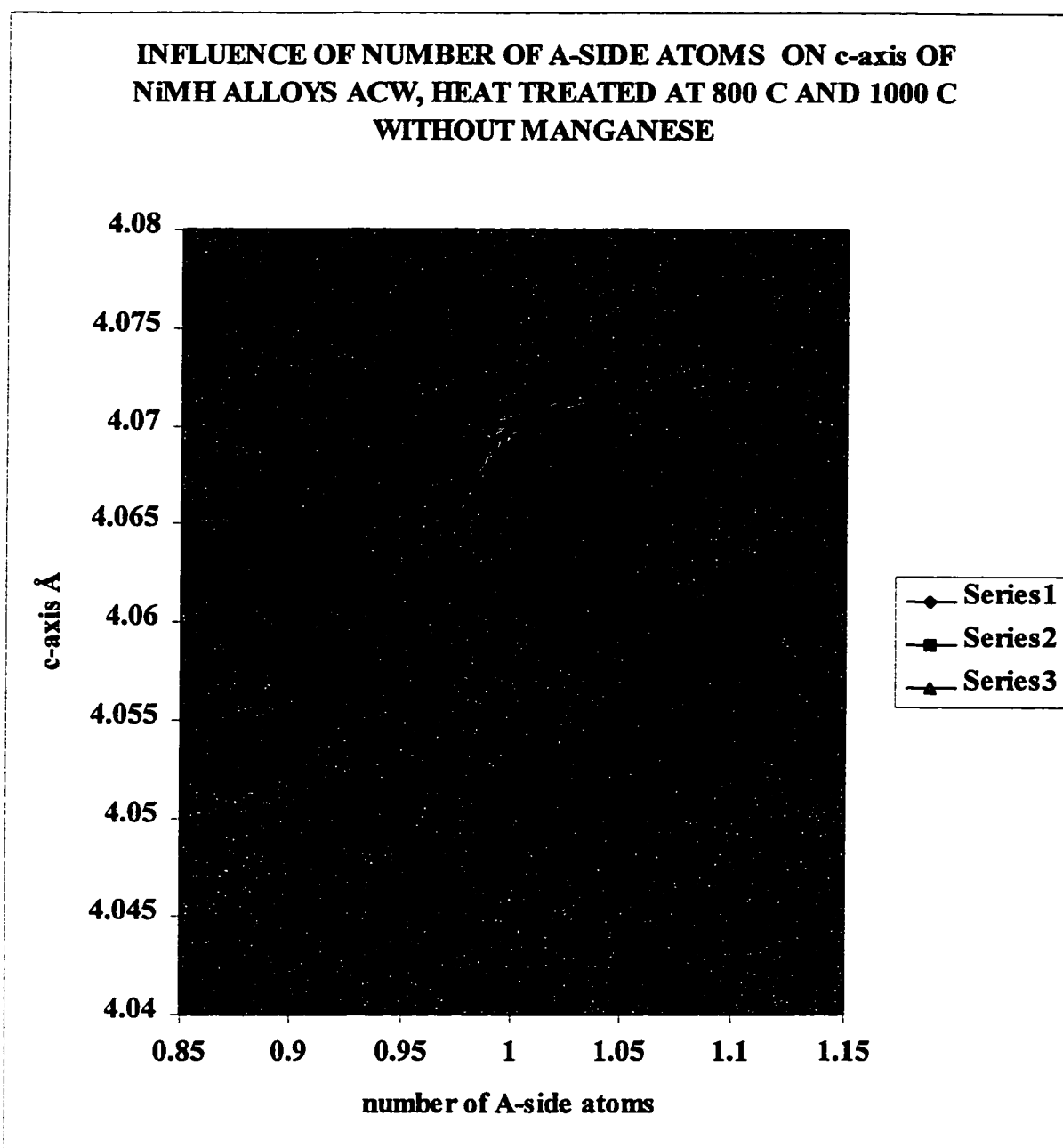


Figure 6.3 Influence of A-side atoms on c-axis of $A_{0.88}B_5$, AB_5 and $A_{1.09}B_5$ -type NiMH alloys without manganese ACW (1), heat-treated at 800 °C (2) and 1000 °C (3).
 $Mm_{0.88}Ni_{3.43}Co_{0.71}Al_{0.76}$, $Mm_{0.99}Ni_{3.5}Co_{0.7}Al_{0.81}$, $Mm_{0.99}Ni_{3.47}Co_{0.73}Al_{0.8}$,
 $MmNi_{3.48}Co_{0.71}Al_{0.81}$, $Mm_{0.99}Ni_{3.48}Co_{0.7}Al_{0.81}$ IMW $Mm_{1.09}Ni_{3.45}Co_{0.72}Al_{0.85}$

Non-stoichiometric $A_{0.88}B_5$ ACW alloy has a cell volume between heat treated at 1000 °C and 800 °C respectively because the a-axis is very big and c-axis is very small (Figure

6.2 and 6.3). Lack of mischmetal atoms and high cooling rate are main reasons for such atom distribution in the crystal cell. Heat treatment at 800 °C decreases the cell volume because of relaxation of the crystal cell along the **a**-axis. Heat treatment at 800 °C and at 1000 °C gave the same result for the **c**-axis. The number of B-side atoms in matrix slightly increase because of heat treatment (Appendix 2 alloy number 3). **c**-axis increased as result of change in chemical composition in the matrix due to heat treatment (Figure 6.3).

Nonstoichiometric $A_{1.09}B_5$ ACW alloys has the second biggest cell volume among series of A_xB_5 alloys (Figure 6.1) because of **a**-axis (Figure 6.2). **a**-axis is a function of chemical composition of the matrix, which changes with heat treatment (Appendix 2).

As general conclusions, the increase of number of A-side of NiMH atoms without manganese from 0.88- 1.09 causes increase of **a**-axis and **c**-axis i.e. cell volume. Cooling rate affects **a**-axis the most. **c**-axis is less affected with cooling rate. Heat treatment at 1000 °C affects the cell volume in whole range of alloys and increases a cell volume. The change in chemical composition of the matrix is the main reason for this change. Heat treatment at 800 °C decrease the cell volume in all ranges of NiMH alloys due to changes of the amounts of mischmetal alloys in matrix and cell relaxation.

c-axis is affected with number of A-side atoms. The increase of number of A-side atoms among series of A_xB_5 ($x=0.88-1.09$) alloys without manganese causes increase of **c**-axis. Heat treatment affects **c**-axis but not significantly. **c**-axis of stoichiometric alloys is less affected than nonstoichiometric. Each increase along the **a**-axis causes decrease along **c**-axis.

The influence of number of B-side atoms on cell volume of AB_x ($x= 4.76-5.376$) NiMH alloys without manganese is presented in Figure 6.4

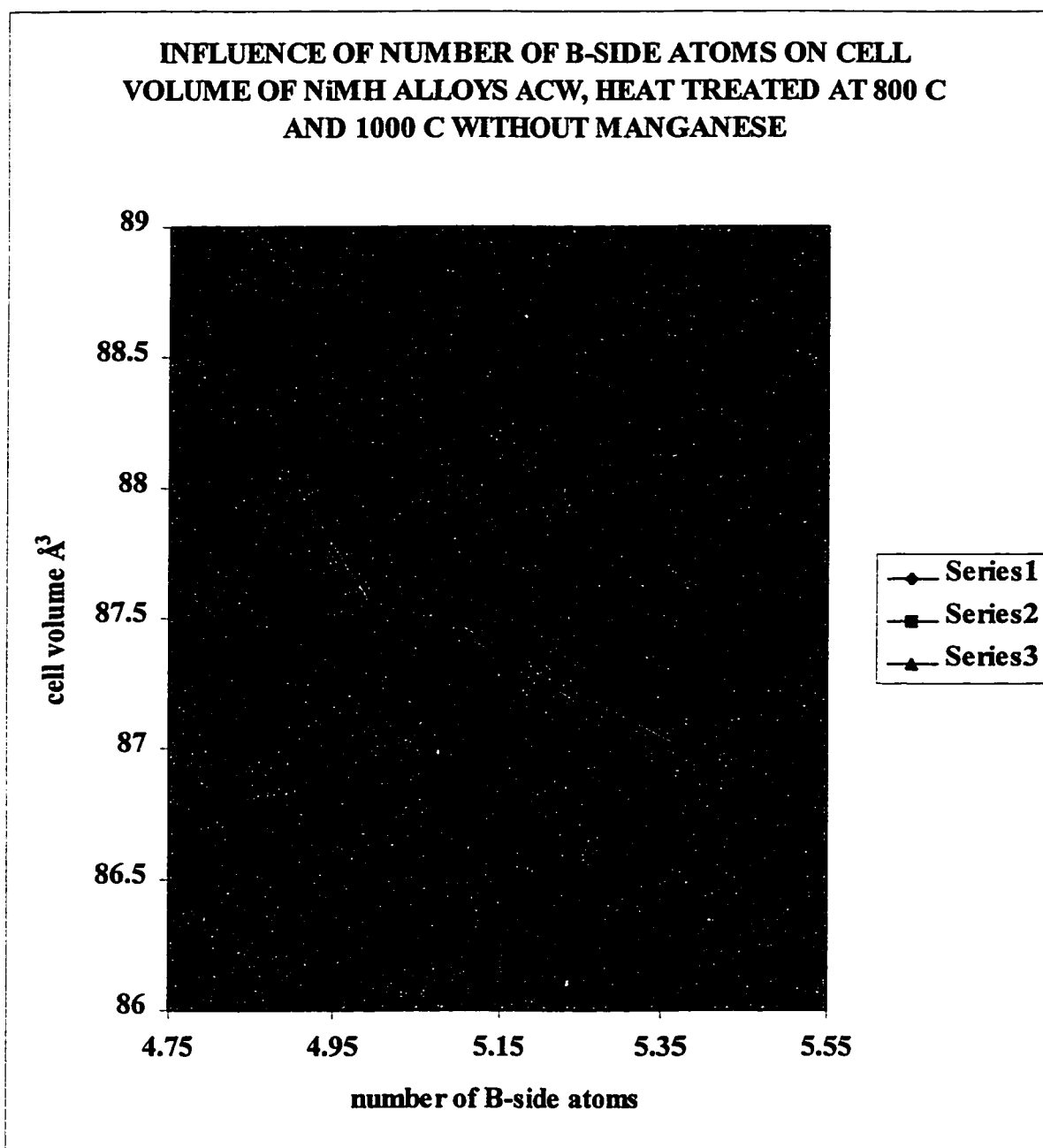


Figure 6.4 Influence of number of B-side atoms on cell volume of AB_x ($x= 4.76-5.376$) NiMH alloys without manganese, ACW (1), heat-treated at 800°C (2) and 1000 °C (3).
 $Mm_{0.92}Ni_{3.33}Co_{0.69}Al_{0.8}$, $MmNi_{3.48}Co_{0.71}Al_{0.81}$, $Mm_{0.99}Ni_{3.48}Co_{0.7}Al_{0.81}IMW$
 $Mm_{0.99}Ni_{3.78}Co_{0.756}Al_{0.84}$

Cell volume of stoichiometric AB_5 alloys without manganese is not affected significantly with the number of B-side atoms in AB_x ($x = 4.76-5.376$) NiMH alloys. Those alloys have almost identical **a**-axis and **c**-axis in ACW and heat-treated condition as presented in Figures 6.5 and 6.6.

Cell volume of nonstoichiometric $AB_{4.78}$ alloys is affected with the number of B-side atoms and heat treatment. $AB_{4.78}$ ACW alloys has the smallest cell volume among AB_x ($x = 4.76-5.376$) NiMH without manganese. This is due to the smallest **a**-axis and **c**-axis as presented in Figures 6.5 and 6.6. At the same time this alloy has less mischmetal atoms than stoichiometry, which affects **a**-axis. Heat treatment changes the amount of B-side elements in the matrix which is presented in Appendix 2, alloy number 7. Nickel content decreases from ACW towards heat-treated at 1000 °C and aluminum content increases in the same manner. The highest amount of nickel and the smallest amount of aluminum result in the smallest cell volume (Figure 6.4). Heat-treated $AB_{4.78}$ alloy at 1000 °C has the biggest cell volume (Figure 6.4) because it has the highest amount of aluminum. The aluminum atom radius is bigger than nickel or cobalt atom radius. The cell volume of $AB_{4.78}$ alloy heat-treated at 800 °C has a value between as cast and heat-treated alloys at 1000°C and is a little smaller than the cell volume of $AB_{4.78}$ alloys heat-treated at 1000 °C. This is due to the size of B-side atoms. The increase of number of B-side atoms in AB_x ($x = 4.76-5.376$) NiMH alloys without manganese causes the decrease of cell volume of heat treated alloys as depicted in Figure 6.4. There is no difference among **a**-axis of ACW, heat-treated at 800 °C and at 1000 °C (Figure 6.5). The main difference is among **c**-axis of $AB_{5.376}$ alloys, which cause the difference in cell volume. The number of

B-side atoms of heat-treated alloys follows the change of chemical composition of the matrix.

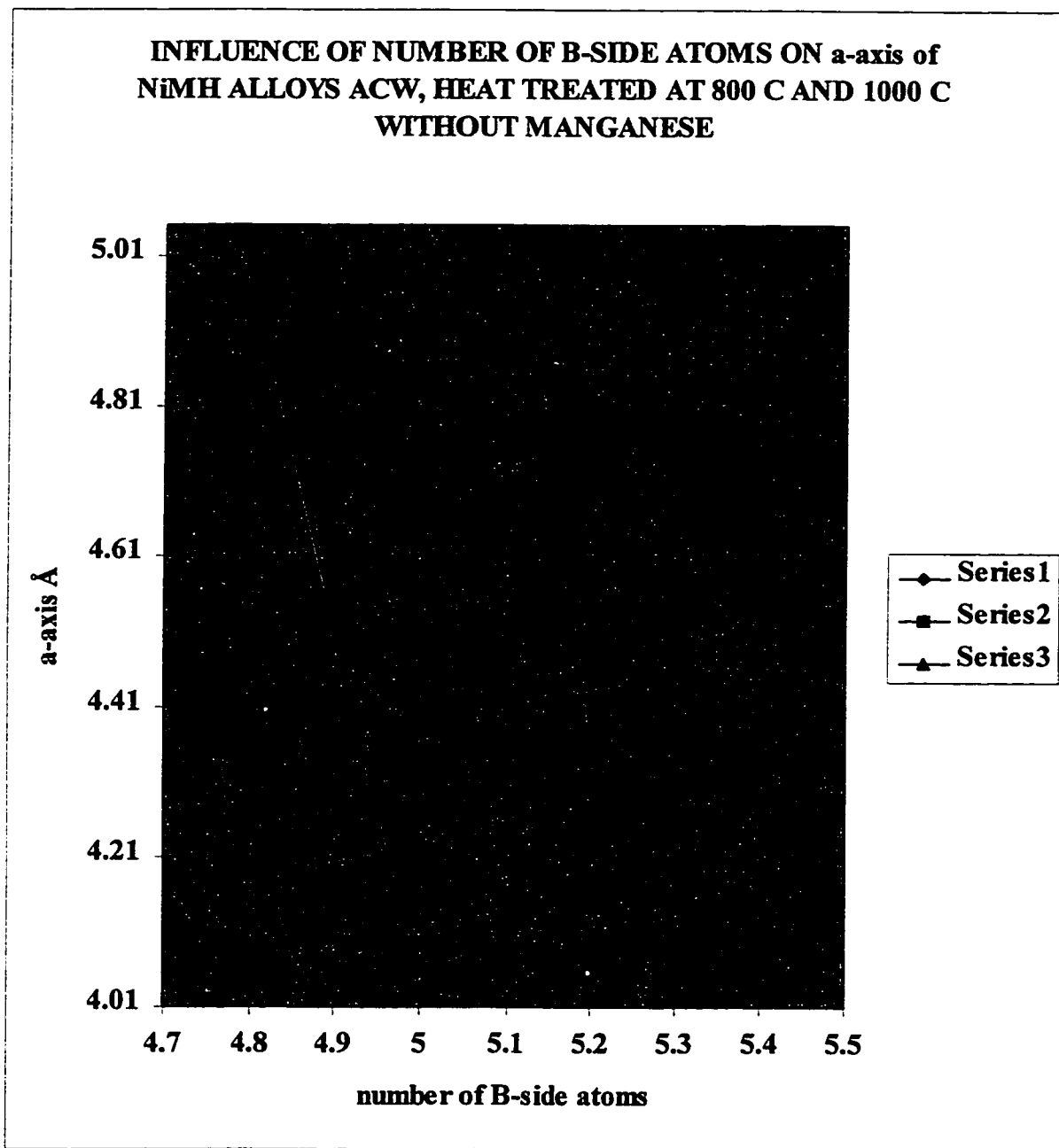


Figure 6.5 Influence of number of B-side atoms on a-axis of AB_x ($x = 4.76-5.376$) NiMH alloys without manganese. ACW (1) heat-treated at 800°C (2) and 1000 °C (3).
 $Mm_{0.92}Ni_{3.33}Co_{0.69}Al_{0.8}$, $MmNi_{3.48}Co_{0.71}Al_{0.81}$, $Mm_{0.99}Ni_{3.48}Co_{0.7}Al_{0.81}$ IMW
 $Mm_{0.99}Ni_{3.78}Co_{0.756}Al_{0.84}$

The smallest a-axis of AB_x ($x = 4.76-5.376$) NiMH alloys has stoichiometric alloys. The influence of number of B-side atoms on c-axis of AB_x ($x = 4.76-5.376$) NiMH alloys is depicted in Figure 6.6.

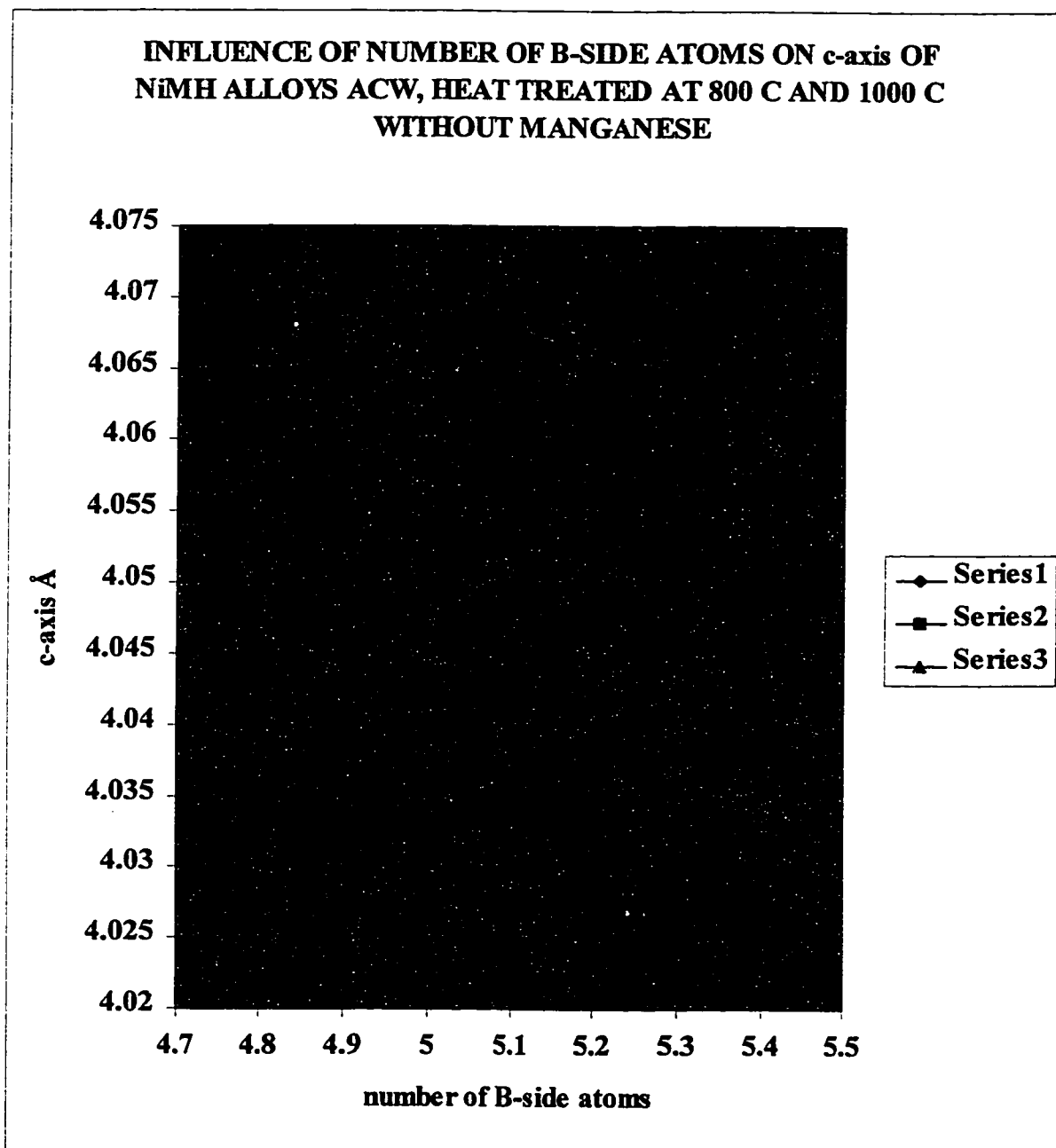


Figure 6.6 Influence of number of B-side atoms on c-axis of AB_x ($x = 4.76-5.376$) NiMH alloys without manganese. ACW (1) heat-treated at 800°C (2) and 1000 °C (3).
 $Mm_{0.92}Ni_{3.33}Co_{0.69}Al_{0.8}$, $MmNi_{3.48}Co_{0.71}Al_{0.81}$, $Mm_{0.99}Ni_{3.48}Co_{0.7}Al_{0.81}$ IMW
 $Mm_{0.99}Ni_{3.78}Co_{0.756}Al_{0.84}$

The biggest c-axis has stoichiometric AB_5 NiMH alloys. C-axis increases from $AB_{4.76}$ to AB_5 and decreases from AB_5 to $AB_{5.367}$ NiMH alloy.

The influence of number of A-side and B-side atoms in A_xB_5 ($x=0.88-1.09$) and AB_x ($x=4.76-5.376$) NiMH alloys without manganese on cell volume was explained in detail. As a conclusion, the cell volume of A_xB_5 ($x=0.88-1.09$), depends on the a-axis which is a function of the number of A-side atoms and heat treatment. It was found that heat treatment changed the amount of mischmetals in the matrix. The increase of number of A-side atoms causes the increase of c-axis of A_xB_5 ($x=0.88-1.09$) and heat treatment does not affect the c-axis significantly.

The cell volume of AB_x ($x=4.76-5.376$) depends significantly on the number of B-side atoms. The cell volume decreases as the number of B-side atoms increases. Heat treatment does not have a significant influence on cell volume. The increase of number of B-side atoms affects both a-axis and c-axis. Both axes are a function of the chemical composition of the matrix, which changes with heat treatment.

6.4.2 XRD Results of NiMH Alloys With Manganese

The same procedure of analysis was used for NiMH alloys with manganese. The influence of the number of A-side atoms on cell volume of A_xB_5 ($x=0.92-1.065$) NiMH alloys with manganese is presented in Figure 6.7. Cell volume increases as the number of A-side atoms increases. Stoichiometric AB_5 NiMH alloys with manganese are little affected by heat treatment. Stoichiometric AB_5 NiMH alloys with manganese heat treated at 800 °C have the biggest cell volume among stoichiometric alloys because it has the

highest amount of mischmetals (Appendix 2, alloys number 9 and 15). These alloys have the biggest a-axis among the stoichiometric alloys (Figure 6.8). Cell volume of AB_5 NiMH alloys with manganese heat treated at 800 °C and 1000 °C are in good agreement with the number of mischmetal atoms in matrix.

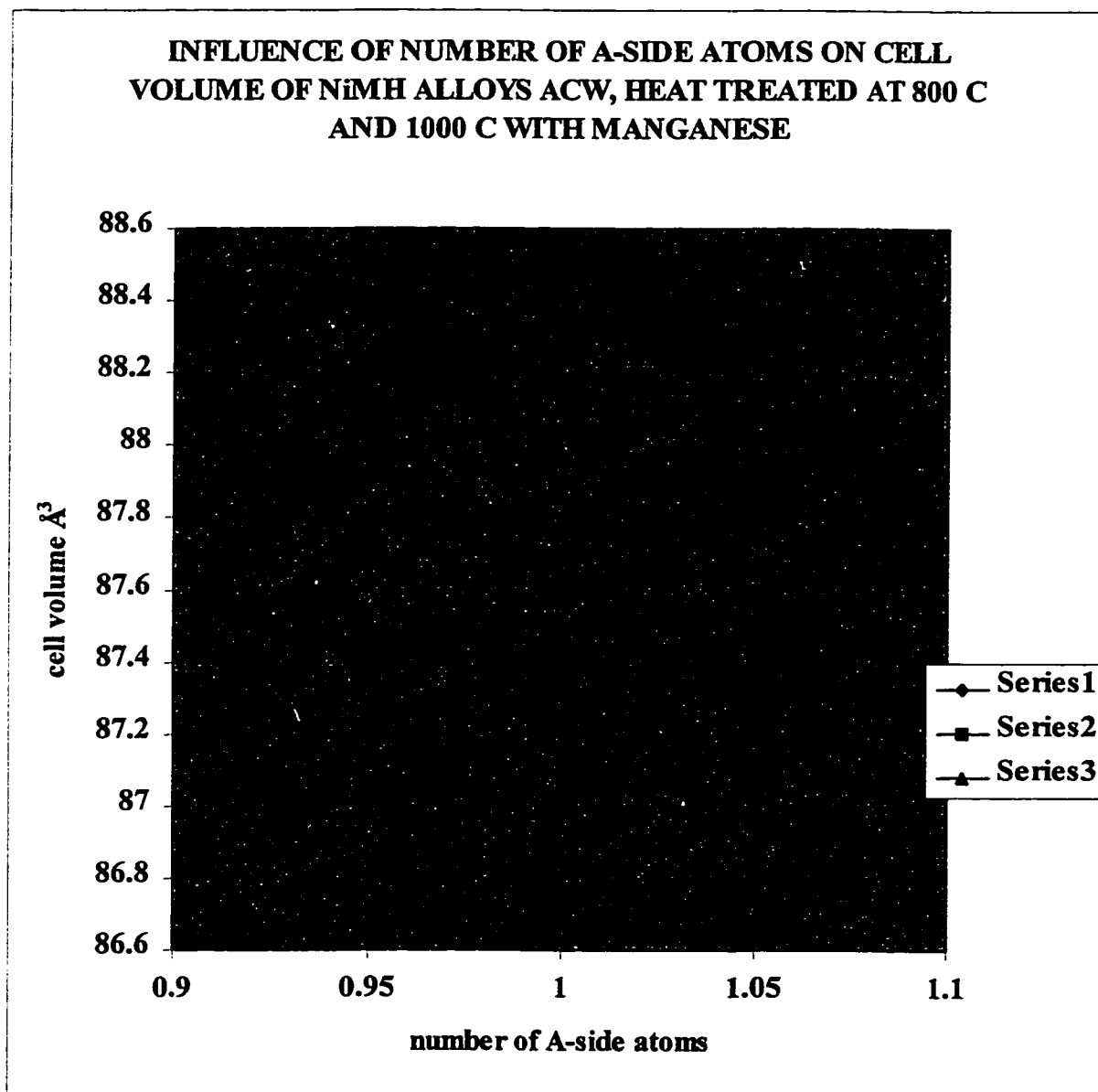


Figure 6.7 Influence of number of A-side atoms on cell volume of A_xB_5 ($x = 0.92-1.065$) NiMH alloys with manganese ACW (1) heat-treated at 800°C (2) and 1000 °C (3)
 $Mm_{0.92}Ni_{3.48}Co_{0.83}Mn_{0.29}Al_{0.31}$ $Mm_{0.99}Ni_{3.45}Co_{0.85}Mn_{0.41}Al_{0.31}$ IMW
 $MmNi_{3.54}Co_{0.82}Mn_{0.34}Al_{0.3}$, and $Mm_{1.065}Ni_{3.51}Co_{0.83}Mn_{0.37}Al_{0.32}$

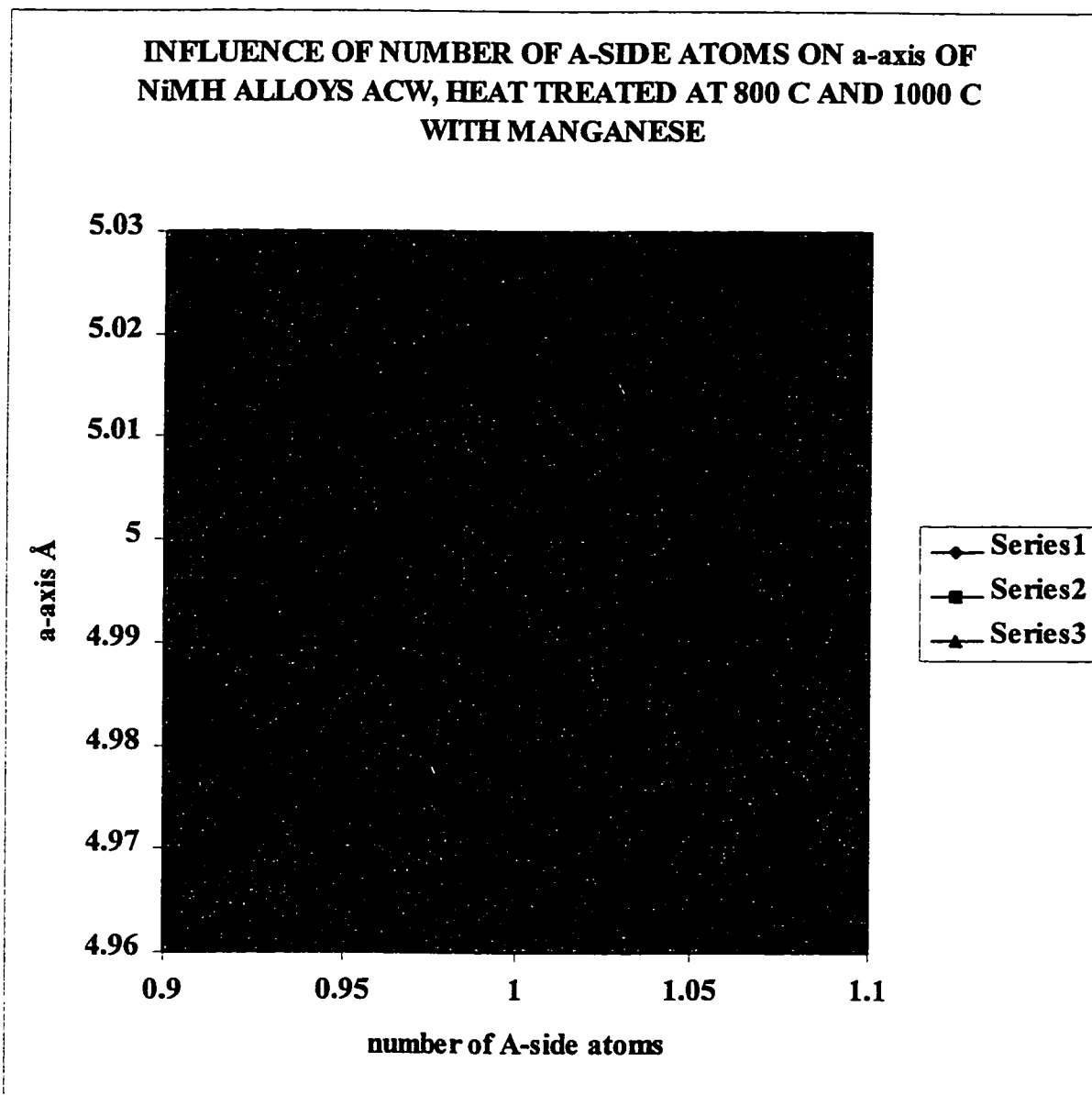


Figure 6.8 Influence of number of A-side atoms on a-axis of A_xB_5 ($x = 0.92-1.065$) NiMH alloys with manganese ACW (1) heat-treated at 800°C (2) and 1000 °C (3) $Mm_{0.92}Ni_{3.48}Co_{0.83}Mn_{0.29}Al_{0.31}$ $Mm_{0.99}Ni_{3.45}Co_{0.85}Mn_{0.41}Al_{0.31}$ IMW $MmNi_{3.54}Co_{0.82}Mn_{0.34}Al_{0.3}$, and $Mm_{1.065}Ni_{3.51}Co_{0.83}Mn_{0.37}Al_{0.32}$

Nonstoichiometric $A_{0.92}B_5$ ACW alloy has the smallest cell volume among $A_{0.92}B_5$ alloys because they have the smallest amount of mischmetal (Appendix 2). This alloy has the smallest **a**-axis (Figure 6.8). The size of the **a**-axis and cell volume of heat-treated NiMH alloys with manganese at 800 °C (2) and 1000 °C (3) are not in good agreement with the amount of mischmetal in the matrix. Alloy $A_{0.92}B_5$ heat-treated at 800 °C (2) has less mischmetal and a bigger cell volume and **a**-axis than $A_{0.92}B_5$ heat-treated at 1000 °C.

The number of mischmetal atoms in matrix of $A_{1.065}B_5$ alloys is not in good agreement with cell volume and **a**-axis. The reason for such behavior might be distribution of manganese atoms along both axes [18].

The behavior of the **c**-axis of A_xB_5 ($x = 0.92-1.065$) NiMH alloys with manganese ACW heat-treated at 800°C and 1000 °C is presented in Figure 6.9. The increase of number of A-side atoms causes a decrease of the **c**-axis. Heat treatment affects the **c**-axis. The highest value of **a**-axis and **c**-axis are in heat treated alloys at 800 °C. The lowest value of **c**-axis are in alloys heat treated at 1000 °C.

As general conclusions the increase of number of A-side atoms causes an increase of cell volume because of increase of **a**-axes. Heat treatment causes change in amount of mischmetals in the matrix and affects the **a**-axes. The change in amount of mischmetals in the matrix is not in good agreement with increase of the **a**-axes. This type of behavior can be understood by distribution of manganese along both axes [18].

The increase of A-side atoms causes a decrease of the **c**-axes. Heat treatment of these alloys causes change in amount of nickel, cobalt, manganese and aluminum atoms in the matrix. The variation of the **c**-axes because of heat treatment is significant.

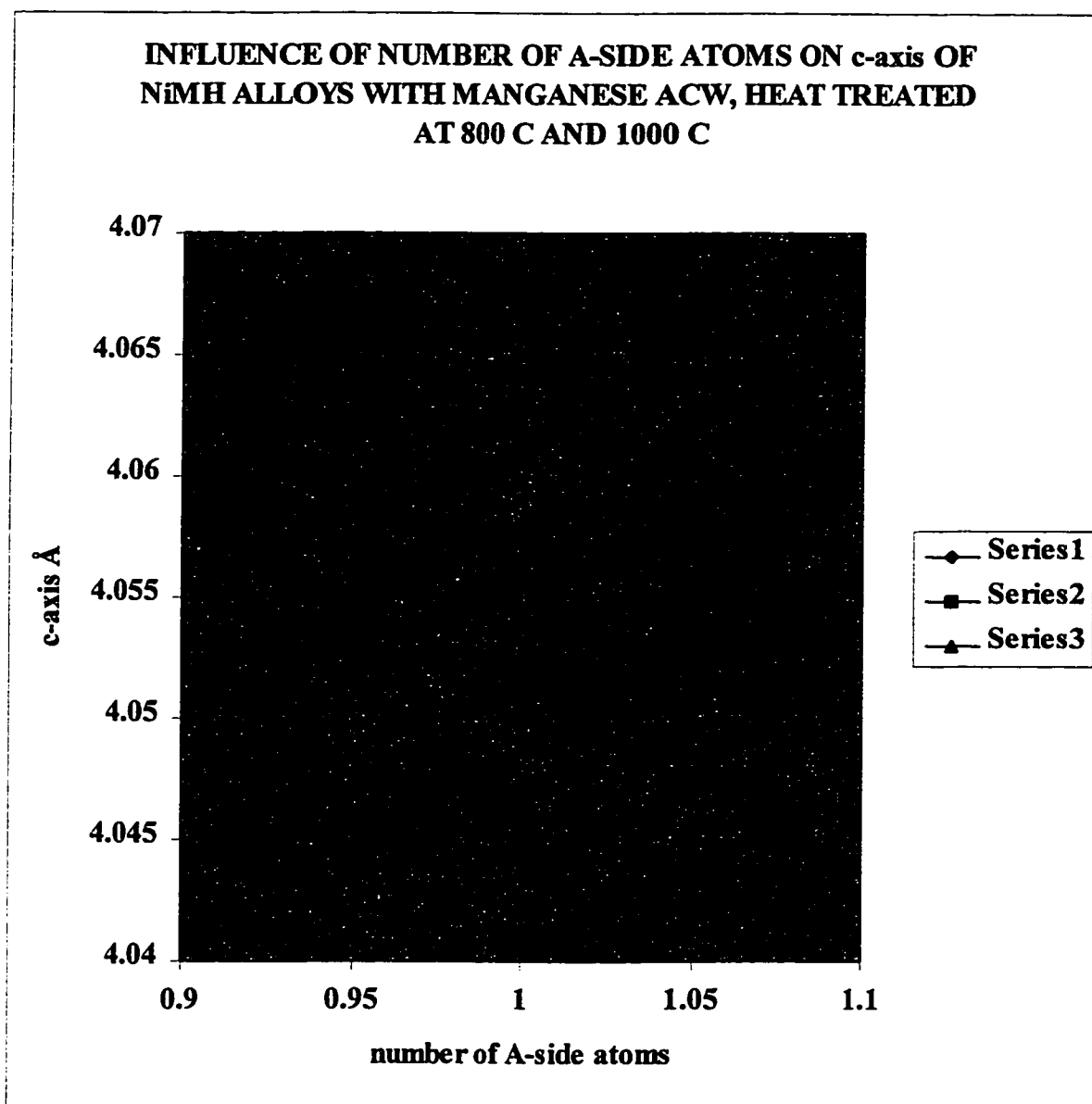
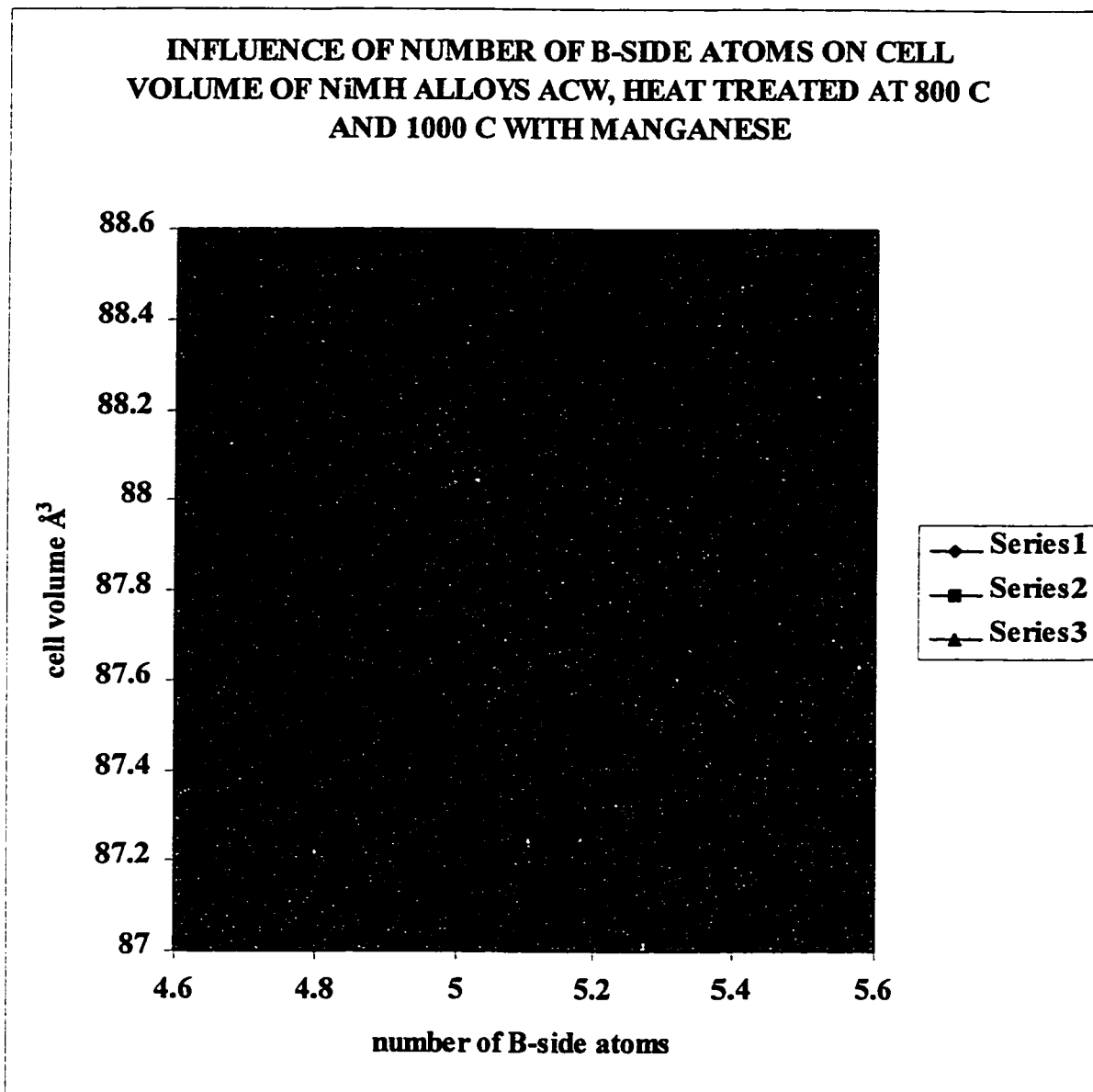


Figure 6.9 Influence of number of A-side atoms on c-axis of A_xB_y ($x = 0.92-1.065$, $y = 5$) NiMH alloys with manganese ACW (1) heat-treated at 800°C (2) and 1000 °C (3) $Mm_{0.92}Ni_{3.48}Co_{0.83}Mn_{0.29}Al_{0.31}$ $Mm_{0.99}Ni_{3.45}Co_{0.85}Mn_{0.41}Al_{0.31}$ IMW $MmNi_{3.54}Co_{0.82}Mn_{0.34}Al_{0.3}$, and $Mm_{1.065}Ni_{3.51}Co_{0.83}Mn_{0.37}Al_{0.32}$

The influence of number of A-side atoms on cell volume and cell parameters was discussed in great detail. The influence of number of B-side atoms on cell volume of AB_x ($x = 4.77-5.42$) is depicted in Figure 6.10.



6.10 Influence of number of B-side atoms on cell volume of AB_x ($x = 4.77-5.42$) NiMH alloys with manganese. ACW (1) heat-treated at 800°C (2) and 1000 °C (3) $Mm_{0.98}Ni_{3.33}Co_{0.79}Mn_{0.35}Al_{0.3}$, $Mm_{0.99}Ni_{3.45}Co_{0.85}Mn_{0.41}Al_{0.31}IMW$
 $MmNi_{3.54}Co_{0.82}Mn_{0.34}Al_{0.3}$ $Mm_{0.99}Ni_{3.79}Co_{0.9}Mn_{0.4}Al_{0.33}$

Cell volume of AB_x ($x = 4.77-5.42$) NiMH alloys with manganese decreases as the number of B-side atoms increases. Heat treatment has the greatest influence on $AB_{4.77}$ type of alloy i.e. alloys with the smallest number of B-side atoms and the smallest influence on the cell volume with the highest number of B-side atoms (Figure 6.10). $AB_{4.77}$ type of alloy has more mischmetal atoms because of lack of B-side atoms. Mischmetal atoms have more space to occupy in the crystal cell, which causes an increase of the **a**-axis. In ACW alloys, mischmetal atoms are close to each other because of a high cooling rate. Heat treatment increases the cell volume drastically because of the **a**-axis i.e. due to increase of mischmetal atoms in the matrix (Appendix 2, alloy number 12).

Heat treatment of AB_5 alloys at 800 °C increases the cell volume of AB_5 alloys the most. Cell volume of AB_5 alloys heat-treated at 1000 °C is between cell volume of ACW and alloys heat-treated at 800 °C.

$AB_{5.42}$ ACW has the smallest amount of mischmetal atoms among AB_x ($x = 4.77-5.42$) alloys and the smallest cell volume. Heat treatment causes an increase in the amount of mischmetal in the matrix and increase of the **a**-axes.

The increase of the number of B-side atoms in AB_x ($x = 4.77-5.42$) alloys causes a decrease of the **a**-axes. **C**-axes of those alloys decrease for ACW and alloys heat-treated at 800 °C and increase for alloys heat-treated at 1000 °C. The behavior of the **a**-axes and the **c**-axes of AB_x ($x = 4.77-5.42$) with manganese are depicted in Figures 6.11 and 6.12.

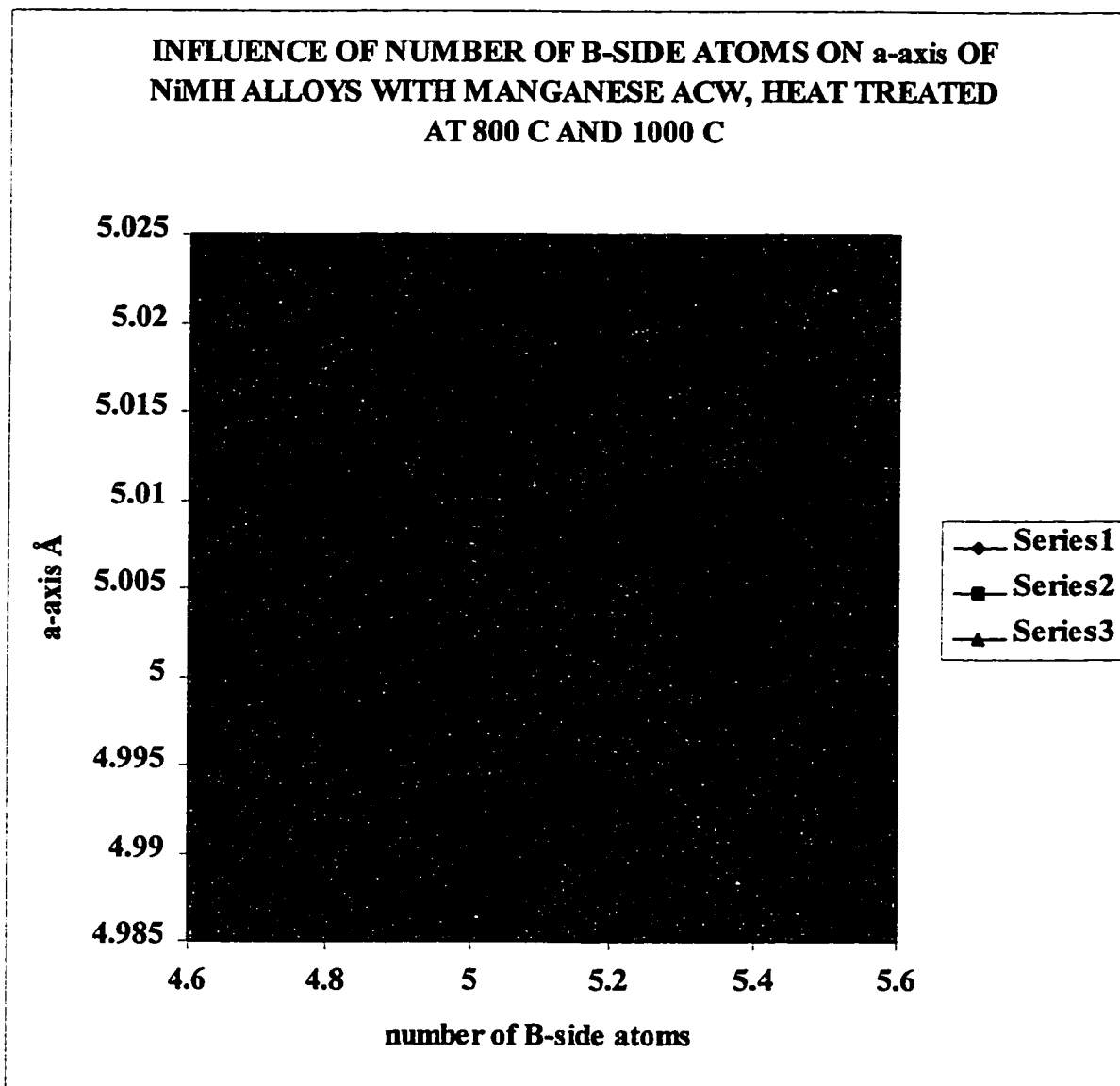


Figure 6.11 Influence of number of B-side atoms on a-axis of AB_x ($x = 4.77-5.42$) NiMH alloys with manganese. ACW (1) heat-treated at 800°C (2) and 1000 °C (3)
 $Mm_{0.98}Ni_{3.33}Co_{0.79}Mn_{0.35}Al_{0.3}$, $Mm_{0.99}Ni_{3.45}Co_{0.85}Mn_{0.41}Al_{0.31}$ IMW
 $MmNi_{3.54}Co_{0.82}Mn_{0.34}Al_{0.3}$ $Mm_{0.99}Ni_{3.79}Co_{0.9}Mn_{0.4}Al_{0.33}$

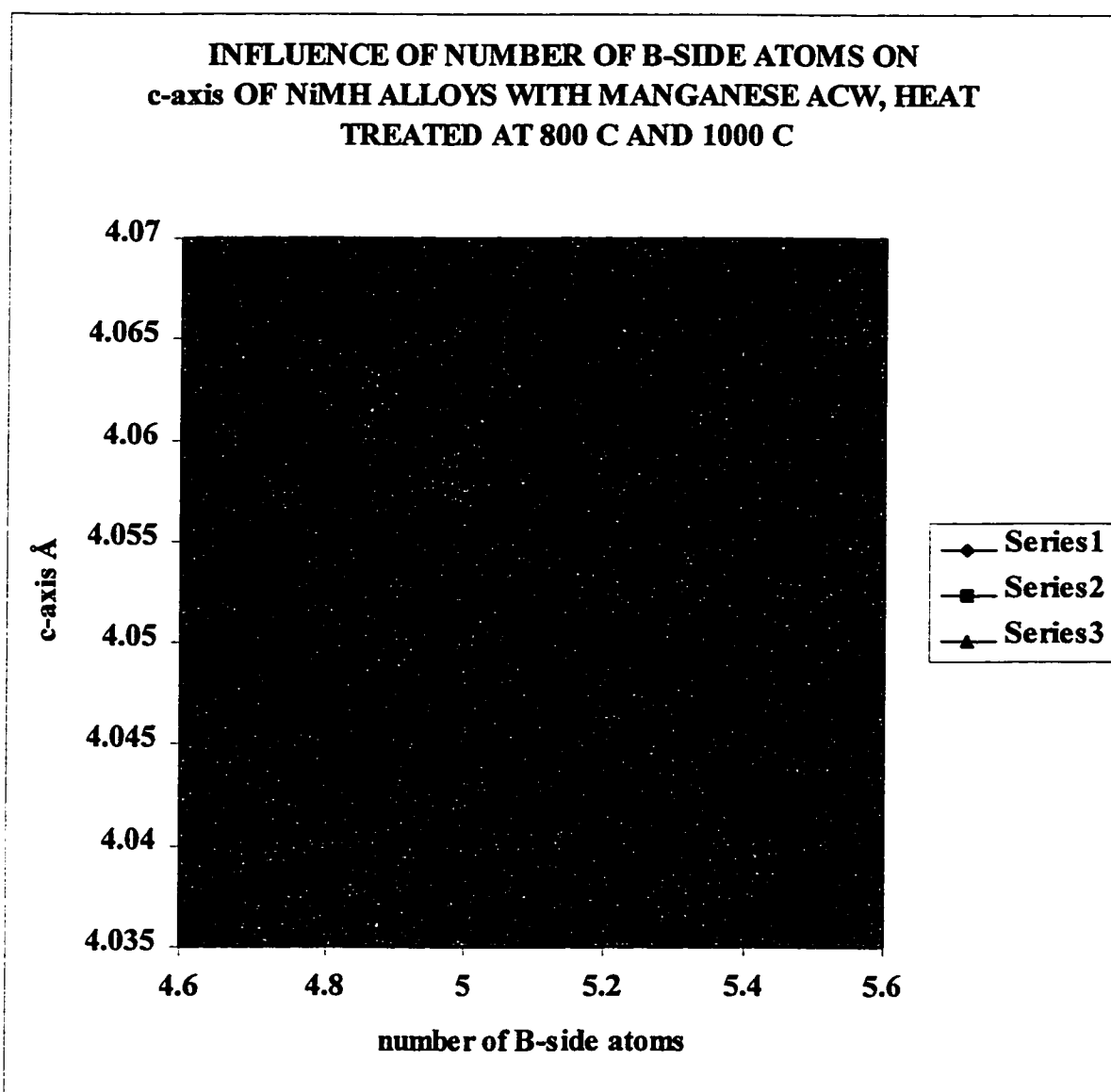


Figure 6.12 Influence of number of B-side atoms on c-axis of AB_x ($x = 4.77-5.42$) NiMH alloys with manganese. ACW (1) heat-treated at 800°C (2) and 1000 °C (3) $Mm_{0.98}Ni_{3.33}Co_{0.79}Mn_{0.35}Al_{0.3}$, $Mm_{0.99}Ni_{3.45}Co_{0.85}Mn_{0.41}Al_{0.31}$ IMW $MmNi_{3.54}Co_{0.82}Mn_{0.34}Al_{0.3}$ $Mm_{0.99}Ni_{3.79}Co_{0.9}Mn_{0.4}Al_{0.33}$

The comparison between Figures 6.1 and 6.7 leads to a conclusion that increase of A-side atoms leads to increase of cell volume for both types of chemical composition. At the same time, heat treatment affects the cell volume of two types of NiMH differently related to presence or absence of manganese. The increase or decrease of cell volume is

due to a change in the number of A-side atoms in the matrix. Alloys with manganese are sensitive to the amount of manganese in the matrix due to manganese distribution along both axes. The EDS results are not always in good agreement with expected values of cell parameters due to complex interaction of manganese.

The increase of number of B-side atoms generally leads to a decrease in cell volume due to a decrease of the **a**-axis. Alloys without manganese are not affected as much with heat treatment as alloys with manganese.

6.5 Discharge Capacity and Rate Capability Results

6.5.1 NiMH Alloys Without Manganese

Discharge capacity of NiMH alloys without manganese depends on stoichiometry, cell volume and heat treatment. The discharge capacity can be changed by changes in the size of the cell volume i.e. by change of the size of the **a**-axis and **c**-axis of the alloys. Figure 5.16 describes the relationship between discharge capacity and cell volume. The increase of cell volume generally causes an increase of discharge capacity.

The influence of heat treatment on discharge capacity of NiMH alloys without manganese is depicted in Figure 6.13.

Heat treatment at 1000°C improves the discharge capacity only of nonstoichiometric $A_{0.88}B_5$ and $AB_{5.376}$ ($Mm_{0.88}Ni_{3.43}Co_{0.71}Al_{0.76}$ and $Mm_{0.99}Ni_{3.78}Co_{0.756}Al_{0.84}$) alloys.

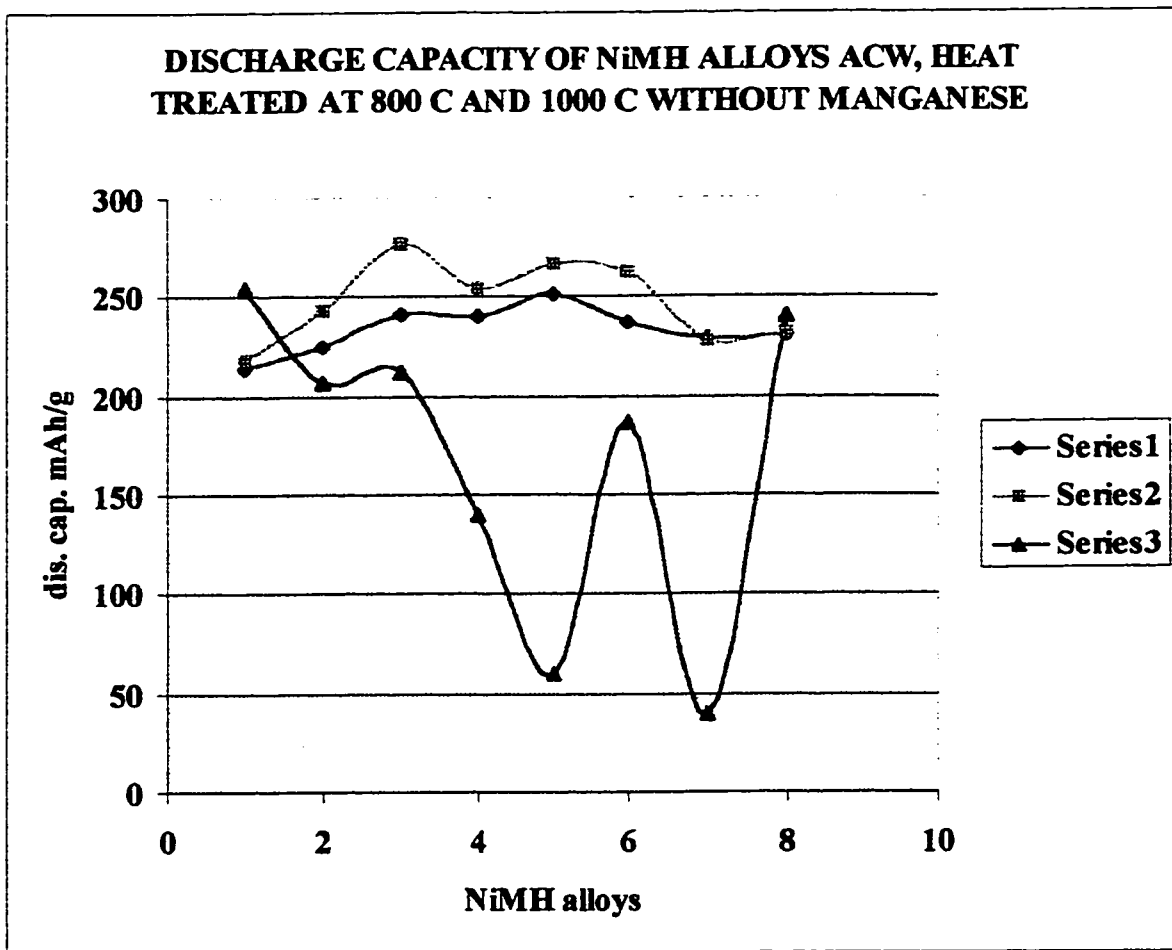


Figure 6.13 Influence of heat treatment on discharge capacity of NiMH alloys. Series 1- ACW Series 2- heat-treated at 800°C, Series 3- heat-treated at 1000°C, No. 1- $Mm_{0.88}Ni_{3.43}Co_{0.71}Al_{0.76}$, No.2- $Mm_{0.99}Ni_{3.5}Co_{0.7}Al_{0.81}$, No.3 - $Mm_{0.99}Ni_{3.47}Co_{0.73}Al_{0.81}$, No. 4- $MmNi_{3.48}Co_{0.71}Al_{0.81}$, 5- $Mm_{0.99}Ni_{3.48}Co_{0.7}Al_{0.81}$ IMW, No.6 - $Mm_{1.09}Ni_{3.45}Co_{0.72}Al_{0.85}$, No.7 - $Mm_{0.92}Ni_{3.33}Co_{0.69}Al_{0.8}$, No.8 - $Mm_{0.99}Ni_{3.78}Co_{0.756}Al_{0.84}$

Those alloys have Ni-Co-Al phase on grain boundaries. Heat treatment decreases the amount of Ni-Co-Al phase but increases cobalt content and increases the grain size of the alloys. The discharge capacity of heat treated alloys at 800°C is a little higher than the discharge capacity of as cast alloys because of lower amount of Ni-Co-Al phase. Heat-treatment at 1000°C drastically decreases the discharge capacity of all other alloys because it increases the grain size. The smaller grain size of alloys has beneficial

influence on alloy resistance to oxidation [18]. Crack propagation along grain boundaries is more difficult in alloys with smaller grain size.

Heat treatment at 800 °C does not change the cell volume of stoichiometric alloys. ACW and heat -treated alloys have almost identical cell volume but heat treated alloys at 800°C have higher discharge capacity than ACW alloys. Heat treatment at 800 °C decreases the hardness of the alloys. During absorption of hydrogen, heat treated alloys do not crack as much as the ACW alloys. This inhibits the formation of fresh surfaces for oxidation. A thin oxide layer protects the alloy from further oxidation.

$\text{Mm}_{0.99}\text{Ni}_{3.48}\text{Co}_{0.7}\text{Al}_{0.81}\text{IMW}$ as cast has higher discharge capacity than $\text{MmNi}_{3.48}\text{Co}_{0.71}\text{Al}_{0.81}$ ACW because it has a slightly larger cell volume. Heat treatment at 800°C decreases the hardness and decreases the degree of crack formation during absorption or desorption of hydrogen.

Heat-treatment at 800°C exhibits similar effects on $\text{Mm}_{1.09}\text{Ni}_{3.45}\text{Co}_{0.72}\text{Al}_{0.85}$ as presented in Figure 6.13.

$\text{Mm}_{0.92}\text{Ni}_{3.33}\text{Co}_{0.69}\text{Al}_{0.8}$ has twice as much neodymium (Appendix 2) than lanthanum and the largest cell volume among all alloys. Heat-treatment at 800°C does not change the discharge capacity because neodymium increases the equilibrium pressure above atmospheric pressure. An amount of hydrogen escaped to atmosphere, which caused a lower discharge capacity than expected. The influence of number of A-side atoms on discharge capacity and rate capability of ACW and heat-treated of NiMH alloys without manganese is depicted in Figure 6.14.

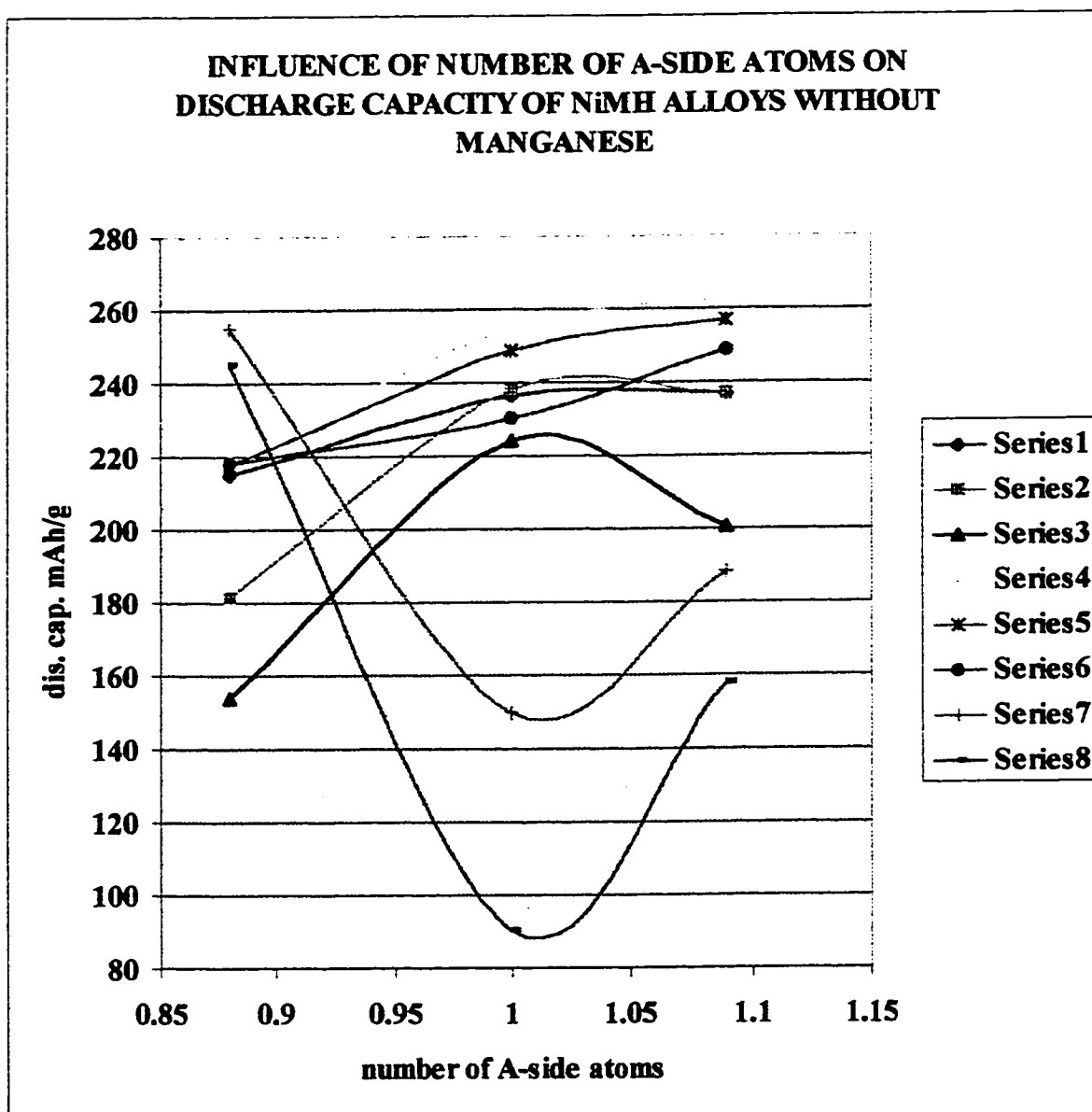


Figure 6.14 Influence of number of A-side atoms on discharge capacity and rate capability of A_xB_5 ($x = 0.88-1.09$) NiMH alloys ACW and heat-treated at 800°C and 1000 °C without manganese. Series 1,2, 3 are ACW alloys discharged with 92, 184 and 248 mA/g to 0.6 V respectively. Series 4,5,6 are heat-treated at 800°C discharged with 92, 184 and 248 mA/g to 0.6 V respectively. Series 7 and 8 are alloys heat-treated at 1000°C and discharged with 92 and 184 mA/g to 0.6 V respectively.

The increase of number of A-side atoms in NiMH alloys without manganese causes an increase of discharge capacity of ACW alloys. $A_{0.88}B_5$ alloys are very sensitive to an increase of discharge current. The increase of discharge current leads to decrease of

discharge capacity. Stoichiometric AB_5 ACW alloys have the same discharge capacity up to the discharge current of 184 mA. $A_{1.09}B_5$ ACW alloys have the same behavior.

Heat treatment at 800°C increases the discharge capacity and the rate capability of A_xB_5 ($x = 0.88-1.09$) alloys. Heat treatment at 1000°C drastically decreases the rate capability of AB_5 alloys and seriously decreases the rate capability of nonstoichiometric alloys.

The influence of number of B-side atoms on discharge capacity and rate capability of NiMH alloys without manganese is presented in Figure 6.15. The increase of number of B-side atoms causes increases of discharge capacity and rate capability of alloys. $AB_{4.77}$ ACW alloy is very sensitive to increase of discharge current. Heat treatment does not change the discharge capacity and rate capability significantly. This alloy has mischmetal with a very small amount of cerium, which increases the discharge capacity and rate capability. Heat treatment increases the cell volume of this alloy drastically. $AB_{5.376}$ ACW alloy has a good rate capability up to 184 mA discharge current. The Ni-Co-Al phase, having high cobalt content and being distributed on grain boundaries, has good resistance to oxidation. Heat treatment decreases the amount of this phase on grain boundaries and increases the amount of cobalt at this location (Appendix 2 alloy number 8). The presence of cobalt on grain boundaries increases the rate capability of the alloy.

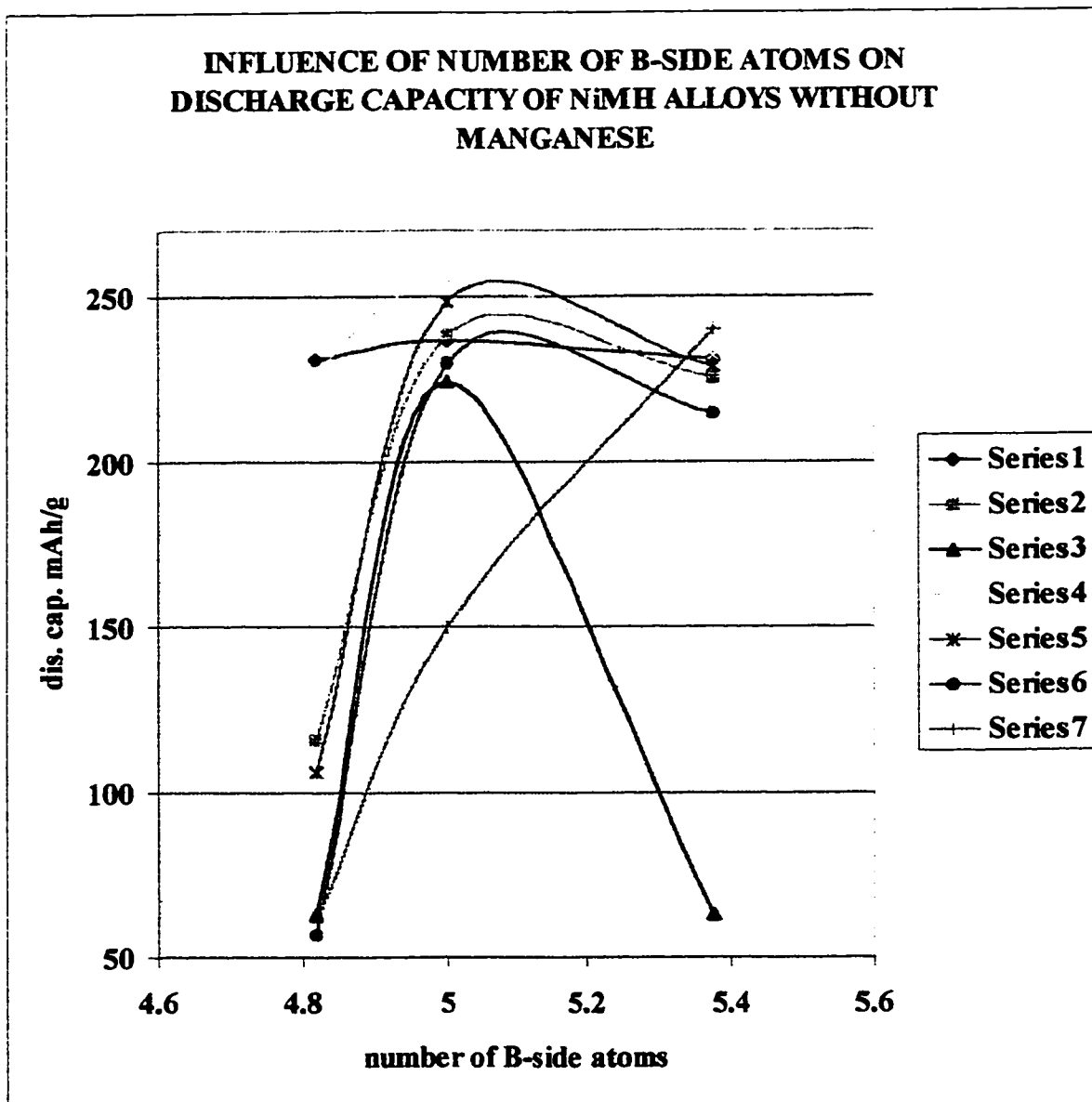


Figure 6.15 Influence of number of B-side atoms on discharge capacity and rate capability of AB_x ($x = 4.82-5.376$) NiMH alloys ACW and heat-treated at 800°C and 1000 °C without manganese. Series 1,2, 3 are ACW alloys discharged with 92, 184 and 248 mA/g to 0.6 V respectively. Series 4,5,6 are heat-treated at 800°C discharged with 92, 184 and 248 mA/g to 0.6 V respectively. Series 7 is alloys heat-treated at 1000°C and discharged with 92 mA/g to 0.6 V.

The influence of stoichiometry and heat treatment on cell volume, discharge capacity and rate capability of NiMH alloys without manganese is summarized in Table 6.1. This table provides the same information presented in above figures but simplified. The symbol + means positive influence, ++ means very strong influence and – means negative influence on crystal cell and electrochemical characteristics of alloys.

Table 6.1 Summary of influence of stoichiometry on cell volume of electrochemical characteristics of NiMH alloys without manganese

Increase of number of A-side atoms in NiMH alloys without manganese				Increase of number of B-side atoms in NiMH alloys without manganese		
	ACW	HT 800 °C	H.T. 1000 °C	ACW	H.T. 800 °C	H.T 1000 °C
Cell vol.	+/-	+	++	+/-	-	-
a-axis	++	+	+	-/+	-/+	-/+
c-axis	+	+	+	--/+	-/+	-/+
Dis. capacity.	+	++	--	+/-	++	+/-
Rate capabili.	+	++	+/-	++	+	-/+

6.5.2 NiMH Alloys With Manganese

The influence of heat treatment on discharge capacity of NiMH alloys with manganese is presented in Figure 6.16.

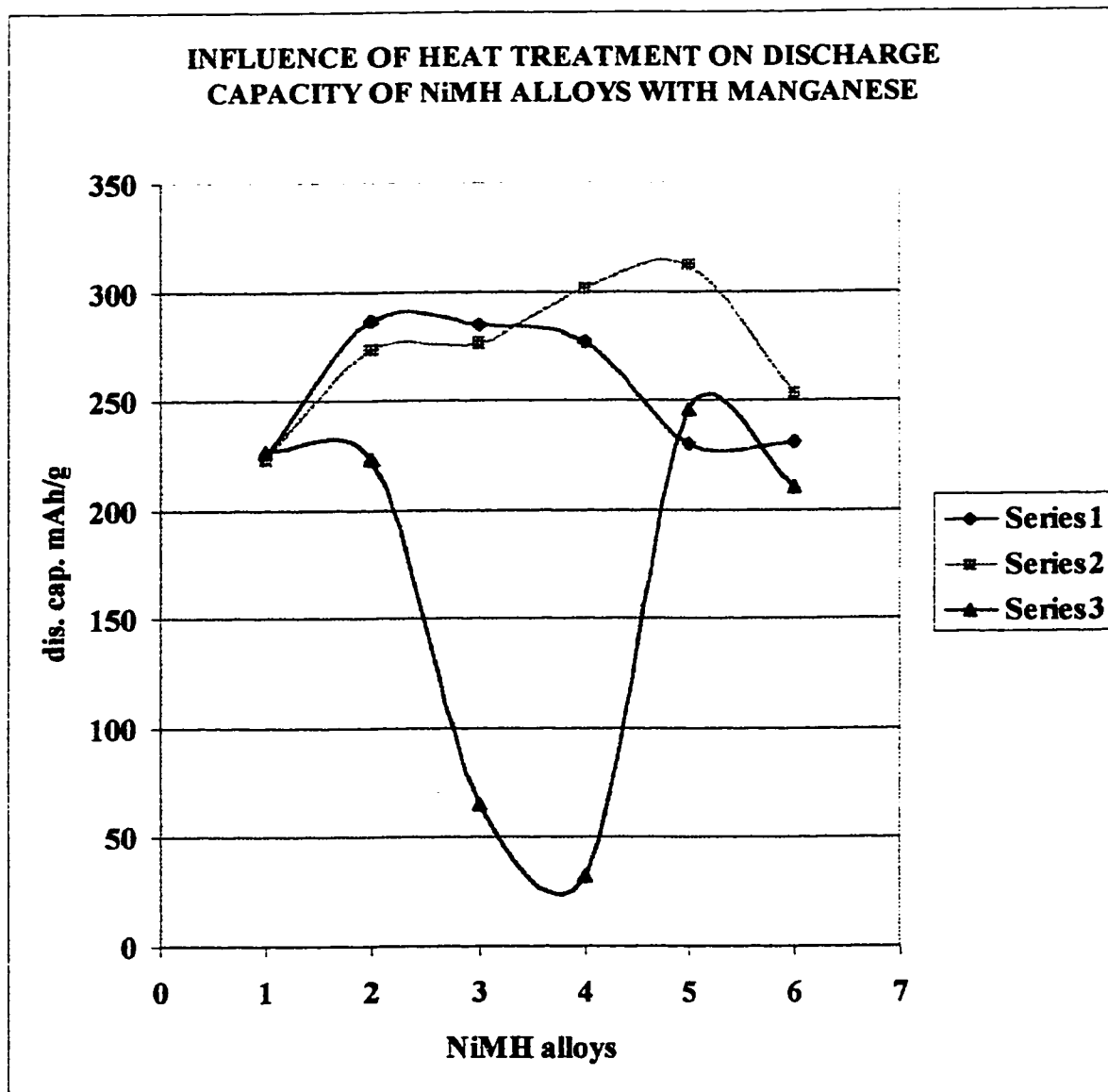


Figure 6.16. Influence of stoichiometry, method of production and heat treatment on discharge capacity of NiMH alloys with manganese. Series 1- ACW. Series 2-heat treated at 800°C, Series 3-heat treated at 1000°C, No.1 - $Mm_{0.92}Ni_{3.48}Co_{0.83}Mn_{0.29}Al_{0.31}$, No.2- $Mm_{1.065}Ni_{3.51}Co_{0.83}Mn_{0.37}Al_{0.32}$, No.3- $MmNi_{3.54}Co_{0.82}Mn_{0.34}Al_{0.3}$ and No.4- $Mm_{0.99}Ni_{3.45}Co_{0.85}Mn_{0.4}Al_{0.3}$ IMW No.5- $Mm_{0.98}Ni_{3.33}Co_{0.79}Mn_{0.35}Al_{0.3}$, and No.6 - $Mm_{0.99}Ni_{3.79}Co_{0.9}Mn_{0.4}Al_{0.33}$

$A_{0.92}B_5$ alloys have the lowest discharge capacity among all NiMH alloys with manganese. The presence of Ni-Co-Mn-Al gave good stability to those alloys. ACW and heat-treated alloys are not sensitive to the higher discharge current. Ni-Co-Mn-Al phase has a high amount of cobalt, which improves resistance to oxidation. The rate capability

increases as the number of A-side atom increases. AB_5 and $A_{1.065}B_5$ ACW have higher discharge capacity than heat-treated alloys because of the beneficial influence of small grain size on discharge capacity. The influence of the number of A-side atoms on discharge capacity and rate capability of NiMH alloys with manganese is presented in Figure 6.17. High cooling rate improves the rate capability of A_xB_5 ($x = 0.92-1.065$) alloys with manganese. Small grain size is barrier for oxidation and crack propagation. ACW alloys are very hard and brittle. During absorption of hydrogen the cell volume increases by about 15 %. Small grain size protects the alloy from formation of new fresh surfaces because the cracks need more energy for propagation. Heat treatment increases the cell volume and grain size of those alloys and decreases the hardness of the alloys. The increase of grain size causes a decrease of rate capability of those alloys (Figure 6.17). The highest number of A-side atoms results in the lowest rate capability.

The influence of number of B-side atoms on discharge capacity and rate capability is presented in Figure 6.18. The increase of number of B-side atoms in AB_x ($x = 4.77-5.42$) NiMH alloys causes decrease of discharge capacity and rate capability of heat treated alloys at 800 °C. ACW AB_x ($x = 4.77-5.42$) NiMH alloys exhibits increases of discharge capacity and rate capability. The major change occurs in $AB_{4.77}$ alloy because of extreme changes of cell volume and a-axis.

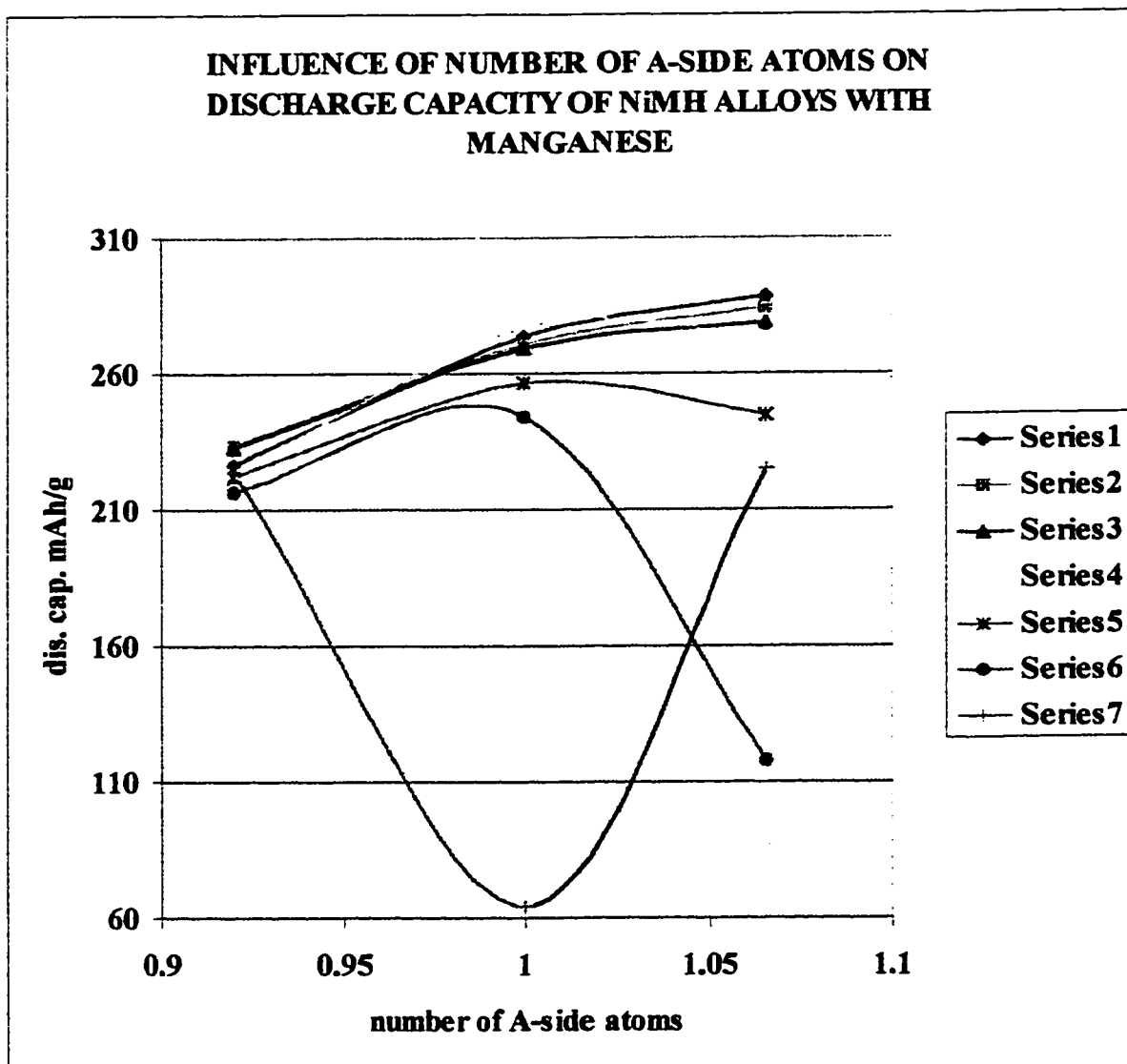


Figure 6.17 Influence of number of A-side atoms on discharge capacity and rate capability of A_xB_5 ($x = 0.92-1.065$) NiMH alloys ACW and heat-treated at 800°C and 1000 °C with manganese. Series 1,2, 3 are ACW alloys discharged with 92, 184 and 248 mA/g to 0.6 V respectively. Series 4,5,6 are heat-treated alloys at 800°C discharged with 92, 184 and 248 mA/g to 0.6 V respectively. Series 7 is alloys heat-treated at 1000°C and discharged with 92 mA/g to 0.6 V

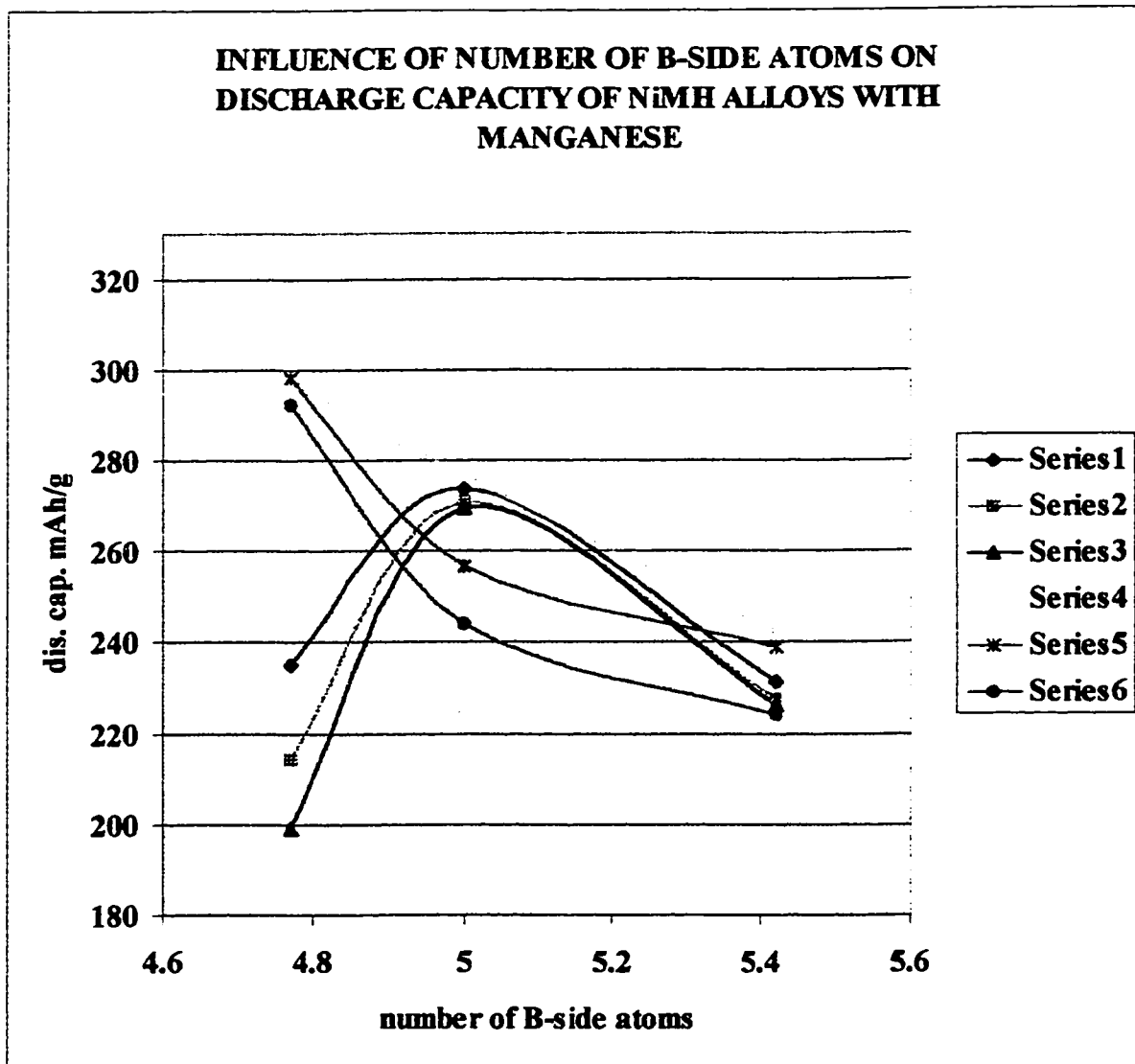


Figure 6.18 Influence of number of B-side atoms on discharge capacity and rate capability of AB_x ($x = 4.77-5.42$) NiMH alloys ACW and heat-treated at 800°C and 1000°C with manganese. Series 1,2, 3 are ACW alloys discharged with 92, 184 and 248 mA/g to 0.6 V respectively. Series 4,5,6 are heat-treated at 800°C discharged with 92, 184 and 248 mA/g to 0.6 V respectively

Cooling rate of IMW alloys is lower than AMW alloys leading to a larger grain size at formation. Heat treatment at 800°C increases the cell volume and discharge capacity of IMW alloys.

The method of production also affects rate capability. A comparison of two IMW, two AMW alloys and two commercial alloys indicated that the best rate capabilities are for

two stoichiometric NiMH AMW alloys (Figure 5.13) with manganese. The stoichiometric AMW alloy has a lower discharge capacity but better rate capability than IMW heat treated at 800°C alloys with manganese. Higher cooling rate is more beneficial for rate capability.

The comparison between two stoichiometric NiMH alloys without manganese shows the same behavior. AMW stoichiometric alloys exhibits lower rate capability and discharge capacity than induction melted alloys. Smaller grain size because of higher cooling rate does not exhibit a beneficial effect on rate capability of stoichiometric NiMH alloys without manganese. IMW heat-treated alloy at 800°C exhibits lower rate capability than AMW stoichiometric NiMH alloys.

Commercial alloys without manganese have poorer discharge capacity and rate capability than commercial alloys with manganese which is opposite to previously reported results [18,44-46].

The absorption of hydrogen in NiMH alloys without manganese depends mostly on the *a*-axis (Table 5.1). The same rule is valid for NiMH alloys with manganese. The cell volumes of hydrides increase mostly because of increase of the *a*-axes of alloys. That means that during absorption hydrogen atoms are situated mostly along the *a*-axis for stoichiometric IMW non heat-treated alloys. The *c*-axis increases also but less than the *a*-axis. That also means that *a*-axis play mayor role in discharge capacity of NiMH alloys.

Table 6.2 is simplified explanation of influence of stoichiometry on crystal cell and electrochemical characteristics of NiMH alloys with manganese. The same symbols are used as in Table 6.1.

Table 6.2 The influence of stoichiometry on crystal cell and electrochemical characteristics of NiMH alloys with manganese

Increase of number of A-side atoms in NiMH alloys with manganese				Increase of number of B-side atoms in NiMH alloys with manganese		
	ACW	HT 800 °C	H.T. 1000 °C	ACW	H.T. 800 °C	H.T 1000 °C
Cell vol.	+/-	++	+	--	-	-
a-axis	+/-	++	+	-	--	--
c-axis	-	-/+	-/-	-	--	+
Dis. capacity.	+	++	--	-/+	-	--
Rate capabili.	+	++	+/-	+/-	+	-/+

6.6 Metallography Results

The metallography results have been discussed previously in terms of its influence on discharge capacity and rate capabilities of NiMH alloys. The presence of another phase in the alloys decreases the discharge capacity. The presence of Ni-Co-Al phase in $A_{0.88}B_5$ alloys without manganese causes a decrease of discharge capacity and rate capability of the alloy. Heat treatment decreases the amount of Ni-Co-Al phase in the matrix and increases the amount of cobalt on grain boundaries leading to better discharge capacity and rate capability of the alloys. The presence of oxide causes decrease in discharge capacity and rate capability because the oxygen is connected with rare earth atoms decreasing the amount of mischmetals available to react with B-side atoms. Lower amounts of mischmetals means lower cell volume because the a-axis is smaller. Stoichiometric alloys usually have small amount of oxides and rare earth inclusions. The presence of rare earth alloys and oxide in small amount does not significantly affect the

discharge capacity and rate capability of NiMH alloys. High amounts of rare earth alloys in $A_{1.09}B_5$ without manganese decreases the discharge capacity and rate capability because a big part of the NiMH alloy is inactive in terms of absorption or desorption of hydrogen.

$AB_{4.82}$ alloy has small amount of rare earth phase and oxide in matrix. The influence of those phases on rate capability and discharge capacity is negligible.

$AB_{5.376}$ alloy without manganese has a Ni-Co-Al phase, which plays a positive role in terms of rate capability.

Stoichiometric AB_5 alloys with manganese have a small amount of Ni-Co-Mn-Al phase and oxides which decrease the discharge capacity and rate capability. This phase was formed after oxidation of a small amount of mischmetals.

$A_{0.92}B_5$ alloys with manganese have a huge amount of Ni-Co-Mn-Al phase on grain boundaries. The high amount of cobalt protects the alloy grain boundaries from oxidation and positively affects rate capabilities of alloys.

$A_{1.065}B_5$ alloys with manganese have oxides and rare earth inclusions, which decrease the rate capabilities of these alloys. Those phases are inactive in absorption process.

The presence of other phases in AB_x with manganese was already described.

The grain size of NiMH alloys was estimated only for nonstoichiometric alloys. The grain size of stoichiometric alloys was not estimated because of poor visibility of grain boundaries.

6.7 DTA Results

DTA gives dependable results in terms of melting point of NiMH alloys but can not give accurate results regarding the phases present in NiMH alloys. For example $Mm_{0.88}Ni_{3.43}Co_{0.71}Al_{0.76}$ exhibits one endothermic peak at 1467.85 °C although it has Ni-Co-Al phase, oxides and AB_5 matrix. Also the presence of these phases was not detected with XRD analysis.

The influence of number of A or B-side atoms on melting point of NiMH alloys with or without manganese is not significant. The melting point of all alloys differ by a couple degrees.

CHAPTER 7

CONCLUSIONS

1. NiMH alloys can be produced in arc and induction melting units. IMW alloys have fewer oxides than AMW alloys because of design of the equipment used.
2. Stoichiometric ACW and IMW alloys have hydrogen equilibrium pressures well below atmospheric pressure, which makes them suitable for battery application. The numbers of absorbed hydrogen atoms obtained in Sievert's apparatus for NiMH alloys with and without manganese correspond to the capacity obtained electrochemically and the literature data.
3. XRD analysis is a suitable method of characterization of NiMH alloys. The precision and accuracy of XRD analysis is high. Cell volume of NiMH alloys is one of the major factors in characterization of NiMH alloys. The cell volumes increase for ACW and alloys heat-treated at 800 °C and decreases for alloys heat-treated at 1000°C.
4. Stoichiometry of NiMH alloys plays an important role. The increase of number of A-side atoms in NiMH alloys generally leads to increase of cell volume and the **a**-axis. The increase of number of A-side atoms leads to decrease of the **c**-axis. Heat treatment affects the chemical composition of the matrix i.e. the size of **a** and **c**-axes. The size of both axes is in good agreement with the number of A or B-side atoms in the matrix of NiMH alloys without manganese. The number of A or B side atoms in matrix is not in good agreement with the size of **a** or **c** –axes for NiMH alloys with manganese because the manganese occupy positions on both axes.

5. The increase of number of B-side atoms in NiMH alloys without manganese causes an increase of cell volume for ACW alloys and a decrease of cell volume for heat-treated alloys. The increase of number of B-side atoms in NiMH alloys with manganese causes a decrease of cell volume.
6. Heat treatment at 800°C increases discharge capacity of NiMH alloys without manganese. Heat treatment at 1000°C drastically decreases the discharge capacity of NiMH alloys without manganese except for nonstoichiometric $A_{0.88}B_5$ alloy and $AB_{4.376}$. Those alloys have the highest discharge capacity and rate capability of heat-treated alloys at 1000°C.
7. The increase of the number of A-side atoms causes decreases of rate capability of NiMH alloys without manganese. Heat treatment at 800 °C increases the rate capability of those alloys.
8. The increase of the number of B-side atoms causes increase of rate capability of NiMH alloys without manganese.
9. The increase of the number of A-side atoms in NiMH alloys with manganese causes an increase of discharge capacity and rate capability. ACW alloys exhibit good rate capability along all ranges. Heat treatment at 800°C decreases the rate capability of A_xB_5 ($x = 0.92-1.065$) NiMH alloys with manganese.
10. The increase of number of B-side atom increases the rate capability of ACW NiMH alloys. The increase of B-side atoms for heat-treated alloys at 800°C causes the decrease of discharge capacity and rate capability.

11. Method of production affects the discharge capacity and rate capability. The IMW alloys have larger grain size and fewer oxides. The discharge capacity and rate capability of those alloys is very good.
12. Stoichiometry affects the melting points of NiMH alloys. DTA analysis is not a suitable tool for phase detection in NiMH alloys.
13. Several new chemical compositions of NiMH alloys were produced and examined. The achieved results are promising for further development and commercialization.

CHAPTER 8

RECOMMENDATIONS FOR FUTURE WORK

1. $\text{Mm}_{0.88}\text{Ni}_{3.43}\text{Co}_{0.71}\text{Al}_{0.76}$ heat-treated at 800°C exhibits a discharge capacity about 220 mAh/g and excellent rate capability. This alloy has about 9.7 % by wt. lanthanum and 17 % by wt. cerium. An alloy with mischmetal composition containing about 17 % by wt. lanthanum and about 10 % cerium would have a larger cell volume and higher discharge capacity. Heat treatment at 800°C would give such an alloy excellent rate capability.
2. $\text{Mm}_{0.92}\text{Ni}_{3.33}\text{Co}_{0.69}\text{Al}_{0.8}$ (new composition) exhibits the largest cell volume among all alloys evaluated in this work. This alloy does not have any cerium. The replacement of one part of neodymium with cerium would increase discharge capacity and rate capability of this alloy. This alloy also has oxides in its microstructure. The induction-melted alloy is virtually free of oxide, which also positively affects the rate capability of alloys. This alloy has to be produced in an induction melting furnaces.
3. $\text{Mm}_{0.99}\text{Ni}_{3.78}\text{Co}_{0.756}\text{Al}_{0.84}$ (new composition) has a discharge capacity about 240 mAh/g and very good stability and rate capability. Further investigation of heat treatment at 1000°C could leads to further improvement of rate capability. The increase of discharge capacity could be achieved by increasing the amount of lanthanum in the mischmetal.
4. $\text{Mm}_{0.98}\text{Ni}_{3.33}\text{Co}_{0.79}\text{Mn}_{0.35}\text{Al}_{0.3}$ heat-treated at 800°C (new composition) has a discharge capacity about 300 mAh/g and excellent rate capability. An attempt should be made to produce the same composition without oxide.
5. $\text{Mm}_{0.92}\text{Ni}_{3.48}\text{Co}_{0.83}\text{Mn}_{0.29}\text{Al}_{0.31}\text{ACW}$ (new composition) has a discharge capacity about 230 mAh/g and excellent rate capability and stability. At a higher discharge rate than 92

mA/g the discharge capacity increased. Further investigations on this composition and the influence of grain size on rate capability are highly recommended.

6. The increase of cobalt-nickel content on grain boundaries brings alloy high rate capability. Further investigation on influence of cobalt-nickel is highly recommended. The experiments with $Mm_{1.02}(Ni-Co)_xAl_{0.8}$ $x = 4.3-4.6$ type alloy or alloys mentioned above but having more nickel and cobalt (nonstoichiometric composition) would lead to higher rate capability of those alloys.

REFERENCES

1. H.H Van Mal, “ Stability of Ternary Hydrides and Some Application”, Thesis, Technological University, Delft, May 1976
2. K.H.J. Buschow, P.C.P. Bouten and A.R. Miedema, “Hydrides Formed from Intermetallic Compounds of Two Transition Metals: a Special Class of Ternary Alloys”, Rep. Prog. Phys., Vol.45, 1982
3. J.J.G. Willems, “Metal Hydride Electrodes Stability of LaNi₅-Related Compounds” Philips Journal of Research, Vol. 39 Suppl. No.1 1984
4. J.J.G. Willems,” Investigation of a New Type of Rechargeable Battery, the Nickel – Hydride Cell “Philips Tech. Rev. 43 No1/2 22-34, Dec.1986
5. F.A.Kuijpers, “RCO₅-H and Related Systems”, Thesis, Technical University, Delft, July 1973, Philips Tech. Repts Suppl. 1973, No.2
6. Shyam Kumar, R. Balasubramaniam, “ Theoretical Analysis of Hysteresis During Hydrogen Transformations in Vanadium-Hydrogen System” Int. J. Hydrogen Energy, Vol. 20, No.3, pp. 211-220, 1995
7. G.D. Sandrock, “The Metallurgy and Production of Rechargeable Hydrides”, The International Nickel Company, Inc. INCO Research and Development Center, Sterling Forest, Suffern, NY 10901 USA
8. Gary Sandrock, “Intermetallic Hydrides: History and Application”, The Electrochemical Proceeding Volume 94-27
9. Iver E. Anderson, M.G. Osborne and T.W. Ellis, “The Effect of Solidification and Atomization on Rare-Earth Alloys, JOM, March 1996

10. H. Diaz, A. Perchiron-Guegan, J.C. Archard, "Thermodynamic and Structural Properties of $\text{LaNi}_{5-y}\text{Al}_y$ Compounds and Their Related Hydrides", Int. J. Hydrogen Energy Vol. 4, pp. 445-454, 1979
11. L. Schlapbach, A. Seiler, H.C. Siegmann, T. v. Waldkirch and P. Zurcher, "Self Restoring of the Active Surface in LaNi_5 ", Int. J. Hydrogen Energy Vol. 4 pp. 21-28 1979
12. K.H.J. Buschow and H.H. Van Mal, "Phase Relations and Hydrogen Absorption in the Lanthanum -Nickel Systems", Journal of Less-Common Metals, 29(1972) 1-5
13. H.H. Van Mal, K.H.J. Buschow and A. Kuijpers, "Hydrogen Absorption and Magnetic Properties of $\text{LaCo}_{5x}\text{Ni}_{5-5x}$ Compounds", Journal of Less Common Metals. 32(1973) 289-296
14. J.H.N. van Vucht, F.A. Kuijpers and H.C.M. Bruning, "Reversible Room - Temperature Absorption of Large Quantities of Hydrogen by Intermetallic Compounds", Philips Res. Repts. 25, 133-140 1970
15. Timothy W. Ellis, Larry L. Jones and Tamara E. Bloomer, "Effect of Oxygen on the Solidification Structure of LaNi_5 " JOM February 1995
16. D.G. Westlake, "Hydrides of Intermetallic Compounds: a Review of Stabilities, Stoichiometries and Preferred Hydrogen Sites", Journal of Less-Common Metals, 91 (1983) 1-20
17. A. Percheron-Guegan, C. Lartigue and J.C. Achard, "Neutron and X-Ray Diffraction Profile Analysis and Structure of LaNi_5 , LaNi_{5-x} , $\text{LaNi}_{5-x}\text{Al}_x$ and $\text{LaNi}_{5-x}\text{Mn}_x$ Intermetallics and Their Hydrides (Deuterides)", Journal of the Less Common Metals, 74 (1980) 1-12

18. T.Sakai, Rare Earth Intermetallics for Metal Hydrogen Batteries”, Handbook on the Physics and Chemistry of Rare Earth Vol. 21 1995, Chapter 142
19. A. Perchereon-Guegan, M. Latroche, J.C.Achard, Y.Chabre, J.Bouet,” Correlation’s Between the Structure and Thermodynamic Properties of LaNi_5 -Type Hydrides and Their Electrodes Performances”, The Electrochemical Society Proceedings Volume 94-27
20. C. Lartigue, A. Perchereon-Guegan and J.C.Achard,” Thermodynamic and structural Properties of $\text{LaNi}_{5-x}\text{Mn}_x$ Compounds and Their Hydrides”, Journal of the Less Common Metals, 75 (1980) 23-29
21. J.Lamloumi, A. Perchereon-Guegan and J.C.Achard, G.Jechano and D. Givord,” Study of the Pseudobinary Compounds $\text{LaNi}_{5-x}\text{Fe}_x$ ($x \leq 1.2$) by X-Ray Diffraction, Mossbauer and Magnetic Measurements”, J. Physique 45(1984) 1643-1652
22. Haruhisa Uchida, Masayishi Tada and Yen C. Huang,” The Influence of Cerium, Praseodymium, Neodymium, and Samarium on Hydrogen Absorption In LaNi_5 Alloys”, Journal of the Less Common Metals, 88 (1982) 81-87
23. G.R. Paulin, “Electrochemistry for Technologists”, Pergamon Press 1969
24. David J.G. Ives and George J. Janz,” Reference Electrodes, Theory and Practice”, Academic Press 1961
25. V.S. Bagotzky and A.M. Skudin,” Chemical Power Sources”, Academic Press, London (1980)
26. A.H. Boonstra, G.J.M. Lippits and T.N.M. Bernards, Degradation Process In LaNi_5 Electrodes”, Journal of the Less Common Metals, 155 (1989) 119-131
27. L.Slapbach, A. Seiler, F. Stucki and H.C Siegmann,” Surface Effects and the Formation of Metal Hydrides”, Journal of the Less Common Metals, 73 (1980) 145-160

28. Tetsuo Sakai, Hiroshy Miamura, Nobuhiro Kutiyama, Akihiko Kato, Keisuke Oguro and Hiroshi Ishikawa,” The Influence of Small Amounts of Added Elements on Various Performance Characteristics for $\text{LaNi}_{2.5}\text{Co}_{2.5}$ Based Alloy”, Journal of the Less Common Metals, 159 (1990) 127-139
29. Tetsuo Sakai, Keisuke Oguro, Hiroshy Miamura, Nobuhiro Kutiyama, Akihiko Kato and Hiroshi Ishikawa,” Some Factors Affecting The Cyclic Lives of LaNi_5 -Based Alloy Electrodes of Hydrogen Batteries”, Journal of the Less Common Metals, 161 (1990) 193-202
30. N. Furukawa,“ Development and Commercialization of Nickel-Metal Hydride Secondary Batteries” Journal of Power Sources, 51 (1994) 45-59
31. Y Osumi, A. Kato, H. Suzuki and M. Nakane,” Hydrogen Absorption-Desorption Characteristics of Mischmetals-Nickel-Alumina alloys”, Journal of the Less Common Metals, 66(1979) 67-75
32. Y. Osumi, H. Suzuki, A.Kato, K. Oguro, M. Nakane, “ Development of Mischmetal – Nickel and Titanium Cobalt Hydrides for Hydrogen Storage”, Journal of the Less Common Metals, 74(1980) 2271-277
33. T. Sakai, T. Hazema, H. Miyamura, N. Kuriyama, A. Kato and H. Ishikawa, “Rare – Earth Based Alloys Electrodes for Nickel –Metal Hydride Battery”, Journal of the Less Common Metals, 172 174 (1991) 1175-1184
34. Y. Osumy, H. Suzuky, A. Kato, K.Oguro and M. Nakane, “Hydrogen Absorption Desorption Characteristics of Mischmetal-Ni-Cr-Mn Alloys”, Journal of the Less Common Metals, 79(1981) 207-214

35. Y. Osumy, H. Suzuki, A. Kato, K.Oguro and M. Nakane,” Hydrogen Absorption-Desorption characteristics of Mm-Ni-Al-M and Mm-Ni-Mn-M Alloys (Mm = Mischmetal)”, Journal of the Less Common Metals, 89(1983) 287-292
36. M. Nogami, K. Moriwaki and N. Furukawa, “ New Development In Nickel Hydride Batteries”
37. Tetsuo Sakai, Hiroshi Miyamura, Noburo Kuriyama, Akhikiko Kato, Keiske Oguro and Hiroshi Ishikawa” Metal Hydride Anodes for Nickel-Hydrogen Secondary Battery”, J. Electrochemi. Soc., Vol. 137 No3, March 1990
38. J. Balej, “Determination of the Oxygen and Hydrogen Overvoltage in Concentrated Alkali Hydroxide Solution”, Int. J. Hydrogen Energy, Vol. 10, No. 6 pp. 365-374,1985
39. A. Anany, A. Visintin, S. Srinivasan, A. J. Appleby, J.J. Reilly and J.R. Jonson, Capacity Retention in Hydrogen Storage Alloys” Electrochemical Society Proceedings Volume 92-5
40. P.H.L. Notten and P. Hokkeiling, “ Double-Phase Forming Compounds: A New Class of Highly Electrocatalytic Materials”, J. Electroche. Soc. Vol. 92-5
41. Tetsuo Sakai, Hiroshi Miyamura, Noburo Kuriyama, Akhikiko Kato, Keiske Oguro and Hiroshi Ishikawa”, Nickel/Metal Hydride Battery using Hydrogen Storage Alloys”.
42. L. Zhang, T. J. O’Hara, M.G. Michel, Microstructure of Hydride Alloy and Its Effect on Cyclic Performance of Nickel Metal Hydride Batteries”, The Electrochemical Society Proceedings Volume 94-27
43. T. Sakai, H. Miyamura, H. Kuriyama, H. Ishikawa and I. Uehara,” Hydrogen Storage Alloys for Nickel-Metal Hydride Battery”, Zeitschrift fur Physikalische Chemie, Bd. 183, S. 333-346

44. Yukio Fukimoto, Masyoshi Miyamoto, Maso Matsuoka, Chiaki Iwakura,” Effect of the Stoichiometric Ratio on Electrochemical Properties of Hydrogen Storage Alloys for Nickel Metal Hydride Batteries”, *Electrochimica Acta*, Vol.40 No. 7 pp. 845-848, 1995
45. M. Tadakoro, M. Nogami, Y.Chikano, M. Kimoto, T. Ise, K. Nishio and N. Furikawa,” Development of Hydrogen Storage Alloys for Nickel Metal Hydride Secondary Batteries”, *Journal of Alloys and Compounds*, 192 (1993) 179-181
46. T. Sakai, H. Miyamura, H. Kuriyama, H. Ishikawa and I. Uehara” Rare-earth-Based Hydrogen Storage Alloys for Rechargeable Nickel Metal-Hydride Batteries”, *Journal of Alloys and Compounds*, 192(1993) 155-157
47. M. Tadakoro, K. Moriwaki, K. Nishio, M. Nogami, I. Inoue, Y.Chikano, M. Kimoto, T. Ise, R. Maeada, F. Mizutaki, M. Takee and N. Furukawa,” Development of Hydrogen Absorbing Alloys for Nickel Metal Hydride Secondary Batteries”, *Development of Hydrogen Absorbing Alloys for Nickel Metal Hydride Secondary Batteries*, The Electrochemical Society Proceedings Volume 92-5
48. T. Sakai, K. Muta, H. Miyamura, N.Kuriyama and H. Ishikawa, “Nickel-Metal Hydride Batteries Using Rare-Earth Base Hydrogen Storage Alloys”, *The Electrochemical Society Proceedings Volume 92-5*
49. T. Sakai, K. Muta, H. Miyamura, N. Kuriyama and H. Ishikawa,” “Nickel-Metal Hydride Batteries Using Rare-Earth Base Hydrogen Storage Alloys”, *Journal of Alloys and Compounds*, 180(1992) 37-54
- 50.T. Sakai, H. Yoshinaga, H. Miyamura, N. Kuriyama, H. Ishikawa and I. Uehara”” Metal Hydride Thin Film Electrodes Prepared by R. F. Sputtering”, *Journal of Alloys and Compounds*, 192(1993) 182-184

51. R. Mishima, H. Miyamura, R. Sakai, N. Kuriyama, H. Ishikawa and I. Uehara, "Hydrogen Storage Alloys Rapidly Solidified by the Melt-Spinning Method and Their Characteristics as Metal Hydride Electrodes", *Journal of Alloys and Compounds*, 192(1993) 176-178
52. K. Takeya, Y. Tsugita, Y. Okayima, T. Sakai, H. Miyamura, N. Kuriyama, H. Ishikawa and I. Uehara, "Hydrogen Storage Alloys Produced By a Reduction –Diffusion Process and Their Electrode Properties", *Journal of Alloys and Compounds*, 192(1993) 167-168
53. Anaba Anani, Arnaldo Visintin, Konstantin Petrov and Supramaniam Srinivasan, "Alloys for Hydrogen Storage in Nickel /Metal Hydride Batteries", *Journal of Power Sources*, 47 (1994) 261-275
54. S. Mukerjee, J. McBreen, J.J. Reilly, J.R. Johnson, G. Adzic, M.P.S. Kumar, W. Zhang and S. Srinivasan, "Effect of Ce composition of Structural and Electronic Characteristics of Some Metal Hydride Electrodes: AXANEX and EXAFS Investigation", *The Electrochemical Proceedings Volume 94-27*
55. G. D. Adzic, J.J. Reilly, J. McBreen, J.R. Johnson, G. Adzic M.P.S. Kumar, W. Zhang and S. Srinivasan, "Composition and Cyclic Life of Multicomponent AB₅ Hydride Electrodes", *The Electrochemical Proceedings Volume 94-27*
56. K. Suzuki, N. Yanagihara, H. Kawano, and A. Ohta, "Effect of Rare Earth Composition on Electrochemical Properties of Mm(Ni-Mn-Al-Co)₅ Alloys", *Journal of Alloys and Compounds*, 192(1993) 173-175

57. Jon-Ha Lee, Ki-Young Lee, Jai Young Lee, “ Self Discharge Behavior of Sealed NiMH Batteries Using $\text{MmNi}_{3.3+x}\text{Co}_{0.7}\text{Al}_{1.0-x}$ Anodes”, Journal of Alloys and Compounds, 232(1996) 197-203
58. Chiaki Iwakura, Masao Matsuoka, Totsuka Kohno,” Mixing Effect of Metal Oxides on Negative Electrode Reaction in The Nickel-Hydride Battery”, J. Electrochem. Soc. Vol. 141, No. 9, September 1994
59. Mingming Geng and Dereck O. Nortwood,” The Characteristics of Negative Electrode of a Nickel Metal Hydride Battery”, Int. J. Hydrogen Energy, Vol. 21 No.10 pp. 887-890, 1996
60. Noburo Sato Minako Onodera, Kazuhiko Yagi, Katsunory Nakaya, “ Electrochemical Properties of Rare Earth Hydrogen Storage Alloy Electrodes and Structural Analysis By Means of The Rietveld Method”, The Chemical Society of Japan 1992, (11) pp. 1294-1300
61. M.M Jaksic, “ Electrocatalisys of Hydrogen Evolution in the Light of the Brewer-Engel Theory for Bonding in Metals and Intermetallic Phases.” Electrochemica Acta, Vol.29 No.11 pp. 1539-1550, 1984
62. M.M Jaksic, “Towards the Reversible Electrode for Hydrogen Evolution in Industrially Important Electrochemical Processes” Int. J. Hydrogen Energy, Vol. 11, pp. 519-532, 1986
63. M.M Jaksic, “Advances in Electrocatalysis for Hydrogen Evaluation in the Light of the Brewer-Engel Valence-Bond Theory”, Journal of molecular Catalysis, 38 (1986) 161-202

64. F. Meli, A. Zuttel and L. Schlapbach", Electrochemical and Surface Properties of Low Cost, Cobalt Free LaNi_5 -type Hydrogen Storage Alloys", Journal of Alloys and Compounds, 202(1993) 81-88
65. Nobuhiro Kuriyama, Tetsuo Sakai, Hiroshi Miyamura, Hidaki Tanaka, Hiroshi Ishikawa, and Itsuki Uehara," Hydrogen Storage Alloys for Nickel/Metal-Hydride Battery", Vacuum, Volume 47/numbers 6-8/pages 889 to 892/1996
66. F. Meli, A. Zuttel and L. Schlapbach", Effect of Silicon on the Properties of AB_5 -Based Alloys for Battery Electrode Application"" Zeitschrift fur Physikalische Chemie, Bd. 183, S. 371-377 (1994)
- 67.Y. Chikano, K. Kimoto, R. Maeda, M. Nogami, K. Nishio, T. Saito, S. Nakahore, S. Murakami and N. Furukawa, " Development of Long Life NiMH Secondary Battery", The Electrochemical Proceedings Volume 94-27
68. I. I. Yonezu and M. Nogami," Development of High Capacity Hydrogen Absorbing Alloys for High Performance Nickel-Metal Hydride Batteries"

APPENDICES

Appendix 1 Chemical composition of $\text{Mm}_{0.99}\text{Ni}_{3.45}\text{Co}_{0.85}\text{Mn}_{0.41}\text{Al}_{0.31}\text{IMW}$ determined by

ICP

	1	2	3	4	5	6	7	8	9	10	avg.	sdev.
Co	11.91	11.94	11.93	11.89	11.93	11.89	11.95	12.01	11.96	11.9	11.93	0.037
Ni	48.25	48.3	48.17	48.39	48.16	48.11	48.46	48.39	48.32	48.14	48.23	0.121
Mn	5.3	5.31	5.3	5.3	5.3	5.3	5.33	5.35	5.33	5.33	5.32	0.018
Al	1.94	1.96	1.96	1.95	1.92	1.93	1.95	1.95	1.93	1.92	1.94	0.015
La	17.13	17.15	17.16	17.23	17.01	17.1	17.27	17.3	17.2	17.12	17.17	0.085
Ce	11.67	11.73	11.69	11.71	11.73	11.72	11.71	11.79	11.73	11.73	11.73	0.034
Pr	1.06	1.06	1.06	1.07	1.04	1.02	1.04	1.07	1.05	1.05	1.05	0.015
Nd	3.65	3.63	3.64	3.67	3.6	3.6	3.61	3.6	3.6	3.65	3.63	0.0249

For wavelength 3988 Å for La the results are as follows:

La	17.17	17.14	17.25	17.19	16.8	16.92	17.11	17.19	17.06	17.04	17.08	0.137
----	-------	-------	-------	-------	------	-------	-------	-------	-------	-------	-------	-------

Appendix 2¹ EDS analysis of matrix, rare earth rich phase, nickel alumina rich phase and oxides of NiMH alloys

	La	Ce	Pr	Nd	Ni	Co	Mn	Al	O
1. IBA # 5 MmNi _{3.5} Co _{0.7} Al _{0.8}	9.4	17.9	2.8	4.3	51.2	10.1		4.3	
2. IBA # 6MmNi _{3.5} Co _{0.8} Mn _{0.4} Al _{0.3}	17.2	11.4	1	3.5	49.7	10.3	5	1.8	
3. Mm _{0.88} Ni _{3.43} Co _{0.71} Al _{0.76} *	9.13	16.9	2.13	4.61	51.2	10.5		4.5	
GRAIN BOUNDARY	1.22	2.8	0.62	0.36	59.8	15.4		19.8	
Mm _{0.88} Ni _{3.43} Co _{0.71} Al _{0.76} **	9.08	16.7	2.72	4.91	51.9	10.2		4.41	
GRAIN BOUNDARY	2.51	5.05	0.59	0.65	56.3	16.2		18.7	
Mm _{0.88} Ni _{3.43} Co _{0.71} Al _{0.76} ***	9.11	16.9	2.86	5.06	51.4	10.1		4.53	
GRAIN BOUNDARY	1.09	2.09	0.18	0.46	59.4	16.6		20.2	
OXIDE	41.5	27.48	2.43	11.6	1.59	0.40		0.07	14.83
4. Mm _{0.99} Ni _{3.5} Co _{0.7} Al _{0.81} *	9.68	16.9	1.28	5.03	51.8	10.7		4.61	
NICKEL ALUMINA PHASE	2.14	3.37	0.11	0.61	58.6	14.1		21.2	
OXIDE	40	25.1	3.33	11.5	3.55	0.87		0.41	15.3
Mm _{0.99} Ni _{3.5} Co _{0.7} Al _{0.81} **	9.94	17.4	1.14	4.63	51.5	10.6		4.88	
NICKEL ALUMINA PHASE	1.03	1.53	0.17	0.37	57	15.7		24.3	
OXIDE	42.5	26.9	2.31	11.3	1.79	0.25		0.11	14.9
5. MmNi _{3.48} Co _{0.71} Al _{0.81} *	9.75	17.4	0.91	4.57	51.8	10.7		4.97	
6. Mm _{1.09} Ni _{3.45} Co _{0.72} Al _{0.85} *	9.41	18.2	2.25	4.29	49.9	10.4		5.52	
RARE EARTH RICH PHASE	12.6	26.7	1.57	3.91	41.9	9.65		3.48	
Mm _{1.09} Ni _{3.45} Co _{0.72} Al _{0.85} **	9.14	18.6	2.68	4.69	49	10.4		5.56	
RARE EARTH RICH PHASE	12.3	25.4	2.07	3.81	43.1	10.2		3.1	
Mm _{1.09} Ni _{3.45} Co _{0.72} Al _{0.85} ***	9.68	19.2	1.85	4.18	48.49	10.42		6.16	

¹ *- ACW

** - heat treated at 800 °C

*** heat treated at 1000 °C

	RARE EARTH RICH PHASE	13.4	25.1	2.83	4.87	40.5	10		3.37
7.	Mm _{0.92} Ni _{3.33} Co _{0.69} Al _{0.8} *	8.9	0.11	3.13	22.9	50.1	10.3		4.51
	RARE EARTH RICH PHASE	42.7	0.14	4.75	19	26.3	5.69		1.31
	Mm _{0.92} Ni _{3.33} Co _{0.69} Al _{0.8} **	9.48	0.13	3.35	22.9	49	10.2		4.89
	RARE EARTH RICH PHASE	26.7	0.11	4.78	25.3	25.7	14.4		2.81
	Mm _{0.92} Ni _{3.33} Co _{0.69} Al _{0.8} ***	9.89	0.01	3.1	23.9	47	9.84		6.06
	RARE EARTH RICH PHASE	34.8	0.3	5.12	29.4	12.3	16.8		0.95
8.	Mm _{0.99} Ni _{3.78} Co _{0.756} Al _{0.84} *	9.09	17.1	2.05	4.85	52.1	10.4		4.64
	GRAIN BOUNDARY	3.8	7.22	2.71	0.72	56.7	13.5		16.4
	Mm _{0.99} Ni _{3.78} Co _{0.756} Al _{0.84} **	9.09	16.9	2.71	5.12	51.3	10.4		4.45
	GRAIN BOUNDARY	1.56	2.93	0.28	0.48	56.3	17		21.4
9.	MmNi _{3.54} Co _{0.82} Mn _{0.34} Al _{0.3} *	16.1	11.2	0.78	3.63	50	11.9	4.06	2.33
	OXIDE	58.3	14.5	1.72	7.35	2.14	0.57	0.43	0
	NICKEL ALUMINA PHASE	2.52	4.24	0.49	0.92	58.2	14.6	0.02	19.1 14.89
	RARE EARTH RICH PHASE	38.6	12.2	1.01	3.67	25.9	14.4	2.75	1.38
	MmNi _{3.54} Co _{0.82} Mn _{0.34} Al _{0.3} **	16.8	11.3	0.85	3.08	49.6	11.4	2.75	1.38
	OXIDE	55.4	19.5	1.39	8.55	0.2	0.04	0.21	0 14.7
	MmNi _{3.54} Co _{0.82} Mn _{0.34} Al _{0.3} ***	16.2	11	1.26	3.44	49.7	11.6	4.54	2.32
	NICKEL ALUMINA PHASE	3.8	3.14	0.78	1.29	48.3	26.6	11.5	4.56
	OXIDE	54.8	17.5	3.44	8.69	0.58	0	0.26	4.56
10.	Mm _{0.92} Ni _{3.48} Co _{0.83} Mn _{0.29} Al _{0.31} *	15.4	9.1	2.06	4.47	52.1	11.8	2.88	2.22
	DARK PHASE	4.11	3.09	0	0.67	48.5	20.6	19.3	3.68
	OXIDE	50.3	12.5	3.19	8.43	7.2	1.89	1	0 15.5
	Mm _{0.92} Ni _{3.48} Co _{0.83} Mn _{0.29} Al _{0.31} **	15.6	9.36	2.06	4.16	51.5	11.95	3.14	2.27
	Mm _{0.92} Ni _{3.48} Co _{0.83} Mn _{0.29} Al _{0.3} ***	15.5	9.06	2.08	4.63	51.6	11.4	3.49	2.34
	DARK PHASE	7.95	4.83	1.52	2.57	26.07	5.90	1.81	1.22
11.	Mm _{1.065} Ni _{3.5} Co _{0.83} Mn _{0.37} Al _{0.32} *	15.4	9.87	3.29	5.15	49.1	11.8	3.22	2.22
	Mm _{1.065} Ni _{3.5} Co _{0.83} Mn _{0.37} Al _{0.32} **	16.1	9.99	2.31	4.86	48.8	11.8	4	2.29
	RARE EARTH RICH PHASE	20	13.5	1.63	3.88	44.8	9.62	5.13	1.45
	WHITE LINES	18.8	12.8	3.34	4.78	44.7	9.88	4.43	1.4
	Mm _{1.065} Ni _{3.5} Co _{0.83} Mn _{0.37} Al _{0.32} ***	15.6	10.1	2.52	4.88	48.6	11.6	4.53	2.27
	Ni-Co-Al-Mn PHASE	2.07	1.11	0.22	0.64	47.97	28.80	15.1	4.01
12.	Mm _{0.98} Ni _{3.33} Co _{0.79} Mn _{0.35} Al _{0.3} *	15.8	10.1	2.6	4.42	49.1	11.5	4.2	2.3
	OXIDE	24.6	9.42	4	7.28	26	6.1	3.11	1.14
	Mm _{0.98} Ni _{3.33} Co _{0.79} Mn _{0.35} Al _{0.3} **	16.1	9.9	2.7	4.8	48.2	11.4	4.4	2.5
	DULL WHITE PHASE	24.5	9.98	3.35	4.27	40.6	11.6	4.22	1.43
	DARK SPOTS	28.2	13.8	6.76	10.7	30.7	7.29	2.63	0.02

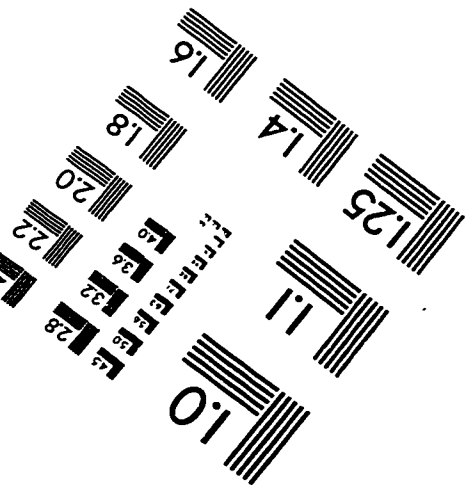
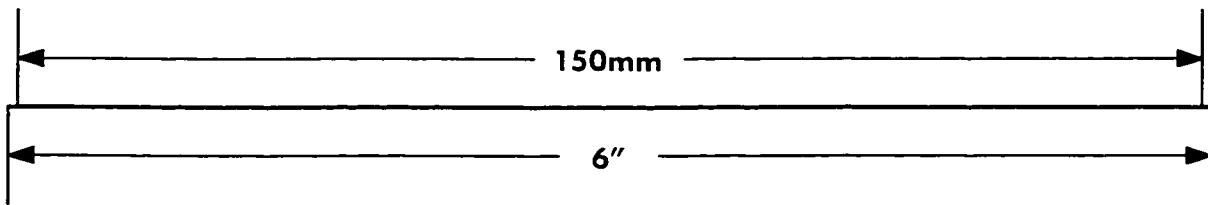
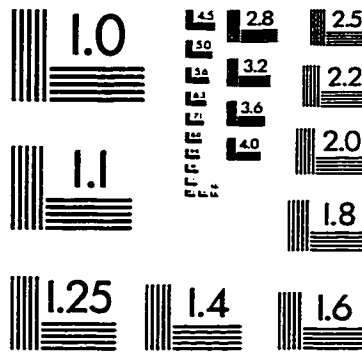
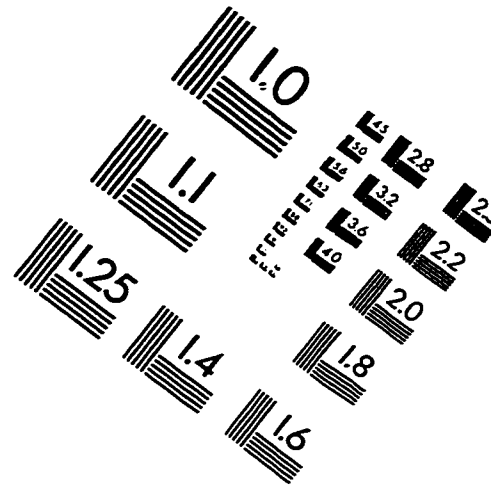
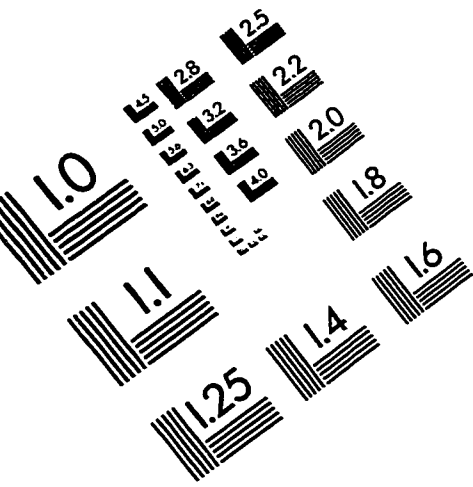
$Mm_{0.98}Ni_{3.33}Co_{0.79}Mn_{0.35}Al_{0.3}$ ***	15.8	9.96	2.84	4.76	48.5	11.4	4.55	2.2	
WHITE PHASE	18.7	13.89	2.41	4.77	45.78	9.40	3.55	1.47	
OXIDE	55.8	11.5	3.89	6.42	5.23	1.41	0.49	0	15.3
14. $Mm_{0.99}Ni_{3.79}Co_{0.9}Mn_{0.4}Al_{0.33}$ *	16	9.37	1.98	4.39	51	11.6	3.45	2.18	
GRAIN BOUNDARY	12.2	8.37	0.81	2.25	47.13	12.67	13.5	2.58	
$Mm_{0.99}Ni_{3.79}Co_{0.9}Mn_{0.4}Al_{0.33}$ **	15.8	8.85	2.76	4.44	50.9	11.4	3.49	2.2	
GRAIN BOUNDARY	9.3	6.1	1.6	1.4	44.4	13.4	18.6	5.3	
14. $Mm_{0.99}Ni_{3.48}Co_{0.7}Al_{0.81}IMW$ *	9.37	17.6	2.61	5.06	49.9	10.1		5.28	
$Mm_{0.99}Ni_{3.48}Co_{0.7}Al_{0.81}IMW$ **	9.82	18	1.19	4.32	50.7	10.3		5.62	
$Mm_{0.99}Ni_{3.48}Co_{0.7}Al_{0.81}IMW$ ***	9.89	18.3	2.96	4.22	50	10.1		5.57	
RARE EARTH RICH PHASE	33.1	22.3	2.28	5.78	17.8	17.1		1.52	
15. $Mm_{0.99}Ni_{3.45}Co_{0.85}Mn_{0.41}Al_{0.31}IMW$ *	16.4	11.1	1.12	3.56	48.5	11.9	5.21	2.26	
OXIDES	59.3	13.2	3.13	9.64	2.85	0.61	0.45	0	15.1
$Mm_{0.99}Ni_{3.45}Co_{0.85}Mn_{0.41}Al_{0.31}IMW$ **	15.9	11.2	1.54	3.65	48.8	11.7	4.7	2.51	
$Mm_{0.99}Ni_{3.45}Co_{0.85}Mn_{0.41}Al_{0.31}IMW$ ***	16	10.9	1.17	3.51	49.2	11.7	5.12	2.35	
OXIDE	19.2	9.81	1.72	3.55	32	10.1	3.17	1.27	19.4

Appendix 3 Discharge capacity, rate capability and stability of NiMH alloy

	Disc.cap.	rate capability	stability
1. $\text{Mm}_{0.88}\text{Ni}_{3.43}\text{Co}_{0.71}\text{Al}_{0.76}^*$	214	-	+/-
2. $\text{Mm}_{0.88}\text{Ni}_{3.43}\text{Co}_{0.71}\text{Al}_{0.76}^{**}$	217	+	+
3. $\text{Mm}_{0.88}\text{Ni}_{3.43}\text{Co}_{0.71}\text{Al}_{0.76}^{***}$	254	+/-	+/-
4. $\text{Mm}_{0.99}\text{Ni}_{3.5}\text{Co}_{0.7}\text{Al}_{0.81}^*$	224	+/--	+/--
5. $\text{Mm}_{0.99}\text{Ni}_{3.5}\text{Co}_{0.7}\text{Al}_{0.81}^{**}$	240	+	+
6. $\text{Mm}_{0.99}\text{Ni}_{3.5}\text{Co}_{0.7}\text{Al}_{0.81}^{***}$	206	+/-	+/-
7. $\text{Mm}_{0.99}\text{Ni}_{3.47}\text{Co}_{0.73}\text{Al}_{0.81}^*$	240	+/-	+/-
8. $\text{Mm}_{0.99}\text{Ni}_{3.47}\text{Co}_{0.73}\text{Al}_{0.81}^{**}$	276	+	+/-
9. $\text{Mm}_{0.99}\text{Ni}_{3.47}\text{Co}_{0.73}\text{Al}_{0.81}^{***}$	211	+/--	+/--
10. $\text{MmNi}_{3.48}\text{Co}_{0.71}\text{Al}_{0.81}^*$	240	+	+/--
11. $\text{MmNi}_{3.48}\text{Co}_{0.71}\text{Al}_{0.81}^{**}$	250	+	+/-
12. $\text{MmNi}_{3.48}\text{Co}_{0.71}\text{Al}_{0.81}^{**}$	211.67	+/-	+/--
13. $\text{Mm}_{1.09}\text{Ni}_{3.48}\text{Co}_{0.72}\text{Al}_{0.85}^*$	236	+	+
14. $\text{MmNi}_{3.48}\text{Co}_{0.71}\text{Al}_{0.81}^{**}$	260	++	+
15. $\text{MmNi}_{3.48}\text{Co}_{0.71}\text{Al}_{0.81}^{***}$	188	-	-
16. $\text{Mm}_{0.92}\text{Ni}_{3.33}\text{Co}_{0.69}\text{Al}_{0.8}^*$	231	-	+/-
17. $\text{Mm}_{0.92}\text{Ni}_{3.33}\text{Co}_{0.69}\text{Al}_{0.8}^{**}$	228	-	+/-
18. $\text{Mm}_{0.92}\text{Ni}_{3.33}\text{Co}_{0.69}\text{Al}_{0.8}^{***}$	39.47	+	+
20. $\text{Mm}_{0.99}\text{Ni}_{3.78}\text{Co}_{0.756}\text{Al}_{0.84}^*$	230	+	+
21. $\text{Mm}_{0.92}\text{Ni}_{3.33}\text{Co}_{0.69}\text{Al}_{0.8}^{**}$	232	+	+
22. $\text{Mm}_{0.92}\text{Ni}_{3.33}\text{Co}_{0.69}\text{Al}_{0.8}^{***}$	240	+	+

23. $\text{MmNi}_{3.54}\text{Co}_{0.82}\text{Mn}_{0.34}\text{Al}_{0.3}^*$	269	++(273)	++
24. $\text{MmNi}_{3.54}\text{Co}_{0.82}\text{Mn}_{0.34}\text{Al}_{0.3}^{**}$	273	+	+/-
25. $\text{MmNi}_{3.54}\text{Co}_{0.82}\text{Mn}_{0.34}\text{Al}_{0.3}^{***}$	65.27	-	-
27. $\text{Mm}_{0.92}\text{Ni}_{3.48}\text{Co}_{0.83}\text{Mn}_{0.29}\text{Al}_{0.31}^*$	225	++(236)	++
28 $\text{Mm}_{0.92}\text{Ni}_{3.48}\text{Co}_{0.83}\text{Mn}_{0.29}\text{Al}_{0.31}^*$	224.6	+	+
29. $\text{Mm}_{0.92}\text{Ni}_{3.48}\text{Co}_{0.83}\text{Mn}_{0.29}\text{Al}_{0.31}^{***}$	227	+	+
30. $\text{Mm}_{1.065}\text{Ni}_{3.51}\text{Co}_{0.83}\text{Mn}_{0.37}\text{Al}_{0.32}^*$	287	+	+
31. $\text{Mm}_{1.065}\text{Ni}_{3.51}\text{Co}_{0.83}\text{Mn}_{0.37}\text{Al}_{0.32}^{**}$	273	+/-	+/-
32. $\text{Mm}_{1.065}\text{Ni}_{3.51}\text{Co}_{0.83}\text{Mn}_{0.37}\text{Al}_{0.32}^{****}$	223	-	-
33. $\text{Mm}_{0.98}\text{Ni}_{3.33}\text{Co}_{0.79}\text{Mn}_{0.35}\text{Al}_{0.3}^*$	234	--	--
34. $\text{Mm}_{0.98}\text{Ni}_{3.33}\text{Co}_{0.79}\text{Mn}_{0.35}\text{Al}_{0.3}^{**}$	312	++	++
35. $\text{Mm}_{0.98}\text{Ni}_{3.33}\text{Co}_{0.79}\text{Mn}_{0.35}\text{Al}_{0.3}^{***}$	246	+/-	+/-
36. $\text{Mm}_{0.99}\text{Ni}_{3.79}\text{Co}_{0.9}\text{Mn}_{0.4}\text{Al}_{0.333}^*$	231	+	+
37. $\text{Mm}_{0.99}\text{Ni}_{3.79}\text{Co}_{0.9}\text{Mn}_{0.4}\text{Al}_{0.333}^{**}$	240	+/-	+
38. $\text{Mm}_{0.99}\text{Ni}_{3.79}\text{Co}_{0.9}\text{Mn}_{0.4}\text{Al}_{0.333}^{***}$	240	+/-	+
39. $\text{Mm}_{0.99}\text{Ni}_{3.48}\text{Co}_{0.7}\text{Al}_{0.81}\text{IMW}^*$	254	++	++
40. $\text{Mm}_{0.99}\text{Ni}_{3.48}\text{Co}_{0.7}\text{Al}_{0.81}\text{IMW}^{**}$	266	+/-	-
41. $\text{Mm}_{0.99}\text{Ni}_{3.48}\text{Co}_{0.7}\text{Al}_{0.81}\text{IMW}^{***}$	57	++	++
42. $\text{Mm}_{0.99}\text{Ni}_{3.45}\text{Co}_{0.85}\text{Mn}_{0.41}\text{Al}_{0.31}\text{IMW}^*$	277	++	++
43. $\text{Mm}_{0.99}\text{Ni}_{3.45}\text{Co}_{0.85}\text{Mn}_{0.41}\text{Al}_{0.31}\text{IMW}^{**}$	300	++	++
44. $\text{Mm}_{0.99}\text{Ni}_{3.45}\text{Co}_{0.85}\text{Mn}_{0.41}\text{Al}_{0.31}\text{IMW}^{***}$	32	+	+

IMAGE EVALUATION TEST TARGET (QA-3)



APPLIED IMAGE, Inc.
1653 East Main Street
Rochester, NY 14609 USA
Phone: 716/482-0300
Fax: 716/288-5989

© 1993, Applied Image, Inc., All Rights Reserved

